UNIVERSIDAD COMPLUTENSE DE MADRID
FACULTAD DE CIENCIAS FÍSICAS
DEPARTAMENTO DE ÓPTICA

TESIS DOCTORAL

Modelling and production of surface and subsurface photonics elements by ultrafastlaser structuring od dielectrics

Modelización y producción de elementos fotónicos en superficie y volumen por estructuración de dieléctricos con pulsos láser ultracortos

MEMORIA PARA OPTAR AL GRADO DE DOCTOR

PRESENTADA POR

Jesús del Hoyo Muñoz

DIRECTOR

Francisco Javier Solís Céspedes

Madrid, 2017

MODELLING AND PRODUCTION OF SURFACE AND SUB-SURFACE PHOTONICS ELEMENTS BY ULTRAFAST-LASER STRUCTURING OF DIELECTRICS

Modelización y producción de elementos fotónicos en superficie y en volumen por estructuración de dieléctricos con pulsos láser ultracortos

Memoria de tesis presentada por

Jesús del Hoyo Muñoz

en el

Departamento de Óptica, Facultad de Ciencias Físicas,
Universidad Complutense de Madrid

para optar al grado de

Doctor en Ciencias Físicas

Memoria de tesis dirigida por

Prof. Francisco Javier Solís Céspedes

Madrid, 2016

Acknowledgements

El trabajo reflejado en esta tesis no podría haberse completado (ni comenzado) sin la ayuda y colaboración de mucha gente, a la que estoy muy agradecido. En primer lugar, quería darle las gracias a mi director de tesis, el Prof. Javier Solís, por permitirme unirme al Grupo de Procesado por Láser del Instituto de Óptica del CSIC. Su profundo conocimiento de la materia, su optimismo y buen hacer han sido imprescindibles en la consecución de este trabajo.

En segundo lugar quería darle las gracias al Dr. Toney Teddy Fernandez. Su profesionalidad e intuición permitió obtener resultados muy interesantes. También quería agradecer al Dr. Andrés Ferrer el haberme acompañado en los primeros pasos en la producción de guías de onda y enseñado a desenvolverme en el laboratorio; también al Dr. Alexandro Ruiz, gran conocedor de las simulaciones por ordenador. Y no puedo olvidar al Dr. Jan Siegel, maestro de la microscopía.

También quiero agradecer al resto de miembros del grupo que han colaborado en los experimentos: el Dr. Miguel Jiménez, el Prof. José María Fernández-Navarro, el Dr. Pedro Moreno-Zárate, el Dr. José Gonzalo, la Dra. Rosalía Serna, Carlos Alonso, la Dra. Ana Villafranca y Lucía Labrador. Merecen especial atención los técnicos, que con su labor permiten que los experimentos funcionen: Fátima Cabello, Sergio Pitel, Julia Atiénzar y Marina García. Por último, mencionar la ayuda prestada por el resto de miembros del grupo: el Dr. Marcial Galván, Iván Camps, el Dr. Javier Fernández-Rueda, Mario García-Lechuga, el Dr. Daniel Puerto, el Dr. Giorgio Baraldi, la Dra. Roberta Morea y el Dr. Alexander Cuadrado. También tengo que agradecer la ayuda prestada por otros investigadores, como la Dra. Belén Mate, el Dr. Javier Portilla, el Dr. Juan Diego Ania y el Dr. Pedro Corredera.

Tampoco me quiero olvidar de nuestros colaboradores. En primer lugar, quería darle las gracias al Departamento de Física Aplicada de la Universidad de Zaragoza, en particular al Prof. Miguel Ángel Rebolledo, al Dr. Juan Vallés y al Dr. Víctor Berdejo. No puedo dejar de darle las gracias al Departamento de Ciencia de Materiales de la Universidad Autónoma de Madrid, concretamente al Prof. Ginés Lifante y al Dr. Jon Martínez de Mendívil. También al resto de nuestros colaboradores del Departamento de Materiales de la Universidad Complutense de Madrid (Prof. Paloma Fernández y Dr. Belén Sotillo), del grupo de Física y Cristalografía de Materiales de la Universidad Rovira i Virgili (Prof. Francesc Díaz, Dra. María-Cinta Pujol y Dra. Magdalena Aguiló), el Centro Nacional de Aceleradores (Dra. Inés Ortega-Feliu), el departamento de Física del Instituto de Fotónica y Nanotecnología del Politecnico di milano

(Prof. Roberto Osellame y Dra. Rebeca Martínez), el Grupo de Fotónica del Imperial College (Dr. Edward Grace), el Departamento de Física y Astronomía de la Univ. De Sussex (Dra. Alessia Pasquazi), y el Departamento de Ingeniería Electrónica de la Universidad Roma Tre (Dr. Gaetano Assanto).

No puedo olvidarme de la gente que conocí durante mi estancia en el Departamento de Óptica del Femto-ST en Besançon, en especial del jefe del grupo, el Prof. François Courvoisier. Toda la gente que conocí allí contribuyó a hacer la estancia muy agradable: Abel Gil, el Dr. Chen Xie, el Dr. Luca Furfaro, Remi Meier, Jose Carrión, y todos los futboleros de los partidillos.

También quiero agradecer la ayuda económica aportada por el Consejo Superior de Investigaciones Científicas (CSIC) y al Fondo Social Europeo en el marco del programa JAE-Pre.

Por último, pero no menos importante, quiero agradecer el apoyo prestado por mi familia y amigos, en especial mi novia Maribel, la que más ha “sufrido” el desarrollo de la tesis, y a mis padres y hermano, que han tenido mucha paciencia en esos momentos difíciles. A todos vosotros, muchas gracias por todo.

Contents

Acknowledgements I
List of abbreviations VII
List of symbols IX
Summary XI
Resumen en español XV
1. Introduction 1
1.1. Ultrafast laser structuring for Photonics 1
1.2. Motivation, objectives and methodology 3
1.3. Structure of the thesis 5
1.4. References 6
2. Physical principles 11
2.1. Propagation of laser beams in dielectric materials 11
2.1.1. Linear propagation 11
2.1.2. Nonlinear propagation 19
2.2. Laser absorption and photoionization 20
2.2.1. Linear absorption 21
2.2.2. Nonlinear absorption 21
2.2.3. Impact ionization 24
2.3. Material modification 25
2.3.1. Electron thermalization 25
2.3.2. Excitons and generation of defects 26
2.3.3. Ablation 26
2.3.4. Heat accumulation effects 26
2.4. Light confinement 28
2.4.1. Multilayer structures 28
2.4.2. Ion diffusion 28
2.4.3. Surface structuring 29
2.4.4. Structural and compositional modification 30
2.5. Spectroscopy of rare earth ions 31
2.5.1. Electronic transitions 31
2.5.2. Erbium – Ytterbium system 32
2.5.3. Ytterbium in KYW 33
2.5.4. Neodymium in $LiNbO_3$ 34
2.6. Waveguide-based photonic devices 34
2.6.1. Light guiding 35
2.6.2. Waveguide configurations 37
2.6.3. Waveguide performance parameters 38
2.6.4. Optical amplifiers 40
2.6.5. Lasers 41
2.7. References 43
3. Experimental and modeling techniques 47
3.1. Waveguide production 48
3.1.1. Laser sources 48
3.1.2. Waveguide writing setups 51
3.1.3. Sample post-processing 56
3.2. Waveguide characterization 56
3.2.1. Guided modes characterization setup 56

3.2.2. Optical amplification characterization setup in fiber 59
3.2.3. Laser characterization setup in fiber 60
3.2.4. Aerial laser characterization setup 61
3.2.5. Standard characterization techniques 62
3.3. Modelization and numerical calculations 64
3.3.1. Waveguide modeling 64
3.3.2. Phase mask calculations 64
3.3.3. Mean texture size determination 68
3.4. Dielectric materials 69
3.4.1. Fabrication of crystalline samples 69
3.4.2. Fabrication of phosphate glass 69
3.4.3. Raw material characterization 71
3.4.4. Sample list 72
3.5. References 73
4. Surface waveguides writing 77
4.1. Waveguide production 77
4.1.1. Materials selection and waveguide design 77
4.1.2. Channel waveguide fabrication 79
4.1.3. Analysis of the ridge roughness 81
4.2. Waveguide-based lasers 87
4.2.1. Determination of the laser structuring parameters 87
4.2.2. $LiNbO_3$ doped with Nd^{3+} 88
4.2.3. KYW doped with Yb^{3+} 90
4.2.4. KYW doped with Er^{3+} and Yb^{3+} 94
4.3. Summary and conclusion 96
4.4. References 96
5. Modelling of nonlinear propagation of laser beams 99
5.1. Numerical simulation code 99
5.1.1. Nonlinear propagation model 99
5.1.2. Description of the program 100
5.1.3. Alternative algorithms 111
5.1.4. Limits of the nonlinear propagation model 112
5.2. Influence of the nonlinear parameters 119
5.2.1. Nonlinear refraction 119
5.2.2. Multiphoton absorption 121
5.2.3. Combined effect of nonlinear refraction and absorption 122
5.3. Determination of nonlinear coefficients 124
5.3.1. Low intensity regime 124
5.3.2. High intensity regime 128
5.4. Wavefront design 132
5.4.1. Pre-compensation of nonlinear distortions 132
5.4.2. “Exotic” energy deposition profiles 134
5.5. Summary and conclusion 136
5.6. References 137
6. Sub-surface waveguides writing 139
6.1. Influence of writing and material parameters 139
6.1.1. Pulse energy and pulse duration 140
6.1.2. Slit shaping 141
6.1.3. Numerical aperture 142
6.1.4. Other parameters 143
6.1.5. Waveguide writing parameters determination 144
6.2. Waveguide morphology 144

6.2.1. Longitudinal morphology 145
6.2.2. Cross-section morphology 146
6.3. Waveguide formation 148
6.3.1. Waveguide formation mechanism 148
6.3.2. Refractive index change 151
6.3.3. Ion migration mechanism 153
6.4. Waveguide-based amplifiers and lasers 156
6.4.1. Search for processing windows 156
6.4.2. Active waveguides in GPL-produced glass 156
6.4.3. Commercial glass 160
6.5. Summary and conclusions 167
6.6. References 168
7. Conclusions 171
A. Computer codes 173
A.1. Propagador 173
A.2. Gerchbert-Saxton algorithm 175
A.3. Mean texture size determination 178
A.4. Waveguide modes analysis 181
B. Calculations of Equations 3.10 and 5.13 183
B.1. Equation 3.10 183
B.2. Equation 5.13 184
B.3. References 185
C. Publications, communications and awards 187
C.1. Publications 187
C.2. Communications 188
C.3. Awards 190

List of abbreviations

AFM	Atomic force microscopy.
ASE	Amplified spontaneous emission.
BMP	Beam propagation method.
CB	Conduction band.
DIC	Differential interference contrast microscopy.
FFT	Fast-Fourier transform.
GSA	Gerchberg-Saxton algorithm.
GVD	Group velocity dispersion.
HRR	High repetition rate.
LRR	Low repetition rate.
NA	Numerical aperture.
NSE	Nonlinear Schrödinger Equation.
OSA	Optical spectrum analyzer.
PIXE	Particle Induced X-Ray Emission spectroscopy.
SA	Spherical aberration.
SEM	Scanning electron microscopy.
SLM	Spatial light modulator.
VB	Valence band.

List of symbols

(x, y, z) Cartesian coordinates.

(r, θ, z) Cylindrical coordinates.

(r, θ, ϕ) Spherical coordinates.

ρ Reduced coordinate $r\,(r/R_{ref})$.

ϑ Reduced coordinate θ $(\sin(\theta) / \sin(\theta^{max}))$.

$\partial_x f$ Partial derivative of f respect to x $(\frac{\partial f}{\partial x})$.

∇ Laplace operator $(\partial_{xx} + \partial_{yy} + \partial_{zz})$.

$\nabla_\perp$ Transverse Laplace operator $(\partial_{xx} + \partial_{yy})$.

α Linear absorption coefficient.

$\hat{A}$ Scalar electric field.

A Electric field amplitude.

a_λ Absorption.

β_K K-photon absorption coefficient.

β_m Beam propagation constant.

C Circularity.

C_x, C_y Beam center positions.

c Speed of light.

Δn Refractive index change.

ΔE Absorbed energy.

ΔE_{total} Total absorbed energy.

ΔEx Diameter ($1/e^2$) of the absorbed energy profile along the X axis (and similarly for Y and Z).

$\Delta\omega$ Spectral content.

Δz Step size.

ε Electric permittivity.

E Energy.

E_g Bandgap.

E_p Photon energy.

E_{tr} Electronic transition energy.

φ Electric field phase.

ϕ Slope efficiency.

F_i, f_i Ion migration factors.

f Focal length.

γ Keldish factor.

G_{enh} Enhancement / relative gain.

G_{int} Internal gain.

G_{net} Net gain.

Gy, Gz Diameter of the guiding region along the Y and Z axes.

$\hbar$ Reduced Plank constant.

η Overlapping factor.

η_0 Vacuum impedance.

θ_{CA} Gauss-Bessel beam conical angle.

H Magnetic field.

I Intensity.

k Wavenumber.

λ Wavelength.

L^{disp} Displacement losses.

L^{over} Overlapping losses.

L^{prop} Propagation losses.

L^{ref} Reflection losses.

L^{tot} Total losses.

μ Magnetic permeability.

m^* Electron reduced mass.

mts Mean texture size.

n Refractive index.

n_2 Nonlinear refractive index.

NAx Numerical aperture in the X axis.

n_{eff} Effective refractive index.

N_x, N_y Number of points of the field matrix in each X and Y dimensions.

χ Electric susceptibility.

P Optical power.

P_{th} Lasing threshold.

P_{tr} Pump transparency.

$\vec{p}$ Jones polarization vector.

p Electrical polarizability.

$\wp$ Perimeter

q_e Electron charge.

ρ Density.

ρ_e Electron density.

R Reflection coefficient.

R_0 Beam waist.

R_{ref} Reference radius.

R_x, R_y Beam radii.

$\mathcal{R}$ Beam curvature radius.

$\Re$ Accelerating beam radius.

σ Cross section.

σ_{IB} Inverse Bremsstrahlung cross section.

S Surface

θ^{max} Maximum angle of incidence.

τ Pulse duration ($1/e^2$ in intensity).

τ_c Average free carrier time.

τ_{FWHM} Pulse duration (FWHM in intensity).

T Transmission coefficient.

T_{sq} Pulse duration (top-hat).

t_i Fresnel transmission coefficients.

t_{MRE} Transition time.

ω Laser frequency.

W_{PI} Photo-ionization rate.

z_r Rayleigh length.

z_{wg} Waveguide length.

Z_i Amplitude of the i-th Zernike polynomial.

Summary

Photonics was born with the advent of lasers. Lasers provided the *kind of light* required for the development of active and passive photonics devices. Ultrafast pulsed lasers provided, in addition, enough optical power to study the interaction of light with matter beyond the linear regime. Non-linear optical phenomena are the base for the development of non-linear laser processing of transparent materials (dielectrics), a laser processing approach that has unique characteristics in terms of resolution, versatility and 3D-processing capabilities for the production of photonic devices.

Fs-laser writing has been indeed successfully applied to the production of a large variety of high performance passive and active devices in 2D and 3D configuration. In spite of this success, sub-surface fs-laser writing has several limitations that hamper its widespread application for the production of photonics devices. The first one is the limited refractive index contrast (Δn) that can be achieved using conventional modification mechanisms (i.e. local glass matrix densification, or polarizability changes, generation of point defects or changes in the glass network configuration). With a few exceptions, the maximum index contrast achievable is normally below 10^{-2}, which limits the performance of the produced devices. Also, the presence of optical nonlinearities is inherent to the propagation of fs-laser pulses inside dielectrics. When the material shows a high non-linear refractive index, as it happens in crystalline materials or glasses with a high linear refractive index, the distortion of the desired energy deposition profile severely affects the control over the morphology of the structure. Finally, fs-laser processing can be similarly used for micro-structuring applications at the surface of dielectrics in order to produce active and passive surface waveguides. However, scattering losses at the channel walls produced by fs-laser ablation usually lead to high losses that strongly limit the performance of fs-laser structured surface waveguide-based devices.

The global aim of thesis is improving the performance of photonic devices fabricated by fs-laser structuring in glasses and crystalline materials. We have considered three different aspects for this improvement: the role of roughness in the performance of fs-laser surface structured photonics devices, the development of a low computational cost nonlinear propagation code to predict optimal processing conditions for subsurface processing of dielectrics under simplified interaction conditions, and the feasibility of producing highly efficient active devices in waveguides produced by fs-laser induced ion migration.

The roughness of ablation channels structured in the surface of crystalline samples using different types of laser beams has been analyzed. Optimized ablation channels inscribed using multiplexed Gaussian beams show a wall roughness with a feature size of ~250 nm. This enables the production of waveguides with propagation loses of the order of 1 dB/cm. In the case of $KY(WO_4)_2$ doped with Yb^{3+}, propagation losses lower than 1.5 dB/cm have been obtained using this approach. A mirror-less laser cavity was implemented in this waveguide (8.2 mm), achieving a 78% of slope efficiency at 1001 nm. The losses of the waveguides could be reduced even further (below 0.5 dB/cm) for waveguides in load configuration. This reduction potentially enables producing even more efficient lasers.

The problem of the influence of nonlinear effects in the energy deposition profile has been boarded by developing a simulation code (*Propagador*) capable of simulating the nonlinear propagation inside dielectric materials in realistic laser processing conditions at low repletion rate (LRR), with calculation time of the order of few minutes in an ordinary computer has been developed. The conditions where the approximations made in the *Propagador* model remain valid have been thoroughly discussed. Simulations performed using *Propagador* matched the results obtained in soliton shaping experiments, enabling the determination of the nonlinear coefficients of the glass where these experiments were performed. The calculated values were nearly identical to the ones obtained using more complex models. Also, the comparison between *Propagador* simulations and sub-surface laser-written waveguides (at LRR) again allowed determining of the material nonlinear coefficients upon multiple pulse exposure. Finally, some other applications of *Propagador* were shown, like the use of SLMs for pre-compensating the distortion generated in the energy deposition profiles by spherical aberration and nonlinear propagation and absorption.

Finally, the problem of the limited Δn in sub-surface fs-laser structured glasses has been solved by producing photonic devices inside glasses using ion migration induced by fs-laser irradiation at high repetition rate (HRR). Waveguides are produced by a cross-migration mechanism between K^+ and La^{3+} ions, Δn being determined by the local enrichment in La^{3+}. A maximum Δn value of 1.5×10^{-2} was achieved, which can potentially be increased for different glass compositions or irradiation conditions. The feasibility of controlling the size of the guiding region, and the refractive index change via laser-writing parameters has been similarly demonstrated. It has been shown that the enrichment in La^{3+} ions, and thus Δn, can be determined by measuring the optical properties of waveguides co-doped with Er^{3+}. The control of the waveguide features via laser writing parameters enables fabricating highly efficient waveguides with different active properties in the same glass. Two active waveguides were

fabricated in the same sample doped with Er^{3+} and Yb^{3+}, one with a net gain of 9 dB, and another with lasing slope efficiency of 38% and lasing threshold of 22 mW at 1534 nm. This is, to our knowledge, the highest slope efficiency at 1534 nm ever achieved in a fs-laser written waveguide in phosphate glass.

Resumen en español

La fotónica surge con la aparición de los láseres, fuentes de luz imprescindibles para el desarrollo de los dispositivos fotónicos activos y pasivos. Junto a ello, el desarrollo de los láseres de pulsos ultracortos ha posibilitado el estudio de la interacción luz-materia más allá del régimen lineal. Los fenómenos de interacción no-lineal son la base del procesado por láser de materiales dieléctricos. Esta técnica tiene numerosas ventajas (elevada resolución y versatilidad, capacidad de procesado tridimensional, reducción de productos contaminantes e instalaciones de elevado coste) para la producción de dispositivos fotónicos.

El procesado por láser de pulsos ultracortos (PLPU) se ha aplicado en numerosas ocasiones para fabricar dispositivos fotónicos de altas prestaciones. Sin embargo, a pesar de sus numerosas ventajas, el procesado de materiales por láser no está exento de dificultades. Una es el limitado contraste de índice de refracción (Δn) que es posible generar usando los mecanismos de modificación convencionales (densificación, cambios de polarizabilidad o estructura, etc.), generalmente menor que 10^{-2}. Ello limita las prestaciones de los dispositivos generados. Por otra parte, los fenómenos de propagación no lineal tienen un gran impacto en el perfil de depósito de energía (PDE) del haz bajo la superficie del material, distorsionándolo y dificultando enormemente encontrar las condiciones de procesado adecuadas en proceso bajo superficie. Por último, la elevada rugosidad producida en las estructuras generadas en superficie por irradiación con pulsos ultracortos genera niveles de pérdidas que merman sustancialmente la eficacia de los dispositivos producidos.

El objetivo global de esta tesis ha sido mejorar las prestaciones de dispositivos fotónicos fabricados mediante PLPU de materiales cristalinos y vítreos. En concreto, se ha tratado de abordar los tres problemas del procesado no-lineal de dieléctricos con pulsos láser ultracortos descritos anteriormente.

El problema de las elevadas pérdidas de propagación producidas por la rugosidad de las guías de onda en superficie estructuradas con pulsos láser de fs se ha abordado de la siguiente manera. Primero, se ha analizado el efecto de diferentes parámetros de escritura para tres tipos de haces diferentes (Gaussianos multiplexados, de Gauss-Bessel y acelerados), consiguiendo rugosidades $\sim$250 nm, que permiten alcanzar perdidas de propagación en el rango de 1 dB/cm. Se han fabricado guías de onda de estructura *ridge* en $LiNbO_3$ y $KY(WO_4)_2$ dopados con Nd^{3+} e Yb^{3+} respectivamente con haces Gaussianos multiplexados, consiguiendo

pérdidas de propagación ~1.5 dB/cm y láseres con una eficiencia del 78%. Por último, se han utilizado guías de onda de estructura *load* para reducir las pérdidas por debajo de 0.5 dB/cm.

El problema de la distorsión producida por los efectos de propagación no-lineal se ha abordado desarrollando *Propagador*, un *software* capaz de simular los efectos no lineales más relevantes experimentados por un pulso laser ultracorto durante su propagación en el seno de un material dieléctrico. Este programa requiere apenas unos minutos en un ordenador corriente. Los límites de validez del modelo se han analizado concienzudamente. También se ha comparado cálculos de *Propagador* con cálculos de modelos más complejos e irradiaciones experimentales, demostrando la validez de los cálculos. Estas comparaciones también han permitido determinar los coeficientes no lineales de los materiales estudiados. Propagador también se ha utilizado para diseñar frentes de onda capaces de precompensar la distorsión producida en el PDE por efectos no lineales.

Finalmente, el problema del bajo Δn que se puede conseguir en PLPU bajo superficie se ha solventado produciendo las guías de onda mediante el novedoso mecanismo de migración iónica usando haces de alta frecuencia de repetición en vidrios de fosfato dopados con Er^{3+} e Yb^{3+}, consiguiendo valores de Δn > 1.5X10^{-2}. Se ha demostrado que se puede controlar el tamaño y valor de Δn de la zona de guiado mediante los parámetros de escritura. La migración del Er^{3+} se ha empleado para medir, de forma indirecta, el valor de Δn y optimizar las prestaciones de los dispositivos. Cabe destacar la obtención de guías con 9 dB de ganancia neta y láseres con una eficiencia del 38%, la más alta conseguida hasta el momento en este tipo de vidrios mediante PLPU.

Chapter 1
Introduction

1.1. Ultrafast laser structuring for Photonics

Photonics was born with the advent of lasers [1]. Lasers provided the *kind of light* required for the development of active and passive photonics and integrated optics devices like fibers and waveguides, optical couplers, waveguide multiplexers and optical filters, or optical amplifiers [2-4]. Maybe, the best example of the importance of lasers and photonics in our society is Internet [5]. It is based on the transmission of information encoded in infrared lasers pulses by means of optical fibers.

Additionally lasers, especially after the appearance of ultrafast laser oscillators and amplifiers [6], provided enough optical power to study the interaction of light with matter beyond the linear regime, including phenomena like harmonic generation and parametric interactions [7-9], non-linear self-focusing (Kerr effect) [10, 11] or non-linear absorption [12, 13]. These non-linear optical phenomena are the base for the development of non-linear laser processing of transparent materials (dielectrics), a laser processing approach that has unique characteristics in terms of resolution, versatility and 3D-processing capabilities [14, 15].

In 1996, Hirao and Mazur groups [16, 17] demonstrated that permanent refractive index changes could be produced inside dielectric materials by non-linear absorption using ultrashort laser pulses. Using this approach, Hirao and coworkers produced the first fs-laser directly written waveguides in different glasses. In the following years, this technique was applied to a wide variety of glasses and crystals [18]. When compared to more conventional techniques for the fabrication of photonics devices (like ion exchange [19], plasma enhanced chemical vapor deposition [20], wet etching [21], ion etching [22], etc.), fs-laser structuring offers an inherent 3D capability, rapid device prototyping, minimal processing steps, and avoids the use of contaminant chemicals or highly expensive clean rooms. Indeed fs-laser writing has been successfully applied to the production of a large variety of passive and active devices in 2D and 3D configuration, A large part of this success is related to the development of high repetition rate, fiber-based fs-laser amplifiers (with repetition rates in the MHz range and pulse energies of several micro-Joules) that enable to combine efficient non-linear absorption and controllable heat accumulation effects during processing [23], leading to very

low-loss structures. In this respect it is worth noting that the use of 100´s of KHz- to MHz repetition rate fs-laser amplifiers is not equivalent to use longer pulses (in the 1-10´s of ps range) in terms of heat accumulation since for the longer pulses multi-photon ionization is much less efficient and uncontrolled avalanche effects are more likely to occur. Regarding the type of devices already demonstrated by fs-laser writing, in the field of passive devices 2D [24] and 3D [25] beam splitters, 2D [26] and 3D [27] directional couplers, 2D [28] and 3D [29] Mach-Zehnder interferometers, Bragg gratings [30] and ring resonators [27] can be cited. In the case of active devices, some illustrative examples are the first laser-written optical waveguide amplifier [31], the first laser-written waveguide laser [32], and the first laser-written optical amplifier operating in the whole C-band (1530-1565 nm) [33], as well as several of the best performing waveguide lasers in doped glasses in terms of slope efficiency (η): Tm^{3+} (η = 50%) [34], Er^{3+}-Yb^{3+} (η = 21%) [35], and Yb^{3+} (η = 79%) [36]. In the case of crystalline materials slope efficiencies over 70% for Nd^{3+} [37] and 84% for Yb^{3+} [38] have been achieved.

In spite of this success, sub-surface fs-laser writing has several limitations that hamper its widespread application for the production of Photonics devices. The first one is the limited refractive index contrast (Δn) that can be achieved using conventional modification mechanisms (i.e. glass matrix densification [39, 40], polarizability changes [41], generation of point defects [42, 43] or changes in the glass network configuration [44]). With a few exceptions [45-48], the maximum index contrast achievable is normally below 10^{-2}, which limits the development of high curvature radius guiding structures, the propagation losses achievable and the 3D-capabilities of the technique. Additionally, the sign and magnitude of the refractive index change induced depends on the material and in most glasses [49] and crystalline materials [50] Δn is negative. Finally, the presence of optical nonlinearities is inherent to the propagation of fs-laser pulses inside dielectrics [51]. When the material shows a high non-linear refractive index, as it happens in crystalline materials or glasses with a high linear refractive index [9], the distortion of the desired energy deposition profile severely affects the control over the morphology of the structure [52].

Fs-laser processing using non-linear absorption can be similarly used for micro-structuring applications at the surface of dielectrics in order to produce active and passive surface waveguides. This approach has been proven successful in some crystalline materials and glasses for producing photonic devices by structuring planar active or passive waveguides [53, 54]. However, scattering losses at the channel walls produced by fs-laser ablation usually lead to high losses that strongly limit the performance of fs-laser structured surface waveguide-based devices.

These limitations of surface and subsurface fs-laser processing can be overcome in some cases by generating ad-hoc designed sub-surface structures like depressed index cladding waveguides [55], type II guiding structures in crystals [38] or playing around the writing parameters to reach an adequate processing window, which is not always possible. Recently, it has been shown that fs-laser writing with high repetition lasers can be used to generate local compositional changes in glasses leading to strong, positive and controllable refractive index changes [56, 57] in glasses with *pre-designed* composition. This mechanism can be applied to other families of glasses [58] by introducing in the glass composition a "refractive index carrying element" [59] that would enrich the guiding region upon high repetition rate fs-laser irradiation. Also it has recently been shown that some surface waveguide designs, like load waveguides [60] can be used to minimize the losses produced by the roughness in the ridge surface.

An additional problem of fs-laser structuring, in many cases, is the difficulty of predicting *a priori* the optimal irradiation conditions for producing a given effect, which can greatly vary depending on the laser source, material and specific application. Nonlinear propagation phenomena strongly increase the complexity of the problem, and heat accumulation effects have to be considered if high repetition rate fs-laser sources are used. There is a great variety of models with different levels of sophistication [61], considering a variety of specific physical problems like heat accumulation effects and diffusion [46], spherical aberration and heat accumulation [62] or thermal ionization effects [63]. In spite of this, there is still a need for low computational cost models for non-linear propagation problems. They are needed in order to reduce the processing optimization time. This would allow testing many irradiation conditions in a reasonable time, reducing the range of irradiation conditions which must be experimentally considered.

1.2. Motivation, objectives and methodology

The global aim of thesis is improving the performance of photonic devices fabricated by fs-laser structuring in glasses and crystalline materials. We have considered three different aspects for this improvement: the role of roughness in the performance of fs-laser surface structured photonics devices, the development of a low computational cost nonlinear propagation code and the feasibility of producing highly efficient active devices in waveguides produced by fs-laser induced ion migration.

This thesis has thus three main objectives:

1. The production of highly efficient photonic devices in crystalline materials by fs-laser surface structuring, overcoming the problem of the roughness of the ablation channel using different strategies.

2. The development of a program capable of simulating the nonlinear propagation of ultrashort laser pulses inside dielectric materials requiring low computation and time cost.

3. The production of highly efficient active waveguides and related devices (waveguide integrated amplifiers and lasers) by fs-laser induced ion migration in glasses by analyzing the controllability that can be exerted in the performance of the passive waveguides and the impact of ion migration in the case of the luminescent dopants in the glass.

The problem of the high losses produced by roughness in the fs-laser ablated channels in dielectrics has been boarded by two different approaches. First, different types of spatially shaped laser beams (multiplexed Gaussian, Gauss-Bessel and accelerated beams) have been used to produce ablation channels forming waveguides in different conditions to analyze the effect on the roughness. Second, the implementation of a waveguide configuration (different than conventional ridges) that should minimize the impact of the channels roughness (load waveguide configuration) has been analyzed.

A software code capable of calculating the most important nonlinear effects occurring in realistic processing conditions, and requiring processing times of the order of few minutes in an ordinary computer has been designed and implemented on the basis of a pre-existent, *ad-hoc* high speed, fast Fourier evolver [64]. The validity limits of the code with respect the processing parameters and derived results have been thoroughly analyzed. The comparison between simulations and real experiments has been performed to analyze the performance of the code and to extract useful information regarding the non-linear parameters of different materials.

Finally, the main characteristics of the ion migration effect responsible for the production of highly efficient passive waveguides upon high repetition rate fs-laser writing in phosphates glasses have been analyzed. The impact of the fs-laser induced ion migration process in the case of rear earths has been assessed and used to optimize the performance of optical amplifiers and lasers based in this migration effect.

For what concerns the materials studied, experiments of surface laser structuring have been performed in planar waveguides fabricated in $LiNbO_3$ and $KY(WO_4)_2$ crystals. The former was chosen due to its wide range of applications and as a reference material, and the latter due to its known high emission and absorption cross sections when doped with

luminescent ions. These planar waveguides were produced by depositing on top of $KY(WO_4)_2$ samples a layer of a different $KLnW$ with different refractive index, or by Zn^{2+} ion diffusion, allowing the control of Δn. The study of sub-surface laser structuring for producing optical amplifiers and lasers by fs-laser assisted ion migration was performed in P_2O_5-La_2O_3-K_2O-based phosphate glasses doped with Er^{3+} and Yb^{3+}. This glass family was chosen since this is the first glass where fs-laser assisted ion-migration producing highly efficient passive waveguides has been demonstrated.

1.3. Structure of the thesis

The thesis is divided in seven chapters and three appendices. Also, two summaries of the thesis, one in English and another in Spanish, are given at the beginning of the thesis.

The physical mechanisms involved in the fs-laser structuring of dielectric materials are described in **Chapter 2**. It starts with the description of the linear and nonlinear propagation of laser pulses in dielectric materials. It follows explaining how the absorption of the laser pulses affects the dielectric material. Then, the fundamentals of light confinement are described. It also includes a basic description of the spectroscopy of the luminescent rare earth ions used in this thesis. Finally, a basic description of passive waveguides, optical amplifiers and lasers is given.

Chapter 3 is devoted to the description of the experimental and modeling techniques. First, all the waveguide production setups by fs-laser irradiation are described, including the main laser sources. Then, the waveguide characterization setups and techniques are described. It follows by explaining the modelization of waveguides and the calculation of phase masks used in some cases during laser writing. Finally, the production of the samples used during this thesis, and the techniques used to characterize them is described.

The results regarding the surface laser structuring of crystalline samples are shown in **Chapter 4**. First, the structuring technique is described. Then, the study of the roughness of the ablation channels produced with different laser beams is described. The waveguide lasers produced in $LiNbO_3$ and $KY(WO_4)_2$ are then described. Finally, the results regarding the fabrication of very low-loss, load waveguides are shown.

The model for calculating the nonlinear propagation of laser pulses inside dielectric materials is described in **Chapter 5**. The chapter starts with the description of the model and its implementation. Then, the limits where the model remains valid are thoroughly analyzed and established. The effect of the nonlinear coefficients on the propagation of the pulses is

then described. Finally, the nonlinear parameters of different materials are determined by comparing simulations with experimental results (soliton shaping and waveguide writing), and additional applications of the code are presented.

The results of sub-surface laser structuring of phosphate glasses are shown in **Chapter 6**. First, some simulations performed using the model described in **Chapter 5** are used to make an *a priori* first-guess of the right irradiation parameters. Then, the morphology and controllability of the produced waveguides is analyzed, followed by a study of the waveguide formation mechanism. Finally, the performance of the produced optical amplifiers and waveguides lasers is analyzed.

Chapter 7 includes a summary of the main conclusions of the thesis.

The details of the different codes used during in this work (including the simulation code described in **Chapter 5**) are shown in **Appendix A**. The simplification of **Equation 5.13** is described in **Appendix B**. Finally, the publications, communications and awards produced during this thesis are listed in **Appendix C**.

1.4. References

[1] T. Maiman, "Stimulated optical radiation in ruby," *Nature,* vol. 187, 1960.

[2] P. K. Tien, "Light Waves in Thin Films and Integrated Optics," *Applied Optics,* vol. 10, pp. 2395-2413, 1971.

[3] D. M. Mullsteff, "Fiber optic communication system," USA Patent, 2011.

[4] E. Desurvire, C. R. Giles, J. R. Simpson, and J. L. Zyskind, "Erbium-doped fiber amplifier," USA Patent, 1991.

[5] F. Idachaba, D. U. Ike, and O. Hope, "Future Trends in Fiber Optics Communication," *Proceedings of World Congress of Enineering,* vol. I, 2014.

[6] D. Strickland and G. Mourou, "Compression of amplified chirped optical pulses," *Optics Communications,* vol. 56, pp. 219-221, 1985.

[7] P. A. Franken, A. E. Hill, C. W. Peters, and G. Weinreich, "Generation of Optical Harmonics," *Physical Review Letters,* vol. 7, pp. 118-119, 1961.

[8] J. A. Armstrong, N. Bloembergen, J. Ducuing, and P. S. Pershan, "Interactions between Light Waves in a Nonlinear Dielectric," *Physical Review,* vol. 127, pp. 1918-1939, 1962.

[9] R. L. Sutherland, D. G. McLean, and S. Kirkpatrick, *Handbook of nonlinear optics*, 2nd ed.: Marcel Dekker, 2003.

[10] Y. R. Shen, "Self-focusing: Experimental," *Progress in Quantum Electronics,* vol. 4, pp. 1-34, 1975.

[11] J. H. Marburger, "Self-focusing: Theory," *Progress in Quantum Electronics,* vol. 4, pp. 35-110, 1975.

[12] A. M. Bonch-Bruevich and V. A. Khodovoĭ, "MULTIPHOTON PROCESSES," *Soviet Physics Uspekhi,* vol. 8, p. 1, 1965.

[13] Y. H. Pao and P. M. Rentzepis, "Multiphoton Absorption and Optical-Harmonic Generation in Highly Absorbing Molecular Crystals," *The Journal of Chemical Physics,* vol. 43, pp. 1281-1286, 1965.

[14] R. Osellame, G. Cerullo, and R. Ramponi, *Femtosecond Laser Micromachining: Photonic and microfluidic devices in transparent materials*: New York Springer, 2012.

[15] H. Misawa and S. Juodkazis, *3D Laser Microfabrication. Principles and Applications*. Weinheim: WILEY-VCH Verlag 2006.

[16] K. M. Davis, K. Miura, N. Sugimoto, and K. Hirao, "Writing waveguides in glass with a femtosecond laser," *Optics Letters,* vol. 21, pp. 1729-1731, 1996.

[17] E. N. Glezer, M. Milosavljevic, L. Huang, R. J. Finlay, T. H. Her, J. P. Callan*, et al.*, "Three-dimensional optical storage inside transparentmaterials," *Optics Letters,* vol. 21, pp. 2023-2025, 1996.

[18] A. H. Nejadmalayeri and P. R. Herman, "Ultrafast laser waveguide writing: lithium niobate and the role of circular polarization and picosecond pulse width," *Optics Letters,* vol. 31, pp. 2987-2989, 2006.

[19] R. V. Ramaswamy and R. Srivastava, "Ion-exchanged glass waveguides: a review," *Journal of Lightwave Technology,* vol. 6, pp. 984-1000, 1988.

[20] K. Shuto, K. Hattori, T. Kitagawa, Y. Ohmori, and M. Horiguchi, "Erbium-doped phosphosilicate glass waveguide amplifier fabricated by PECVD," *Electronics Letters,* vol. 29, pp. 139-141, 1993.

[21] H. Hu, R. Ricken, W. Sohler, and R. B. Wehrspohn, "Lithium Niobate Ridge Waveguides Fabricated by Wet Etching," *IEEE Photonics Technology Letters,* vol. 19, pp. 417-419, 2007.

[22] J. L. Jackel, R. E. Howard, E. L. Hu, and S. P. Lyman, "Reactive ion etching of LiNbO3," *Applied Physics Letters,* vol. 38, pp. 907-909, 1981.

[23] S. Eaton, H. Zhang, P. Herman, F. Yoshino, L. Shah, J. Bovatsek*, et al.*, "Heat accumulation effects in femtosecond laser-written waveguides with variable repetition rate," *Optics Express,* vol. 13, pp. 4708-4716, 2005.

[24] D. Homoelle, S. Wielandy, A. L. Gaeta, N. F. Borrelli, and C. Smith, "Infrared photosensitivity in silica glasses exposed to femtosecond laser pulses," *Optics Letters,* vol. 24, pp. 1311-1313, 1999.

[25] S. Nolte, M. Will, J. Burghoff, and A. Tuennermann, "Femtosecond waveguide writing: a new avenue to three-dimensional integrated optics," *Applied Physics A,* vol. 77, pp. 109-111, 2003.

[26] W.-J. Chen, S. M. Eaton, H. Zhang, and P. R. Herman, "Broadband directional couplers fabricated in bulk glass with high repetition rate femtosecond laser pulses," *Optics Express,* vol. 16, pp. 11470-11480, 2008.

[27] A. M. Kowalevicz, V. Sharma, E. P. Ippen, J. G. Fujimoto, and K. Minoshima, *Optics Letters,* vol. 30, pp. 1060-1062, 2005.

[28] K. Minoshima, A. M. Kowalevicz, E. P. Ippen, and J. G. Fujimoto, "Fabrication of coupled mode photonic devices in glass by nonlinear femtosecond laser materials processing," *Optics Express,* vol. 10, pp. 645-652, 2002.

[29] A. Crespi, Y. Gu, B. Ngamsom, H. J. W. M. Hoekstra, C. Dongre, M. Pollnau*, et al.*, "Three-dimensional Mach-Zehnder interferometer in a microfluidic chip for spatially-resolved label-free detection," *Lab on a Chip,* vol. 10, pp. 1167-1173, 2010.

[30] M. Thiel, G. Flachenecker, and W. Schade, "Femtosecond laser writing of Bragg grating waveguide bundles in bulk glass," *Optics Letters,* vol. 40, pp. 1266-1269, 2015.

[31] C. Florea, K. A. Winick, Y. Sikorski, A. Said, and P. Bado, "Optical waveguide amplifier in Nd-doped glass written with near-IR femtosecond laser pulses," in *Lasers and Electro-Optics, 2000. (CLEO 2000). Conference on*, 2000, pp. 128-129.

[32] S. Taccheo, G. Della Valle, R. Osellame, G. Cerullo, N. Chiodo, P. Laporta*, et al.*, "Er:Yb-doped waveguide laser fabricated by femtosecond laser pulses," *Optics Letters,* vol. 29, pp. 2626-2628, 2004.

[33] G. Della Valle, R. Osellame, N. Chiodo, S. Taccheo, G. Cerullo, P. Laporta*, et al.*, "C-band waveguide amplifier produced by femtosecond laser writing," *Optics Express,* vol. 13, pp. 5976-5982, 2005.

[34] D. G. Lancaster, S. Gross, H. Ebendorff-Heidepriem, K. Kuan, T. M. Monro, M. Ams*, et al.*, "Fifty percent internal slope efficiency femtosecond direct-written Tm3+:ZBLAN waveguide laser," *Optics Letters,* vol. 36, pp. 1587-1589, 2011.

[35] G. Della Valle, S. Taccheo, R. Osellame, A. Festa, G. Cerullo, and P. Laporta, "1.5 μm single longitudinal mode waveguide laser fabricated by femtosecond laser writing," *Optics Express,* vol. 15, pp. 3190-3194, 2007.

[36] R. Mary, S. J. Beecher, G. Brown, R. R. Thomson, D. Jaque, S. Ohara, *et al.*, "Compact, highly efficient ytterbium doped bismuthate glass waveguide laser," *Optics Letters,* vol. 37, pp. 1691-1693, 2012.

[37] T. Calmano and M. S, "Crystalline Waveguide Lasers in the Visible and Near-Infrared Spectral Range," *IEEE Journal of Selected Topics in Quantum Electronics,* vol. 21, pp. 401-413, 2015.

[38] G. Palmer, S. Gross, A. Fuerbach, D. G. Lancaster, and M. J. Withford, "High slope efficiency and high refractive index change in direct-written Yb-doped waveguide lasers with depressed claddings," *Optics Express,* vol. 21, pp. 17413-17420, 2013.

[39] A. Ferrer, D. Jaque, J. Siegel, A. R. d. la Cruz, and J. Solís, "Origin of the refractive index modification of femtosecond laser processed doped phosphate glass," *Journal of Applied Physics,* vol. 109, p. 093107, 2011.

[40] J. W. Chan, T. Huser, S. Risbud, and D. M. Krol, "Structural changes in fused silica after exposure to focused femtosecond laser pulses," *Optics Letters,* vol. 26, pp. 1726-1728, 2001.

[41] D. J. Little, M. Ams, P. Dekker, G. D. Marshall, and M. J. Withford, "Mechanism of femtosecond-laser induced refractive index change in phosphate glass under a low repetition-rate regime," *Journal of Applied Physics,* vol. 108, p. 033110, 2010.

[42] K. Hirao and K. Miura, "Writing waveguides and gratings in silica and related materials by a femtosecond laser," *Journal of Non-Crystalline Solids,* vol. 239, pp. 91-95, 1998.

[43] A. M. Streltsov and N. F. Borrelli, "Study of femtosecond-laser-written waveguides in glasses," *Journal of the Optical Society of America B,* vol. 19, pp. 2496-2504, 2002.

[44] O. M. Efimov, L. B. Glebov, K. A. Richardson, E. Van Stryland, T. Cardinal, S. H. Park, *et al.*, "Waveguide writing in chalcogenide glasses by a train of femtosecond laser pulses," *Optical Materials,* vol. 17, pp. 379-386, 2001.

[45] R. Osellame, N. Chiodo, G. D. Valle, G. Cerullo, R. Ramponi, P. Laporta, *et al.*, "Waveguide lasers in the C-band fabricated by laser inscription with a compact femtosecond oscillator," *IEEE Journal of Selected Topics in Quantum Electronics,* vol. 12, pp. 277-285, 2006.

[46] S. M. Eaton, H. Zhang, M. L. Ng, J. Li, W.-J. Chen, S. Ho, *et al.*, "Transition from thermal diffusion to heat accumulation in high repetition rate femtosecond laser writing of buried optical waveguides," *Optics Express,* vol. 16, pp. 9443-9458, 2008.

[47] A. Arriola, S. Gross, N. Jovanovic, N. Charles, P. G. Tuthill, S. M. Olaizola, *et al.*, "Low bend loss waveguides enable compact, efficient 3D photonic chips," *Optics Express,* vol. 21, pp. 2978-2986, 2013.

[48] R. Martínez-Vazquez, R. Osellame, G. Cerullo, R. Ramponi, and O. Svelto, "Fabrication of photonic devices in nanostructured glasses by femtosecond laser pulses," *Optics Express,* vol. 15, pp. 12628-12635, 2007.

[49] L. Bressel, D. de Ligny, C. Sonneville, V. Martinez, V. Mizeikis, R. Buividas, *et al.*, "Femtosecond laser induced density changes in GeO2 and SiO2 glasses: fictive temperature effect [Invited]," *Optical Materials Express,* vol. 1, pp. 605-613, 2011.

[50] M. Heinrich, K. Rademaker, and S. Nolte, "Waveguides in crystalline materials," in *Femtosecond Laser Micromachining: Photonic and microfluidic devices in transparent materials*, R. Osellame, G. Cerullo, and R. Ramponi, Eds., ed: New York Springer, 2012.

[51] A. Couairon and A. Mysyrowicz, "Femtosecond filamentation in transparent media," *Physics Reports,* vol. 441, pp. 47-189, 2007.

[52] J. Siegel, J. M. Fernández-Navarro, A. García-Navarro, V. Diez-Blanco, O. Sanz, J. Solis, *et al.*, "Waveguide structures in heavy metal oxide glass written with femtosecond laser pulses above the critical self-focusing threshold," *Applied Physics Letters,* vol. 86, p. 121109, 2005.

[53] J. Gottmann, D. Wortmann, I. Vasilief, L. Moiseev, and D. Ganser, "Manufacturing of Nd:Gd3Ga5O12 ridge waveguide lasers by pulsed laser deposition and ultrafast laser micromachining," *Applied Surface Science,* vol. 254, pp. 1105-1110, 2007.

[54] J. Martínez de Mendívil, J. del Hoyo, J. Solís, M. C. Pujol, M. Aguiló, F. Díaz, *et al.*, "Mirrorless Yb3+-Doped Monoclinic Double Tungstate Waveguide Laser Combining Liquid Phase Epitaxy and Multiplexed Beam fs Laser Writing," *Journal of Lightwave Technology,* vol. 33, pp. 4726-4730, 2015.

[55] A. G. Okhrimchuk, A. V. Shestakov, I. Khrushchev, and J. Mitchell, "Depressed cladding, buried waveguide laser formed in a YAG:Nd3+ crystal by femtosecond laser writing," *Optics Letters,* vol. 30, pp. 2248-2250, 2005.

[56] T. Toney Fernandez, P. Haro-González, B. Sotillo, M. Hernandez, D. Jaque, P. Fernandez*, et al.*, "Ion migration assisted inscription of high refractive index contrast waveguides by femtosecond laser pulses in phosphate glass," *Optics Letters,* vol. 38, pp. 5248-5251, 2013.

[57] J. del Hoyo, R. M. Vazquez, B. Sotillo, T. T. Fernandez, J. Siegel, P. Fernández*, et al.*, "Control of waveguide properties by tuning femtosecond laser induced compositional changes," *Applied Physics Letters,* vol. 105, p. 131101, 2014.

[58] T. T. Fernandez, M. Hernandez, B. Sotillo, S. M. Eaton, G. Jose, R. Osellame*, et al.*, "Role of ion migrations in ultrafast laser written tellurite glass waveguides," *Optics Express,* vol. 22, pp. 15298-15304, 2014.

[59] J. Solis, T. T. Fernandez, J. d. Hoyo, J. Siegel, and P. M. Zarate, "Femtosecond-laser-induced compositional changes for high-performance photonics," *SPIE Newsroom,* 2015.

[60] J. Martínez de Mendívil, J. Hoyo, J. Solís, M. C. Pujol, M. Aguiló, F. Díaz*, et al.*, "Channel waveguide fabrication in KY(WO4)2 combining liquid-phase-epitaxy and beam-multiplexed femtosecond laser writing," *Optical Materials,* vol. 47, pp. 304-309, 2015.

[61] B. Rethfeld, "Free-electron generation in laser-irradiated dielectrics," *Physical Review B,* vol. 73, p. 035101, 2006.

[62] Y. Dai, G.-J. Yu, G.-R. Wu, H.-L. Ma, X.-N. Yan, and G.-H. Ma, "The effect of spherical aberration on temperature distribution inside glass by irradiation of a high repetition rate femtosecond pulse laser," *Chinese Physics B,* vol. 21, p. 025201, 2012.

[63] M. Sun, U. Eppelt, W. Schulz, and J. Zhu, "Role of thermal ionization in internal modification of bulk borosilicate glass with picosecond laser pulses at high repetition rates," *Optical Materials Express,* vol. 3, pp. 1716-1726, 2013.

[64] E. J. Grace. (2009). *A toolbox for solving evolutionary nonlinear PDEs* Available: www.mathworks.co.uk/matlabcentral/fileexchange/24016

Chapter 2
Physical principles

This chapter is devoted to the description of the physical principles underlying the models, methodology, experimental setups and results presented in this thesis.

2.1. Propagation of laser beams in dielectric materials

The basic principles of propagation of laser beams are explained in this section. Although absorption effects are part of the propagation, they are described separately in **Section 2.2**.

2.1.1. Linear propagation

2.1.1.1. Wave equations

The propagation of electromagnetic waves in a linear uncharged dielectric material is described by the Maxwell equations [1]:

$$\vec{\nabla} \cdot \vec{\mathrm{A}} = 0 \qquad \textbf{2.1}$$

$$\vec{\nabla} \cdot \vec{\mathrm{H}} = 0 \qquad \textbf{2.2}$$

$$\vec{\nabla} \times \vec{\mathrm{A}} = \mu \partial_t \vec{\mathrm{H}} \qquad \textbf{2.3}$$

$$\vec{\nabla} \times \vec{H} = \varepsilon\, \partial_t \vec{\mathrm{A}} \qquad \textbf{2.4}$$

$\vec{\mathrm{A}}$ and $\vec{\mathrm{H}}$ being the electric and magnetic field vectors, ε the electric permittivity and μ the magnetic permeability of the material. These expressions lead to the wave equations:

$$\nabla^2 \vec{A} = \mu\varepsilon \partial_{tt} \vec{A} \qquad \textbf{2.5}$$

$$\nabla^2 \vec{H} = \mu\varepsilon \partial_{tt} \vec{H} \qquad \textbf{2.6}$$

In most cases, it is only necessary to solve one of the two equations, as the other field can be calculated from the relation between $\vec{A}$ and $\vec{H}$ given by the Maxwell equations. For this reason, from now on only the electric field will be considered in this description.

Vectorial representation can be substituted by a scalar description in homogeneous isotropic media, where all the scalar components of the electric field vector satisfy an equation similar to **Equation 2.5**:

$$\nabla^2 \hat{A} = \mu\varepsilon\partial_{tt}\hat{A} = \frac{n^2}{c^2}\partial_{tt}\hat{A} \qquad \textbf{2.7}$$

c being the speed of light and n the refractive index of the material. The latter is related to the first-order electric susceptibility of the material $\chi^{(1)}$ by the equation:

$$n = \sqrt{1 + \chi^{(1)}} \qquad \textbf{2.8}$$

Equation 2.7 leads to the monochromatic wave approximation:

$$\hat{A}(x, y, z, t) = Re\{A(x, y, z)e^{i\omega t}\} \qquad \textbf{2.9}$$

This results in the Hemholtz equation:

$$\nabla^2 A + \frac{n^2}{c^2}\omega^2 A = \nabla^2 A + k^2 A = 0 \qquad \textbf{2.10}$$

k being the wavenumber, $k_0 = k/n$ the wavenumber in vacuum and $\lambda = 2\pi/k_0$ the wavelength.

Many problems in optics consist on a propagating light source, which defines a preferred direction (Z). This is the case of laser pulses. In this case:

$$\hat{A}(x, y, z, t) = Re\{A(x, y, z)e^{i(\omega t - kz)}\} \qquad \textbf{2.11}$$

ω being the angular frequency. This results in the equation:

$$\partial_{zz}A - 2ik\partial_z A + (\partial_{xx} + \partial_{yy})A = 0 \qquad \textbf{2.12}$$

At this point, the paraxial approximation can be introduced. $\partial_{zz}A$ is neglected compared to $k\partial_z A$, so **Equation 2.12** is reduced to:

$$\partial_z A = \frac{i}{2k}(\partial_{xx} + \partial_{yy})A \qquad \textbf{2.13}$$

This equation simply describes the diffraction of the beam along its propagation axis in an homogeneous medium, but it is the backbone of more complex models that will be presented in **Sections 2.1.2** and **2.2**.

It is possible to express the intensity of the wave (the amount of energy per unit of time and surface carried by the wave) from the electric field:

$$I = \frac{c\varepsilon_0 n|A|^2}{2} = \frac{n|A|^2}{2\eta_0} \quad \textbf{2.14}$$

ε_0 being the vacuum electric permittivity and η_0 the vacuum impedance.

2.1.1.2. Fresnel diffraction

Different formalisms can be utilized for calculating the propagation of waves. Among all of them, Fresnel diffraction equation allows calculating the field at any z position from a initial field cross section [1]:

$$A(x,y,z) = \frac{e^{ikz}}{i\lambda z}\iint_{-\infty}^{\infty} A(x',y',0)\exp\left\{\frac{ik}{2z}[(x-x')^2+(y-y')^2]\right\}dx'dy' \quad \textbf{2.15}$$

There is though an approximation in the calculation of this equation that makes it inaccurate for $z \sim \lambda$.

2.1.1.3. Gaussian beams and focal volume

One family of exact solutions of **Equation 2.13** are circular Gaussian beams [2]:

$$A(r,z) = A_0\frac{R_0}{R(z)}e^{-r^2/R^2(z)}e^{ikr^2/\mathcal{R}(z)}e^{i\,\mathrm{atan}(z/z_R)} \quad \textbf{2.16}$$

$R(z)$ being the beam radius and $\mathcal{R}(z)$ its curvature radius at position z, R_0 the beam waist, z_R the Rayleigh length, A_0 the electric field amplitude, and (r,θ,z) the cylindrical coordinates. Most lasers generate Gaussian beams due to the type of optical resonators commonly used.

Figure 2.1 shows a plot of the intensity and radius position of a Gaussian beam focused by a lens with focal length f at $z = 0$. It shows that the region of highest intensity is confined in a volume centered on the focus. This region is often called the focal volume. The intensity profile in this region will determine the energy deposition profile, as it will be shown in **Section 2.2**. Its size can be described by the double of the beam waist and the Rayleigh length:

$$2\mathrm{R}_0 = \frac{2\lambda}{\pi NA} \quad \textbf{2.17}$$

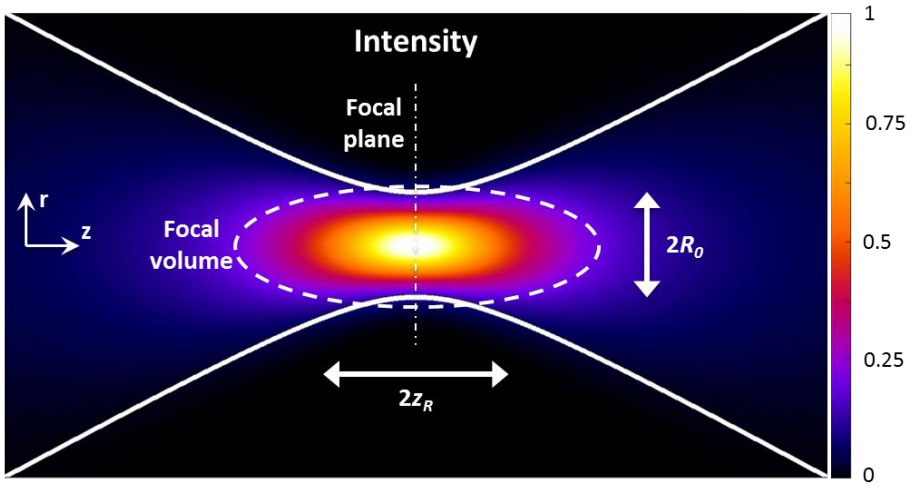

Figure 2.1: *Z-R intensity distribution in the focal region of a circular Gaussian beam with A_0 = 1. The continuous white lines correspond to the position of the 1/e^2 radius ($\mathcal{R}(z)$).*

$$2z_R = \frac{2n\lambda}{\pi NA^2} \qquad \textbf{2.18}$$

NA being the numerical aperture of the lens:

$$NA = n\sin\left[\operatorname{atan}\left(\frac{R(f)}{f}\right)\right] \qquad \textbf{2.19}$$

where f is the focal length of the lens in the medium.

There is another family of solutions of **Equation 2.13** which are the elliptical Gaussian beams. They are very similar to circular ones, but they have independent beam and curvature radii for X and Y axes. This means that they have different beam waists in each dimension, but a common Rayleigh length (given by the highest NA). Varying the ratio between X and Y beam radii, the intensity distribution at the focal volume can be tailored. This is illustrated in **Figure 2.2**, where the intensity distribution at the focal volume of a circular and an elliptical beam with R_y = R_x/20 are shown. The intensity distribution in the Z-Y plane changes from an elongated ellipsoid to a nearly circular disk, a very desirable distribution for waveguide writing [3]. The other difference is that the maximum intensity is decreased by the same factor of 1/20.

Elliptical Gaussian beams can be obtained by different means from circular Gaussian beams, like using cylindrical telescopes [4]. This produces high quality beams, but it requires a fine alignment of the cylindrical telescope used. A second approach is the slit shaping technique [5]. It consists on placing a slit in the beam path. The produced beam is not exactly an elliptical Gaussian beam, and depending on the slit width a large portion of the energy of the beam can be lost, but the result is sufficiently close and it is much experimentally simpler.

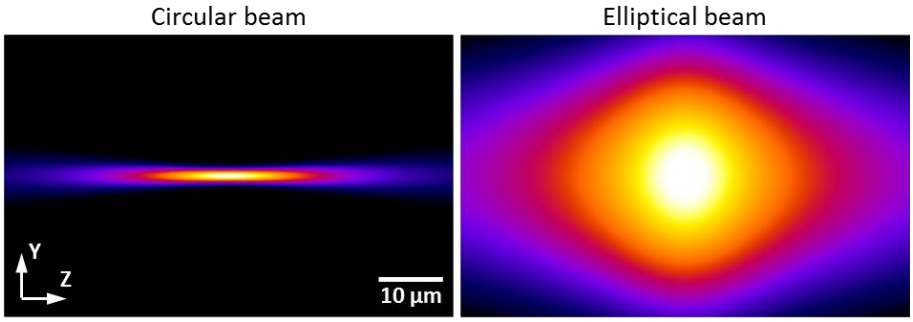

Figure 2.2: *Z-Y intensity distribution at the focal region for a circular and an elliptical Gaussian beam with $R_y = R_x / 20$, for a NA = 0.17 lens. In the case of the elliptical beam, the intensity profile shows a nearly circular disk shape. Both images are normalized o their maximum value.*

2.1.1.4. Gauss-Bessel beams

Bessel beams [6] are a type of optical beams whose field amplitude transversal cross section is given by the Bessel function of the first kind. They can be described as the superposition of a set of monochromatic conical waves. Bessel beams show very interesting properties: non diffractive nature (their cross-section doesn't vary upon propagation in a medium with constant refractive index) and self-healing (even if a portion of the beam is absorbed or blocked, it recovers the Bessel cross section after the obstacle).

However, Bessel beams do not exist in nature, as they would require infinite energy distributed in an infinite cross section. Gauss-Bessel beams are an approximation which shows the properties of the Bessel beams over a finite region of space.

Gauss-Bessel beams can be generated using a Gaussian beam and an axicon [7] or a SLM [8], as shown in **Figure 2.3**. The axicon or the SLM introduce a conical wavefront that produces a convergence effect. In a Z-Y view (see **Figure 2.3**) it can be envisioned as two plane waves with the same angle respect to propagation direction but with opposite sign. The interference region is where the Besselian properties arise: the size of the distribution is preserved as if diffraction was not present (as it can be seen in the Z-Y intensity plot).

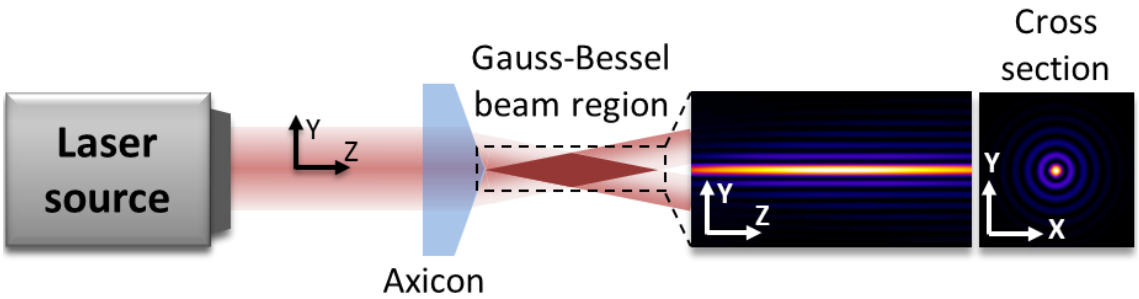

Figure 2.3: *Basic scheme of the generation of a zeroth-order Gauss-Bessel beam. An axicon or an SLM is placed in the path of the Gaussian beam. The beam acquires a conical wavefront that "focuses" the beam over a rhomboidal-like region, where the Besselian properties arises.*

However, for Gauss-Bessel beams peak intensity varies along Z. Also, the beam show self-healing properties [9].

2.1.1.5. Accelerating beams

Accelerating beams [10] are a kind of beams whose intensity lobe describes a curved trajectory. More precisely, they show a localized region of high intensity associated with the caustic envelope of a family of tangential geometrical rays. When this caustic envelope c(z) describes a parabolic trajectory, the beam is often referred to as Airy beam. The intensity distribution of an Airy beam with a caustic of the form $c(z) = a\,x^2$ is shown in **Figure 2.4a**.

The family of rays tangent to the caustic trajectory is represented in **Figure 2.4b**. The direction of the beam rays at $z = 0$ can be calculated from the wavefront of the beam by the equation:

$$\partial_y \varphi(y) = k \sin\theta \qquad \textbf{2.20}$$

Now, considering that $c'(z) = dc(z)/dz = \tan\theta$, and using the properties of trigonometric functions:

$$\partial_y \varphi(y) = \frac{k\,c'(z)}{\sqrt{1 + [c'(z)]^2}} \qquad \textbf{2.21}$$

Using **Equation 2.21** and $c'(z) = y/z$, it is possible to calculate the wavefront necessary to produce the accelerating beam described by the caustic $c(z)$.

This description utilizes geometrical optics, but it can be generalized to wave optics by diffraction integral theory considering only scalar unidirectional propagation. In this case, it is possible to calculate the required phase mask that produces the desired caustic in the Fourier space [11]:

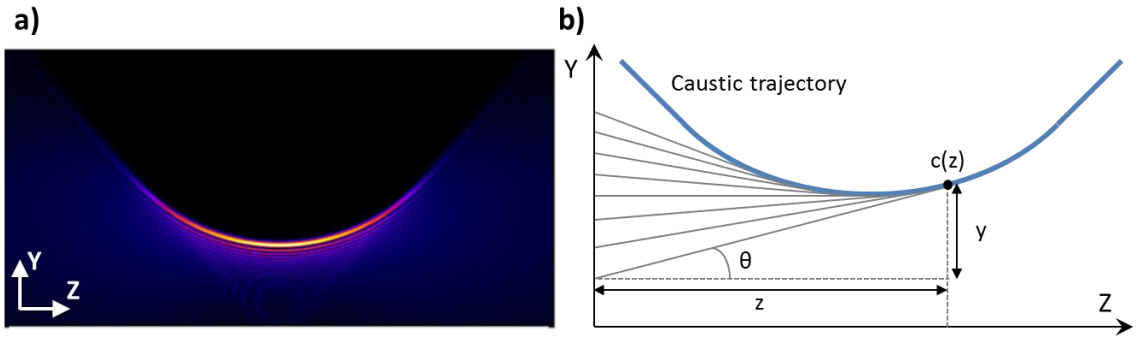

Figure 2.4: *(a) Example of the intensity distribution of an accelerating beam with parabolic caustic trajectory: $c(z) = a\,x^2$. (b) Scheme of the envelope caustic and its family of tangent rays.*

$$\partial_{y_F}\varphi(y_F) = k\frac{c(z) - z\,c'(z)}{f} \qquad \textbf{2.22}$$

$$y_F = f\frac{c'(z)}{\sqrt{1 + [c'(z)]^2}} \qquad \textbf{2.23}$$

where y_F is the vertical coordinate in the focal plane of the lens.

2.1.1.6. Spherical aberration

One of the effects of the propagation of a focusing beam through materials with different refractive indices is spherical aberration (SA), which distorts the size and intensity distribution at the focal volume [12].

SA can be easily understood using the geometrical optics formalism. When a light ray propagates through the boundary of two media with refractive indices n_i and n_t, its propagation angle respect to the normal of the surface changes according to the Snell law:

$$n_i \sin(\theta_i) = n_t \sin(\theta_t) \qquad \textbf{2.24}$$

SA is called possitive if the beam crosses to a material with higher refractive index than the incidence medium, and negative in the opposite case. **Figure 2.5a** shows the effect of positive SA on a collimated beam focused inside a medium through a flat interface. The higher is the incidence angle, the deeper the ray is focused inside the dielectric material. This stretches the focal volume along the optical axis.

It is possible to introduce the effect of the SA as an additional phase term in the electric field at the interface between both materials [13]:

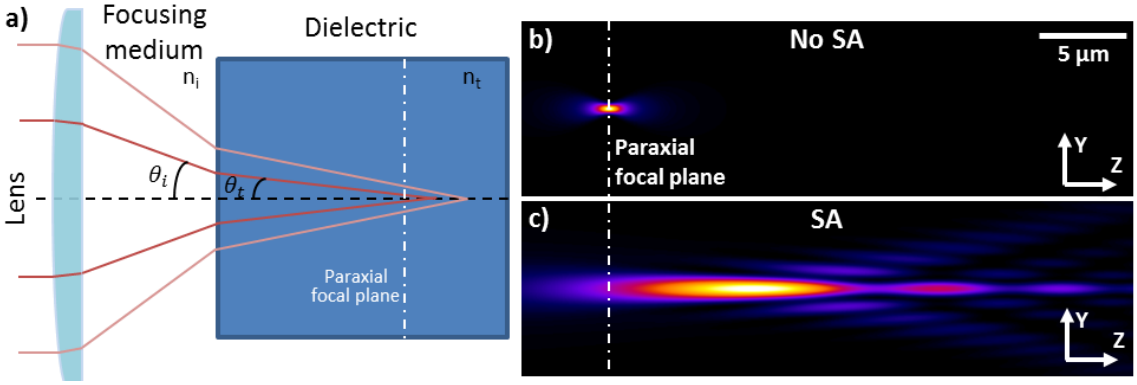

Figure 2.5: *(a) Schematic diagram of a collimated beam focused inside a dielectric material with $n_t > n_i$. The rays incident at large angles are focused after the paraxial focus position. (b, c) Z-Y intensity distribution at the focal volume for a circular Gaussian beam at (800 nm wavelength) focused by a lens (NA = 0.66) 100 µm below the surface of a dielectric material with n = 1.55 without (b) and with SA (c).*

$$\varphi_{SA}(\rho) = \left(\sqrt{\csc^2\theta_i^{max} - \csc^2\vartheta} - \sqrt{\csc^2\theta_t^{max} - \csc^2\vartheta}\right) d\ NA \qquad \textbf{2.25}$$

ϑ being $\sin(\theta_i)/\sin(\theta_i^{max})$, θ_i^{max} and θ_t^{max} the maximum angle of incidence in the incident and dielectric material respectively, and d the depth of the paraxial focal plane. **Figure 2.5b-c** show two intensity distributions on the Z-Y plane as examples. The first is calculated for a circular Gaussian beam without SA effects, while in the second is calculated using **Equation 2.25**. Without computing SA effects, the focal volume is very small, smaller than 1 μm^3. When SA effects are introduced, the focal volume is greatly stretched and shifted inside the dielectric. Also, the focal volume splits in several lobes of different sizes and intensities.

Figure 2.5 shows the effect of positive SA. Negative SA would produce a similar effect, but the rays with large incidence angles would be focused before the paraxial focal plane. In that case, the intensity distribution would be stretched and shifted towards the surface of the material.

It is usual to describe wavefronts in a base of orthogonal polynomials, like Zernike polynomials. In this case, SA wavefront can be described as an infinite sum of the cyrcularly symetrical polynomials [14]. Each of those terms are often called n-th order SA.

2.1.1.7. Pulsed laser beams

The propagation of pulsed laser beams is normally performed using the slow varying envelope approximation (SVEA). It is expressed as

$$\hat{A}(x,y,z,t) = Re\{A(x,y,z,t)e^{i\omega_0 t}\} \qquad \textbf{2.26}$$

with the condition $\partial_t \mathrm{A}/A \ll \omega_0$. This is the equivalent to assume that the spectral content of the pulse is much narrower than the central frequency ω_0. SVEA leads to the same propagation equations shown in **Section 2.1.1.1** for the monochromatic wave approximation.

In many cases, the electric field amplitude of the pulse can be decomposed as:

$$\mathrm{A}(\mathrm{x},\mathrm{y},\mathrm{z},\mathrm{t}) = A(x,y,z)f(t) \qquad \textbf{2.27}$$

This allows solving **Equation 2.13** for the spatial amplitude $A(x,y,z)$ and calculating the final solution by multiplying it by the temporal function.

A common parameter for describing a pulse is its FWHM intensity, which is often referred to as pulse duration (τ_{FWHM}). It approximately corresponds to the time lapse with highest intensity. In materials laser processing, it is common to call short pulses to those with

pulse duration of the order of nanoseconds or hundreds of picoseconds, and ultrashort pulses those with pulse durations in picosecond and femtosecond ranges.

For a Gaussian temporal envelope:

$$f(t) = e^{-t^2/\tau^2} \quad \textbf{2.28}$$

This leads to $\tau_{FWHM} = \sqrt{2\ln 2}\,\tau$.

2.1.2. Nonlinear propagation

2.1.2.1. Nonlinear refractive index

In the presence of strong electric fields, the polarization of the material can be expressed as a series of increasing powers of the electric field. Isotropic materials (like amorphous glass) have zero even order nonlinear optical susceptibilities. For them, in most cases, the contribution of terms of order 5 and higher can be neglected. In the case of linearly polarized beams [2]:

$$\vec{\mathrm{P}} = \varepsilon_0 \left[\chi^{(1)} + \frac{3}{4}\chi^{(3)}_{xxxx}\left|\vec{\mathrm{A}}\right|^2\right]\vec{\mathrm{A}} \quad \textbf{2.29}$$

$\chi^{(3)}$ being the third-order susceptibility of the material. As a consequence of **Equation 2.29**, the refractive index of the material is given by:

$$n \simeq \sqrt{1 + \chi^{(1)} + \frac{3}{4}\chi^{(3)}_{xxxx}\left|\vec{\mathrm{A}}\right|^2} \simeq n_0 + n_2 I = n_0 + \Delta n_{Kerr} \quad \textbf{2.30}$$

n_0 being the linear refractive index and $n_2 = 3\eta_0\chi^{(3)}_{xxxx}/4n_0^2$ the nonlinear refractive index, which is positive in most materials. This variation in the refractive index with the intensity of light is often referred to as Kerr effect. Nonlinear refraction can be included in **Equation 2.13** as:

$$\partial_z A = \frac{i}{2k}\left(\partial_{xx} + \partial_{yy}\right)A + \frac{ikn_2|A|^2}{2\eta_0}A \quad \textbf{2.31}$$

In the case of a circularly polarized beam, the nonlinear refractive index is given by [2]:

$$n_2 = \frac{3\eta_0\chi^{(3)}_{xxyy}}{2n_0^2} \quad \textbf{2.32}$$

Since in isotropic homogeneous media $\chi^{(3)}_{xxxx} = 3\chi^{(3)}_{xxyy}$ [15]:

$$n_2^{lin} = \frac{3}{2} n_2^{circ} \qquad \textbf{2.33}$$

Therefore, the nonlinear refractive index is lower for circular than for linear polarization. This is one of the reasons why waveguide fabrication by fs-laser writing is commonly performed with circularly polarized beams.

2.1.2.2. Self-focusing and filamentation

From **Equation 2.16** it follows that Gaussian beams are more intense at the center of the distribution than in the wings. If we consider the propagation of a collimated intense Gaussian beam, due to the Kerr effect the center of the beam experiences a higher refractive index than the outer region. This situation is similar to traverse through a convergent lens, so the beam is focused as it propagates, i.e., it is self-focused.

Self-focusing becomes stronger as the beam propagates. For very high intensities the beam would shrink to a point singularity [16]. However, in a real situation other effects (like nonlinear absorption or plasma defocusing) prevent the beam collapse [17]. All these effects combined may produce filamentation: the beam remains tightly focused for long distances well above the Rayleigh length without diffracting [17].

2.1.2.3. Other effects

Many other effects may occur during propagation of intense laser pulses. Nonlinear absorption [18] may severely reduce the pulse intensity. The Kerr contribution to refractive index produces also self-phase modulation [19] and self-steepening [20] effects, which may broaden the pulse temporally and spectrally. Group velocity dispersion may increase the pulse duration in highly dispersive materials or over long propagation distances [21]. Also, plasma defocusing may be produced by the electrons excited by nonlinear absorption [22].

Nonlinear absorption mechanisms will be described in the following section. The effect of the rest of these mechanisms will be discussed in more detail in **Section 5.1.4**.

2.2. Laser absorption and photoionization

Mechanisms responsible of the absorption of laser light in dielectric materials are briefly explained in this section.

2.2.1. Linear absorption

Dielectric materials are characterized by an energy gap E_g between the conduction band (CB) and the valence band (VB). This means that the material is transparent to photons of energy $E_p = \hbar\omega$ lower than E_g, while photons of higher energy are absorbed, promoting electrons from the CB to the VB.

Ideal materials do not have electronic levels between the VB and the CB. However, real materials have point defects (vacancies, substitutional, interstitial) which produce the apparition of electronic levels in the gap [23, 24]. This enables electronic transition with energies E_{tr} lower than E_g. In that case, photons of energy $E_p = E_{tr}$ may be absorbed, producing the electronic transition.

Linear absorption is described by the equation [25]:

$$\partial_z I = -\alpha(\omega) I \qquad \textbf{2.34}$$

This mechanism can be introduced in **Equation 2.13** by the addition of one term:

$$\partial_z A = \frac{i}{2k}\left(\partial_{xx} + \partial_{yy}\right)A - \frac{\alpha(\omega)}{2}A \qquad \textbf{2.35}$$

$\alpha(\omega)$ being the linear absorption coefficient of the material at the frequency ω. It is important to note that **Equation 2.35** is valid only when the density of excited electrons is small compared to the unexcited electron density, as it will be shown in **Section 2.5.1**.

Also, there is one mechanism that produces absorption in dielectrics with an appreciable electronic population in the CB. It is inverse Bremsstrahlung [17, 26], which allows free electrons to absorb energy from the incoming photons and increase their kinetic energy. In this case, the absorption coefficient will be proportional to the free electron density ρ_e:

$$\partial_z I = -\sigma_{IB}\rho_e I \qquad \textbf{2.36}$$

σ_{IB} being the inverse Bremsstrahlung cross section.

2.2.2. Nonlinear absorption

Dielectric materials are transparent for light photons with energy lower than E_g. However, for sufficiently high intensities, processes involving the absorption of several photons may occur. A scheme for multiphoton absorption is shown in **Figure 2.6a**. The

absorption of K photons occurs when $E = K E_p$ is higher than E_g. Multiphoton absorption is described by the equation [27, 28]:

$$\partial_z I = -\beta_K I^K \qquad \textbf{2.37}$$

β_K being the K-photon absorption coefficient. This coefficient is very small, so very high intensities ($\sim 10^{15} - 10^{16}\ W/m^2$) are required for producing an appreciable absorption. These high intensities can be easily achieved at the focal volume of ultrashort laser pulses. The energy absorption is thus localized, which is desirable in many applications in laser processing.

Multiphoton absorption can be introduced in **Equation 2.31** as an additional term:

$$\partial_z A = \frac{i}{2k}(\partial_{xx} + \partial_{yy})A + \frac{ikn_2|A|^2}{2\eta_0}A + \frac{\beta_K}{2}\left(\frac{n_0}{2\eta_0}\right)^{K-1}|A|^{2K-2}A \qquad \textbf{2.38}$$

A different nonlinear absorption mechanism is tunneling. In presence of a very intense electric field, the band structure is distorted, enabling the transition of electrons from the BV to the CB by tunnel effect, as shown in **Figure 2.6**b. The required magnitude of the electric field necessary to produce this effect is of the order of $\sim 10^9 - 10^{10}\ V/m$. This is achieved at intensities of $\sim 10^{16}$-$10^{17}\ W/m^2$ or higher [27].

Keldysh developed a rigorous formalism for calculating the ionization rate that includes both mechanisms [18]. It is possible to establish which is the dominant nonlinear absorption mechanism by determining the adiabatic parameter [18, 27]:

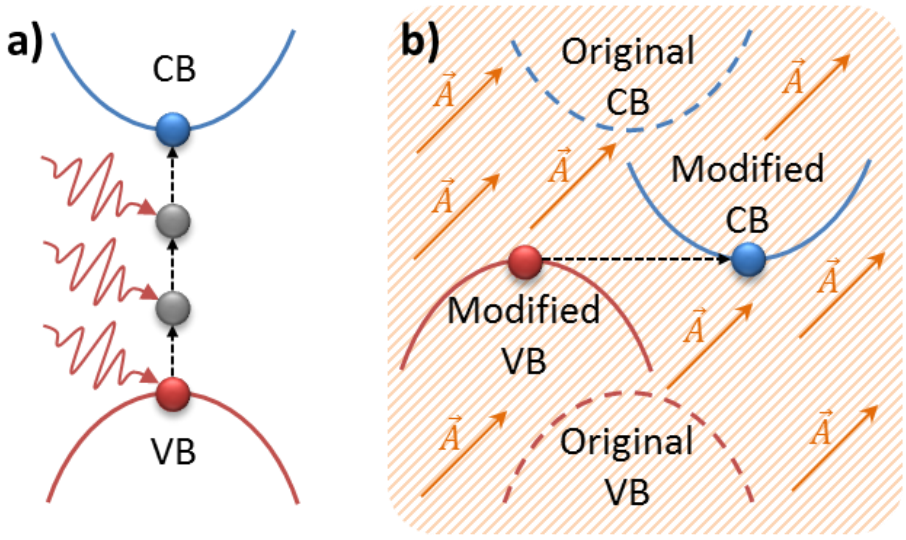

Figure 2.6: *Schematic diagram of the multiphoton ionization (a) and tunneling ionization (b) processes.*

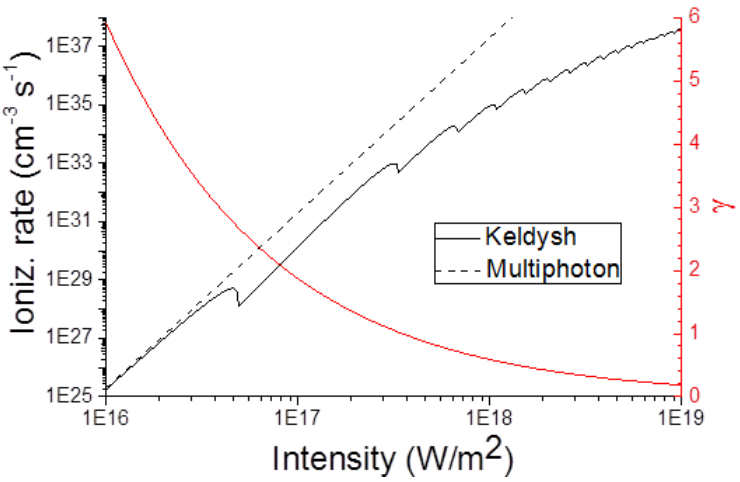

Figure 2.7: *Calculation of the nonlinear ionization rate by the Keldysh model and for a pure 6-photon absorption for a 800 nm laser in fused silica. Figure adapted from [26].*

$$\gamma = \frac{\omega\sqrt{m^* E_g}}{q_e|A|} \qquad \textbf{2.39}$$

m^* being the reduced electron mass and q_e the electron charge. If $\gamma \gg 1$, the process is dominated by multiphoton absorption, while if $\gamma \ll 1$ the process is dominated by tunnelling. If $\gamma \sim 1$, none of both mechanisms can be neglected.

Figure 2.7 shows a comparison of the ionization rate calculated for a pure 6-photon absorption process and by the Keldysh model in fused silica [27]. For intensities lower than 5×10^{16} W/m^2 (γ > 2.5), Keldysh and multiphoton ionization rates converge. For intensities between 5×10^{16} and 2×10^{17} W/m^2 the ionization rate produced by the Keldysh model is reduced by one order of magnitude with respect to multiphoton absorption, but still proportional to I^6. For intensities higher than 2×10^{17} W/m^2 (γ = 1) the difference starts to grow exponentially, as tunneling effect starts to dominate.

Equation 2.38 can be modified to include the Keldysh model instead of multiphoton absorption:

$$\partial_z A = \frac{i}{2k}\left(\partial_{xx} + \partial_{yy}\right)A + \frac{ikn_2|A|^2}{2\eta_0}A + \frac{W_{PI}(|A|)E_g}{2|A|^2}A \qquad \textbf{2.40}$$

$W_{PI}(|A|)$ being the photoionization rate calculated according to the Keldysh model [27].

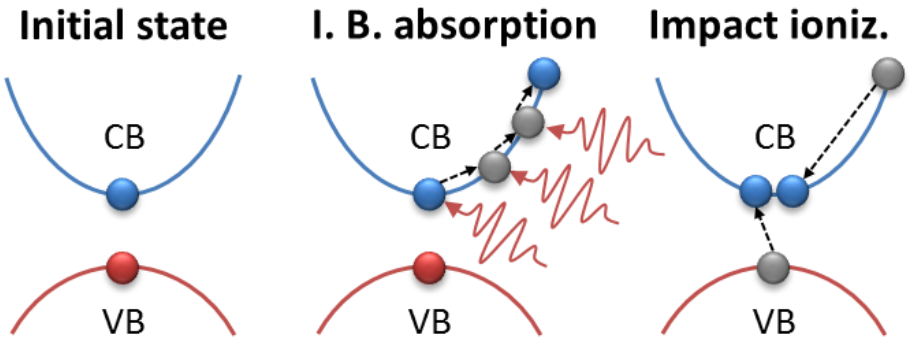

Figure 2.8: *Scheme of the avalanche ionization process. Electrons in the conduction band absorb energy from the pulse by inverse Bremsstrahlung. Then, the accelerated electron may impact another electron in the valence band, leading to a new interband transition.*

2.2.3. Impact ionization

Nonlinear absorption provides a mechanism for populating the CB of a dielectric material with electrons by laser irradiation. As described in **Section 2.2.1**, these free electrons can absorb energy from the laser by inverse Bremsstrahlung, increasing their kinetic energy. A new ionization mechanism may arise in this situation. If an electron absorbs enough photons to increase its kinetic energy above E_g, it can promote new electrons to the CB by inelastic scattering with the electrons in the VB. The schematic diagram of this process is shown in **Figure 2.8**. The rate of impact ionization is given by [29]:

$$\frac{d\rho_e}{dt} = \frac{\sigma_{IB}}{E_g}\rho_e I \qquad \textbf{2.41}$$

This mechanism is self-feeding, leading to an exponentially growing electron density. This is the reason why the combination of inverse Bremsstrahlung and impact ionization is often called avalanche ionization.

Rethfeld and coworkers studied the proportion of electrons excited by multiphoton absorption and impact ionization in fused silica for different irradiation parameters [30]. They developed a model including multiple rate equations (MRE) of the excited electrons. These rate equations consider the fact that the absorption of multiple photons by an electron in the conduction band is not an instantaneous process as it involves the emission/absorption of phonons. A series of equations involving the absorption of one photon per interaction process (until the electron reaches enough kinetic energy to ionize an electron in the valence band) is thus used. They used the transition time t_{MRE} to characterize the transition between multiphoton absorption and avalanche dominated regimes. Their results are shown in **Figure 2.9**. The authors determined the avalanche-dominated regime for $I \times t_{MRE}$ values higher than 10 J/cm^2.

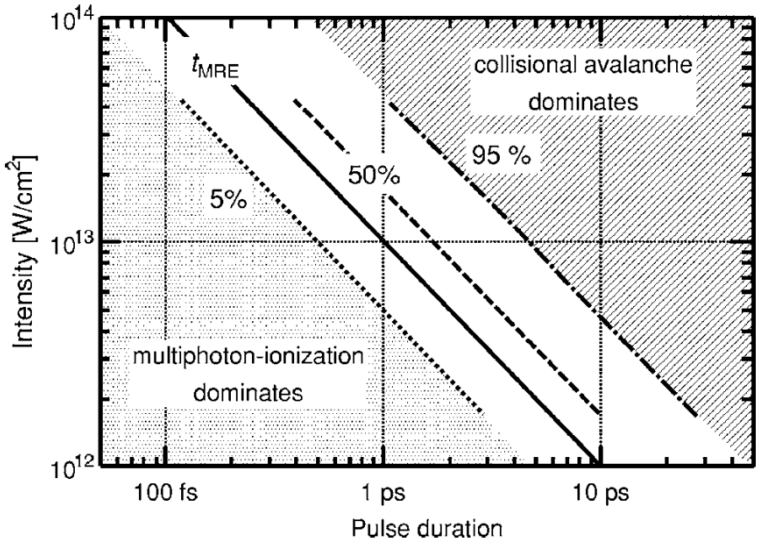

Figure 2.9: *Fraction of avalanche-ionized electrons as a function of laser peak intensity and pulse duration. Figure extracted from [30].*

It is important noting that avalanche ionization can occur in dielectrics for pulses with durations of picoseconds and nanoseconds without multiphoton absorption due to their lower peak intensities. In that case, the initial electronic population in the CB is due to ionized impurities and defects in the material lattice. However, due to the random nature of these free charge sources, the results are hardly reproducible.

2.3. Material modification

Nonlinear absorption and avalanche ionization may produce an electron plasma. This section is devoted to the description of the mechanisms responsible for the energy transfer from the electron plasma to the material lattice and the subsequent structural modifications produced.

2.3.1. Electron thermalization

As a consequence of Coulomb interactions between electrons (electron-electron scattering), plasma temperature is homogenized in some tens of femtoseconds [31, 32]. After the plasma reaches thermal equilibrium, it starts to interact with the lattice by inelastic collisions (electron-phonon scattering). This transfers the energy from the electrons to the lattice, leading to thermal equilibrium. The time of electron-lattice thermalization greatly depends on the material, but it is usually of the order of several picoseconds [32]. The diffusion of heat outside of the irradiated volume occurs in timescales of tens of picoseconds and longer.

2.3.2. Excitons and generation of defects

In fused silica and other wide bandgap materials, the most important electron relaxation mechanism is the production and localization of excitons [33]. As described in **Section 2.2.2**, the absorption of laser pulses produced the excitation of electrons from the VB to the CB. Additionally, the ionization mechanism leaves holes in the VB. These excited electrons and holes may be bounded by Coulomb forces, generating excitons (quasi-particles with neutral charge) [34, 35]. In dielectrics with wide bandgap, these excitons are strongly bound and localized near a single atom (self-trapped excitons). The binding process often requires times lower than 1 ps [33]. When the energy stored in self-trapped excitons is released, it can produce point defects (in particular color centers) in the lattice [33]. Point defects may show energy states in the gap ($E < E_g$). They may produce linear absorption, as described in **Section 2.2.1**. In general, the type of produced defects will depend on the material and electronic band structure [33, 36, 37].

2.3.3. Ablation

If absorption occurs at the surface of the material, material ejection processes may arise if the generated plasma density is sufficiently high. Ultrafast laser pulse induced ablation may show two different regimes.

Gentle ablation [38, 39] occurs for electronic densities below 10^{21} cm^{-3}. It is caused by excited electrons that are extracted from the material, leaving a charge unbalance. The ionized atoms are then rejected due to electrostatic repulsion. This process occurs in just a few picoseconds, before thermal processes start to arise. This is the reason why this process is sometimes called Coulomb explosion. The usual depth of the so produced craters is very small, 5-25 nm.

Strong ablation [38, 39] in turn occurs for electronic densities higher than 10^{21} cm^{-3}. This mechanism is much more violent than gentle ablation. The absorbed energy produces a considerable increase of temperature and pressure, resulting in an ejection of material in the form of ions, atoms and molecular species. The depth of the produced craters is typically one order of magnitude higher than for gentle ablation.

2.3.4. Heat accumulation effects

The energy absorbed from the pulse and transferred to the lattice may heat the material well beyond its melting point. This process typically starts some tens of picoseconds

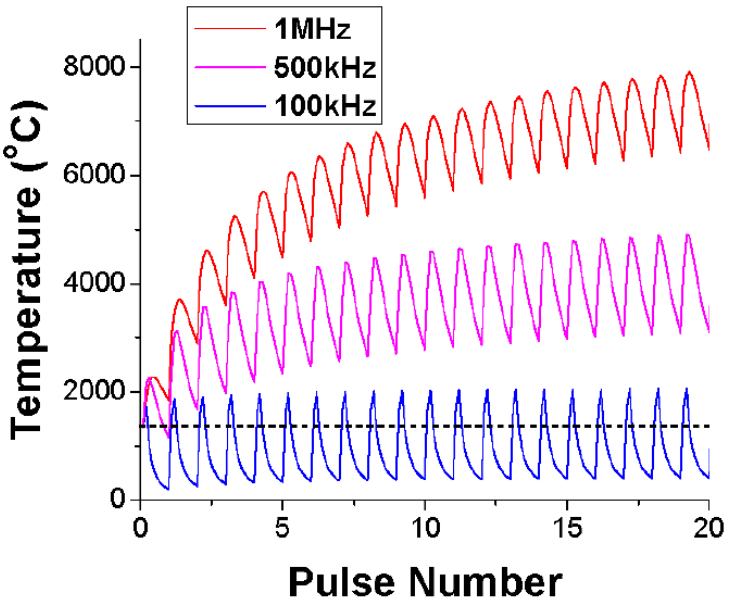

Figure 2.10: *Finite-difference thermal model calculation for ultrashort laser pulse irradiation at different repetition rates. Low repetition rate corresponds to 100 kHz, while 500 kHz and 1 MHz fall into the high repetition rate regime. Figure extracted from [41].*

after the pulse ends [40]. Due to thermal diffusion, the heated region can extend out of the optically excited one.

When the surface is irradiated, the elevated pressure favors material ejection for the highest intensities, as described in the previous section. However, even if ablation occurs, it may remain a non-ejected layer of molten material underneath the ablated crater [40]. On the other hand, if the material is irradiated beneath surface, the heated material cannot be ejected, maintaining a high temperature and pressure until it relaxes by generating structural modifications and by thermal diffusion. The whole process (heating, diffusion, melting, cooling) may require times of the order of microseconds in dielectrics [41].

Depending on the laser repetition rate and the material properties, the irradiation process may be divided into two different regimes [42], as shown in **Figure 2.10**. In the low repetition rate (LRR) regime, the cooling time is smaller than the time lapse between consecutive pulses, and the thermal effect of each pulse can be considered independently. On the other hand, in the high repetition rate (HRR) regime, the cooling time is higher than the time lapse between pulses, and heat accumulation effects arise. This has two effects: it elevates the temperature of the material above the temperature achievable in the LRR regime (for the same absorbed energy), and the time during which the material remains at high temperature is increased. This may affect the nature of the modifications produced in the material [42].

Excitation and relaxation of the material may favor some structural and composition modifications, as it will be described in **Section 2.4.4**. It includes the increase [43] or decrease [44] of the material density, the amorphization of the crystalline lattice [45], the modification of atomic bounds and polarizability of the glass network [46] and the generation of nanogratings [47] or voids [48].

2.4. Light confinement

The fabrication of integrated photonic devices requires of light guiding elements, the equivalent of wires in electronic devices. For guiding light, it is necessary to produce a region with higher refractive index than its surroundings, i.e., a positive refractive index contrast ($\Delta n > 0$), as described in more detail in **Section 2.6.1**. In this section several of the mechanisms and/or techniques capable of producing refractive index contrast and guiding structures are described.

2.4.1. Multilayer structures

One way of producing light confinement in one dimension consists on generating a multilayered structure composed of materials with different refractive index. One of these layers must have a refractive index higher than that of the surrounding layers. **Figure 2.11a** shows an example of a three-layered structure. There are several techniques for producing these layers, like liquid phase epitaxy [49] or pulsed laser deposition [50]. In this kind of structures, Δn is determined by the refractive index of the materials used. However, different effects such as interfacial stress limit the combination of materials that can be combined.

2.4.2. Ion diffusion

Ion diffusion is another mechanism capable of producing light confinement in one or two dimensions [51]. It consists on the diffusion of ions inside the dielectric material, as shown

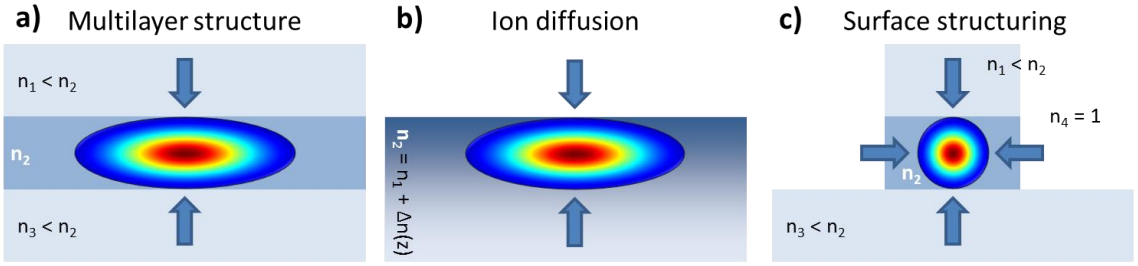

Figure 2.11: *Schematic representation of (a) 1D light confinement by a multilayer structure, (b) 1D confinement in an ion diffusion structure and (c) 2D confinement by surface structuring on a multilayer structure. The arrows correspond to the directions of confinement.*

in **Figure 2.11b**. This can be done by different means. One technique consists on depositing a thin metallic layer on top of the surface of the material and heating it in order to increase the mobility of ions. Then, these ions will penetrate inside the host material. The penetration magnitude and depth will in general depend on the type of ions, host material, temperature and time, but it can reach several microns in depth. The maximum achievable Δn will depend on the ion and host material, but Δn values of the order of 10^{-2} have routinely been reported [51]. The same effect can be induced by ion implantation [52].

Another widely used technique that falls in this category is ion exchange [53]. It consists on the exchange of ions in the host material by ions delivered by an external source. The host material, which must contain single valence cations, is submerged in a molten salt containing a different single valence cation. For the right temperature (thermally assisted) or electric (field assisted) conditions, the cation present in the molten salt diffuses inside the host material. In order to maintain charge neutrality, the host cation diffuses into the molten salt. Two of the most used ions in optical applications are Na^+ (host) and Ag^+ (external) due to the high achievable refractive index contrast and material diffusivity. Again, the penetration depth can reach several microns. Δn values of the order of 10^{-2} have been reported [54].

Ion diffusion and ion exchange allow light confinement in one dimension when the ion diffusion occurs in a whole facet of the material. It is possible to produce confinement in two dimensions, but it requires the deposition of lithographic masks before the diffusion process [53]. This usually requires the use of clean rooms, increasing the complexity of the process.

2.4.3. Surface structuring

Surface structuring can be used for producing light confinement in two dimensions in a system already confining in one dimension. The procedure consists on removing surface material by different techniques, like laser ablation [55]. **Figure 2.11c** shows a scheme of surface structuring on a multilayer structure. Light confinement in the additional dimension is produced by the different refractive index of the material and air. The structure can be covered by a different material in order to properly adjust Δn. Other widely-used techniques for surface structuring are wet etching [56] and ion etching [57], but they also require the deposition of masks.

2.4.4. Structural and compositional modification

Refractive index of materials mainly depends on their structure and composition. In a phenomenological approach, using the Lorentz-Lorenz and Clausious-Mosotti expressions [58], the refractive index can be written as:

$$\frac{n^2-1}{n^2+2} = b\,\rho\,p \qquad \textbf{2.42}$$

b being a constant, ρ the density and p the electrical polarizability of the material. Any change in one of these magnitudes affects the refractive index, so light confinement can be produced by an increment of density [43] or polarizability [46].

It has been shown in **Section 2.3.2** that the formation of self-trapped excitons and its subsequent recombination can produce defects that will also contribute to the refractive index. Also, as described in **Section 2.3.4**, the material can be molten and experience very high pressure, especially upon sub-surface irradiation. When the heat diffuses and the material resolidifies, its structure may change in many ways.

The exact nature of the modifications responsible for the refractive index change upon fs-laser subsurface structuring is controversial in many cases. Structural modifications producing refractive index changes upon irradiation of dielectrics are usually divided in two types, depending on their effect in the refractive index [43, 59, 60]. Type I modification increases the refractive index of the irradiated region, while type II modification produces the opposite effect. It is usual that type I modifications are surrounded by small region of reduced refractive index, and vice-versa. The required intensities for producing type I modifications are just above modification threshold, while type II modification normally require higher ones. However, it is not possible producing both types of modifications in many materials. In any case, the usual magnitudes of Δn produced by subsurface fs-laser irradiation are in the order of 10^{-4} – 10^{-3}.

Since the refractive index strongly depends on the material composition, refractive index contrast can be also induced by modifying the local composition of the material. Structural changes produced at LRR are known to be accompanied by small changes in composition certain cases, although their contribution to Δn is usually negligible. Stronger compositional modifications have been reported at HRR involving a cross ion migration mechanism, both in static [61] and dynamic [62] irradiation conditions, although with little effect in the refractive index. Only recently, positive and large Δn values by compositional

changes have been produced [63-65] due to a careful design of the glass composition and irradiation conditions.

2.5. Spectroscopy of rare earth ions

The production of active photonic devices such as amplifiers and lasers requires the use of luminescent ions. Rare earths (elements located in the Periodic Table after lanthanum, along with lanthanum, yttrium and scandium), are often used as luminescent ions for application in near infrared. In the following sub-sections different systems using rare earths used for optical amplification and laser emission used during this thesis are briefly discussed.

Rare earths show similar chemical properties due to their incomplete 4f electronic layer, which is shielded by the outer 5s and 5p layers. Due to this fact, their electronic band structure is less affected by the surrounding medium, which is desirable for the design and fabrication of active photonic devices.

2.5.1. Electronic transitions

The transition from one electronic level to another in an isolated ion in a condensed medium involves a change in the electron energy E_{tr}. If the energy of the end level is lower than that of the starting level, the electron will emit this energy in the form of a photon (radiative decay) or one or several phonons (non-radiative decay). In the opposite case, the electron must absorb a photon with the same energy than E_{tr} [66].

The probability of a non-radiative decay transition is determined by the medium where the atom is embedded. The probability of a radiative decay mainly depends on the type of transition: dipolar electric, dipolar magnetic, quadrupole electric, etc. Each type has its own selection rules for allowed transitions.

There are two mechanisms for radiative decay. In the spontaneous emission mechanism, the electron emits a photon of angular frequency $\omega = \Delta E/\hbar$ with random phase, propagation direction and polarization. Stimulated emission occurs in the presence of photons of angular frequency $\omega = \Delta E/\hbar$, but in this case, the emitted photon is coherent with the background radiation.

The equations that govern absorption and radiative emission in a two level system are [67]:

$$\frac{d\rho_2(t)}{dt} = \left[\frac{\sigma_{12}}{\hbar\omega}\rho_1(t) - \frac{\sigma_{21}}{\hbar\omega}\rho_2(t)\right] I(\omega,t) - \frac{1}{\tau_2}\rho_2(t) \qquad \textbf{2.43}$$

$$\frac{dI(\omega,z,t)}{dz} = [\sigma_{21}(\omega)\,\rho_2(z,t) - \sigma_{12}(\omega)\rho_1(z,t)]\, I(\omega,z,t) = \alpha(\omega,z,t) I(\omega,z,t) \qquad \textbf{2.44}$$

$$\rho_1(z,t) + \rho_2(z,t) = \rho_{at} \qquad \textbf{2.45}$$

ρ_1 and ρ_2 being the ground and excited electron density, ρ_{at} the active ion concentration, σ_{12} and σ_{21} the absorption and stimulated emission cross sections, and τ_2 the lifetime of the excited level. These equations can be easily extended to a system with a higher number of levels.

The physical meaning of α depends on its sign. If $\alpha > 0$, net gain is produced, α being a gain coefficient. In the opposite case, the light signal is absorbed, α being a linear absorption coefficient, as shown in **Equations 2.34-2.36**. The term *small signal regime* is used to describe a situation where the presence of the external signal doesn't perturb the electronic configuration of the system. In the case of a two level system, this means that $\rho_2 << \rho_1$, so the absorption coefficient $\alpha(\omega) = -\sigma_{12}(\omega)\rho_{at}$, is proportional to the active ion concentration.

In thermal equilibrium, the absorption rate at a certain wavelength is always higher than the emission [23]. This means that it is impossible to produce amplification in a two level system. However, the excited level can be populated by transitions from a third level, so $\sigma_{21}\rho_2 > \sigma_{12}\,\rho_1$ and amplification is produced. This situation is called population inversion.

2.5.2. Erbium – Ytterbium system

Figure 2.12 shows the scheme of the electronic levels of the Yb^{3+} ion, along with the

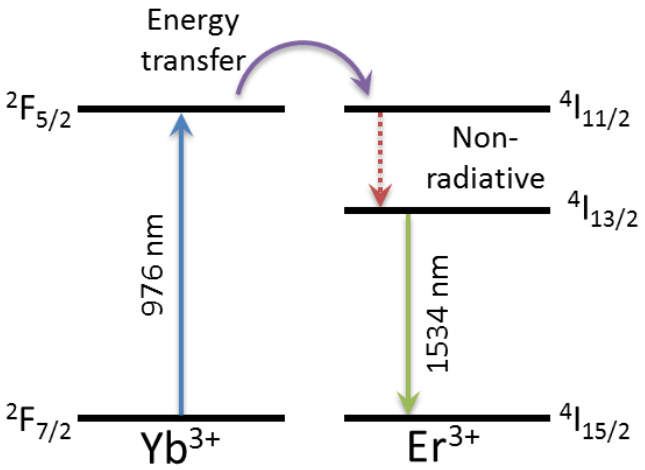

Figure 2.12: *Scheme of the lower electronic levels of the Er-Yb system and the allowed electronic transitions.*

three lowest levels of Er^{3+} ion [68]. The emission of interest in this system is the transition from level $^4I_{13/2}$ and $^4I_{15/2}$ centered around 1534 nm, in the telecommunications C-band. Level $^4I_{11/2}$ can be reached from the ground level by absorption of photons around 976 nm. However, the absorption cross section of this transition is low. This problem can be solved by the addition of Yb^{3+} ions, as they present a much higher absorption cross section at the same wavelength. Then, due to the similarity between $^2F_{5/2}$ and $^4I_{11/2}$ levels, energy transfer occurs between Yb^{3+} and Er^{3+} ions, populating the $^4I_{11/2}$ level. Then, these excited electrons decay to the $^4I_{13/2}$ level mainly by non-radiative transitions. Therefore, amplification/lasing can be achieved at 1534 nm by pumping at 976 nm [67].

It is worth noting that Er^{3+} ions have levels more energetic than the $^4I_{11/2}$ which can be reached by the absorption of several photons, or processes involving two electrons where one increases and the other decreases its energy. These phenomena, collectively denominated upconversion processes, allow the emission at shorter wavelengths. While some devices exploit them in order to generate these emission wavelengths [69, 70], in the devices considered in this thesis upconversion is an undesired effect that reduces the emission efficiency at 1535 nm.

2.5.3. Ytterbium in KYW

Yb^{3+} is in itself a two level system and thus it would be impossible to produce gain using it as gain element. However, in highly anisotropic crystalline materials, the crystalline field can split the Stark sublevels sufficiently so the system operates as a quasi-three or quasi-four levels system. **Figure 2.13** shows the energy levels for Yb^{3+} in a $KY(WO_4)_2$ (KYW) crystal

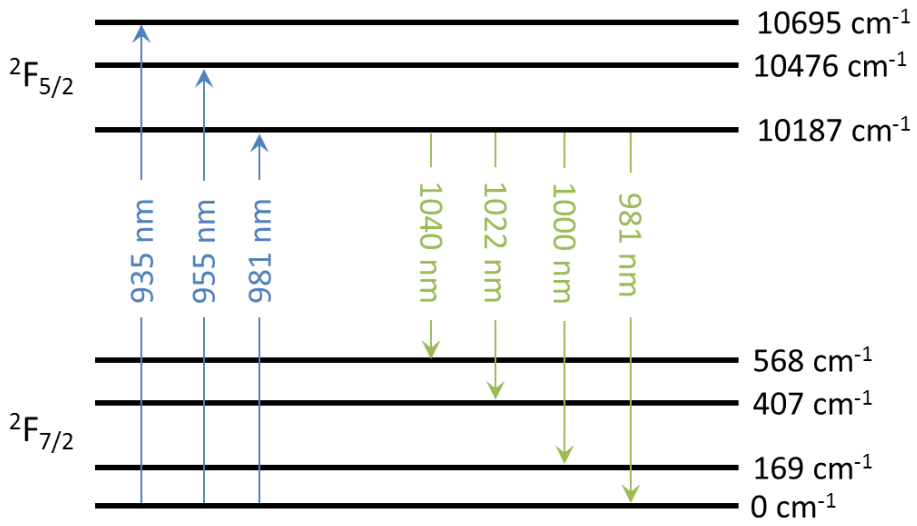

Figure 2.13: *Scheme of the Stark sublevels of Yb^{3+} ions in KYW crystals at 77 K. Figure adapted from [68]*

calculated at 77 K[71].

For this system, pumping can be centered at 935, 955 and 981 nm. For the two first wavelengths, electrons will non-radiatively decay to the lowest sublevel of $^2F_{5/2}$. The emission can be centered at 1040, 1022, 1000 or 981 nm. In the third case, the gain cannot be produced at 981 nm, as it would correspond again to a two level system. The optimum absorption and emission cross sections must be determined beforehand in order to select the optimum configuration. As crystalline field effect relies on symmetry of the material, the corresponding cross-section values are polarization dependent.

2.5.4. Neodymium in $LiNbO_3$

Neodymium electronic levels landscape in $LiNbO_3$ crystals is more complex than that of the previously described systems [72], as shown in **Figure 2.14**. The transitions which show highest cross section occur between $^4I_{9/2}$ and the mixed levels $^2H_{9/2}$ and $^4F_{5/2}$ (~810 nm) for absorption, and between $^4F_{3/2}$ and $^4I_{11/2}$ (~1080 nm) for emission. However, efficient emission at different wavelengths can be obtained if the device is properly configured. Non-radiative decays between Stark sublevels and between close levels will also be present.

2.6. Waveguide-based photonic devices

There is an enormous variety of the waveguide-based photonic devices, even restricting to fs-laser written ones [73-75]. They can be divided into two different types: active

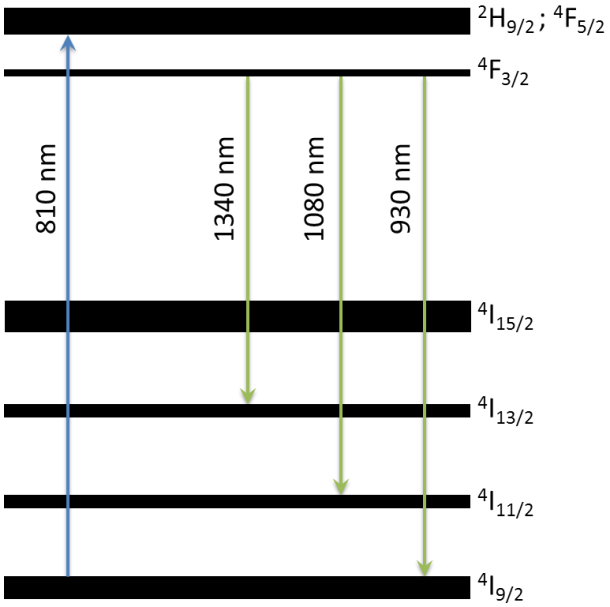

Figure 2.14: *Schematic representation of Nd^{3+} electronic levels in $LiNbO_3$ crystal. Stark sublevels are represented as a continuous energy band.*

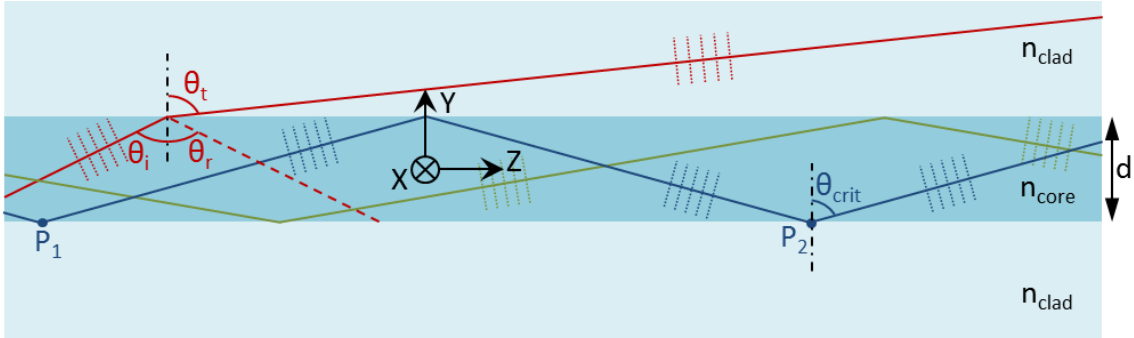

Figure 2.15: *Schematic representation of a waveguide using the planar waves formalism. Dot lines correspond to wavefront.*

and passive. Active devices require energy provided by an additional source, while passive devices don't. Some examples of passive devices are waveguides (used to guide light), Bragg gratings (they reflect/filter certain optical signals), directional couplers (the multiplex or de-multiplex optical signals) or interferometers (more utilized in sensing applications). Examples of active devices are amplifiers (they amplify an optical signal), lasers (optical sources) or lossless couplers (a combination of amplifier and coupler with zero losses) [76]. These devices can be combined, conforming integrated photonic circuits. In the following sub-sections different devices fabricated during the course of this thesis are described in more detail.

2.6.1. Light guiding

Waveguides are the simplest photonic devices in integrated optics. They are used to confine and guide light. They can be described by more simple or detailed models [73, 77, 78]. The simplest description of a step-index waveguide can be done with the planar wave formalism, as schematized in **Figure 2.15** [79].

Consider a region of refractive index n_{core} surrounded by a second one with n_{clad}, with $n_{core} > n_{clad}$. The reflection angles (θ_r) of waves from the core region incident in the interface with the cladding are the same than the incidence angle (θ_i), while the transmitted angle (θ_t) is given by the Snell law (**Equation 2.24**). For low angles (red wave), part of the energy of the wave is reflected and the majority is transmitted outside of the waveguide. However, as $n_{core} > n_{clad}$, there is a critical angle ($\theta_{crit} = \mathrm{asin}(n_{clad}/n_{core})$) whose transmitted angle is 90° (blue wave). For smaller angles (green wave) there is no transmitted, all the energy is reflected and the ray stays inside the waveguide.

In this system, waves with angles higher than θ_{crit} will be confined in the Y direction in the core region (planar waveguides). If the system has cylindrical symmetry, or the refractive index distribution in the X direction is similar, the light will be confined in two dimensions

(channel waveguides). The regions may have different cladding refractive indices; the only requisite is that the highest refractive index corresponds to the core region.

The "zig-zag" of the confined waves can be decomposed as the superposition of two waves, a longitudinal wave propagating along the waveguide (Z direction), and a transversal stationary wave reflected back and forth in the interfaces between core and cladding (Y direction). The stationary wave produces the transverse resonance condition: the phase of the transversal wave in the path between two reflections on the same interface (path between points P_1 and P_2 for the blue wave in **Figure 2.15**) must be multiple of 2π:

$$\varphi = 2k_0 n_{core} d\cos(\theta_r) + 2\varphi_{ref}(\theta_r) = 2\pi m \qquad \textbf{2.46}$$

φ_{ref} being a phase introduced in the reflection which varies from 0 for θ_{crit} to π for normal incidence, d the width of the core layer and m an integer. This means that only waves with certain angles will be guided, which leads naturally to the concept of guided modes. The propagation constant β_m of each mode, the wavenumber of the longitudinal wave, can be defined as:

$$\beta_m = k_0 n_{core}\sin(\theta_r) = k_0 n_{eff} \qquad \textbf{2.47}$$

This constant leads to the definition of the effective refractive index n_{eff}, which can be viewed as the refractive index experienced by the longitudinal wave.

This approximation is too simple in most cases for describing the propagated electric field. In order to do that, the Maxwell equations must be solved in the waveguide. For most cases, there is not an analytic solution and they must be solved numerically. Several models exists for such a purpose, like the beam propagation method (BPM) [78].

It is important noting that the planar wave formalism predicts that the guided modes will not lose power during propagation. More accurate models predict that guided modes will experience losses [78], usually higher for high order modes. In general, losses will depend on the refractive index profile (like Δn magnitude, area, spatial distribution, waveguide curvature, etc.), but will be lower for higher Δn values. Also, additional losses are produced due to irregularities along the propagation direction. The most common source is scattering losses produced at the outer envelope of the waveguide.

2.6.2. Waveguide configurations

Surface waveguides are based in the use of multilayer structures or ion diffusion to produce light confinement. Different geometries for channel waveguides produced in the surface of dielectrics are possible. **Figure 2.16** shows four of the most commonly used ones. The first two may be produced by fs-laser writing. Ridge waveguides are fabricated in a sample with a planar waveguide with the guiding layer directly in contact with air. Then, the material at both sides of the waveguide is removed. A cladding can be deposited afterwards around the core (producing a buried waveguide). Load waveguides are produced similarly to ridge waveguides, but starting with a planar waveguide covered with a cladding layer. Although it may appear that the light is only confined in one dimension, the removal of the material in the cladding layer modifies the n_{eff} of the mode in the core layer, confining the light in the second dimension. **Figure 4.2** shows an example of the calculation of n_{eff} for a load waveguide.

Other configurations can be produced by structuring techniques different than laser writing. Strip waveguides are very similar to ridge waveguides. The difference in the name is due to the difference in fabrication process (by directly depositing a stripe of material over the bulk dielectric). This technique also permits the production of load waveguides, depositing a cladding stripe over a planar waveguide, although in this case they share the same name. Finally, buried waveguides can be created by ion diffusion combined with masks to produce the localized refractive index change.

Sub-surface waveguides, on the other hand, achieve light confinement by structural modifications. They can be produced by fs-laser writing, and the possible waveguide

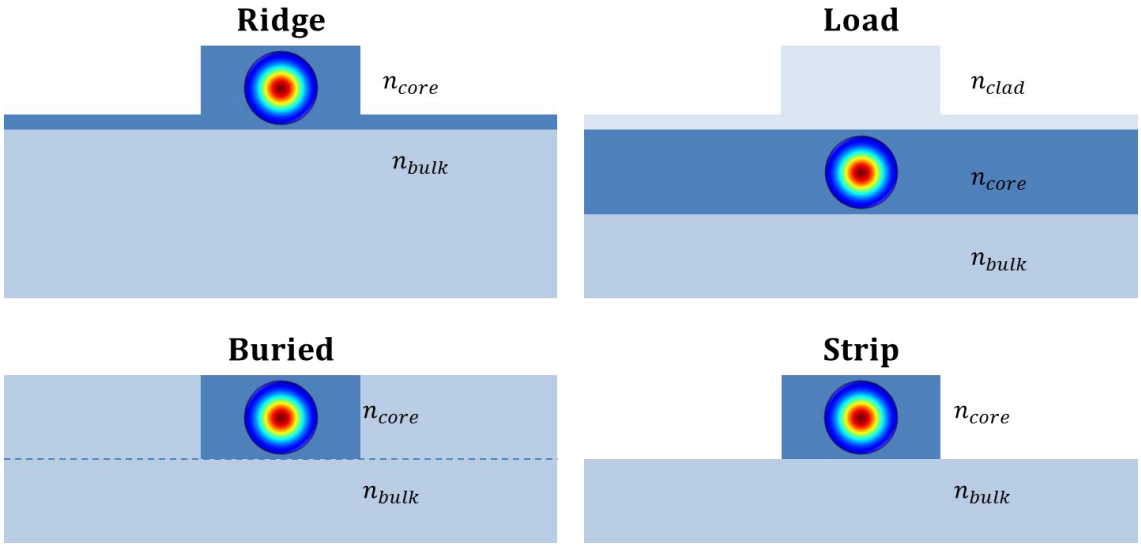

Figure 2.16: *Schematic drawing of the cross section of different surface channel waveguide geometries.*

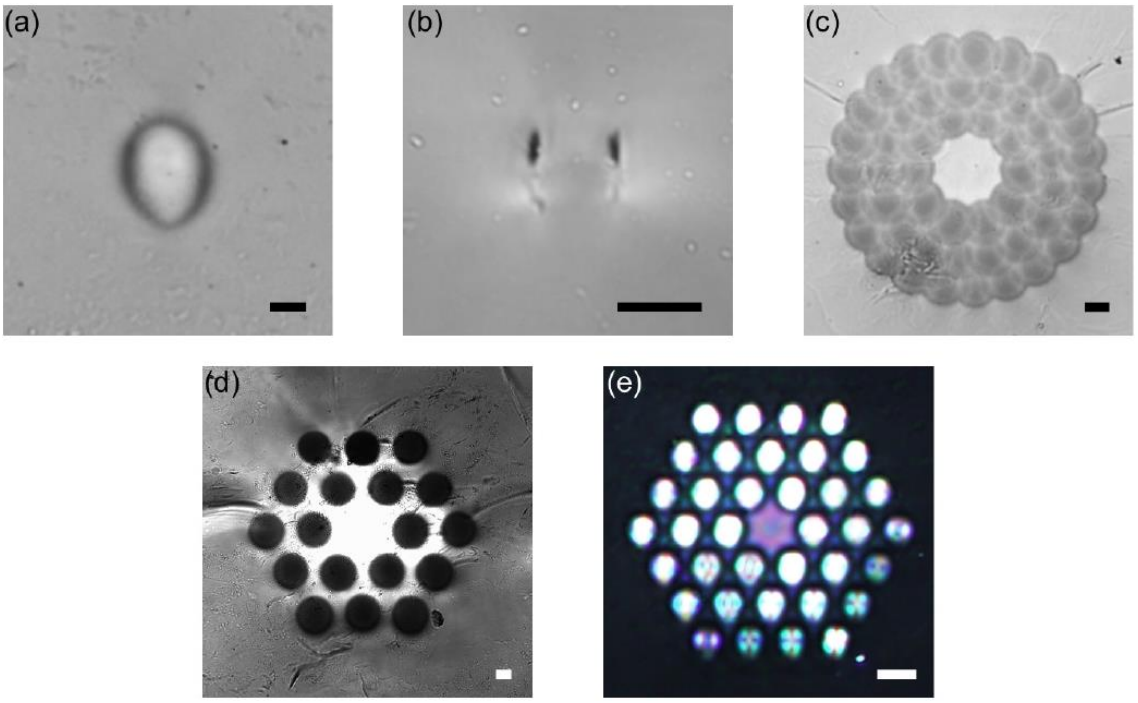

Figure 2.17: *Microscope images of different types of sub-surface waveguides produced by fs laser irradiation. The scale bars correspond to 10 µm. Image taken from [77].*

configurations depend on the Δn produced by the irradiation. Several configurations for sub-surface fs-laser structured waveguides are shown in **Figure 2.17** [80]. **Figure 2.17a** corresponds to a waveguide generated by a type I modification in a boro-aluminosilicate glass exhibiting a central region of increased Δn surrounding a region with decreased Δn. **Figure 2.17b** corresponds to a waveguide generated in titanium-doped sapphire by type II modification, producing two tracks of decreased Δn surrounded by a region of slightly increased Δn. The reduced Δn is produced by damage, and the positive Δn region by stress. The guided mode is located between both tracks. **Figure 2.17c** shows a depressed Δn cladding waveguide based on type I modification in ZBLAN glass. **Figure 2.17d** shows a waveguide generated in the same glass with the same modifications in a different structure. Finally, **Figure 2.17e** shows an ARROW waveguide (anti-resonant reflector optical waveguide [81]) in a boro-aluminosilicate glass based on positive Δn produced by type I modification.

2.6.3. Waveguide performance parameters

The main purpose of waveguides is guiding light signals, so they are essentially characterized by their losses. The loss (l) is an adimensional parameter that represents the amount of signal power lost. For practical purposes, it is usual to express loss in logarithmic scale, (L, in decibels). Both parameters are related by the equation:

$$L = -10\log_{10}(1-l) \quad \textbf{2.48}$$

Propagation losses are related to the power lost during the propagation of the signal inside the waveguide:

$$L^{prop} = -10\log_{10}\left[\frac{P_{out}}{P_{in}}\right] \quad \textbf{2.49}$$

P_{out} being the signal power at the output of the waveguide and P_{in} the power at the input. With a few exceptions, propagation losses are proportional to the signal power:

$$\frac{dP(z)}{dz} = -\alpha_L P(z) \quad \textbf{2.50}$$

α_L being the propagation losses coefficient, which is related with the propagation losses:

$$L^{prop}(\omega) = 10\alpha_L z_{wg}\log_{10}(e) \quad \textbf{2.51}$$

z_{wg} being the total waveguide length. In this case, the power of the signal decreases exponentially.

The waveguide will show additional losses if the intensity distribution of the inserted signal (A_{in}) does not match the guided mode distribution (A_{wg}). The overlapping losses (L^{over}) can be calculated as [82]:

$$L^{over} = -10\log_{10}[\eta^2(\lambda)] \quad \textbf{2.52}$$

$$\eta(\lambda) = \frac{\iint_{-\infty}^{\infty} A_{in}(x,y)A_{wg}(x,y)dx\,dy}{\sqrt{\iint_{-\infty}^{\infty} A_{in}^2(x,y)dx\,dy \iint_{-\infty}^{\infty} A_{wg}^2(x,y)dx\,dy}} \quad \textbf{2.53}$$

η being the overlapping factor and $A(x,y)$ the spatial distribution of the electric field amplitude. In general, both propagation and coupling losses will depend on wavelength. In the first case, scattering at the envelope of the waveguide is one common source of propagation losses [83]. Scattering losses scale with λ^4 [84]. Total losses of the waveguide (L_{total}) are calculated as the addition of propagation and overlapping losses.

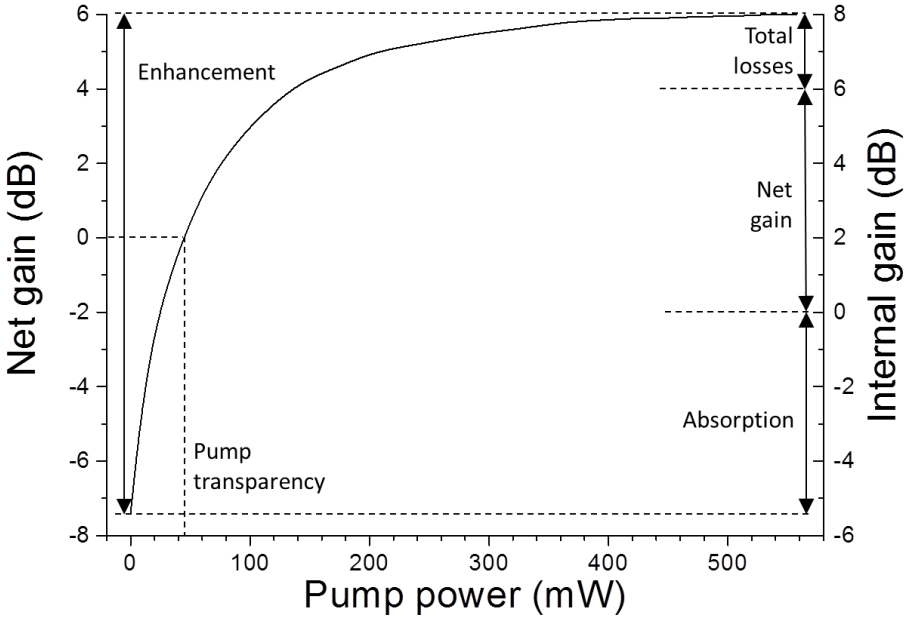

Figure 2.18: *Plot showing the most important parameters of an optical amplifier.*

2.6.4. Optical amplifiers

Optical amplifiers are devices that increase the optical power of an input signal. Optical signals can be amplified by spontaneous emission, typically of rare-earths ions, as described in **Section 2.5.1**. Population inversion is necessary for producing gain, which is normally achieved by pumping at a shorter wavelength.

$$G_{net}(P_{pump}) = 10\log_{10}\left[\frac{P_{out}(P_{pump})}{P_{in}}\right] \qquad \textbf{2.54}$$

Figure 2.18 shows the most important parameters of an optical amplifier in the small signal regime. The main one is the net gain (G_{net}): the relation between the extracted (P_{out}) and the inserted (P_{in}) signal power, which will depend on the pump power (P_{pump}), and is usually given in decibels:

$$G_{net}(P_{pump}) = 10\log_{10}\left[\frac{P_{out}(P_{pump})}{P_{in}}\right] \qquad \textbf{2.54}$$

Optical amplifiers are often implemented in fibers or waveguides, which show certain losses. The internal gain (G_{int}) is defined as the net gain obtained by an ideal device with no losses:

$$G_{int}(P_{pump}) = G_{net}(P_{pump}) + L^{tot} \quad \textbf{2.55}$$

This parameter represents the maximum potential net gain achievable in the selected material. Other parameters of the amplifier are the enhancement (G_{enh}, also called relative gain), which represents the increment in the signal between the *pump* and *no pump* configurations:

$$G_{enh}(P_{pump}) = 10\log_{10}\left[\frac{P_{out}(P_{pump})}{P_{out}(0)}\right] \quad \textbf{2.56}$$

Absorption losses (a_λ) represent the absorption of the signal by the active ions at wavelength λ when the pump is switched off:

$$a_\lambda = 10\log_{10}\left[\frac{P_{in}}{P_{out}(0)}\right] - L^{tot} \quad \textbf{2.57}$$

The relation between absorption losses and the absorption coefficient from **Equation 2.34** can be calculated as:

$$a_\lambda = 10\alpha(\omega)z_{wg}\log_{10}(e) \quad \textbf{2.58}$$

These parameters are related by the equation:

$$G_{enh}(P_{pump}) = G_{net}(P_{pump}) + L^{tot} + a_\lambda \quad \textbf{2.59}$$

Finally, pump transparency (P_{tr}) is defined as the pump power required for the signal output power to be the same as the inserted power, i.e., the pump power necessary for the amplifier to start generating net gain:

$$P_{out}(P_{tr}) = P_{in} \quad \textbf{2.60}$$

2.6.5. Lasers

Lasers are also implemented by taking advantage of the spontaneous emission mechanism. The radiation seed for initiating the stimulated emission is provided by spontaneous emission. However, it is necessary to implement a system that enables feedback. This is the laser cavity, which maintains the majority of the radiation confined inside the gain medium, while extracting some of them, which becomes the laser emission. This is achieved,

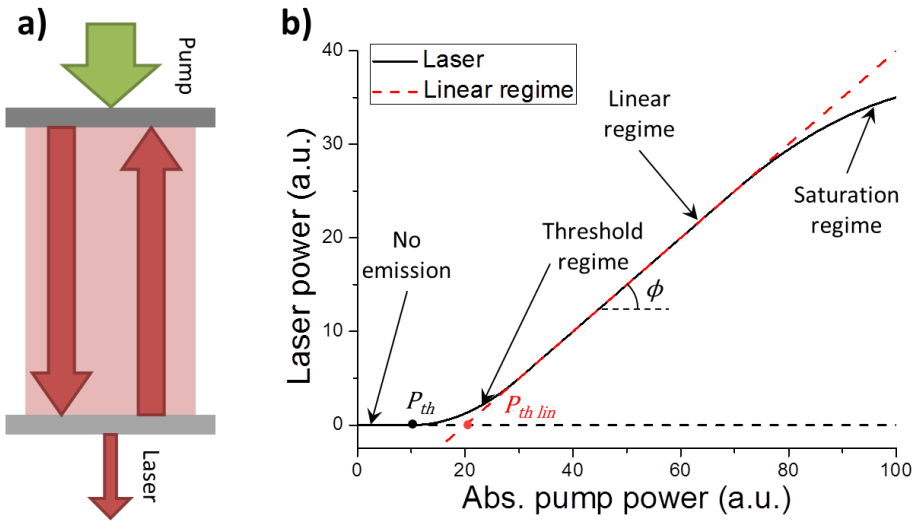

Figure 2.19: *(a) Laser cavity scheme. (b) Scheme of laser emission versus absorbed pump power showing the different operation regimes.*

for example, by placing a total and a partial reflecting mirror at the ends of an optical amplifier, as shown in **Figure 2.19a**.

It is usual to describe lasing emission in terms of absorbed pump power. It can be calculated from the waveguide absorption coefficient α_{pump}, the waveguide propagation losses coefficient α_L and the overlapping factor η_{pump} for pump wavelength. Then, the absorbed pump power is:

$$P_{abs} = P_0 \eta_{pump}^2 \frac{\alpha_{pump}}{\alpha_L + \alpha_{pump}} \left[1 - e^{-(\alpha_L + \alpha_{pump}) z_{wg}}\right] \qquad \textbf{2.61}$$

P_0 being the inserted pump power and z_{wg} the waveguide length.

Figure 2.19b shows a sketch of a laser emission process as a function of pump power. For low pump powers, the stimulated emission cannot overcome the cavity losses (net gain is negative), and laser emission does not occur. The pump power required for producing net gain, and thus start the lasing emission, is called lasing threshold (P_{th}).

The laser emission is linear respect to the absorbed pump power in most lasing models. The slope of this linear fit gives the slope efficiency of the laser (ϕ). This parameter represents the energy conversion rate from pump to signal wavelengths. This efficiency has a maximum given by the energy conservation principle:

$$\phi_{max} = \frac{\lambda_{pump}}{\lambda_{laser}} \qquad \textbf{2.62}$$

which corresponds to a conversion one to one from pump to laser photons.

Experimentally, the lasing curves deviate from the theoretical model. Near the lasing threshold, there is sometimes lasing emission at pump powers lower than that predicted from the linear regime. Also, there is a point for all lasers where emission starts to saturate, when the population inversion is sufficiently high, depending on the lifetime of the excited state and the active ions concentration.

2.7. References

[1] J. Goodman, "Introduction to Fourier Optics," in *Electrical and Computer Engineering*, 2nd ed: McGraw-Hill, 1996.

[2] R. Sutherland, *Handbook of nonlinear optics*, 2nd edition ed. New York: Marcel Dekker, Inc., 2003.

[3] R. R. Thomson, N. D. Psaila, H. T. Bookey, D. T. Reid, and A. K. Kar, "Controlling the Cross-section of Ultrafast Laser Inscribed Optical Waveguides," in *Femtosecond Laser Micromachining: Photonic and microfluidic devices in transparent materials*, R. Osellame, G. Cerullo, and R. Ramponi, Eds., ed: New York Springer, 2012.

[4] R. Osellame, S. Taccheo, M. Marangoni, R. Ramponi, P. Laporta, D. Polli, *et al.*, "Femtosecond writing of active optical waveguides with astigmatically shaped beams," *Journal of the Optical Society of America B,* vol. 20, pp. 1559-1567, 2003.

[5] M. Ams, G. D. Marshall, D. J. Spence, and M. J. Withford, "Slit beam shaping method for femtosecond laser direct-write fabrication of symmetric waveguides in bulk glasses," *Optics Express,* vol. 13, pp. 5676-5681, 2005.

[6] J. Durnin, J. J. M. Jr., and J. H. Eberly, "Diffraction-free beams," *Physical Review Letters,* vol. 58, pp. 1499-1501, 1987.

[7] J. Arlt and K. Dholakia, "Generation of high-order Bessel beams by use of an axicon," *Optics Communications,* vol. 177, pp. 297-301, 2000.

[8] L. Froehly, M. Jacquot, P. A. Lacourt, J. M. Dudley, and F. Courvoisier, "Spatiotemporal structure of femtosecond Bessel beams from spatial light modulators," *Journal of the Optical Society of America A,* vol. 31, pp. 790-793, 2014.

[9] S. Vyas, Y. Kozawa, and S. Sato, "Self-healing of tightly focused scalar and vector Bessel–Gauss beams at the focal plane," *Journal of the Optical Society of America A,* vol. 28, pp. 837-843, 2011.

[10] G. A. Siviloglou and D. N. Christodoulides, "Accelerating finite energy Airy beams," *Optics Letters,* vol. 32, pp. 979-981, 2007.

[11] A. Mathis, F. Courvoisier, R. Giust, L. Furfaro, M. Jacquot, L. Froehly, *et al.*, "Arbitrary nonparaxial accelerating periodic beams and spherical shaping of light," *Optics Letters,* vol. 38, pp. 2218-2220, 2013.

[12] M. Gu and G. Zhou, "Spherical Aberration and its Compensation for High Numerical Aperture Objectives," in *3D Laser Microfabrication*, ed: Wiley-VCH Verlag 2006, pp. 37-56.

[13] M. J. Booth, M. A. A. Neil, and T. Wilson, "Aberration correction for confocal imaging in refractive-index-mismatched media," *Journal of Microscopy,* vol. 192, pp. 90-98, 1998.

[14] J. C. Wyant and K. Creath, *Basic wavefront aberration theory for optical metrology* vol. XI. New York: Academic Press, 1992.

[15] S. V. Popov, Y. P. Svirko, and N. I. Zheludev, *Susceptibility tensors of nonlinear optics*: CRC Press, 1995.

[16] J. H. Marburger, "Self-focusing: Theory," *Progress in Quantum Electronics,* vol. 4, pp. 35-110, 1975.

[17] A. Couairon and A. Mysyrowicz, "Femtosecond filamentation in transparent media," *Physics Reports,* vol. 441, pp. 47-189, 2007.

[18] L. V. Keldysh, "Ionization in the Field of a Strong Electromagnetic Wave," *JEPT,* vol. 20, 1965.

[19] A. Brodeur and S. L. Chin, "Ultrafast white-light continuum generation and self-focusing in transparent condensed media," *Journal of the Optical Society of America B,* vol. 16, pp. 637-650, 1999.

[20] F. DeMartini, C. H. Townes, T. K. Gustafson, and P. L. Kelley, "Self-Steepening of Light Pulses," *Phys. Rev.,* vol. 164, pp. 312-323, 1967.

[21] M. Kolesik, G. Katona, J. V. Moloney, and E. M. Wright, "Physical Factors Limiting the Spectral Extent and Band Gap Dependence of Supercontinuum Generation," *Phys. Rev. Lett.,* vol. 91, p. 043905, 2003.

[22] Y. P. Raĭzer, "Breakdown and heating of gases under the influence of a laser beam," *Soviet Physics Uspekhi,* vol. 8, p. 650, 1966.

[23] B. Henderson and G. F. Imbusch, *Optical Spectroscopy of Inorganic Solids*: Clarendon Press, 1989.

[24] D. M. Krol, "Spectroscopic Characterization of Waveguides," in *Femtosecond Laser Micromachining: Photonic and microfluidic devices in transparent materials*, ed: New York Springer, 2012.

[25] B. Henderson and G. F. Imbusch, "Radiative transitions and selection rules," in *Optical Spectroscopy of Inorganic Solids*, ed: Clarendon Press, 1989.

[26] Y. P. Raizer, "Heating of a gas by a powerful light source," *JETP-USSR,* vol. 21, p. 9, 1965.

[27] A. Couairon, L. Sudrie, M. Franco, B. Prade, and A. Mysyrowicz, "Filamentation and damage in fused silica induced by tightly focused femtosecond laser pulses," *Physical Review B,* vol. 71, p. 125435, 2005.

[28] M. Göppert-Mayer, "Über Elementarakte mit zwei Quantensprüngen," *Annalen der Physik,* vol. 401, pp. 273-294, 1931.

[29] B. Rethfeld, "Unified Model for the Free-Electron Avalanche in Laser-Irradiated Dielectrics," *Physical Review Letters,* vol. 92, p. 187401, 2004.

[30] B. Rethfeld, "Free-electron generation in laser-irradiated dielectrics," *Physical Review B,* vol. 73, p. 035101, 2006.

[31] N. S. Shcheblanov and T. E. Itina, "Femtosecond laser interactions with dielectric materials: insights of a detailed modeling of electronic excitation and relaxation processes," *Applied Physics A,* vol. 110, pp. 579-583, 2013.

[32] B. Rethfeld, K. Sokolowski-Tinten, D. von der Linde, and S. I. Anisimov, "Timescales in the response of materials to femtosecond laser excitation," *Applied Physics A,* vol. 79, pp. 767-769, 2004.

[33] S. S. Mao, F. Quéré, S. Guizard, X. Mao, R. E. Russo, G. Petite*, et al.*, "Dynamics of femtosecond laser interactions with dielectrics," *Applied Physics A,* vol. 79, pp. 1695-1709, 2004.

[34] M. Ueta, H. Kanzaki, K. Kobayashi, Y. Toyozawa, and E. Hanamura, *Excitronic Processes in Solids*. Berlin-Heidelberg-New York: Springer, 1986.

[35] R. T. Williams and K. S. Song, "The self-trapped exciton," *Journal of Physics and Chemistry of Solids,* vol. 51, pp. 679-716, 1990.

[36] P. Martin, S. Guizard, P. Daguzan, G. Petite, P. D'Oliveira, P. Meynadier*, et al.*, "Subpicosecond study of carrier trapping dynamics in wide-band-gap crystals," *Physical Review B,* vol. 55, pp. 5799-5810, 1997.

[37] O. M. Efimov, K. Gabel, S. V. Garnov, L. B. Glebov, S. Grantham, M. Richardson*, et al.*, "Color-center generation in silicate glasses exposed to infrared femtosecond pulses," *Journal of the Optical Society of America B,* vol. 15, pp. 193-199, 1998.

[38] D. Ashkenasi, A. Rosenfeld, H. Varel, M. Wähmer, and E. E. B. Campbell, "Laser processing of sapphire with picosecond and sub-picosecond pulses," *Applied Surface Science,* vol. 120, pp. 65-80, 1997.

[39] R. Stoian, D. Ashkenasi, A. Rosenfeld, and E. E. B. Campbell, "Coulomb explosion in ultrashort pulsed laser ablation of Al2O3," *Physical Review B,* vol. 62, pp. 13167-13173, 2000.

[40] A. Ben-Yakar, A. Harkin, J. Ashmore, R. L. Byer, and H. A. Stone, "Thermal and fluid processes of a thin melt zone during femtosecond laser ablation of glass: the formation of rims by single laser pulses," *Journal of Physics D: Applied Physics,* vol. 40, p. 1447, 2007.

[41] M. Sakakura, M. Terazima, Y. Shimotsuma, K. Miura, and K. Hirao, "Heating and rapid cooling of bulk glass after photoexcitation by a focused femtosecond laser pulse," *Optics Express,* vol. 15, pp. 16800-16807, 2007.

[42] S. Eaton, H. Zhang, P. Herman, F. Yoshino, L. Shah, J. Bovatsek, *et al.*, "Heat accumulation effects in femtosecond laser-written waveguides with variable repetition rate," *Optics Express,* vol. 13, pp. 4708-4716, 2005.

[43] J. W. Chan, T. Huser, S. Risbud, and D. M. Krol, "Structural changes in fused silica after exposure to focused femtosecond laser pulses," *Optics Letters,* vol. 26, pp. 1726-1728, 2001.

[44] J. W. Chan, T. R. Huser, S. H. Risbud, J. S. Hayden, and D. M. Krol, "Waveguide fabrication in phosphate glasses using femtosecond laser pulses," *Applied Physics Letters,* vol. 82, pp. 2371-2373, 2003.

[45] T. Gorelik, M. Will, S. Nolte, A. Tuennermann, and U. Glatzel, "Transmission electron microscopy studies of femtosecond laser induced modifications in quartz," *Applied Physics A,* vol. 76, pp. 309-311, 2003.

[46] D. J. Little, M. Ams, P. Dekker, G. D. Marshall, and M. J. Withford, "Mechanism of femtosecond-laser induced refractive index change in phosphate glass under a low repetition-rate regime," *Journal of Applied Physics,* vol. 108, p. 033110, 2010.

[47] M. Beresna, M. Gecevičius, and P. G. Kazansky, "Polarization sensitive elements fabricated by femtosecond laser nanostructuring of glass [Invited]," *Optical Materials Express,* vol. 1, pp. 783-795, 2011.

[48] S. Juodkazis, K. Nishimura, S. Tanaka, H. Misawa, E. G. Gamaly, B. Luther-Davies, *et al.*, "Laser-Induced Microexplosion Confined in the Bulk of a Sapphire Crystal: Evidence of Multimegabar Pressures," *Physical Review Letters,* vol. 96, p. 166101, 2006.

[49] J. J. Carvajal, M. C. Pujol, and F. Diaz, "High-Temperature Solution Growth: Application to Laser and Nonlinear Optical Crystals," in *Springer Handbook of Crystal Growth*, G. Dhanaraj, K. Byrappa, V. Prasad, and M. Dudley, Eds., ed: Springer Berlin Heidelberg, 2010.

[50] D. H. Lowndes, D. B. Geohegan, A. A. Puretzky, D. P. Norton, and C. M. Rouleau, "Synthesis of Novel Thin-Film Materials by Pulsed Laser Deposition," *Science,* vol. 273, pp. 898-903, 1996.

[51] R. V. Schmidt and I. P. Kaminow, "Metal-diffused optical waveguides in LiNbO3," *Applied Physics Letters,* vol. 25, pp. 458-460, 1974.

[52] F. Chen, X.-L. Wang, and K.-M. Wang, "Development of ion-implanted optical waveguides in optical materials: A review," *Optical Materials,* vol. 29, pp. 1523-1542, 2007.

[53] A. Tervonen, B. R. West, and S. Honkanen, "Ion-exchanged glass waveguide technology: a review," *Optical Engineering,* vol. 50, pp. 071107-071107-15, 2011.

[54] G. Jose, G. Sorbello, S. Taccheo, G. Della Valle, E. Cianci, V. Foglietti, *et al.*, "Ag+–Na+ ion exchange from dilute melt: guidelines for planar waveguide fabrication on a commercial phosphate glass," *Optical Materials,* vol. 23, pp. 559-567, 2003.

[55] J. Cugat, A. R. d. l. Cruz, R. Sole, A. Ferrer, J. J. Carvajal, X. Mateos, *et al.*, "Femtosecond-Laser Microstructuring of Ribs on Active (Yb,Nb):RTP/RTP Planar Waveguides," *Journal of Lightwave Technology,* vol. 31, pp. 385-390, 2013.

[56] H. Hu, R. Ricken, W. Sohler, and R. B. Wehrspohn, "Lithium Niobate Ridge Waveguides Fabricated by Wet Etching," *IEEE Photonics Technology Letters,* vol. 19, pp. 417-419, 2007.

[57] J. L. Jackel, R. E. Howard, E. L. Hu, and S. P. Lyman, "Reactive ion etching of LiNbO3," *Applied Physics Letters,* vol. 38, pp. 907-909, 1981.

[58] J. M. Fernández-Navarro, *El vidrio: constitución, fabricación, propiedades*, 3rd ed. Madrid: CSIC, 2003.

[59] R. Stoian, "Optimizing Laser-Induced Refractive Index Changes in Optical Glasses via Spatial and Temporal Adaptive Beam Engineering," in *Femtosecond Laser Micromachining: Photonic and microfluidic devices in transparent materials*, R. Osellame, G. Cerullo, and R. Ramponi, Eds., ed: New York Springer, 2012.

[60] O. M. Efimov, L. B. Glebov, K. A. Richardson, E. Van Stryland, T. Cardinal, S. H. Park, *et al.*, "Waveguide writing in chalcogenide glasses by a train of femtosecond laser pulses," *Optical Materials,* vol. 17, pp. 379-386, 2001.

[61] Y. Liu, M. Shimizu, B. Zhu, Y. Dai, B. Qian, J. Qiu, *et al.*, "Micromodification of element distribution in glass using femtosecond laser irradiation," *Optics Letters,* vol. 34, pp. 136-138, 2009.

[62] P. Mardilovich, L. B. Fletcher, N. W. Troy, L. Yang, H. Huang, S. H. Risbud, *et al.*, "Ultrafast Laser Fabrication of Hybrid Micro- and Nano-Structures in Semiconductor-doped Borosilicate Glasses," *International Journal of Applied Glass Science,* vol. 4, pp. 87-99, 2013.

[63] J. del Hoyo, R. M. Vazquez, B. Sotillo, T. T. Fernandez, J. Siegel, P. Fernández, *et al.*, "Control of waveguide properties by tuning femtosecond laser induced compositional changes," *Applied Physics Letters,* vol. 105, p. 131101, 2014.

[64] J. Solis, T. T. Fernandez, J. d. Hoyo, J. Siegel, and P. M. Zarate, "Femtosecond-laser-induced compositional changes for high-performance photonics," *SPIE Newsroom,* 2015.

[65] T. Toney Fernandez, P. Haro-González, B. Sotillo, M. Hernandez, D. Jaque, P. Fernandez, *et al.*, "Ion migration assisted inscription of high refractive index contrast waveguides by femtosecond laser pulses in phosphate glass," *Optics Letters,* vol. 38, pp. 5248-5251, 2013.

[66] R. C. Powell, *Physics of Solid-State Laser Materials*, 1st edition ed. New York: Springer-Verlag New York, 1998.

[67] J. A. Valles, M. A. Rebolledo, and J. Cortes, "Full characterization of packaged Er-Yb-codoped phosphate glass waveguides," *IEEE Journal of Quantum Electronics,* vol. 42, pp. 152-159, 2006.

[68] B. Henderson and G. F. Imbusch, "Spectroscopy of lanthanide (rare-earth) and actanide ions in solids," in *Optical Spectroscopy of Inorganic Solids*, ed: Clarendon Press, 1989.

[69] A. Miguel, R. Morea, J. Gonzalo, M. A. Arriandiaga, J. Fernandez, and R. Balda, "Near-infrared emission and upconversion in Er3+-doped TeO2–ZnO–ZnF2 glasses," *Journal of Luminescence,* vol. 140, pp. 38-44, 2013.

[70] T. Lu, L. Yang, R. V. A. van Loon, A. Polman, and K. J. Vahala, "On-chip green silica upconversion microlaser," *Optics Letters,* vol. 34, pp. 482-484, 2009.

[71] N. V. Kuleshov, A. A. Lagatsky, A. V. Podlipensky, V. P. Mikhailov, and G. Huber, "Pulsed laser operation of Yb-doped KY(WO4)2 and KGd(WO4)2," *Optics Letters,* vol. 22, pp. 1317-1319, 1997.

[72] V. T. Gabrielyan, A. A. Kaminskii, and L. Li, "Absorption and luminescence spectra and energy levels of Nd3+ and Er3+ ions in LiNbO3 crystals," *Physica status solidi (a),* vol. 3, pp. K37-K42, 1970.

[73] R. Osellame, G. Cerullo, and R. Ramponi, *Femtosecond Laser Micromachining: Photonic and microfluidic devices in transparent materials*: New York Springer, 2012.

[74] G. D. Valle, R. Osellame, and P. Laporta, "Micromachining of photonic devices by femtosecond laser pulses," *Journal of Optics A: Pure and Applied Optics,* vol. 11, p. 013001, 2009.

[75] R. R. Gattass and E. Mazur, "Femtosecond laser micromachining in transparent materials," *Nat Photon,* vol. 2, pp. 219-225, 2008.

[76] P. Camy, J. E. Roman, F. W. Willems, M. Hempstead, J. C. V. D. Plaats, C. Prel, *et al.*, "Ion-exchanged planar lossless splitter at 1.5 um," *Electronics Letters,* vol. 32, pp. 321-323, 1996.

[77] G. Lifante, *Integrated Photonics: Fundamentals*. Chichester, UK: John Wiley & Sons Ltd., 2003.

[78] G. Lifante, *Beam Propagation Method for Design of Optical Waveguide Devices*: John Wiley & Sons, Ltd, 2015.

[79] H. Kogelnik, "Theory of Optical Waveguides," in *Guided-Wave Optoelectronics*, T. Tamir, Ed., ed: Springer Berlin Heidelberg, 1988, pp. 7-88.

[80] S. Gross, M. Dubov, and M. J. Withford, "On the use of the Type I and II scheme for classifying ultrafast laser direct-write photonics," *Optics Express,* vol. 23, pp. 7767-7770, 2015.

[81] S. Gross, M. Alberich, A. Arriola, M. J. Withford, and A. Fuerbach, "Fabrication of fully integrated antiresonant reflecting optical waveguides using the femtosecond laser direct-write technique," *Optics Letters,* vol. 38, pp. 1872-1874, 2013.

[82] A. K. Mairaj, P. Hua, H. N. Rutt, and D. W. Hewak, "Fabrication and characterization of continuous wave direct UV (lambda =244 nm) written channel waveguides in chalcogenide (Ga:La:S) glass," *Lightwave Technology, Journal of,* vol. 20, pp. 1578-1584, 2002.

[83] J. A. Valles, J. Solis, J. A. Sanchez-Martin, A. R. d. l. Cruz, M. A. Rebolledo, and A. Ferrer, "Assessment of Rayleigh and non-Rayleigh Contributions to the Transmission Losses in fs-Laser Written Er/Yb- Codoped Phosphate Glass Waveguides," *Journal of Laser Micro/Nanoengineering,* vol. 5, pp. 39-42, 2010.

[84] L. Tong, R. R. Gattass, I. Maxwell, J. B. Ashcom, and E. Mazur, "Optical loss measurements in femtosecond laser written waveguides in glass," *Optics Communications,* vol. 259, pp. 626-630, 2006.

Chapter 3
Experimental and modeling techniques

This chapter is divided into four main sections. First, the main experimental setups used for producing active and passive waveguides by direct laser writing are described. Second section describes the experimental setups used to characterize the properties of the fabricated waveguides. Third section includes the description of the models used for the design of the beams utilized in the fabrication of waveguides, as well as in the determination of the characterization parameters. Due to its complexity, the model for calculating the propagation of ultrashort laser pulses inside dielectric materials is described in **Section 5.1**. Finally, the last section describes the fabrication procedures of the dielectric samples used in this thesis.

The production of both surface and sub-surface waveguides has been performed at the Laser Processing Group of the Institute of Optics of CSIC, Madrid, Spain (GPL-CSIC). The surface ablation channels using Gauss-Bessel and accelerating beams were produced during a stay at the Optics Department of Femto-ST, Besançon, France (OD-Femto-ST), in collaboration with Prof. François Courvoisier. The characterization of the surface waveguides was performed at the GPL and at the Materials Science Department of Universidad Autónoma de Madrid, Spain (MSD-UAM), in collaboration with Prof. Ginés Lifante and Dr. Jon Martínez de Mendivil. The characterization of the sub-surface waveguides was performed at GPL-CSIC and at the Applied Physics Department of the Universidad de Zaragoza, Spain (APD-Unizar), in collaboration with Prof. Miguel Ángel Rebolledo and Prof. Juan Vallés. The modeling of the optical performance of the surface and sub-surface waveguides was performed in collaboration with the groups at MSD-UAM and APD-Unizar respectively. EDX local compositional measurements were performed at the Material Physics Department of Universidad Complutense of Madrid, Madrid, Spain (MPD-UCM), in collaboration with Prof. Paloma Fernández and Dr. Belen Sotillo. Refractive index profilometry was performed at the Physics Department of the Politecnico di Milano / Institute of Photonics and Nanotechnology of the CNR, Milan, Italy (PD-IPN), in collaboration with Dr. Roberto Osellame and Dr. Rebeca Martínez. $KY(WO_4)_2$ crystals were produced at the Physics and Crystallography of Materials Group of Universidad Rovira i Virgili, Tarragona, Spain (FICMA-URV) in collaboration with Prof. Francesc Díaz, while $LiNbO_3$ crystals were produced at the MSD. Non-commercial phosphate glasses were produced at the GPL-CSIC with the advice of Prof. José María Fernández-Navarro. Phosphate glass composition characterization by PIXE measurements were performed at

Centro Nacional de Aceleradores, Seville, Spain (CNA), in collaboration with Dr. Inés Ortega-Feliu. The rest of the processing and characterization techniques were performed at the GPL-CSIC.

3.1. Waveguide production

3.1.1. Laser sources

During the development of this thesis, three laser sources have been employed. They can be divided in two types: low repetition rate (LRR) and high repetition rate (HRR). Their main characteristics are listed in **Table 3.1**.

3.1.1.1. Low repetition rate laser sources

Two LRR laser sources were used, one at the GPL-CSIC and the other at OD-Femto-ST. Both LRR lasers share a similar design. The schematic representation is shown in **Figure 3.1**. They consist on two subsystems: an oscillator that generates the femtosecond laser pulses, and a regenerative amplifier that increases the energy of the pulses. The amplifiers work in the Chirped Pulse Amplifier (CPA) configuration [1].

LS1 uses a Tsunami laser (Spectra Physics) as fs-oscillator. Tsunami uses a continuous solid state pump laser (Milenia V, Spectra Physics) with a Nd^{3+}-doped YVO_4 crystal active medium. Nd^{3+} emission at 1064 *nm* is doubled in frequency to 532 *nm*. This laser is used to pump the active medium of the oscillator (Ti:Saphire crystal). Oscillator mode locking is based in the Kerr lens mechanism [2]. The output of the oscillator is a pulsed beam of ~100 *fs* (9.5 *nm* spectral width) pulses at 82 *MHz*, 9 *nJ* pulse energy and with a central wavelength tunable between 720 and 1050 *nm*. The oscillator of LS2 is a Maï-Taï (Spectra Physics) that provides pulses of 100 *fs* and 10 *nJ* pulse energy centered between 690 and 1040 *nm* at 80 *MHz*. Both lasers are operated at a 800 *nm* central wavelength.

The amplifier of both laser systems is a Spitfire (Spectra Physics), which is itself divided in three subsystems: pulse stretcher, regenerative amplifier and pulse compressor. The laser pulse is temporally stretched by the introduction of chirp in the stretcher. This is done by

Table 3.1: *Main parameters of the pulsed laser sources used in this thesis.*

Name	Location	Type	Max. repetition rate (kHz)	Min. pulse duration (fs)	Pulse energy (μJ)	Wavelength (nm)
LS1	GPL	LRR	1	100	1000	800
LS2	Femto-ST	LRR	5	100	200	800
LS3	GPL	HRR	2000	350	10	1030

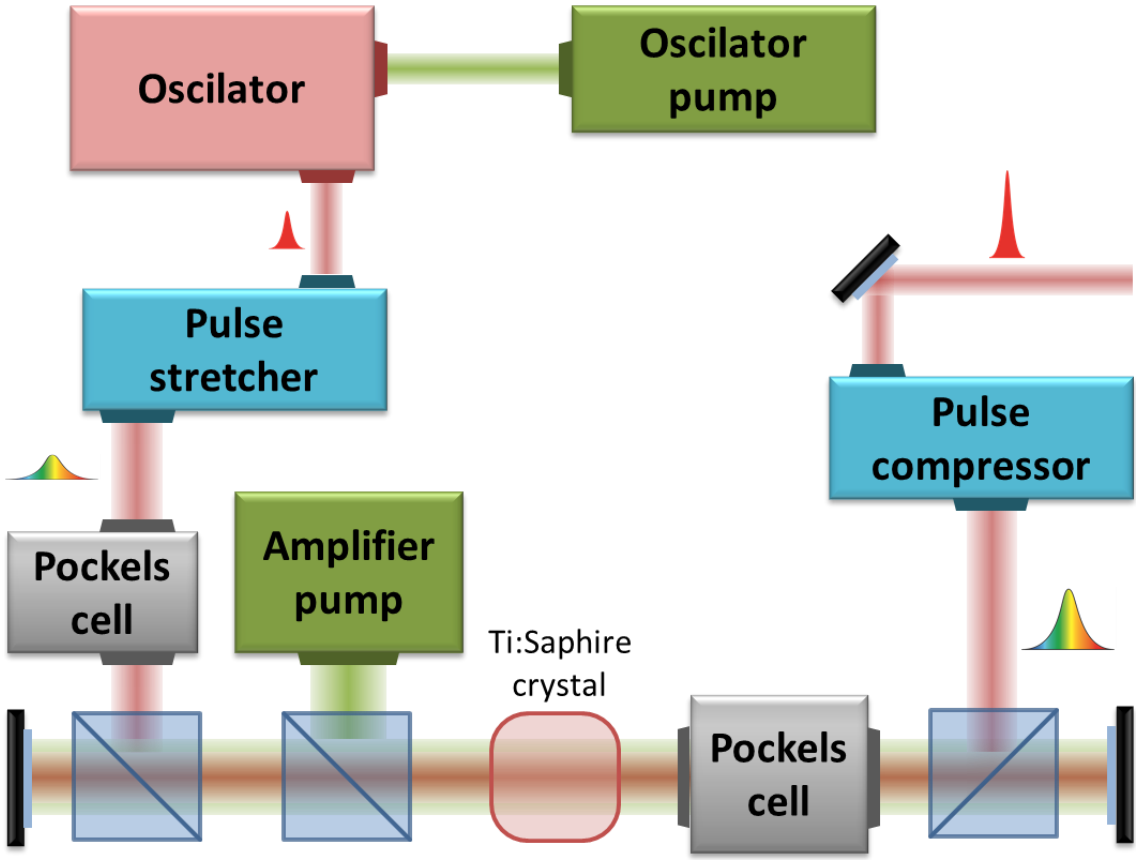

Figure 3.1: *Schematic representation of the LRR lasers. The seed generated by the oscillator is temporally stretched by the pulse stretcher to be inserted in the Pockels cell of the regenerative amplifier cavity. There, the pulse gets amplified during several roundtrips through the active medium before being expelled of the regenerative cavity and compressed again to the final pulse duration.*

introducing different times of flight in the different wavelengths. This way, the maximum intensity is greatly reduced, avoiding damaging the optical elements in the amplification stage by nonlinear absorption.

The regenerative amplifier works as a laser cavity. A combination of a Pockels cell and a thin-layer polarizer (polarizer cube in the figure for simplicity) controls the entrance of oscillator pulses in the cavity to match the pump laser frequency. The active medium is a Ti:Saphire crystal pumped by a laser (Evolution, Spectra Physics) working in Q-switched configuration. This pump laser (532 *nm*) produces pulses of 130 *ns*, 7 *mJ* at 1 *kHz* repetition rate (LS1). A second Pockels cell and thin film polarizer extracts the pulse of highest energy after a given number of roundtrips of the pulse inside the regenerative cavity. The extraction frequency can be controlled to match the one of the pump laser (1 *kHz* for LS1 and 5 *kHz* for LS2) or be reduced down to single shot operation.

Finally, the beam is inserted in the pulse compressor, which has the opposite effect of the stretcher: it temporally compresses the pulse again to 100 *fs*. If a longer pulse duration is

required, the compressor can be adjusted to induce positive or negative chirp, so the pulse shows a stretched temporal profile up to a maximum of ~3 *ps*. The output pulse energy is ~1 *mJ* for LS1 and ~200 *μJ* for LS2. The final beam diameter is 7.4 *mm* diameter ($1/e^2$ in intensity) in both cases.

3.1.1.2. High repetition rate laser

The third laser source (LS3) is a fs fiber-amplifier laser (Tangerine, Amplitude Systems) at HRR. Its diagram is shown in **Figure 3.2**. Similarly to the LRR lasers, it consists on an oscillator that produces the pulses and an amplifier to increase the pulse energy. The active medium is an Yb^{3+}-doped crystal, and mode locking is performed using a semiconductor saturable absorber mirror (SESAM), which is reflective only above a certain peak power. The system requires some noise to start pulsing, which is achieved by mechanically rocking one of the mirrors of the oscillator. When pulsing, the oscillator emits pulses at 1030 *nm* central wavelength with a spectral width of 4 *nm*, and a pulse duration of ~300 *fs* with pulse energies of ~40 *nJ*, at a rate of 50 *MHz*.

The pulses are then temporally stretched, and their repetition rate reduced by an

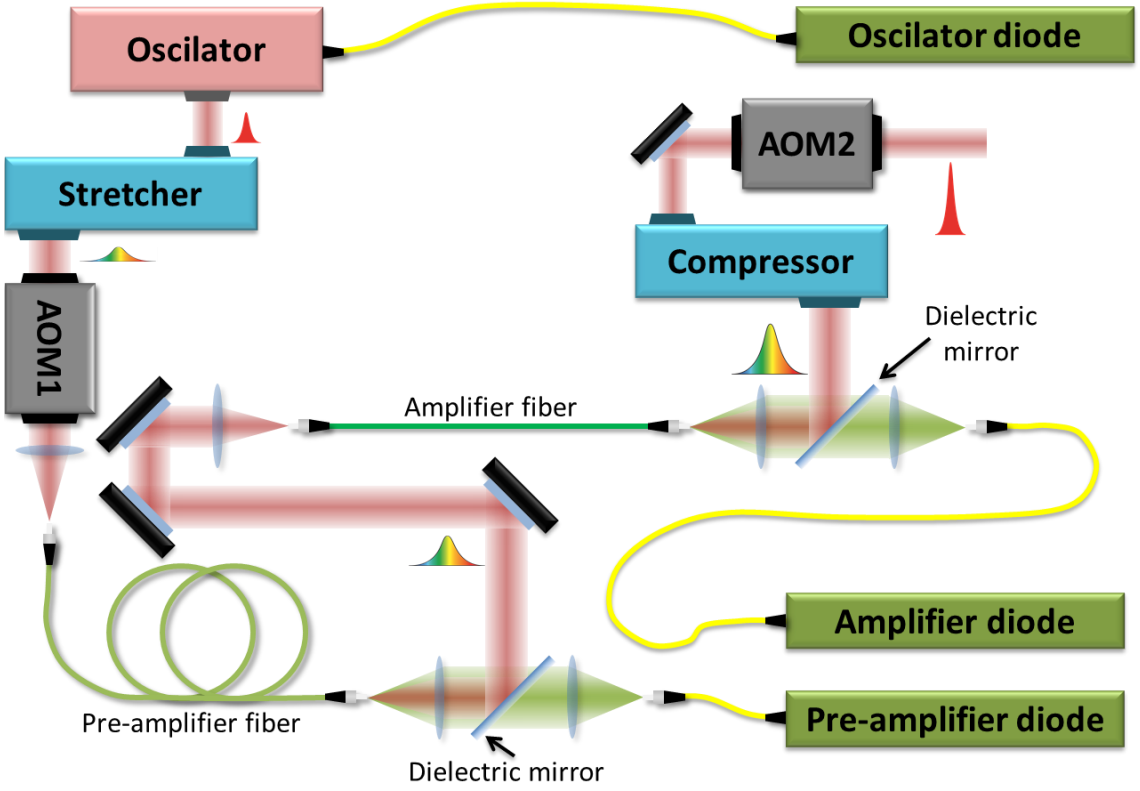

Figure 3.2: *Schematic representation of the HRR laser. The seed generated by the oscillator is temporally stretched. An acousto-optic modulator (AOM1) reduces the frequency of the pulse train to 2 MHz before inserting the beam in the pre-amplifier, based on an Yb-doped fiber. The energy of the pulses is furtherly increased in an Yb-doped photonic crystal fiber. The final repetition rate is controlled by AOM2.*

acousto-optic modulator (AOM1) to 2 *MHz*. The beam is then introduced in a two-step fiber-based amplifier. The pre-amplifier uses a 3 *m* length Yb^{3+}-doped fiber, whose output is used as the seed of the second stage amplifier, composed by a 1.5 *m* length photonic crystal fiber, also doped with Yb^{3+} ions. This fiber is designed to propagate large area modes to avoid damage during amplification. Both fibers are pumped by diodes emitting at 976 *nm* in a counter-propagating configuration.

After amplification, the pulse is recompressed, and its final repetition rate is selected by a second AOM (AOM2), which can reduce it from 2 MHz down to 1 kHz. The output pulses have 10 *μJ* energy and ~350-400 *fs* pulse duration. This longer pulse duration compared to the seed generated by the oscillator is produced by self-phase modulation and group-velocity dispersion effects during the propagation of the beam through the optical components (such as the amplifier fibers) which cannot be totally compensated by the compressor diffraction gratings.

3.1.2. Waveguide writing setups

The basic scheme of the waveguide writing setup is shown in **Figure 3.3**. It consists on a fs-laser source, and a group of different optical elements used to spatially shape the laser beam and control its properties (like polarization or energy). Then, the laser beam is focused in the sample to achieve the high intensities required to produce multiphoton absorption. Finally, the sample is placed over a motorized stage to control the relative displacement between the beam focus and the sample for producing the waveguides. In both cases, the pulse duration is measured by an autocorrelator (SSA, Positive Light, for the surface waveguide writing setup; and Mini, APE Berlin, for the sub-surface waveguide writing setup).

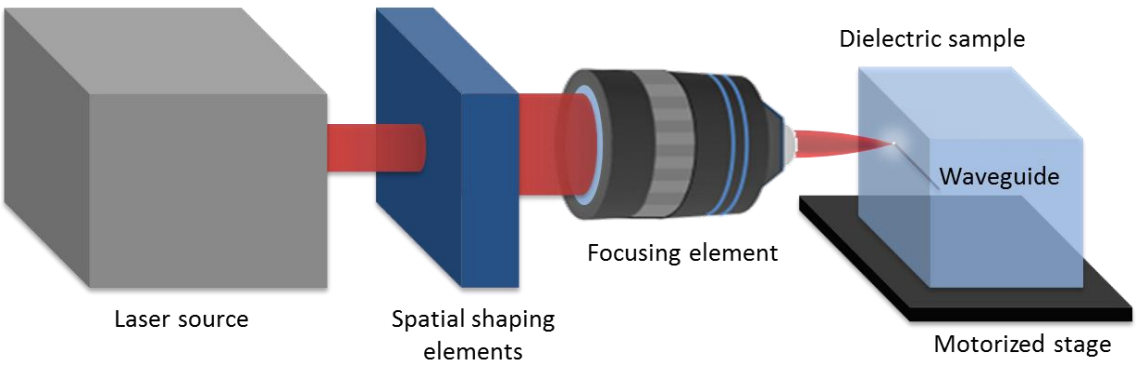

Figure 3.3: *Basic scheme of the waveguide writing setups. The laser is spatially shaped using different optical elements (represented in the figure as a beam expander). Then, the beam is focused by an element (typically a microscope objective or an aspheric lens) at the surface or inside the dielectric sample, which is moved by a motorized stage to produce the desired structures (a sub-surface waveguide in the figure).*

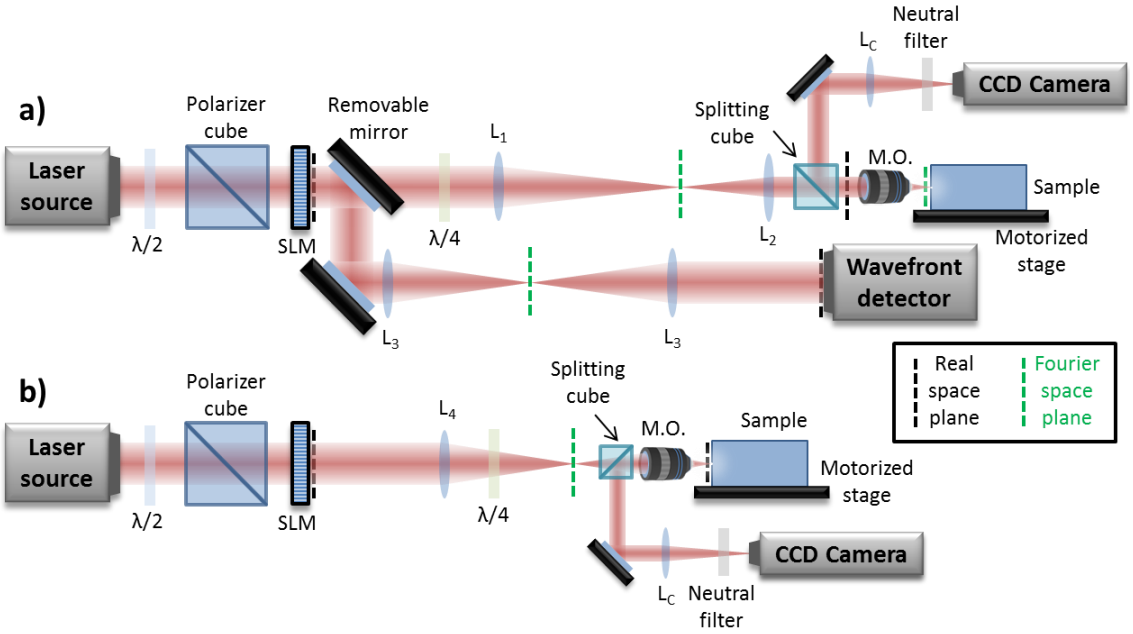

Figure 3.4: *Schematic representation of the different surface waveguide writing configurations: (a) Fourier plane irradiation setup, where a removable mirror allows choosing between irradiation and wavefront measurement paths. (b) Real plane irradiation setup. Real and Fourier planes are marked by black and green dashed lines respectively. A splitting cube or glass plate allows imaging the surface of the sample and the back-reflection of the beam.*

3.1.2.1. Surface waveguide writing setups

The surface waveguide writing setups used in this work exploit the capabilities associated to beam wavefront shaping. Two different experimental setups were used for such a purpose, one at the GPL-CSIC and the other at OD-Femto-ST.

The two possible configurations of the setup are shown in **Figure 3.4**. The pulse energy of the LRR laser beam is controlled by the combination of a retarding half-wave plate (λ/2 plate) and a double pass thin-film Brewster polarizer, or a Pockels cell and a polarizer cube (in the figure this is represented by a λ/2 plate and a polarizer cube for simplicity).

The wavefront is shaped using a spatial light modulator (SLM). Two different models were used, Hamamatsu X8267 (SLM1) and Hamamatsu X10468 (SLM2). Their characteristics are listed in **Table 3.2**. They work in reflection, although in **Figure 3.4** they are represented as working in transmission again for simplicity. The phase jump introduced in each pixel is linear

Table 3.2: *Characteristics of the SLMs.*

	SLM1	SLM2
Type of addresing	Optical	Electrical
Size (mm)	20x20	16x12
Size (pixels)	768x768	800x600
Modulation levels	256 (8 bits)	256 (8 bits)
Max. phase modulation	2.4π	>2.3π
Setup	OD-Femto-ST	GPL-CSIC

respect to the applied voltage only up to the ~230 level (or a phase jump of 2π). Usually, the used phase maps have phase values higher than 2π. For this reason, phase wrapping was used, substracting multiples of 2π so the final phase map uses values between 0 and 2π. However, using phase wrapped maps in SLMs may have an undesired effect: the phase mask partially behaves as a diffraction grating [3]. This effect is furtherly increased by the square pixelated structure of the SLM [4]. Also, the imperfect antirreflection coatings and the inert areas of the SLM reflect the unmodulated beam [4]. This produces a superposition between the zeroth-order of the modulated beam and the reflected unmodulated beam. In practice, this problem is severe in the case of SLM1 and barely noticeable with SLM2. Anyway, it is solved by different means, depending on the utilized phase map, and will be described in **Section 3.3.2**.

The electric field distributions at the two focal planes of a lens are related by a Fourier transform [5]. The writing beam path may include one or two lenses and a microscope objective (MO), depending if the sample is going to be irradiated by a Fourier-transformed beam (**Figure 3.4a**) or a non-transformed beam (**Figure 3.4b**). These situations will be referred to as irradiating in the Fourier space or in the real space respectively. In the setup for irradiating in the Fourier space, the lenses have a focal length of 50 (L_1) and 20 (L_2) *cm* and are placed in an image relaying configuration [6] (the front focal plane of L_1 is placed in the back focal plane of L_2). They image the plane of the SLM in the back focal plane of the microscope objective with a magnification of 2/5. The demagnification is introduced to accommodate the size of the beam to the size of the entrance pupil of the MO. For irradiating in the real space, only one lens (L_4) of 1 *m* focal length is used, in an image relaying configuration with the MO.

In both cases, a retarding quarter waveplate (λ/4 plate) is placed before the MO to produce circular polarization. Circular polarization reduces the nonlinear refractive index (as shown in **Section 2.1.2.1**), and also reduces the production of LIPSS (laser induced periodic surface structures) in the ablation craters [7], which would increase the roughness of the produced channels.

A splitting element (like a splitting cube or a partially reflecting mirror) is introduced before the MO. It allows imaging the part of the beam that is reflected by the sample in a CCD

Table 3.3: *Description of the characteristics of the CCD cameras used in the experimental setups.*

Name	Company	Model	Detector	Resolution (pix)	Size (mm)	Wavelength range (nm)	Levels (bits)
Cam1	AmScope	MU1003	Silicon	3584x2748	6.1x5.6	380 – 650	8
Cam2	PCO Imaging	Pixelfly	Silicon	1360x1024	6.3x4.8	300 – 700	12
Cam3	Goodrich	SU320-1.7	InGaAs	320x256	8.0x6.4	900 – 1700	12

Table 3.4: *Specifications of the microscope objectives (MO) and aspheric lenses (AL) used in the different experimental setups.*

Name	Company	Magnifi-cation	NA	Focal length (*mm*)	Wavelength range
MO1	Mitutoyo	20X	0.40	10.0	Near IR
MO2	Olympus	20X	0.40	9.0	Near IR
MO3	Mitutoyo	50X	0.42	4.0	Visible
MO4	Mitutoyo	50X	0.42	4.0	Near IR
MO5	Olympus	10X	0.25	16.5	Near IR
MO6	Comar	60X	0.85	2.91	Near IR
AL1	Newport	-	0.40	6.24	Near IR
AL2	Newport	-	0.68	3.10	Near IR

camera (Cam1 in **Table 3.3**) by an additional lens (L_C) in a microscope configuration. Different neutral filters can be inserted to avoid saturation of the camera. When the SLM is inactive, the sample is placed exactly at the focal plane of the MO when the reflected beam has highest peak intensity and minimum radius (this alignment operation is performed at minimum energy to avoid modifying the surface of the sample). Finally, a MO optimized for near-infrared wavelengths (MO1 at GPL and MO2 at OD-Femto-ST**)** is placed at the end of the beam path to focus the beam on the surface of the dielectric sample. The specifications of the different MOs are listed in **Table 3.4.**

The sample is placed on a three-axis motorized stage (XPS VP-25XA, Newport), calibrated for linear speeds between 50 and 500 $\mu m/s$ with a minimum step of 100 nm and a position reproducibility of 200 nm. The sample holder is attached to a θ–ϕ platform which allows controlling the angle of incidence of the beam on the sample. Perpendicularity of the sample is assured by checking that the beam remains focused at the surface of the sample when the sample is moved perpendicularly to the irradiation beam.

After the SLM, a removable mirror can be inserted to measure the beam wavefront. This second path consists on a Shack-Hartman wavefront detector (Haso76, Imagine Optic) and two lenses of 20 *cm* focal length in a 4F configuration (same as for image relying but with lenses of the same focal length). This way the system images the plane of the SLM in the detector. This is used to measure the wavefront of the beam when the SLM is inactive. By using an iterative algorithm, it is possible to calculate the phase mask necessary for compensating the beam wavefront aberrations (an RMS wavefront flatness below 0.05 μm can be achieved).

3.1.2.2. Sub-surface waveguide writing setup

The sub-surface waveguide processing setup at the GPL-CSIC is shown in **Figure 3.5a**. The laser source used in this case is LS3 (**Table 3.1**). The power control is performed by a λ/2

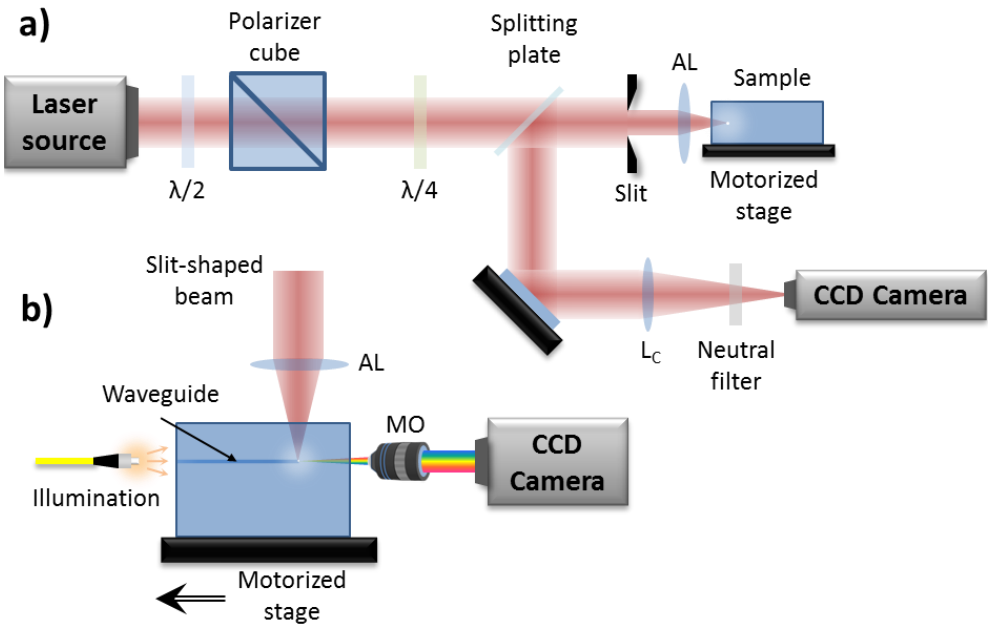

Figure 3.5: *(a) Scheme of the sub-surface waveguide writing setup. The beam is slit-shaped before being focused by an aspheric lens (AL) or a MO underneath the surface of the sample. (b) Scheme of the additional elements introduced for plasma imaging. A second MO and a CCD camera are used to image the visible light emission of the plasma generated during the irradiation. An auxiliary light source is also used to image the end surface of the waveguide in order to correlate the position of the plasma with respect to the generated structure.*

plate and a double thin film polarizer (represented by a polarizer cube in the figure for simplification). A λ/4 plate enables working with circular polarization. Circular polarization again reduces the nonlinear refractive index experienced by the beam, but more importantly, prevents the formation of nanogratings in the irradiated material, which would drastically increase the losses of the produced waveguides [8].

The beam is spatially shaped in amplitude with a slit, producing a quasi-elliptic Gaussian beam. It is then focused by an aspheric lens (AL1 and AL2, see **Table 3.4**) underneath the sample surface. A removable thin beam splitter plate can be used to image the reflection of the beam at the surface of the sample in a CCD camera (similarly than in the previous setup). This operation must be performed without the slit and with very low energy to avoid modifying the sample. The sample is placed on a three-axis motorized stage (ANT95-50 and ABL10050, Aerotech), with a resolution in position of 10 nm, and velocities between 1 $\mu m/s$ and 10 m/s in the waveguide fabrication direction. The sample holder is attached to a θ–ϕ platform that controls the angle between the sample and the irradiation beam. Perpendicularity of the beam to the sample surface is ensured in a similar way than in the previous setup.

It is worth noting that one of the differences between this setup and the surface writing one is the type of spatial shaping introduced in the beam. While in the previous one the shaped magnitude is the beam wavefront (phase), in this case the shaped magnitude is the beam amplitude.

This setup can be adapted to perform *in-situ* plasma emission imaging and microscopy experiments, as shown in **Figure 3.5b**. For this purpose, a long working distance MO (MO3, see **Table 3.4**) and a CCD camera (Cam2 in **Table 3.3**) are used. This way, the visible light emitted by the plasma during the production of the waveguide can be recorded. The depth of focus of MO3 is $\sim 4\ \mu m$, so the time the plasma remains focused in the camera is very low for speeds higher than a few $\mu m/s$. In that case, a video is recorded and the photogram with highest signal is selected, as it corresponds to the plane where the emission is focused in the camera. By adding a light source at the opposite side of the sample, the end surface of the waveguide can be recorded in the same way than the plasma emission, enabling the comparison of the plasma emission images with the produced structure.

3.1.3. Sample post-processing

After fabrication, the waveguides showed in most cases irregularities at both end facets. The samples were thus polished using increasingly smaller abrasive grain size disks, down to 0.5 μm. The same procedure was used if the waveguide length had to be reduced by a small amount. For larger shortenings, the sample was cut and then polished. After the polishing step, samples were carefully cleaned with ethanol or acetone with ultrasonics.

3.2. Waveguide characterization

In this section the experimental setups employed in the passive and active characterization of the produced waveguides are described.

3.2.1. Guided modes characterization setup

The setup for near-field mode characterization is shown in **Figure 3.6**. In this case, only the passive behavior of the waveguide is relevant. Different laser sources are used: two laser diodes operating at $\sim 976\ nm$ (see **Table 3.5**) and a tunable laser source between 1420 and 1640 *nm* (LS4). An optical isolator in the 976 nm arm is placed to avoid back reflections that could affect the pump laser performance. A wavelength-division multiplexer (WDM) is used for multiplexing both laser sources. A coupling fiber is connected to the common arm. Three

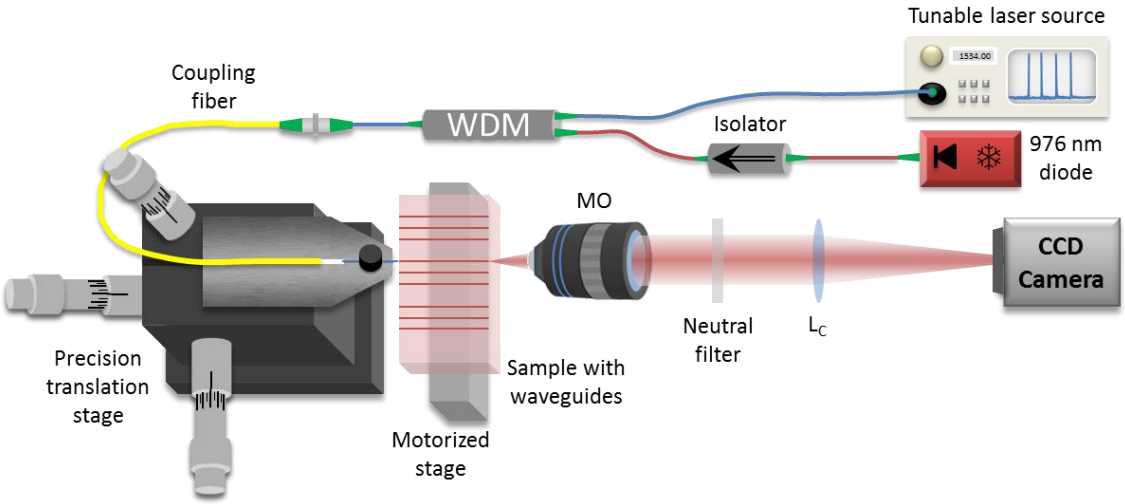

Figure 3.6: *Scheme of the mode characterization setup. Two different light sources are used, a laser diode emitting at ~980 nm and a tunable laser source (1420 – 1640 nm). A WDM multiplexes them in a single fiber, which is used to couple the light into the waveguide. A 50X MO and a tube lens of 1 m focal length images the near-field mode into a CCD camera.*

different coupling fiber models were used, Hi1060, SM980 and SMF-28. Their mode field diameter at different wavelengths is shown in **Table 3.6**

The coupling fiber end is stripped, cleaved and mounted on a three-axis translation stage with submicron resolution. The sample is mounted on a θ–ϕ platform for controlling the perpendicularity between sample and fiber, which in turn is placed over a two-axis motorized stage that enables placing the desired waveguide in front of the fiber. An imaging system connected to a CCD camera (Cam1 in **Table 3.3**) is used to image the sample and the fiber from the top, to help adjusting the sample perpendicularity respect to the fiber, and to monitor the fiber-waveguide distance. This top-view imaging system will be used in all fiber characterization setups.

A 50X MO (MO4 in **Table 3.4**) is mounted in front of the output of the waveguide, with its focal plane located at its end facet. A tube lens of 1 m focal length (L_C in the figure) focuses the near-field mode in a camera (Cam3 in **Table 3.3**). Neutral filters can be inserted before the camera to avoid saturation. This system has a magnification of ~250, the exact value

Table 3.5: *Specifications of the laser diodes and additional laser sources used in the characterization setups.*

Name	Company	Model	λ (*nm*)	Δλ (*nm*)	Max. power (mW)
D1	JDSU	S30-7602-406	974.0	0.20	~300
D2	JDSU	S30-7402-406	976.5	0.15	~300
D3	Furukawa	FOL1402PJX	1480	1.0	~120
LS4	Yokogawa	AQ2201	1420 - 1640	Narrow-band	~15
LS5	Spectra Physics	3900	700 - 1000	Narrow-band	~300

Table 3.6: *Supplier specifications and experimentally measured mode diameters of the used fibers. Measurements of the fiber modes have been performed at 976 nm and 1534 nm instead of 980 nm and 1550 nm.*

Name	980 *nm*		1550 *nm*		1640 *nm*	
	Specified	**Measured**	**Specified**	**Measured**	**Specified**	**Measured**
Hi1060	5.9	5.8	-	8.3	-	8.9
SM980	5.8	6.0	10.4	8.8	-	10.9
SMF-28	Multimode	8.0	10.4	11.0	-	14.3

depending on the laser source wavelength.

Fine alignment during fiber-waveguide coupling is achieved by maximizing the signal of the mode in the camera. This ensures that the recorded image corresponds to the coupling position that produces lowest loss. By removing the sample and placing the end tip of the fiber in the focal plane of the MO it is possible to record the mode of the fiber. This allows calculating the overlapping losses, as shown in **Section 2.6.3**. Experimentally, the overlapping factor is calculated as:

$$\eta = \frac{\sum_{i,j} \sqrt{I_f(i,j)} \sqrt{I_w(i,j)}}{\left(\sum_{i,j} I_f(i,j) \; \sum_{i,j} I_w(i,j)\right)^{1/2}} \qquad \textbf{3.1}$$

I_f and I_w being the fiber and waveguide modes discrete intensity distribution and i and j the indices of the pixels. The losses of the waveguide can be determined by measuring the power at the output of the waveguide (P_λ^{wg}) and the inserted power (P_λ^{in}) for a given wavelength λ, which is measured by removing the sample, similarly as for the fiber mode determination. The total losses are calculated as:

$$L_\lambda^{tot} = -10 \log_{ref} \frac{P_\lambda^{wg}}{P_\lambda^{in}} \qquad \textbf{3.2}$$

They can be decomposed as:

$$L_\lambda^{tot} = L_\lambda^{over} + 2L^{ref} + L_\lambda^{prop} + a_\lambda \qquad \textbf{3.3}$$

L_λ^{over} being the overlapping losses, L^{ref} the reflection (Fresnel) losses, L_λ^{prop} the propagation losses and a_λ the absorption measured in dB. Reflection losses are calculated from the refractive index of the waveguide (n_w) and the surrounding medium (n_m):

$$L^{ref} = -10 \log \left[1 - \left(\frac{n_w - n_m}{n_w + n_m}\right)^2\right] \qquad \textbf{3.4}$$

Propagation losses can be calculated from **Equation 3.3** for wavelengths with negligible absorption in the waveguide material ($a_\lambda = 0$), like 1640 nm in Er^{3+} doped samples.

The mode size diameter at $1/e^2$ is determined from the Gaussian fit of the image recorded by the camera. The spatial calibration of the image can be made with two different methods. The first one consists on recording an image of a dust particle present on the sample surface. A second image is recorded after moving the sample a known distance with the motorized stage. The calibration is performed by comparing the position of the particle in both images. The second method consists on comparing the size of the fiber mode to the value specified by the manufacturer (which has an error of ± 0.5 μm). Both methods provide a similar error in the waveguide mode size estimation.

3.2.2. Optical amplification characterization setup in fiber

In this experiment, the performance of the waveguide as an optical amplifier is assessed. Two different setups were used, one at GPL-CSIC and the other at APD-Unizar. They have the same scheme shown in **Figure 3.7**. The signal to be amplified is generated by LS4 (see **Table 3.5**), operating at 1534 *nm*. Its power is decreased by a variable attenuator down to ~100 μW in order to operate the amplifier in the small signal regime (as described in **Section 2.6.4**). The signal is fiber-coupled in the waveguide as described in the previous setup, and fiber-decoupled to be measured with an Optical Spectrum Analyzer (OSA, AQ6370Z,

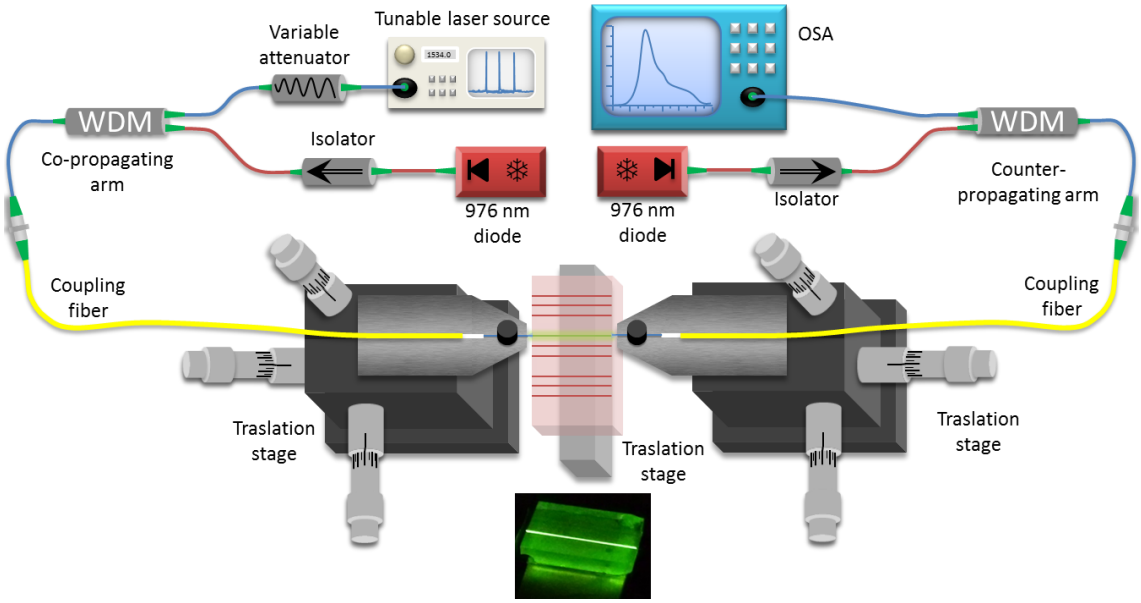

Figure 3.7: *Scheme of the optical amplifier characterization setup. The waveguide is pumped at 976 nm from both ends. The signal generated by the tunable source is attenuated and inserted in the waveguide from the co-propagating arm by the coupling fiber. The amplified signal is decoupled and inserted into the OSA for measurement from the counter-propagating arm. A photograph of a fully pumped waveguide is included, showing the green upconversion emission.*

Yokogawa). An index-matching gel may be inserted between the coupling fibers and the waveguide facets in order to minimize reflection losses. The pump is provided by D1 and D2, and multiplexed into the co and counter-propagating arms (respect to the signal) by means of two WDMs, as in the previous setup. The alignment process is monitored with the same imaging system described for the previous setup.

The inserted signal power (P_λ^{in}) is measured by removing the sample and coupling the two fibers. Net gain, internal gain and enhancement are calculated as described in **Section 2.6.4**. In this case, the total losses can be decomposed as:

$$L_\lambda^{tot} = 2L_\lambda^{over} + +2L^{ref} + L_\lambda^{prop} + L_\lambda^{disp} + a_\lambda \qquad \textbf{3.5}$$

L_λ^{over} being the overlapping losses, L^{ref} the reflection losses, L_λ^{prop} the propagation losses, a_λ the absorption and L_λ^{disp} being the displacement losses, as next explained. After measuring the maximum net gain, the total losses at 1640 nm (L_{1640}^{tot}) are measured without varying the coupling conditions. However, it may happen that the coupling position that produces maximum net gain does not produce the minimum losses at 1640 nm. This is due to the fact that the coupling conditions for minimum losses at 976, 1534 and 1640 nm can slightly vary. Therefore, the coupling conditions are adjusted for minimizing losses at 1640 nm. The difference between this value and L_{1640}^{tot} is L_{1640}^{disp}. Then, propagation losses at 1640 nm can be calculated (as a_{1640} = 0). Finally, extrapolating the propagation losses to 1534 nm (proportional to λ^4 [9]), the absorption at this wavelength can be determined. Pump propagation losses are also calculated by extrapolating the propagation losses at 1640 nm.

It is worth noting that during the optical amplification experiments, amplified spontaneous emission (ASE) and upconversion signals are generated. Erbium ASE has a broad spectrum, with small spectral density. If the OSA wavelength resolution is set to minimum (0.05 nm), the measured ASE power is negligible respect to the inserted signal power. On the other hand, upconversion light is emitted mainly at visible wavelengths, outside the OSA detection range.

3.2.3. Laser characterization setup in fiber

A scheme of the waveguide lasers characterization setup in fiber is shown in **Figure 3.8**. Again, two similar setups were used, one at GPL-CSIC and a second one at APD-Unizar. This setup is similar to the optical amplifier characterization setup. The laser is implemented as a linear cavity. Two fiber Bragg gratings are used as mirrors: one of them with 99.9%

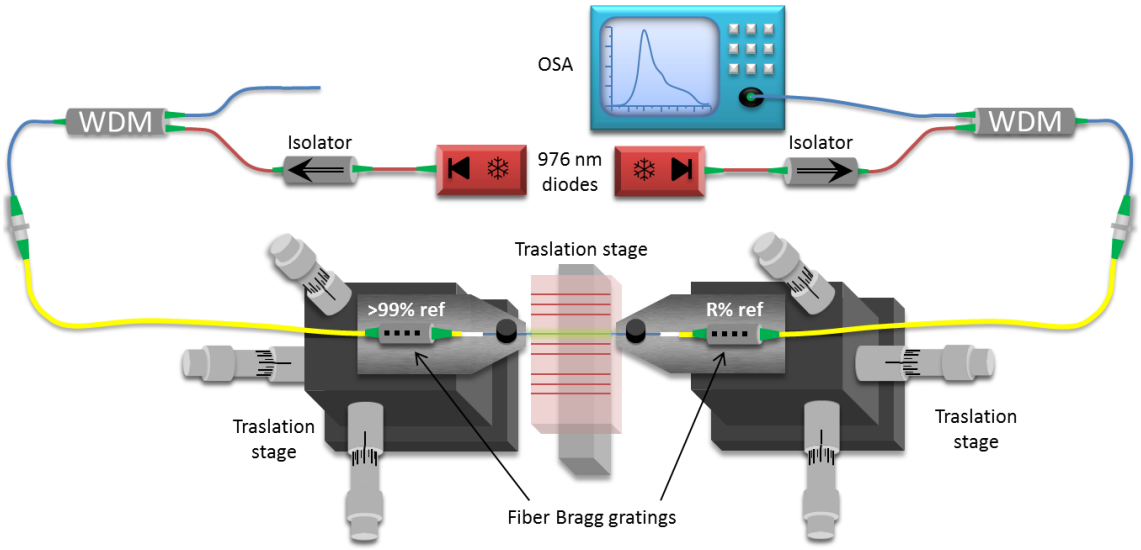

Figure 3.8: *Scheme of the waveguide lasers characterization setup in fiber. The waveguide is pumped at 976 nm from both ends. A 100%-R% of the generated laser power is extracted from the cavity by using different fiber Bragg gratings.*

reflectivity at 1534 nm and a second one with a lower reflectivity acting as an output coupler (**Table 3.7** shows the characteristics of the fiber Bragg gratings used). The emitted laser power is measured by the OSA. Wavelength resolution is set to 1 nm in order to measure the total power, or to 0.05 nm for measuring the laser spectrum. The losses of the optical elements between the waveguide output and the OSA were measured (2.6 dB) in order to calculate the total power emitted by the cavity. Absorbed pump power was calculated using the model described in **Section 3.3.1**. Laser pump absorption may be calculated by two different methods. The first one consists on modeling the active performance of the waveguides, as described in **Section 3.3.1**. The second one is described in **Section 2.6.5**.

3.2.4.Aerial laser characterization setup

This setup is located at the MSD-UAM. It has several differences with respect to the previous characterization setups. The mean difference is that propagation is aerial and coupling and collection is performed with two MOs. Also, it allows characterizing guided modes, amplifier and laser properties altogether.

Table 3.7: *Specifications of the fiber Bragg gratings used in the laser cavities.*

Name	Company	λ (*nm*)	Δλ (*nm*)	Reflectivity (%)
T1	Custom-made*	1532.52	1.02	99.9
T2	O/E Land	1534.33	1.00	99.3
P1	Custom-made*	1532.65	0.25	94.9
P2	O/E Land	1534.30	0.96	69.0
P3	O/E Land	1534.32	0.21	67.7

**Fabricated by the Photonics Engenieering Group of Universidad de Cantabria.*

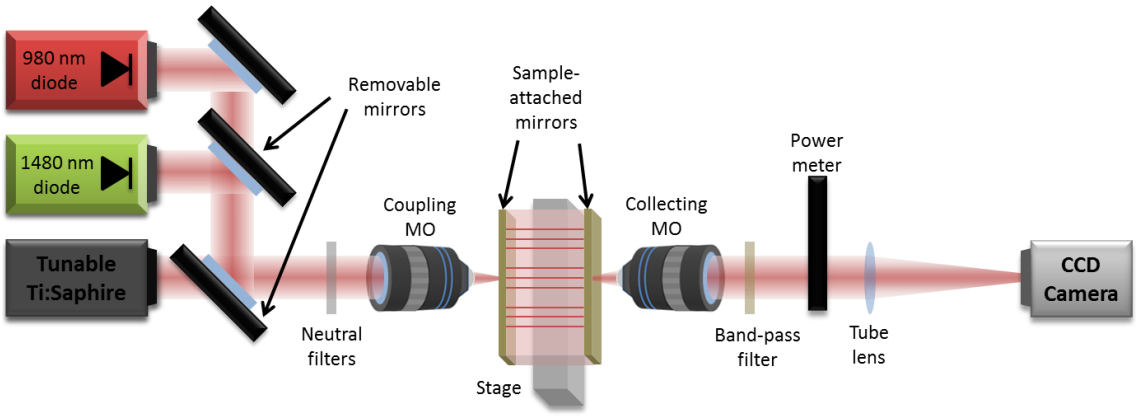

Figure 3.9: *Scheme of the aerial characterization setup. Different light sources can be coupled in the waveguide with an MO. The output of the waveguide is collected by a second MO, and measured by a power meter or a CCD camera.*

The light source (D1, D3 or LS5 in **Table 3.5**) is selected by inserting or removing different mirrors in the pump laser path. Laser power is adjusted with different filters. The light is coupled into the waveguide using MO5 (10X) and collected by MO2 (20X). Both MOs are placed on three-axis stages, allowing coupling optimization. Near field guided mode images are recorded using a tube lens and a CCD camera (Cam3 in **Table 3.3**). Output power is measured by using a multilayer band-pass filter and a power meter. This allows measuring losses, amplification or laser emission as described for previous setups.

The laser cavity can be built in two different configurations. The easiest one is using Fresnel reflections at the waveguide-air interfaces. However, the reflectivity is fixed by the material refractive index, typically ~10% for the crystalline materials used in this thesis, which may not suffice in many cases. The second one is attaching mirrors with adequate reflectivity at the ends facets of the waveguide.

3.2.5. Standard characterization techniques

Several standard techniques have been used to characterize the waveguides. One of them was white light optical microscopy, performed in an Eclipse Ti (Nikon) microscope. The microscope can be configured to acquire images in Köhler or differential interference contrast (DIC) illumination [10]. While the first is commonly used and produces high quality images, the second provides qualitative information about the local refractive index of sub-surface waveguides. The images were also used for determining the size of the guiding structures.

Optical microscopy was also employed for estimating the depth of the ablation channels of surface waveguides. The process is shown in **Figure 3.10a**. First, the surface of the sample is focused (**Figure 3.10b**). Then, the sample is moved so the deepest feature of the

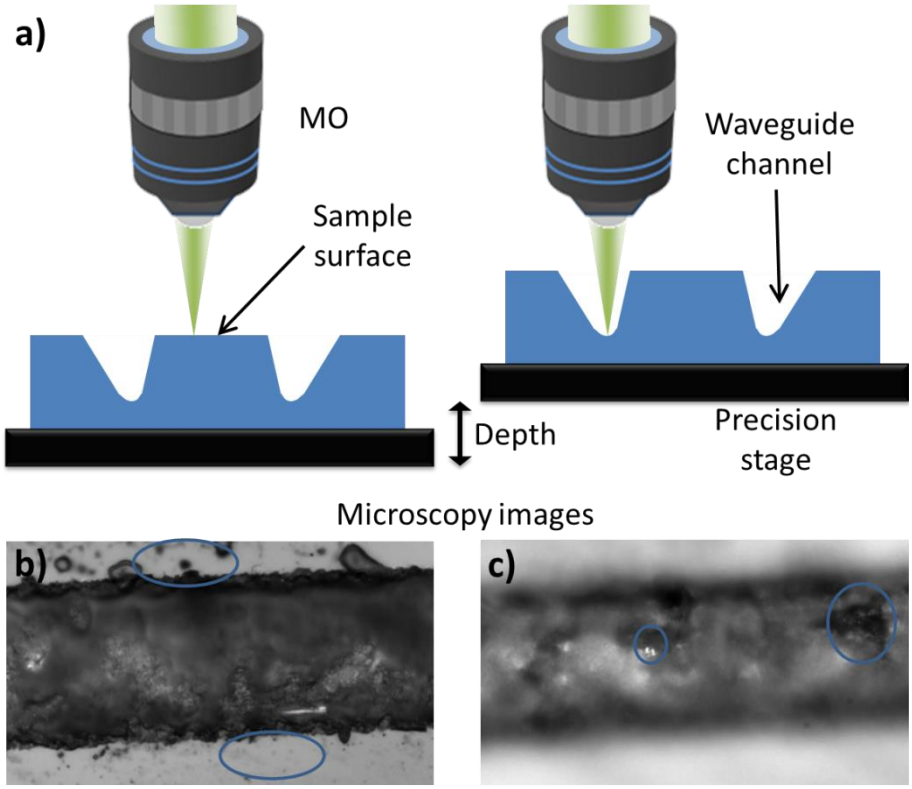

Figure 3.10: *Schematic representation of the determination of surface waveguide channels depth. First, the surface is imaged, and then the deepest feature is taken to the focus position. The difference between the sample positions along the vertical axis is the channel depth.*

channel is placed on focus (**Figure 3.10c**). This process is performed with the MO of highest magnification (100X) to reduce the focus depth as much as possible, and repeated several times to reduce observation errors. The achieved resolution is relatively poor ($\sim 0.5\ \mu m$), but this is a rapid procedure to make a reliable estimation. The channels depth was more precisely determined by atomic force microscopy (AFM), although each measure requires about 1 hour.

Scanning electron microscopy (SEM) was used for two different purposes. First, it was utilized for imaging the small features of the surface waveguides ablated channels. The second one was the determination of the local composition of laser irradiated regions in a SEM equipped with EDX (energy-dispersive X-ray spectroscopy [11]) at MD-UCM. The error in these measurements is determined by the type of element and its concentration. For instance, lanthanides show low X-ray emission cross-sections in EDX, and thus errors will be normally larger than for other elements. In order to reduce noise on *line* EDX compositional measurements, each point value was averaged with their 4 nearest neighbors.

The refractive index distribution of the sub-surface waveguides was measured using the near field refractive index profilometry technique [12]. These measurements were performed in a Rink Elektronik profilometer PD-IPN operating at 670 nm. In brief, a laser beam

is focused at normal incidence onto the sample, and parallel to the waveguides. Most of the rays walk out of the sample into a reference glass block which is in optical contact with the sample due to a layer of refractive index matching oil. The beams rays escaping the reference block are measured with a large area photodiode after passing an aperture stop that generates a linear dependence between the measured light power and the refractive index value at the focus of the beam [13].

3.3. Modelization and numerical calculations

3.3.1. Waveguide modeling

3.3.1.1. Surface waveguide modeling

For a correct design of the ridge and load waveguides, it is important calculating their expected guided modes distribution, propagation losses and lasing behavior. This was done in collaboration with Prof. Ginés Lifante at the MSD-UAM. The used code calculates the guided modes and their tunneling losses by the effective refractive index method with a multilayer approximation [14]. The passive and active behavior of the waveguides was calculated using a combination of the overlapping integral method and Beam Propagation Method (BPM) [15]. A more detailed description can be found in [16].

3.3.1.2. Sub-surface waveguide modelization

The modelization of the active performance of the sub-surface waveguides was performed in collaboration with Prof. Juan Vallés of APD-Unizar. The model [17] solves **Equations 2.43-2.45** for the Er-Yb system. This system includes the rate equations for the electronic populations of Yb^{3+} $^2F_{7/2}$ and $^2F_{5/2}$ levels, Er^{3+} $^4I_{15/2}$, $^4I_{13/2}$ and $^4I_{11/2}$ levels, along with the equations for pump, signal and ASE propagation along the waveguide. Several parameters, such as absorption and emission cross sections, are fit by comparing the simulation to experimental gain measurements. With these simulations, predictions of the optimal length for amplification or laser emission can be performed.

3.3.2. Phase mask calculations

In the production of surface waveguides, different phase masks were used to shape the wavefront of the beam with a SLM. They were obtained using different calculation methods.

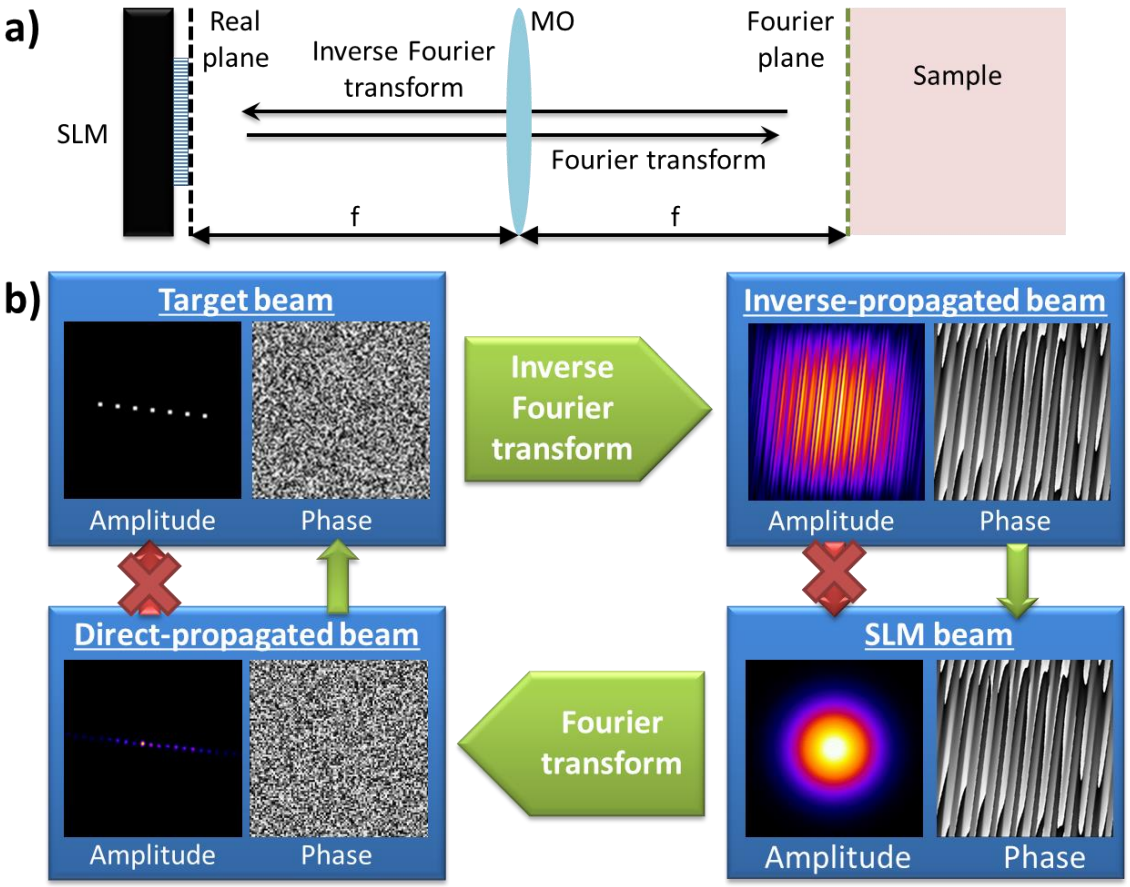

Figure 3.11: *(a) Scheme of the Gerchberg-Saxton algorithm. (b) Flow diagram of the program. Initially, the algorithm uses a predefined phase, which is combined with the target amplitude distribution. Then, the beam is back-propagated to the SLM-plane by an inverse FFT. The algorithm takes then the calculated phase and combines it with the known field distribution in the SLM plane. This field is propagated to the focal plane by a FFT. If the difference between the target and the calculated intensity is sufficiently low, the phase at the SLM plane is extracted as the algorithm result. If not, a new iteration is performed.*

3.3.2.1. Gerchberg-Saxton algorithm for multiplexed beams

Gerchberg-Saxton algorithm (GSA) [18] is an iterative algorithm used for calculating the phase of a pair of complex distributions related by a propagation function. In this case, it is used for calculating the wavefront required for producing a distribution consisting on several Gaussian spots with the same intensity in the focal plane of a lens (multiplexed beam). This is shown in **Figure 3.11a**. However, since only spatial phase variations (not amplitude) are introduced by the SLM, a perfect solution cannot be achieved.

The flow diagram of the GSA is shown in **Figure 3.11b**. The amplitude distribution of the field in the SLM plane (real plane) is taken as Gaussian, and the initial phase of the target beam (Fourier plane), as random. The size of the spots of the target distribution is of only few pixels, so the target distribution consists on top-hat profiles of two by two pixels. Anyway, the produced distribution will consist on several Gaussian profiles.

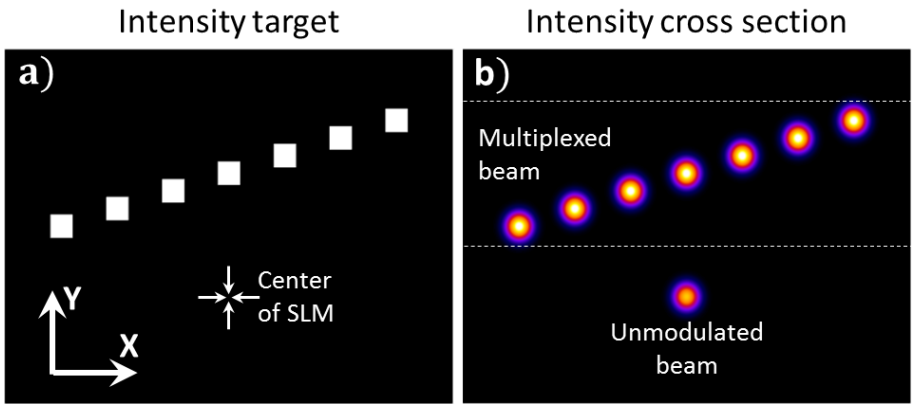

Figure 3.12: *(a) Target intensity distribution and (b) final intensity distribution of multiplexed beams when the distribution is displaced to avoid overlapping with the unmodulated beam.*

Each iteration of the algorithm starts combining the Fourier-plane phase mask calculated in the previous iteration (the initial random phase mask in the first iteration) with the target amplitude distribution. In the next step, the algorithm back-propagates the beam to the SLM plane using an inverse FFT. It extracts the phase of that field and stores it as a possible output. Then, it combines the stored phase with the known amplitude distribution of the field in the real plane and propagates it to the Fourier plane using a FFT. Finally, the algorithm computes the difference between calculated and target distribution. If the value is lower than a certain tolerance value, the stored phase distribution is output as the result. Otherwise, a new iteration begins.

GSA can be furtherly improved to increase the convergence speed and reduce the difference in intensity level between peaks by introducing a weighing function when calculating the complex distribution in the Fourier-plane at the start of each iteration:

$$A_{Fourier}(x,y) = W(x,y)\left|A_{target}(x,y)\right| \exp[i\,\varphi_{calc}(x,y)] \qquad \textbf{3.6}$$

It is called the weighed Gerchberg-Saxton algorithm (WGSA) [19]. The code of the implementation of WGSA is given in **Appendix A**.

During the course of this thesis, the difference between calculated and target amplitude distributions saturates after several tens of iterations, so a limit of 100 iterations was established. The code of the program utilized for these calculations is shown in **Appendix A**.

As mentioned in **Section 3.1.2.1**, the final intensity distribution may be affected by the reflection of the unmodulated beam. In order to prevent it from distorting the desired distribution, the target distribution was displaced respect to the center of the distribution, so

the residual unmodulated beam is focused below the multiplexed beams, as shown in **Figure 3.12**.

3.3.2.2. Gauss-Bessel beams

Gauss-Bessel beams can be generated from Gaussian beams using a SLM, as described in **Section 2.1.1.4**. The phase map is described by the equation:

$$\varphi_{Bessel} = k\, r \sin(\theta_{CA}) \qquad \textbf{3.7}$$

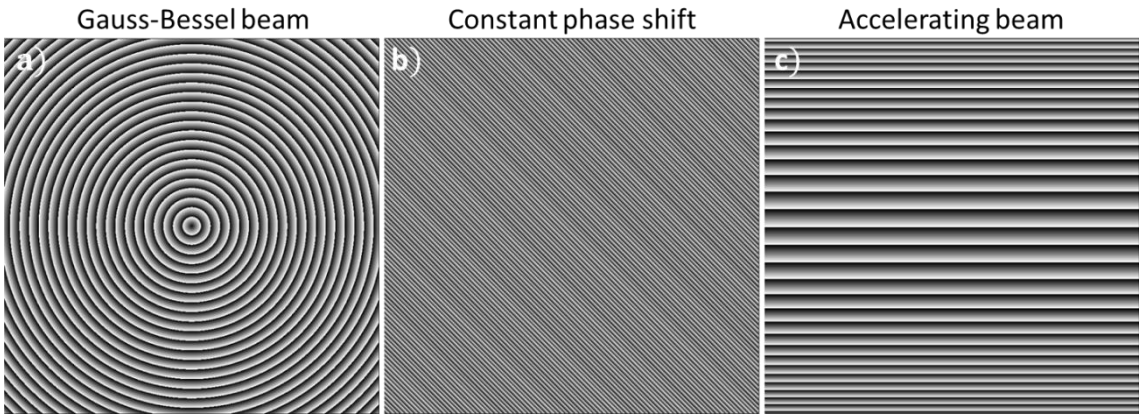

Figure 3.13: *Phase maps for a Gauss Bessel beam (θ_{CA} = 10°, a), a constant phase shift (θ_{1st} = 4.5 mrad, b), and an accelerating beam with circular trajectory ($\Re$ = 300 µm and d = 280 µm, c).*

r being the radial coordinate, k the wavenumber and θ_{CA} the conical angle. The phase map for θ_{CA} = 10° is shown in **Figure 3.13a**.

In the case of Gauss-Bessel beams, in order to avoid the distortion produced by the zeroth-order unmodulated beam (see **Section 3.1.2.1**) and spatially separate diffraction orders, a linear phase shift is added [3] (**Figure 3.13b**):

$$\varphi_{LS} = k(x + y) \sin(\theta_{1st}) \qquad \textbf{3.8}$$

θ_{1st} being the deviation angle of the first diffraction order. The rest of the diffraction orders are spatially filtered. **Figure 3.13b** shows the phase map for θ_{1st} = 4.5 $mrad$.

3.3.2.3. Accelerating beams

Accelerating beams are described in **Section 2.1.1.5**. In this thesis, the accelerating beams have been tailored to have a circular trajectory:

$$c(z) = -\sqrt{\Re^2 - z^2} + d \qquad \textbf{3.9}$$

$\Re$ being the curvature radius, and d chosen so the trajectory is placed near the optical axis, but without overlapping the unmodulated zeroth-order. The corresponding phase map is:

$$\varphi(y_F) = k\Re \operatorname{atan}\left(\frac{y_F\sqrt{f^2 - y_F^2}}{y_F^2 - f^2}\right) - \frac{kd}{f}y_F \qquad \textbf{3.10}$$

y_F being the Y coordinate in the focal plane of the microscope objective and f its focal length. The calculation of **Equation 3.10** from **Equations 2.22-2.23** and the caustic trajectory of **Equation 3.9** is shown in **Appendix B**. The phase map for $\Re$ = 300 μm and d = 280 μm is shown in **Figure 3.13c**.

3.3.3. Mean texture size determination

Ridge roughness is one of the most important parameters that determine propagation losses in ridge waveguides. Its determination for the lateral facets of the waveguides produced by fs-laser structuring during this thesis was challenging, since ablation channels are of few microns width and depth.

In this thesis the roughness of the walls of the ridge is described in terms of a mean texture size. The reasons for this choice are discussed in **Section 4.1.3.1**. The size of the grain features was determined from SEM images of the wall of the ridge (**Figure 3.14a**). Then, the size of the grains along the channel (as shown in **Figure 3.14b**) was measured with the help of a computer code. In order to help in the determination of the grain size, a program was implemented. It plots the calibrated SEM images of the ablation channels. The spatial calibration of the image is provided itself by the SEM measurement. Then, the user selects manually the X size of the features, and the program calculates the average of the feature size. The mean texture size is computed as the average of all the measured sizes, while the error is

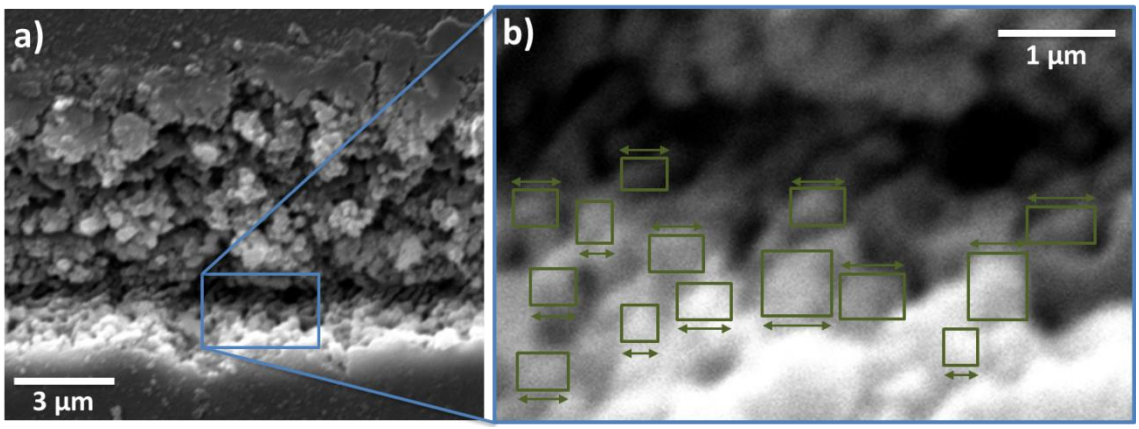

Figure 3.14: *(a) SEM image of one channel of a surface waveguide. (b) Magnification of the channel that corresponds to the facet of interest. Dark green rectangles correspond to the measured grains. The arrows indicate the estimated size of each grain.*

calculated as twice the standard deviation. The code used for these calculations is given in **Appendix A**.

It is worth noting that this method would produce more accurate results if the dimension of the features is determined by software instead of manually. However, the wall features are small, they present a relatively low contrast between center and edges, and the mean gray level decreases for higher depths. For these reasons, manual selection procedure was used.

3.4. Dielectric materials

This section is dedicated to de description of the experimental techniques used for producing the non-commercial (home-made) samples used in this thesis. The first subsection is dedicated to crystalline materials and the second to optical glasses. The third sub-section describes the main techniques used to characterize the materials before laser processing. The main characteristics of the samples are listed in the last sub-section.

3.4.1. Fabrication of crystalline samples

The growth of $KY(WO_4)_2$ (KYW) crystals was performed at FICMA-URV. The crystals were grown using the top seed solution growth (TSSG) technique at slow cooling rate [20, 21]. On top of them, an active layer of several microns (and an additional cladding layer in one sample) was grown by liquid phase epitaxy (LPE) [22, 23].

The growth of $LiNbO_3$ crystals was performed at the MSD-UAM. The crystals were grown using the Czochralsky technique [24]. A planar waveguide was fabricated on top of one of them by metallic indifussion of Zn^{2+} ions [25, 26]. The fabrication process of the particular crystalline samples used in this thesis is described in more detail in [16].

3.4.2. Fabrication of phosphate glass

The production of glass samples was performed using the standard melting and casting technique [27] in a Thermo-Star furnace at the Institute of Optics. The glass compositions were designed with two objectives: analyzing the role of La_2O_3, K_2O and Al_2O_3 in the waveguides produced by laser writing, and producing samples with variable contents of Er^{3+} and Yb^{3+}.

The initial mixture was composed of the following high purity (>99.99 %) products: H_3PO_4, $Al(PO_3)_3$, K_2CO_3, SiO_2, La_2O_3, CeO_2, Er_2O_3, and Yb_2O_3. All of them except phosphoric

acid were mixed in a ball mill before placing them in an alumina crucible. The phosphoric acid was incorporated at the end of the process because it is highly hydrophilic.

The mixture experiences the following chemical reactions:

$$2Al(PO_3)_3 \rightarrow Al_2O_3 + 3P_2O_5 \quad \textbf{3.11}$$

$$2H_3PO_4 \rightarrow P_2O_5 + 3H_2O \quad \textbf{3.12}$$

$$K_2CO_3 \rightarrow K_2O + C_2O \quad \textbf{3.13}$$

During melting, two undesirable effects appear. First, the mixture incorporates part of the alumina of the crucible. Second, part of the P_2O_5 evaporates. These effects were considered in the calculation of the initial products proportion in order to precompensate them.

The glass fabrication process was as follows. The mixture is rapidly heated up to 200 °C. From that temperature, the heating rate was reduced to 15 $^{o}C/min$. This is the temperature where most of the H_2O (produced in the reaction in **Equation 3.12** or incorporated from the atmosphere by H_3PO_4) evaporates from the mixture. For higher heating rates, the evaporated H_2O may expel part of the mixture from the crucible.

The mixture was then heated up to 1400 ^{o}C. It remained at that temperature for three hours. Then, it was extracted from the crucible and casted into water directly without previous cooling. The formed glassy material was removed from the water, dried and crushed in a mortar and in a ball mill to form fine powder. The process was repeated again, maintaining the mixture at 1400 ^{o}C for one hour, crushing and mixing the glass. The mixture was heated again to 1400 ^{o}C and maintained one hour at that temperature before casting it in a stainless steel mold, previously heated at 600 °C. The glass was then annealed for one hour at 600 °C (slightly below the glass transition temperature T_g) to remove stresses, and then cooled down to room temperature at 3 $^{o}C/min$.

Two parameters are very important in the fabrication of these glasses. The first one is homogeneity. The sample is crushed, mixed in the ball mill and melted three times in order to improve it. The second one is the presence of OH^- ions in the glass. This is a very undesired effect, as OH^- ions are one of the main sources of Er^{3+} 1534 nm luminescence quenching [28, 29]. The high temperature and the long time the glass remains molten helps to reduce the OH^- content of the final glass up to some extent.

The commercial phosphate glass sample used was a piece of QX100, fabricated by Kigre Inc. Due to the mass production process, the samples made of this glass present high homogeneity. Also, the control of the atmosphere during melting allows producing a glass with a very low OH^- content.

3.4.3. Raw material characterization

3.4.3.1. Composition

In order to determine the chemical composition of the phosphate glasses Particle Induced X-Ray Emission spectroscopy (PIXE) [30] was used. The experiment was performed at the CNA using 1 mA current protons accelerated to 2 MeV.

3.4.3.2. Absorption spectroscopy

Absorption spectroscopy has been used for the determination of Er^{3+} and Yb^{3+} absorption bands and effective ion concentration. Measurements were performed using a commercial spectrophotometer (Cary 5000, Varian).

The absorption was determined by comparing the intensity of a reference (I_0) and a probe (I) beam, detected after being transmitted through a sample of length l. The probe beam is affected by the reflection of the beam at the two air-sample interfaces and by the absorption of the sample. The transmission of the sample for each wavelength can be determined as:

$$T(\lambda) = \frac{I(\lambda)}{I_0(\lambda)} = (1-R)^2 e^{-\alpha(\lambda) l} \qquad \textbf{3.14}$$

where α and R are the absorption and reflection coefficients respectively.

3.4.3.3. Fourier transform infrared spectroscopy

Fourier transform infrared spectroscopy (FTIR) [31] is often used for characterizing the OH^- content of different materials. In our case, the phosphate glass samples have been characterized using a FTIR spectrometer (Bruker Vertex70). The OH^- absorption band is located around 3000 cm^{-1}. The absorption at the IR wavelengths can be directly correlated to OH^- concentration in the glass [31].

3.4.3.4. Er^{3+} emission lifetime in phosphate glass

The properties of the ytterbium-erbium system were described in **Section 2.5.2**. For active applications, the lifetime of the Er^{3+} $^4I_{11/2}$ level is an important parameter, as a higher

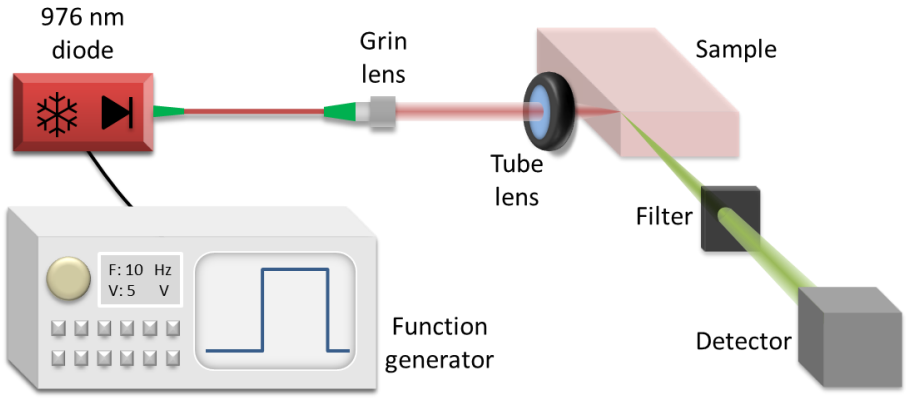

Figure 3.15: *Schematic representation of the experimental setup for luminescence measurements in Yb/Er-doped phosphate glasses.*

lifetime implies better optical amplification performance. **Figure 3.15** shows the scheme of the experimental setup at IO-CSIC used for the determination of lifetime in the phosphate glass samples.

A fiber-coupled 976 nm laser diode was used as the pump source for exciting the Er^{3+} ions. A function generator is connected to the gate control of the diode for turning on and off the pump source. The fiber output is collimated by a grin lens, and then focused by a lens inside the sample.

The Er^{3+}–doped glass emits light at 1534 nm in all directions. The detector is placed at 90° from the illumination arm in order to minimize scattered pump light effects. The focus is placed near the edge to produce the most intense possible signal. A low-pass filter is placed in front of the detector to further reduce scattered pump light. The detector consists on a monochromator (centered at 1534 nm) and a photomultiplier. When the pump laser is switched off, the population from the $^4I_{13/2}$ excited level decays exponentially. The recorded signal temporal dependence is fit to an exponential function in order to determine the lifetime.

3.4.4. Sample list

In this sub-section all the samples used in this thesis are listed. The tables include relevant information as composition or lifetime.

Table 3.8: *Samples utilized in surface processing.*

Name	Substrate	Active layer	Active ions	Layer thickness	Other
KYW1	$KY(WO_4)_2$	$KY0_{0.59}Gd_{0.185}Lu_{0.21}(WO_4)_2$	Yb_2O_3 (1.5 %mol.)	4 µm	
KYW2	$KY(WO_4)_2$	$KY_{59\%}Gd_{19\%}Lu_{21\%}(WO_4)_2$	Er_2O_3 (0.5 %mol.) Yb_2O_3 (0.5 %mol.)	4 µm	10 μm cladding * (same as substrate)
LiNb1	$LiNbO_3$	No	-	-	
LiNb2	$LiNbO_3$	$LiNbO_3$ + Zn ion diffusion	Nd_2O_3 (0.23 %mol.)	5 µm ($1/e^2$)	
Sil1	SiO_2	No	-	-	Suprasil, Schott

** Cladding: This sample presents a second layer on top of active layer acting as a cladding. It was grown by LPE, the same as the active layer, and has the same composition and crystal orientation than the bulk.*

The glass composition was determined by PIXE. Only CeO_2 concentration was below resolution.

Table 3.9: *Components of phosphate glasses measured by PIXE. Only* CeO_2 *concentration was below resolution. All concentrations are molar.*

Name	P_2O_5	Al_2O_3	La_2O_3	K_2O	SiO_2	CeO_2	Er_2O_3	Yb_2O_3
Self1	67.9	3.4	17.5	4.4	4.6	< res.	0.8	1.4
Self2	64.4	5.7	17.6	4.2	6.0	< res.	0.7	1.4
Self3	59.7	1.7	21.8	5.2	3.9	< res.	3.0	4.8
Self4	64.7	5.5	16.9	4.1	4.4	< res.	1.5	2.9
Com1	70.0	4.4	9.8	6.8	6.5	< res.	0.8	1.7
Error	±3.7	±0.5	±0.9	±0.2	±1.2	< res.	±0.1	±0.2

Table 3.10: *Measured properties of phosphate glass samples.*

Name	$[OH^-]$ (ppm)	Lifetime (ms)	α_{976} (cm^{-1})	α_{1534} (cm^{-1})	n_{1030}	n_{1640}	Commercial name
GPL1	79.6	6.0	3.87	1.03	1.553	1.547	
GPL2	84.1	5.2	3.78	0.98	1.556	1.553	
GPL3	95.9	2.9	7.16	1.91	1.556	1.552	
GPL4	81.9	4.1	5.76	1.58	1.553	1.549	
Com1	18.2	8.5	3.98	1.06	1.545	1.542	Kigre Inc. QX100

3.5. References

[1] D. Strickland and G. Mourou, "Compression of amplified chirped optical pulses," *Optics Communications,* vol. 56, pp. 219-221, 1985.

[2] T. Brabec, C. Spielmann, P. F. Curley, and F. Krausz, "Kerr lens mode locking," *Optics Letters,* vol. 17, pp. 1292-1294, 1992.

[3] L. Froehly, M. Jacquot, P. A. Lacourt, J. M. Dudley, and F. Courvoisier, "Spatiotemporal structure of femtosecond Bessel beams from spatial light modulators," *Journal of the Optical Society of America A,* vol. 31, pp. 790-793, 2014.

[4] V. Arrizón, E. Carreón, and M. Testorf, "Implementation of Fourier array illuminators using pixelated SLM: efficiency limitations," *Optics Communications,* vol. 160, pp. 207-213, 1999.

[5] J. Goodman, "Introduction to Fourier Optics," in *Electrical and Computer Engineering*, 2nd ed: McGraw-Hill, 1996.

[6] S. Amano and T. Mochizuki, "Image Relaying in a High-Average-Power Slab Laser System," *The Review of Laser Engineering,* vol. 29, pp. 679-682, 2001.

[7] D. Dufft, A. Rosenfeld, S. K. Das, R. Grunwald, and J. Bonse, "Femtosecond laser-induced periodic surface structures revisited: A comparative study on ZnO," *Journal of Applied Physics,* vol. 105, p. 034908, 2009.

[8] M. Beresna, M. Gecevičius, and P. G. Kazansky, "Polarization sensitive elements fabricated by femtosecond laser nanostructuring of glass [Invited]," *Optical Materials Express,* vol. 1, pp. 783-795, 2011.

[9] L. Tong, R. R. Gattass, I. Maxwell, J. B. Ashcom, and E. Mazur, "Optical loss measurements in femtosecond laser written waveguides in glass," *Optics Communications,* vol. 259, pp. 626-630, 2006.

[10] M. Davidson and M. Abramowitz, "Optical Microscopy," in *Encyclopedia of imaging science and technology*, 1st Ed. ed: John Wiley & Sons, 2002.

[11] D. Brandon and W. D. Kaplan, *Microstructural Characterization of Materials*, 2nd Ed. ed.: (John Wiley & Sons Ltd, 2008.

[12] R. Göring and M. Rothhardt, "Application of the Refracted Near-Field Technique to Multimode Planar and Channel Waveguides in Glass," in *Journal of Optical Communications* vol. 7, ed, 1986, p. 82.

[13] R. Elektronik. Available: http://www.rinck-elektronik.info/www/pages/speicheFrameset1.htm

[14] G. Lifante, *Integrated Photonics: Fundamentals*. Chichester, UK: John Wiley & Sons Ltd., 2003.

[15] M. D. Feit and J. A. Fleck, "Light propagation in graded-index optical fibers," *Applied Optics,* vol. 17, pp. 3990-3998, 1978.

[16] J. Martínez de Mendívil, "Láseres integrados en dobles tungstatos y niobato de litio basados en guías de onda ridge," Departamento de Física de Materiales, Universidad Autónoma de Madrid, 2015. PhD Thesis

[17] J. A. Valles, M. A. Rebolledo, and J. Cortes, "Full characterization of packaged Er-Yb-codoped phosphate glass waveguides," *IEEE Journal of Quantum Electronics,* vol. 42, pp. 152-159, 2006.

[18] T. Haist, M. Schönleber, and H. J. Tiziani, "Computer-generated holograms from 3D-objects written on twisted-nematic liquid crystal displays," *Optics Communications,* vol. 140, pp. 299-308, 1997.

[19] R. Di Leonardo, F. Ianni, and G. Ruocco, "Computer generation of optimal holograms for optical trap arrays," *Optics Express,* vol. 15, pp. 1913-1922, 2007.

[20] W. Bolaños Rodriguez, "Development and characterization of waveguide lasers on monoclinic potassium double tungstates," Departament de Química Física i Inorgànica, Universitat Rovira i Virgili, 2011.

[21] X. Mateos, R. Solé, J. Gavaldà, M. Aguiló, J. Massons, and F. Díaz, "Crystal growth, optical and spectroscopic characterisation of monoclinic KY(WO4)2 co-doped with Er3+ and Yb3+," *Optical Materials,* vol. 28, pp. 423-431, 2006.

[22] B. Ferrand, B. Chambaz, and M. Couchaud, "Liquid phase epitaxy: A versatile technique for the development of miniature optical components in single crystal dielectric media," *Optical Materials,* vol. 11, pp. 101-114, 1999.

[23] J. J. Carvajal, M. C. Pujol, and F. Diaz, "High-Temperature Solution Growth: Application to Laser and Nonlinear Optical Crystals," in *Springer Handbook of Crystal Growth*, G. Dhanaraj, K. Byrappa, V. Prasad, and M. Dudley, Eds., ed: Springer Berlin Heidelberg, 2010.

[24] A. A. Ballman, "Growth of Piezoelectric and Ferroelectric Materials by the Czochralski Technique," *Journal of the American Ceramic Society,* vol. 48, pp. 112-113, 1965.

[25] R. V. Schmidt and I. P. Kaminow, "Metal-diffused optical waveguides in LiNbO3," *Applied Physics Letters,* vol. 25, pp. 458-460, 1974.

[26] R. Nevado and G. Lifante, "Low-loss, damage-resistant optical waveguides in Zn-diffused LiNbO3 by a two-step procedure," *Applied Physics A,* vol. 72, pp. 725-728, 2001.

[27] J. M. Fernández-Navarro, *El vidrio: constitución, fabricación, propiedades*, 3rd ed. Madrid: CSIC, 2003.

[28] Y. Yan, A. J. Faber, and H. de Waal, "Luminescence quenching by OH groups in highly Er-doped phosphate glasses," *Journal of Non-Crystalline Solids,* vol. 181, pp. 283-290, 1995.

[29] S. N. Houde-Walter, P. M. Peters, J. F. Stebbins, and Q. Zeng, "Hydroxyl-contents and hydroxyl-related concentration quenching in erbium-doped aluminophosphate, aluminosilicate and fluorosilicate glasses," *Journal of Non-Crystalline Solids,* vol. 286, pp. 118-131, 2001.

[30] A. S. Johansson and T. B. Johansson, "Analytical application of particle induced x-ray emission," *Nuclear Instruments and Methods,* vol. 137, 1976.

[31] P. R. Griffiths and J. A. Haseth, *Fourier Transform Infrared Spectrometry*. New Jersey: John Wiley & Sons Inc., 2007.

Chapter 4
Surface waveguides writing

This chapter describes the production of channel waveguides by fs-laser surface structuring of crystalline materials. The design of the initial samples and the waveguides, as well as the structuring procedure are first described. The second part describes the effect of Gaussian, Gauss-Bessel and accelerating beams on the roughness of the walls of the waveguides. Finally, several examples of the production of low loss waveguides and high efficiency lasers are presented.

4.1. Waveguide production

4.1.1. Materials selection and waveguide design

Two different materials were selected for the production of waveguides by fs-laser surface structuring: monoclinic yttrium double tungstates ($KY(WO_4)_2$, KYW) and lithium niobate ($LiNbO_3$). The first was chosen due to the high absorption and emission cross-sections of Er^{3+} and Yb^{3+} ions when embedded in this matrix. Short-length, high-gain devices can be thus produced [1-3]. On the other hand, $LiNbO_3$ presents excellent nonlinear, electro-optic and acousto-optic properties, along with a relatively-high capability for being doped with luminescent ions [4-6]. This makes $LiNbO_3$ a very versatile material in photonics applications. Both crystals show a high refractive index, which potentially enables the production of devices with small curvature radius [7] and waveguides with small guided modes, which also enhances the efficiency of active devices [8].

The design of the waveguide parameters (geometry and refractive index) is crucial for achieving high performance. Optimization is performed by simulating the behavior of waveguides with different parameters in order to find the optimal ones before laser processing. This was done in collaboration with Prof. Ginés Lifante (MSD-UAM), using the models described in **Section 3.3.1.2**. There are two different configurations suitable for the production of channel waveguides by fs-laser surface structuring: ridge waveguides [9] (**Figure 4.1a**, **Figure 4.1c**) and load waveguides [10] (**Figure 4.1b**). These waveguides are produced from a sample where a planar waveguide is already present. The planar waveguide may be produced by different techniques, like liquid phase epitaxy (LPE) or ion diffusion, as described in **Section 3.4.1**. Three different crystalline samples were produced, one by Zn^{2+} ion diffusion

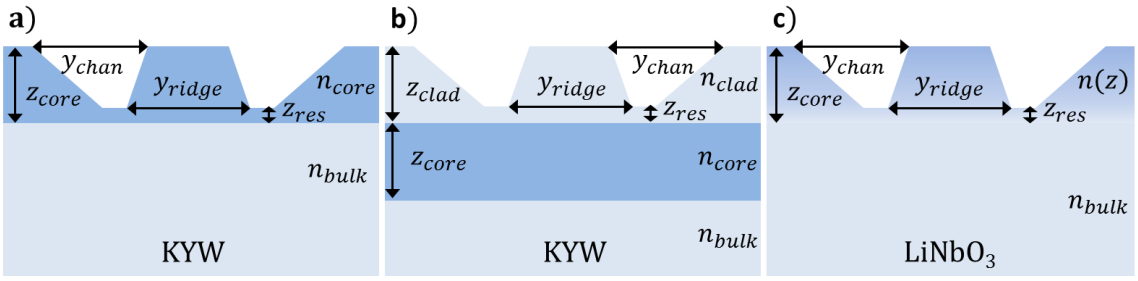

Figure 4.1: *Scheme of the design parameters of ridge (a, c) and load (b) channel waveguides. Figure partially adapted from [10]*

(LiNb2) and two by LPE (KYW1 and KYW2). Their main characteristics are listed in **Section 3.4.4**. The core layer may be additionally covered by a cladding layer (sample KYW2) for the production of load waveguides.

Table 4.1 shows the calculated optimal parameters for the planar waveguides. The core layer thickness and refractive index of the different layers is calculated in order to produce a planar single mode waveguide in the Z dimension for both pump and signal wavelengths. In the case of KYW, the composition of the core layer is selected in order to produce differences in the lattice parameter as close to zero as possible, leading to a Δn = 5×10^{-3} and z_{core} = 4.0 μm. For load waveguides, it was determined that the height of the cladding must be z_{clad} > 4.0 μm (10 μm was used). In the case of $LiNbO_3$, the determined parameters were $\Delta n_0 = 5\times10^{-3}$ and z_{core} = 5 μm.

The channel waveguide is produced by removing material on the top surface by ablation with fs-laser pulses. In the case of ridge waveguides, lateral confinement is produced by the contrast between refractive index of the core layer and the air that fills the ablated channels. For load waveguides, the refractive index contrast is produced by the distortion that the ablated channels produce in the effective refractive index profile [11] (**Figure 4.2a**).

The losses of the waveguide will depend on the parameters shown in **Figure 4.1**. For ridge waveguides, simulations show that propagation losses are negligible for a ridge width (y_{ridge}) above ~5 μm, a negative residual core (z_{res}), which implies ablating the underlying substrate layer), and a channel width (y_{chan}) above ~15 μm. However, as it will be shown in **Section 4.2,** the produced waveguides may show propagation losses well above the simulated values. This is due to the fact that simulations don't take into account propagation losses

Table 4.1: *Design parameters of the planar waveguides.*

Material	Planar waveguide Δn	Δn	z_{core} (µm)	z_{clad} (µm)
KYW	$\Delta n = n_{core} - n_{bulk}$	5×10^{-3}	4.0	> 4.0
Material	**Planar waveguide Δn**	**Δn_0**	**z_{core} (µm)**	
$LiNbO_3$	$\Delta n(z) = \Delta n_0 e^{-z/z_{core}}$	5×10^{-3}	5.0	

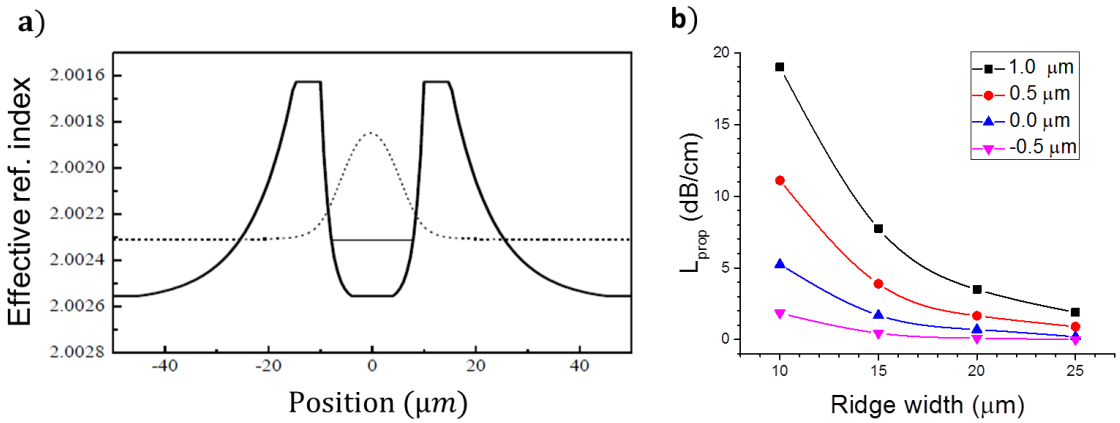

Figure 4.2: *(a) Effective refractive index distribution (continuous line) and fundamental mode intensity distribution (dashed line) of a load waveguide with y_{ridge} of 20 μm. (b) Calculated propagation losses at 1640 nm for load waveguides with different y_{ridge} and z_{clad} in KYW1 sample. Figure adapted from [10].*

caused by Rayleigh scattering at the ridge walls due to roughness. The scattered intensity is proportional to d^6 [12], d being an effective "particle" size associated to roughness. The roughness at the ablation channels is thus an important issue. It will be analyzed in **Section 4.1.3**.

For the case of load waveguides, the intensity of the mode at the structured region is negligible if $z_{res} > 0$, so the losses are directly determined by the effective refractive index profile [11]. **Figure 4.2b** shows the calculated losses at 1640 nm for waveguides of different ridge widths and residual cladding. The minimum losses are produced for negative z_{res} values, but then roughness losses start to arise. The optimal structuring parameter will thus correspond to a positive z_{res} value as close to zero as possible.

4.1.2. Channel waveguide fabrication

The production of the channel waveguides requires the ablation of two parallel channels of pre-designed depth and width, with minimal wall roughness in the case of ridge waveguides. The first step for the production of the waveguides is the determination of the best parameters for producing the ablation channels.

When the ultrashort-pulsed laser beam is focused on the surface of the material it may produce multiphoton ionization and ablation if the pulse energy is sufficiently high. If the sample is moved transverse to the propagation axis, ablation channels may be fabricated. However, the roughness of the produced structures will normally be high, thus producing high propagation losses. This is due to two different reasons. First, craters produced under the strong ablation regime are rough. In the gentle ablation regime are smoother, but with crater depths too low for producing channel waveguides. Also, during the production of the channels,

part of the ablated material redeposits around the ablated regions, generating additional roughness.

In order to produce smoother structures, the ablation channels are produced using the approximation scanning technique [13] (see **Figure 4.3**). The ablation channel is irradiated several times, slightly displacing the sample perpendicularly to the channel direction. Several parallel overlapping irradiation tracks are produced. The first track produces a rough channel, but the second one finds a different surface profile which favors the ejection of material towards the crater produced by the first ablation track. This reduces the amount of redeposited material in the region that is going to be irradiated, and also produces a deeper channel. This effect is increased with each subsequent irradiation, reducing the roughness of one of the walls of the ablation channel. The waveguide will be fabricated using the smoother wall of the channel for the ridge.

The approximation scanning technique has an additional advantage. The final width (and depth) of the channels depends on the number of irradiation tracks. While the channel width could be controlled by the focusing NA or the pulse energy, the number of irradiation tracks constitutes a much precise control method. Regarding the channel depth during the production of the waveguides, it has been determined that it is a parameter much more sensitive to pulse energy than to the number of irradiation tracks.

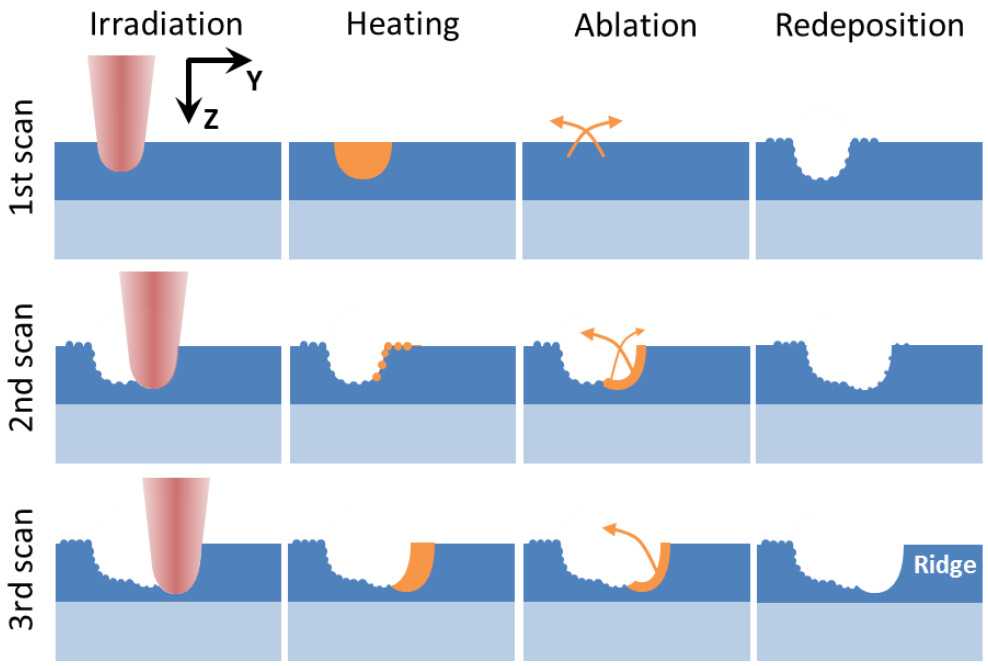

Figure 4.3: *Schematic representation of the scanning approximation technique. It consists on irradiating several times the sample, slightly displacing it respect to the focal position in each scan in order to produce smoother ablation channel walls.*

4.1.3. Analysis of the ridge roughness

Since the ridge roughness is crucial for the production of efficient channel waveguides, the possibility of reducing it by employing laser beams with different spatial profiles different than Gaussian ones has been analyzed. The ablation channels have been produced using the surface waveguide production setups at OD-Femto-ST described in **Section 3.1.2.1**.

Three different laser beam types have been analyzed. The first one is a multiplexed beam [14]. It consists on a set of multiplexed Gaussian beams produced by an SLM, as shown in **Figure 4.4**. The phase map imprinted in the SLM is calculated using the Gerchbert-Saxton algorithm described in **Section 3.3.2.1**. As mentioned in **Section 3.3.2.1**, the target intensity spots have top-hat profile due to the resolution of the SLM, although the intensity cross-section in the focal plane of the MO will have Gaussian profile. The advantage of this configuration is the reduction in the processing time: all the irradiation tracks of the approximation scanning technique are produced at the same time, eliminating the necessity of performing several scans for producing the channel. This is achieved due to the separation between beams in the X dimension, and the partial overlapping between spots in the Y dimension. The disadvantage of this technique is the relatively low resolution in the overlapping between spots, which is determined by the pixel size of the SLM. With the used SLMs, this resolution corresponds to ~1/3 of the beam diameter at the focal plane of the MO.

Two other types of beams have been analyzed. The second type are Gauss-Bessel beams [15], described in **Section 2.1.1.4**. They may potentially produce more constant energy deposition profiles by reducing the screening due to surface features produced by previous irradiation tracks. The third type are accelerating beams [16], described in **Section 2.1.1.5**. Their curved trajectory can be used to irradiate the material directly at the walls rather than from the top. This may reduce the roughness of the channel walls.

Two different materials have been used in this study: fused silica (Sil1) and lithium

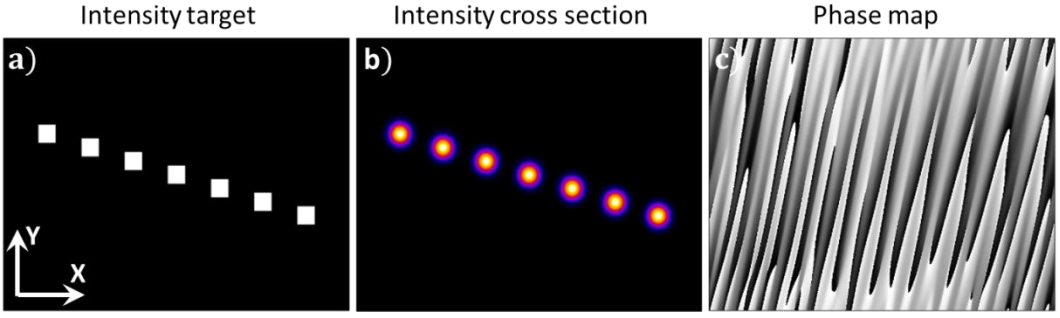

Figure 4.4: *Intensity target distribution (a), final intensity cross section distribution calculated by the algorithm (b) and calculated phase map (c) of a multiplexed beam.*

niobate (LiNb1), as described in **Table 3.8**. The depth of the ablation channels was not analyzed since the study was focused on the roughness.

4.1.3.1. Roughness determination

The determination of the roughness of the channels is not a simple task. There are indeed multiple parameters that can be used for assessing the roughness of a surface. A detailed description of some of them can be found in [17]. The most commonly used parameters are the root-mean-square (RMS) R_q and the correlation length l_c [18] of the topography map of the surface. In an ideal situation it would be possible to measure the topography map of the wall of the ablated channel. However, as it can be seen in **Figure 4.5**, surface features are of the order of few hundreds of nanometers, and thus a topography map cannot be acquired by optical means.

Atomic force microscopy (AFM) allows measuring topography maps very accurately. **Figure 4.5a** shows an AFM measurement of a waveguide produced using a multiplexed writing beam. Unfortunately, the quality of the topography map of the vertical wall is not good enough, as it can be appreciated by comparing it with the SEM image included in **Figure 4.5b**. This is due to the fact that the wall is almost perpendicular to the sample surface of the material and also to the size of the AFM tip. Tilting the sample does not improve the situation due to the small width of the channels.

Several attempts describing how to correlate SEM images with topography have been published. One possibility is measuring several images at different angles and combine them to calculate the surface map [19, 20]. Nonetheless, this requires very sophisticated and time-consuming algorithms to reconstruct the image, along the requirement of several images. Another method proposed is the so-called “shapes from shades” [21], which consists on measuring the number of back-scattered or secondary electrons in a SEM, along with their

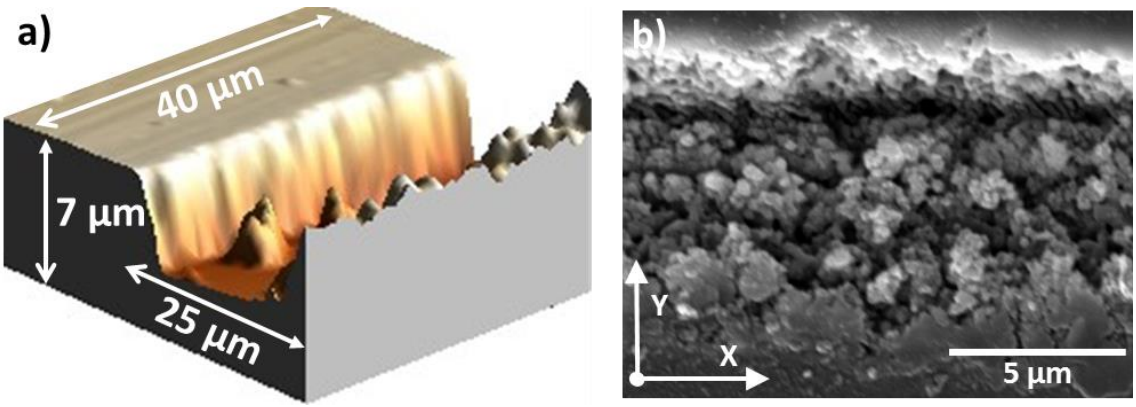

Figure 4.5: *Surface map measured by AFM (a) and SEM image (b) of one channel produced using a multiplexed Gaussian inscribing beam. (b)*

emission direction. Certain algorithms can combine this information to provide topography maps. However, it requires a specifically designed detector and is limited to angles below ~70°. Also, several mixed techniques have been proposed, as FIB (focused ion beam) – SEM [22] and CV (cyclic voltammetry) – SEM [23]. The first one is a destructive technique, while the second is suited only for electroactive materials.

Given the above mentioned considerations, a pseudo-quantitative approach for roughness determination based on SEM images has been developed. It is important noting that measurements were performed only along the X direction. This is due to the fact that the characterized wall has an angle of almost 90° respect to the image plane, which may vary between channels. This angle will affect any measurement in the Y direction, but not along X.

The method takes advantage from the fact that the edges of the features at the surface are easily determined in the SEM images. The size of the surface features was used to assess the roughness. This parameter was called "mean texture size" (mts). The method for determining the mts is described in more detail in **Section 3.3.3**. It is important noting that the error bars are calculated from the standard deviation of the feature sizes. For most random processes, the roughness features show Gaussian profile [23], so the surface features will show correlated their height and width. This means that the roughness of the wall will decrease with the mts.

4.1.3.2. Role of pulse energy and beam parameter

This sub-section describes the effect on roughness of pulse energy and beam parameter for the "exotic" beams (conical angle for Gauss-Bessel beams, and curvature radius for accelerating beams).

Figure 4.6 shows the *mts* of the walls for channels irradiated with different pulse energies and beam types: a multiplexed beam of 7 spots of 2 pixels width and one pixel overlapping (the one shown in **Figure 4.4**), Gauss-Bessel beams with conical angles of 10°, 15° and 20°, and accelerating beams with circular trajectory with 150, 200 and 300 μm of curvature radius. All channels were written at 0.5 mm/s, with a separation of 1 μm between the 7 irradiation tracks for Bessel and accelerating beams. In the case of $LiNbO_3$ with Gauss-Bessel and accelerating beams of 300 μm curvature radius, it was not possible to measure a mean texture size because the channel walls were produced at 90° respect to the material surface, and the features of the wall were not observable.

The accelerating beams require less energy for producing homogenous channels. However, if we consider the pulse energy *per irradiation track*, multiplexed Gaussian beams

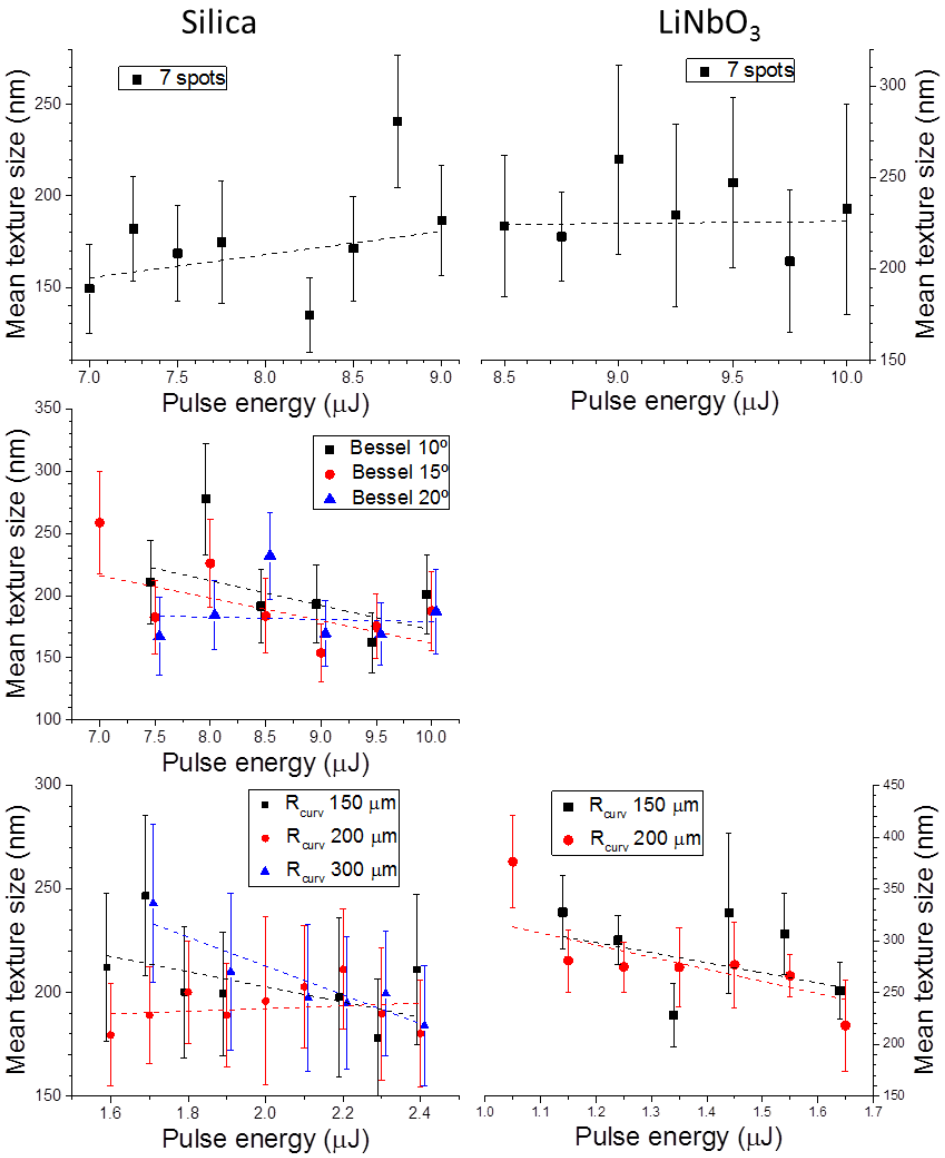

Figure 4.6: *Mean texture size for multiplexed, Gauss-Bessel and accelerating beams versus pulse energy. Dashed lines are linear fits of the corresponding experimental values. For Gauss-Bessel and accelerating beams some values have been slightly displaced along the X axis for a better visualization.*

show the lower threshold in fused silica. In $LiNbO_3$ accelerating beams show the lowest threshold. Bessel beams require much more energy to produce channels in both materials. This is due to the fact that only part of the beam energy is located in the central intense lobe that produces multiphoton absorption.

The evolution of the *mts* for Gauss-Bessel and accelerating beams versus pulse energy shows in most cases a decaying tendency, while for multiplexed beams is hard to find a clear trend. The decaying tendency seems to be stronger for higher conical angles for the Gauss-Bessel beams. In general, *mts* is lower in fused silica than in $LiNbO_3$. Also, the minimum value of *mts* is similar for all the different beam types.

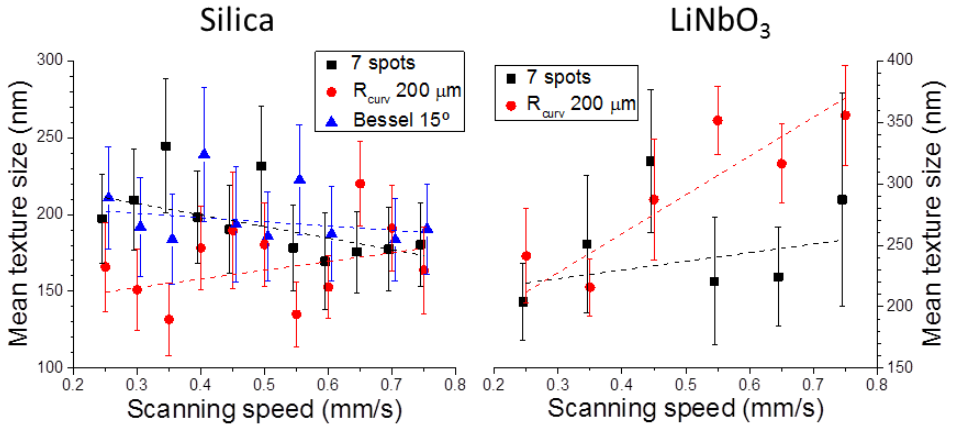

Figure 4.7: *Mean texture size for multiplexed, Gauss-Bessel and accelerating beams for different scanning speeds. Dashed lines are linear fits of the corresponding experimental values. Some values have been slightly displaced along the X axis for a better visualization.*

4.1.3.3. Role of sample scanning speed

The channels were inscribed with pulse energies of 8, 7 and 2 μJ for multiplexed Gaussian, Gauss-Bessel and accelerating beams in fused silica, and 9 and 1.45 μJ in $LiNbO_3$. The separation between the irradiation tracks is maintained in 1 μm for Gauss-Bessel and accelerating beams. The results are shown in **Figure 4.7**. For fused silica, it is hard to define a clear tendency. In the case of $LiNbO_3$, mean texture size seems to increase with scanning speed, especially in the case of accelerating beams.

4.1.3.4. Role of the separation between irradiation tracks

Here the effect of the separation between different irradiation tracks for the same channel is described. This parameter is not studied for multiplexed beams due to the low resolution in this parameter (see **Section 3.1.2.1**). The channels were inscribed with pulse energies of 2 and 7 μJ for accelerating and Gauss-Bessel beams in fused silica, and 1.45 μJ in $LiNbO_3$, all of them at 0.5 mm/s of sample scan speed.

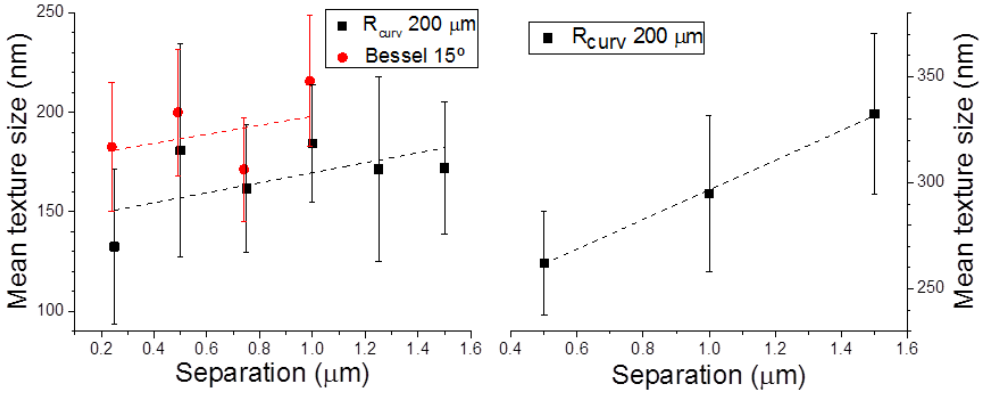

Figure 4.8: *Mean texture size for accelerating and Gauss-Bessel beams as a function of dot separation. Dashed lines are linear fits of the corresponding experimental values. Some values have been slightly displaced along the X axis for a better visualization.*

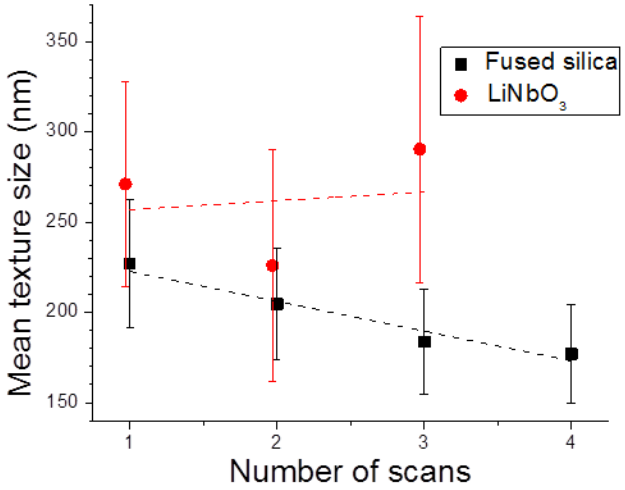

Figure 4.9: *Mean texture size for multiplexed beams with different number of irradiations. Dashed lines are linear fits of the corresponding experimental values. Some values have been slightly displaced along the X axis for a better visualization.*

The results are shown in **Figure 4.8**.In all cases, the mean texture size is reduced for decreasing separations between irradiation tracks. This reduction is relatively small in fused silica, but more pronounced in $LiNbO_3$. In the case of Gauss-Bessel beams, their small central lobe size prevents the production of homogenous channels for separations higher than 1 μm.

4.1.3.5. Number of scans

Finally, the effect of re-irradiating the channel several times in order to reduce roughness was analyzed. This experiment was performed using multiplexed Gaussian beams. The channels were produced at 8 μJ in fused silica and 9 μJ in $LiNbO_3$, at 0.5 mm/s in both cases. The results are shown in **Figure 4.9**. In the case of fused silica, the mean texture size is clearly reduced by re-irradiation of the channels, reaching a very low value of ~150 nm.

4.1.3.6. Conclusion

Table 4.2 shows the average mts for the different parameters considered. It can be seen that mts is smaller for fused silica than for $LiNbO_3$. This is probably due to the fact that silica is a glass. The second result is the difference between beam types. In the case of fused silica, the differences between the different beam types is small, while in $LiNbO_3$ multiplexed Gaussian beams seem to produce smoother ablation channels than accelerating beams. However, the high error in the determination of the mts does not allow us to draw a definitive conclusion.

The mts of the produced ablation channels seems to be little affected by the analyzed writing parameters. In the case of $LiNbO_3$, channels produced with multiplexed beams produce the same or lower mts. As the production of one ablation channel with a multiplexed

Table 4.2: *Mean value of mean texture size for each studied parameter and type of beam.*

	Fused silica			$LiNbO_3$	
	Multiplexed Gaussian	**Accelerating beam**	**Gauss-Bessel beam**	**Multiplexed Gaussian**	**Accelerating beam**
Energy	176±63	201±36	195±66	231±41	285±86
Velocity	196±49	169±53	199±39	251±91	295±116
Separation	-	167±41	192±42	-	296±73
Scans	198±48	-	-	262±76	-
All	189±55	186±52	196±55	244±68	289±89

Gaussian beam requires much less time, they are better suited for the production of surface waveguides in crystalline materials. Any further conclusion would require measurements with smaller error. Anyway, the produced channels show mts of ~250 nm, which allows producing waveguide with losses around 1.5 dB/cm.

4.2. Waveguide-based lasers

This section analyzes the production of waveguides by surface structuring of crystalline materials, and their use for producing lasers. Two different materials were used: $LiNbO_3$ and KYW. They were doped with different rare earths in order to produce lasers at different wavelengths.

4.2.1. Determination of the laser structuring parameters

Several test channels and ridges were produced with multiplexed Gaussian beams in order to determine the optimal writing parameters for the waveguides. Surface structuring was performed with the setup located in the Institute of Optics described in **Section 3.1.2.1**. Several pulse energies and scanning speeds were used. The channel width was measured by optical microscopy. The depth was determined by the two different methods also described in **Section 3.2.5**.

The selected phase map, its target and produced intensity profile are shown in **Figure 4.10a**. It consists on a 7 spot beam with a separation in the vertical dimension of 2 pixels for odd spots and 1 pixel for even ones (different from the multiplexed beam used in **Section 4.1.3**). This is done in order to increase the channel width without increasing too much its depth. With these parameters, channel depths between 3 and 5 μm, depending on the pulse energy, can be produced. Higher depths were obtained by re-scanning with pulses of the same energy and spatial distribution. The phase map is oriented so the last two spots present an overlap of 1 pixel.

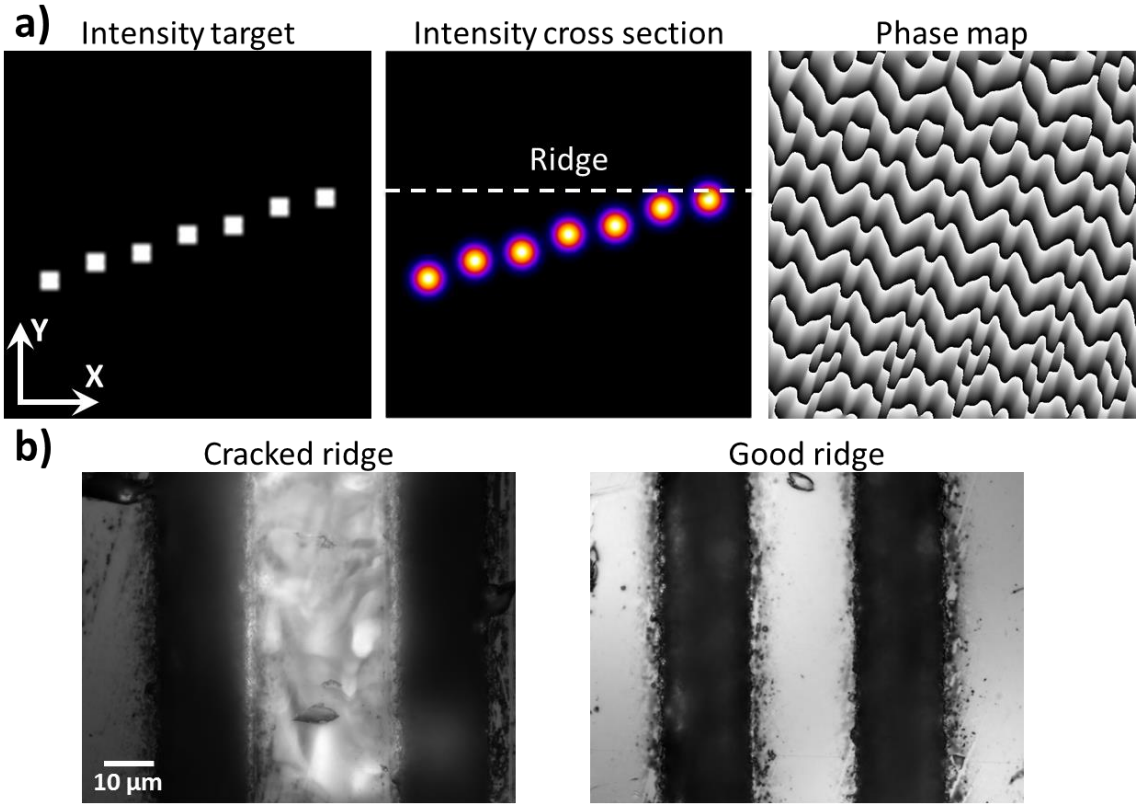

Figure 4.10: *(a) Intensity target distribution, final intensity cross section and the calculated phase map necessary to produce the desired distribution. (b) Top-view reflection microscopy images of a cracked and a good ridge waveguide produced at 300 and 100 µm/s respectively with pulses of 2.7 µJ in a KYW sample.*

The optimum scanning speed was found to be 0.1 mm/s. Higher velocities produced ridges with cracks, as shown in **Figure 4.10b**, while lower velocities increased too much the depth and processing time. Since the area of the ablated channels increases with pulse energy, the ridge width decreases with pulse energy too. This decrease in the ridge width was precompensated by increasing the distance between the channels.

4.2.2. $LiNbO_3$ doped with Nd^{3+}

These waveguides were produced in LinNb2 sample (see **Table 3.8**). This $LiNbO_3$ sample (doped with 0.23% wt. Nd^{3+}, with a planar waveguide fabricated by Zn^{2+} ions diffusion) was ad-hoc fabricated for producing ridge waveguides upon laser irradiation.

The optimal design parameters for the waveguides were shown in **Section 4.1.1**: Δn_0 = 5×10^{-3}, z_{core} = 5 μm, z_{res} < 0, y_{chan} > 15 μm, and y_{ridge} ~20-30 μm. The planar waveguide was characterized by comparing the guided modes at 633, 700 and 980 nm with simulations, leading to Δn_0 = 3×10^{-3} and d_0 = 5.5 μm. The channels were irradiated with pulse energies between 2 and 3.5 μJ. The length of the waveguides after polishing both ends was 8.2 mm.

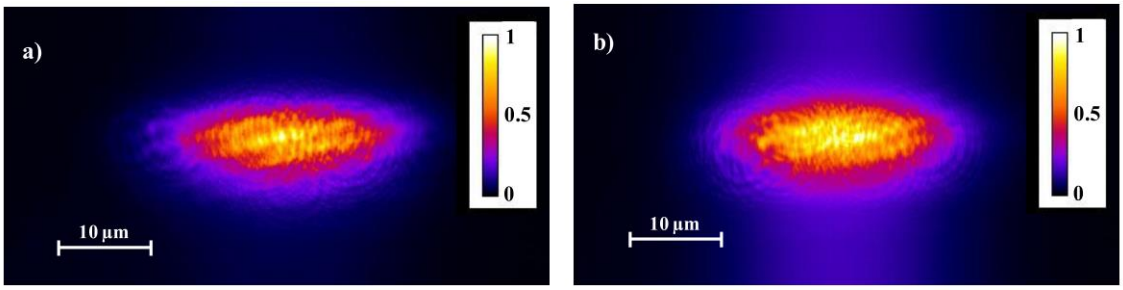

Figure 4.11: *Guided modes at 980 nm of WgA (a) and WgB (b).*

The waveguides were characterized using the aerial characterization setup described in **Section 3.2.4**.The passive characterization of the waveguides showed high losses for most of the waveguides at 980 nm. Only the waveguides with 27 and 30 μm ridge written width with 3.5 μJ pulse energy (WgA and WgB respectively) showed moderate losses of 4.0 and 5.7 dB/cm. These losses are caused by a leak of light towards the bulk due to a Δn_0 value lower than designed. Their guided modes at 980 nm are shown in **Figure 4.11** and their main parameters are listed in **Table 4.3**.

Table 4.3: *Main parameters of WgA and WgB.*

Wg.	Pulse energy (µJ)	Ridge width (µm)	Propagation losses (dB/mm)	Laser slope efficiency	Abs. ump lasing threshold (mW)
WgA	3.5	27	4.0	5.7	31
WgB	3.5	30	5.7	-	-

The laser cavity was constructed using two mirrors whose spectral reflectivity is shown in **Figure 4.12a**. The fist mirror is almost transparent to the pump wavelength (815 nm), while totally reflective at the laser wavelength (1085 nm). The second mirror, on the other hand, is totally reflective at the pump wavelength (effectively doubling the length of the waveguide for pump absorption) while showing a ~95% reflectivity at laser wavelengths. This is shown schematically in **Figure 4.12b**.

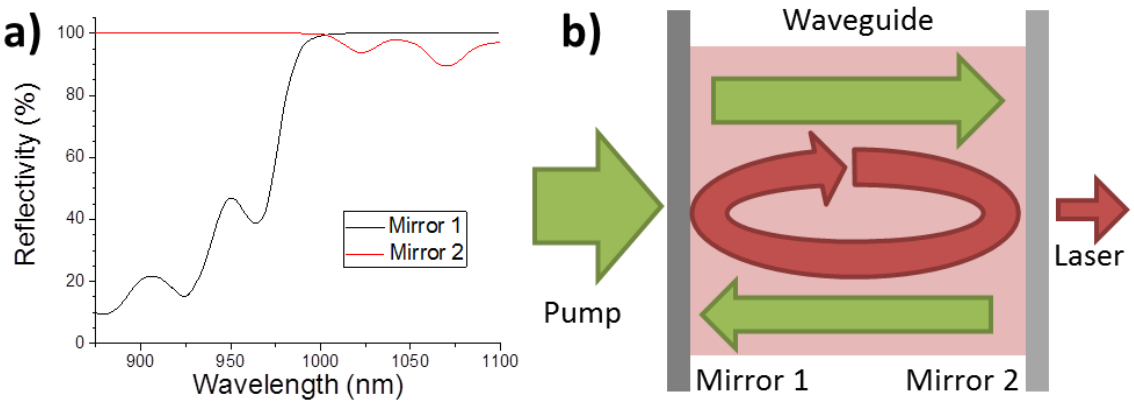

Figure 4.12: *(a) Spectral reflectivity of the mirrors used for constructing the laser cavity in $LiNbO_3$ waveguides. (b) Scheme of the laser cavity configuration.*

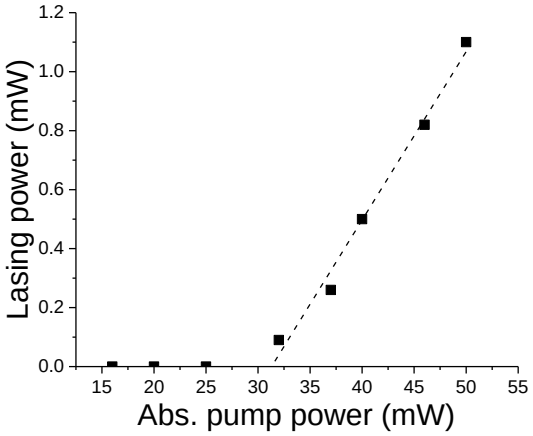

Figure 4.13: *Laser power emission versus pump power for WgA. Dashed line is the linear fit.*

The optimum result was obtained in WgA (due to the lower losses). The obtained lasing emission was centered at 1085 nm with a bandwidth of 0.6 nm. The laser emission power as a function of pump power is shown in **Figure 4.13**. The lasing threshold was found to be 31 mW, with a slope efficiency of 5.7%. This result is worse than that observed in waveguides fabricated in a similar material [24]. The reason is the high propagation losses caused by the low refractive index contrast of the planar waveguide.

4.2.3. KYW doped with Yb^{3+}

As shown in **Section 2.5.3**, Yb^{3+} embedded in crystalline KYW can be used as active ion for amplification and lasing applications around 1 μm. In this case, a sample with an active layer of 4 μm doped with Yb^{3+} was grown for the production of ridge waveguides. The results are reported in [9].

The required depth for the channels was 4 μm or higher. The waveguides were produced using the same wavefront and scanning speed than in $LiNbO_3$, but with slightly

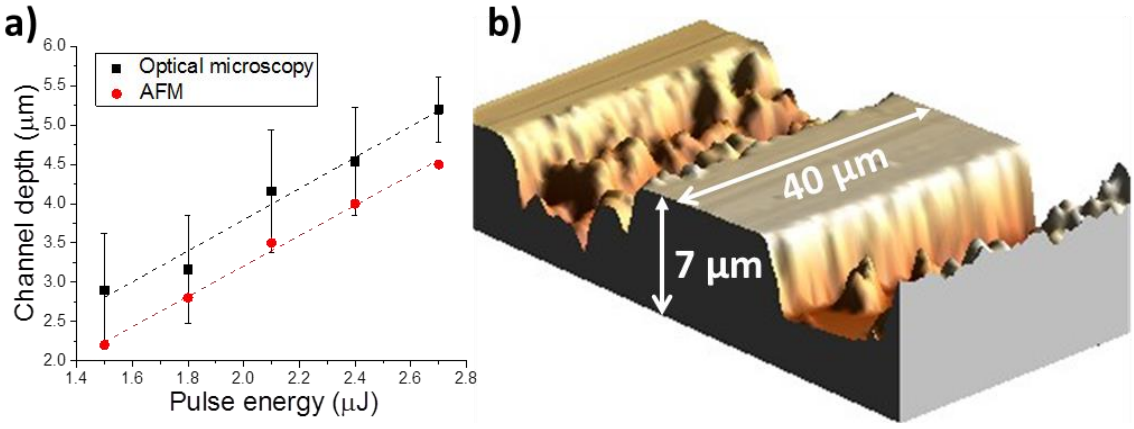

Figure 4.14: *(a) Channel depth versus pulse energy for single scan in KYW. Dashed lines are linear fits. (b) AFM measurement of WgC.*

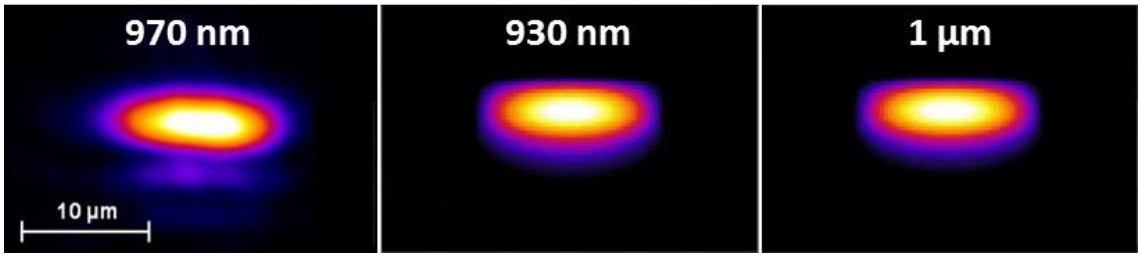

Figure 4.15: *Experimentally measured guided mode at 970 nm, and simulated modes at 930 nm and 1 µm of WgE in KYW1 sample.*

reduced pulse energies: between 1.5 and 2.7 μJ. The relation between channel depth and pulse energy is shown in **Figure 4.14a**, with the measurements performed by optical microscopy showing ~0.5 μm higher depth than AFM measurements. Waveguides were fabricated with 6, 8, 10, 12 and 15 μm of ridge width.

Table 4.4: *Fabrication parameters and propagation losses of WgC, WgD and WgE.*

Waveguide	Ridge width (µm)	Channel depth (µm)	Propagation losses (dB/cm)
WgC	10	2.8	7.9
WgD	12	3.5	2.6
WgE	15	4.1	1.3

The losses of the waveguides were characterized at 800 nm in order to avoid Yb^{3+} absorption bands. Due to the proximity between wavelengths, it is assumed that the losses at 800 nm are the same than for 930 nm and 1 μm. The best results were obtained for WgC, WgD and WgE, as shown in **Table 4.4**.

Figure 4.15 shows the experimentally measured guided mode at 970 nm of WgE, along the simulated modes at 930 nm and 1 μm (corresponding to the pump and signal wavelengths for Yb^{3+} lasers). The simulated widths and heights of the modes coincide with the experimental ones with two small differences: the experimental mode is more symmetric in the vertical dimension, and it shows a small leak towards the bulk. The horizontal FWHM of the guided modes of WgC, WgD and WgE were measured and simulated, resulting both in 7.2, 8.5 and 11.0 μm respectively. The overlapping factor between simulated modes for all waveguides was higher than 0.99 (due to the proximity between pump and signal wavelengths) which enhances the efficiency of amplifiers and lasers.

Two mirrors were attached to the end facets of the waveguides in order to produce a laser cavity with the configuration shown in **Figure 4.12b**. The spectral reflectivity of the used mirrors is shown in **Figure 4.16**. The first mirror is a total reflector at the laser wavelength while it shows high transmission at the pump wavelength. The second one presents a reflectivity of 100% for wavelengths shorter than 1 μm (again doubling the effective length for

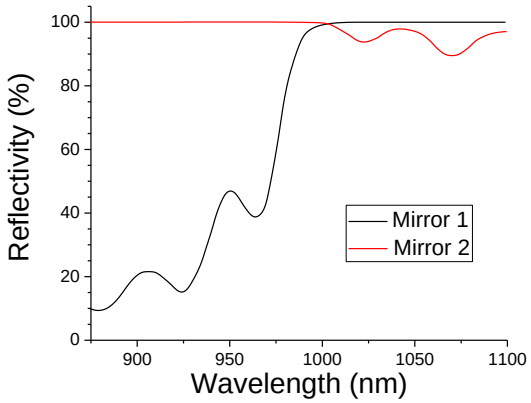

Figure 4.16: *Reflectivity of the cavity mirrors respect to the wavelength.*

pump absorption) and two decreased reflectivity bands around 1025 and 1075 nm. This forces laser emission to occur around 1025 nm in the waveguides.

Figure 4.17 shows the laser emission power of the three waveguides, and **Table 4.5** the lasing parameters. In all cases, the most efficient pump wavelength was 933 nm. The reduction in losses from WgC to WgD results in a reduction of the lasing threshold and an increase in the slope efficiency. However, the further reduction in losses of WgE results in a shift of the emission wavelength.

Table 4.5: *Lasing parameters of WgC, WgD and WgE in mirror cavity configuration.*

Waveguide	Slope eff. (%)	Lasing thres. (mW)	Central λ (nm)	Δλ (nm)
WgC	5.4	11	1025	0.8
WgD	9.2	8	1025	0.8
WgE	9.1	11	1030	0.7

The low propagation losses of the waveguides and the high refractive index of KYW,

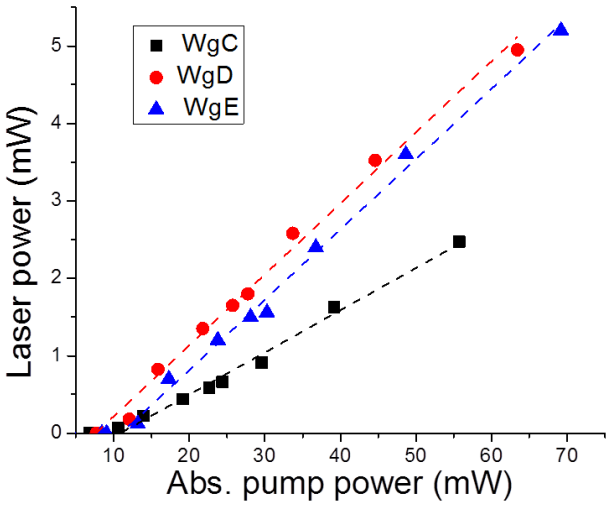

Figure 4.17: *Laser emission power of WgC, WgD and WgE versus absorbed pump power. Dashed lines are linear fits.*

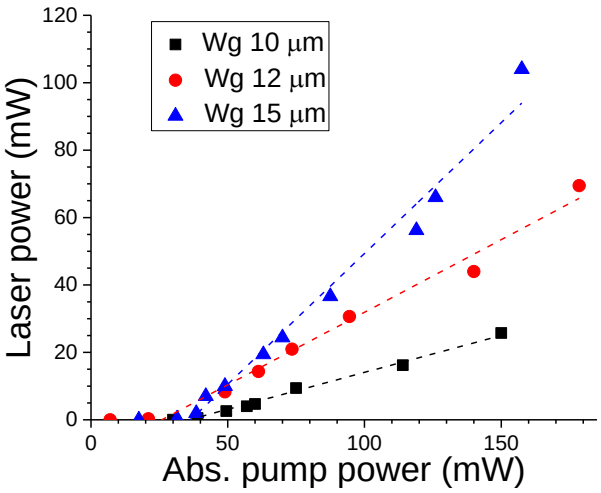

Figure 4.18: *Laser emission power of WgC, WgD and WgE versus absorbed pump power in the mirrorless cavity configuration. Dashed lines are linear fits.*

enables mirrorless lasing emission. In this case, the reflectivity at both ends of the waveguide is generated by Fresnel reflections. The calculated reflectivity of the KYW-air interface is 11%. Although laser output was measured at one end of the waveguide, it emits from both ends, so the total output is calculated as the double of the measured power.

Figure 4.18 shows the laser power emission versus absorbed pump power in this new configuration, while **Table 4.6** shows the laser parameters. In this case, WgC emits at 981.5 nm, while the other two waveguides emit at 1001 nm. Simulations show that this occurs because the lasing threshold is lower at 1001 nm than at 981.5 nm if waveguide losses are lower than 3 dB/cm; which is the case of WgD and WgE, but not WgC [25].

Table 4.6: *Laser emission parameters of WgC, WgD and WgE in a mirrorless cavity configuration.*

Waveguide	Slope eff. (%)	Lasing thres. (mW)	Central λ (nm)	Δλ (nm)
WgC	21.9	36	981.5	0.6
WgD	43.1	26	1001.0	0.7
WgE	77.6	36	1001.0	0.7

The lasing threshold increases respect to the mirror cavity configuration, as expected by the increase in the output factor. The slope efficiency also increases for the same reason. WgC is the waveguide with the highest slope efficiency, 77.6%, showing a lasing threshold as low as 36 mW, which is a highly remarkable result. This slope could even be increased by placing mirrors of different reflectivities. This result is of the same magnitude than the lasers produced by Palmer and coworkers in [26], where they obtained a slope of 84%, although in their case they produced the waveguides by sub-surface fs-laser writing using Type II modifications (see **Section 2.6.2**).

4.2.4. KYW doped with Er^{3+} and Yb^{3+}

Er^{3+} and Yb^{3+} ions can be used for building up an amplification system pumped at 976 nm that emits at 1535 nm. This system has been used for the inscription of active waveguides in KYW material. The results are analyzed in more detail in [10].

The waveguides were produced in the KYW2 sample. The active layer was designed to be doped with 1% wt. of Er^{3+} and Yb^{3+} ions in order to implement active devices, although the sample timely available had a concentration of just 0.1 %wt., so no active measurements were possible. However, it was possible to show the feasibility of producing waveguides with very low losses.

The sample has a 10 μm width cladding over the active layer (see **Figure 4.1b**), composed of the same material of the substrate. In this case, load-type waveguides were inscribed. As shown in **Section 4.1.1**, the lowest losses are produced for channels of the same depth as the cladding width, i.e., waveguides with z_{res} = 0. This is a parameter difficult to tune, so several pulse energies were tried in order to obtain values of z_{res} between 1.5 and 0 μm. In order to increase the depth of the ablation channels, they were irradiated three times. Also, different waveguide widths were inscribed. The final length of the waveguides after polishing was 2.8 mm. **Figure 4.19a** shows the measured channel depth measured by optical microscopy and AFM. As shown in **Figure 4.19a**, AFM measurements show a depth ~0.8 μm higher, so the estimated z_{res} value is between 1.0 and -0.5 μm. **Figure 4.19**b shows the 3D topographic map of a waveguide measured by AFM.

The passive characterization of the waveguides was performed in the mode and amplifier characterization setups in fiber described in **Section 3.2.2** without index matching gel

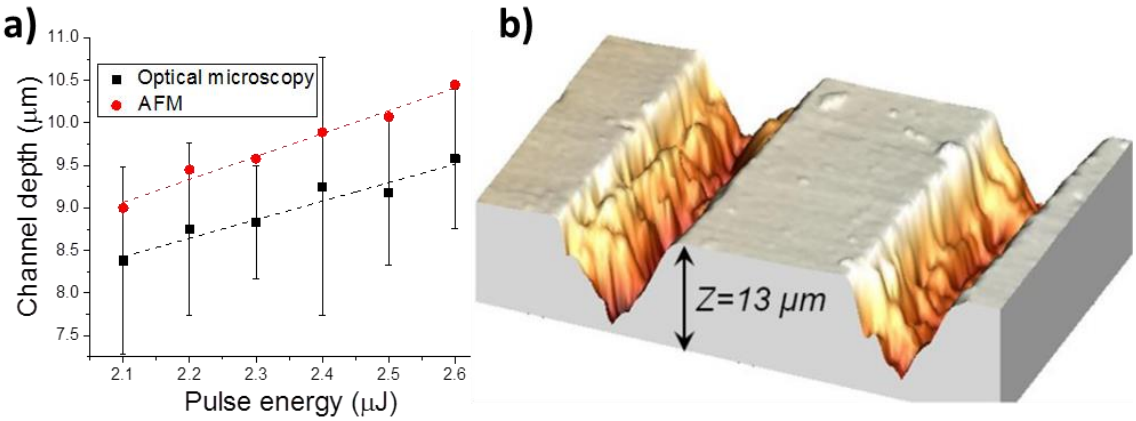

Figure 4.19: *(a) Channel depth measured for all the produced waveguides by optical microscopy and AFM. Each ablation channel was irradiated three times. Dashed lines are linear fits. (b) AFM measurement of the waveguide of 25 μm ridge width and 2.6 μJ of pulse energy.*

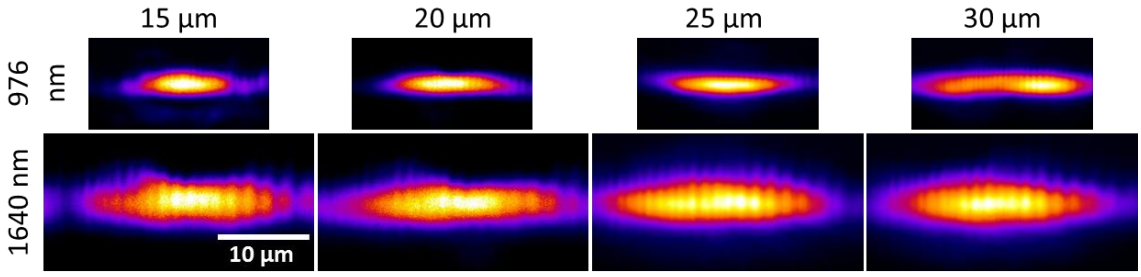

Figure 4.20: *Guided modes at 976 and 1640 nm for waveguides of different ridge widths inscribed at 2.2 µJ in KYW2 sample. The material surface is located on top of the images. All images are plotted at the same scale.*

(it would fill the channels, impeding guiding). The guided mode at 976 and 1640 nm of each waveguide was recorded. **Figure 4.20** shows the modes for waveguides of different widths inscribed at 2.2 μJ. Due to the difference in wavelength, the mode size at 976 nm is smaller than the mode at 1640 nm. As expected, the mode horizontal diameter increases with the ridge width. The mode at 976 nm seems slightly multimode for the ridge of 30 μm.

As expected from the simulations, guiding was worse for shorter ridge widths, which can be inferred from the higher noise level in the images for 15 and 20 μm ridge widths. This is confirmed by the propagation losses measurements shown in **Table 4.7**. Due to the high coupling and Fresnel losses, and the short length of the waveguides, the error in the loss measurement is high, (~0.5 dB/cm). Also, not all the waveguides loss could be measured, as some of them showed losses higher than 10 dB/cm, probably due to defects on the ridge or the input/output facets after polishing. In spite of this, a good agreement between experiment and numerical predictions is found.

Table 4.7: *Calculated (Calc.) and experimental (Exp.) losses for different waveguides measured in dB/cm. Experimental error is 0.5 dB/cm.*

z_{res}	1.0 µm		0.5 µm		0.0 µm		-0.5 µm	
Ridge width	**Calc.**	**Exp.**	**Calc.**	**Exp.**	**Calc.**	**Exp.**	**Calc.**	**Exp.**
10 µm	15.7	-	9.6	-	4.95	-	2	-
15 µm	6.3	6.5	3.3	-	1.4	2.3	0.5	-
20 µm	2.8	2.8	1.3	4.7	0.5	<0.5	0.2	-
25 µm	1.8	-	0.6	1.1	0.2	<0.5	<0.1	<0.5
30 µm	0.7	-	0.3	<0.5	0.1	<0.5	<0.1	-

Even if no active measurements were possible, it can be seen that it is feasible to produce load waveguides with losses below 0.5 dB/cm by fs-laser writing. As shown in **Section 4.2.3**, ridge waveguides with losses of 1.3 dB/cm can be used for producing Yb^{3+} lasers with slope efficiencies of 78%, so this result can potentially be improved structuring load waveguides leading to substantially lower losses.

4.3. Summary and conclusion

In this chapter, the capabilities of fs-laser surface structuring for producing waveguides in crystalline dielectrics have been shown.

First, the methodology for the design of the waveguides has been discussed, showing the feasibility of producing ridge and load waveguides. Then, it has been shown how the approximation scanning technique can be used for producing channels with a ridge wall of low roughness ($\leq$250 nm), leading to propagation losses lower than 2 dB/cm, which is essential for the production of efficient active waveguides and lasers.

A new method for the characterization of the channel wall roughness from SEM images has been proposed. This method was used for assessing the roughness of the channel walls inscribed by three different types of laser: multiplexed Gaussian, Gauss-Bessel and accelerating beams. In terms of mean texture size, no clear difference in the roughness can be appreciated between channels structured using the three different types of beam.

Finally, multiplexed Gaussian beams have been used for the production of ridge-type waveguides in $LiNbO_3$ doped with Nd^{3+} and KYW doped with Yb^{3+}, and load waveguides in KYW doped with Er^{3+} and Yb^{3+}. In the case of the $LiNbO_3$ waveguides, roughness of the order of 250 nm but with a low Δn lead to a waveguide with losses of 4 dB/cm, although simulations show that this parameter can be improved increasing Δn. These waveguides showed lasing emission at 1085 nm with an efficiency of 6% and a lasing threshold of 31 mW. In the case of Yb^{3+}-doped KYW, the fabricated waveguides with roughness of the order of 250 nm and high Δn lead to a waveguide losses down to 1.3 dB/cm. The waveguides showed laser emission at 981.5, 1001, 1025 and 1031 nm, depending on the waveguide and cavity configuration. The best result (for a waveguide of 1.3 dB/cm propagation losses in a mirrorless-cavity configuration) corresponds to a slope efficiency of 78% with an absorbed pump lasing threshold of 36 mW. In the case of the load configuration in KYW, several waveguides with propagation losses lower than 0.5 dB/cm were fabricated. This result indicates that the 78% slope efficiency result in the Yb^{3+}-doped KYW may be further improved if the waveguides are fabricated in load configuration.

4.4. References

[1] M. Pollnau, Y. E. Romanyuk, F. Gardillou, C. N. Borca, U. Griebner, S. Rivier, *et al.*, "Double Tungstate Lasers: From Bulk Toward On-Chip Integrated Waveguide Devices," *IEEE Journal of Selected Topics in Quantum Electronics,* vol. 13, pp. 661-671, 2007.

[2] X. Mateos, R. Solé, J. Gavaldà, M. Aguiló, J. Massons, and F. Díaz, "Crystal growth, optical and spectroscopic characterisation of monoclinic KY(WO4)2 co-doped with Er3+ and Yb3+," *Optical Materials,* vol. 28, pp. 423-431, 2006.

[3] A. A. Kaminskii, L. Li, A. V. Butashin, V. S. Mironov, A. A. Pavlyuk, S. N. Bagayev*, et al.*, "New Crystalline Lasers on the Base of Monoclinic KR(W04)2:Ln3+ Tungstates (R=Y and Ln)," *Optical Review,* vol. 4, pp. 309-315, 1997.

[4] M. Lawrence, "Lithium niobate integrated optics," *Reports on Progress in Physics,* vol. 56, p. 363, 1993.

[5] Y. He and D. Xue, "Bond-Energy Study of Photorefractive Properties of Doped Lithium Niobate Crystals," *The Journal of Physical Chemistry C,* vol. 111, pp. 13238-13243, 2007.

[6] R. Nevado and G. Lifante, "Low-loss, damage-resistant optical waveguides in Zn-diffused LiNbO3 by a two-step procedure," *Applied Physics A,* vol. 72, pp. 725-728, 2001.

[7] A. Arriola, S. Gross, N. Jovanovic, N. Charles, P. G. Tuthill, S. M. Olaizola*, et al.*, "Low bend loss waveguides enable compact, efficient 3D photonic chips," *Optics Express,* vol. 21, pp. 2978-2986, 2013.

[8] E. Cantelar, D. Jaque, and G. Lifante, "Waveguide lasers based on dielectric materials," *Optical Materials,* vol. 34, pp. 555-571, 2012.

[9] J. Martínez de Mendívil, J. del Hoyo, J. Solís, M. C. Pujol, M. Aguiló, F. Díaz*, et al.*, "Mirrorless Yb3+-Doped Monoclinic Double Tungstate Waveguide Laser Combining Liquid Phase Epitaxy and Multiplexed Beam fs Laser Writing," *Journal of Lightwave Technology,* vol. 33, pp. 4726-4730, 2015.

[10] J. Martínez de Mendívil, J. Hoyo, J. Solís, M. C. Pujol, M. Aguiló, F. Díaz*, et al.*, "Channel waveguide fabrication in KY(WO4)2 combining liquid-phase-epitaxy and beam-multiplexed femtosecond laser writing," *Optical Materials,* vol. 47, pp. 304-309, 2015.

[11] G. Lifante, *Beam Propagation Method for Design of Optical Waveguide Devices*: John Wiley & Sons, Ltd, 2015.

[12] R. Martínez-Vazquez, R. Osellame, G. Cerullo, R. Ramponi, and O. Svelto, "Fabrication of photonic devices in nanostructured glasses by femtosecond laser pulses," *Optics Express,* vol. 15, pp. 12628-12635, 2007.

[13] J. Gottmann, G. Schlaghecken, R. Wagner, and E. W. Kreutz, "Fabrication of erbium-doped planar waveguides by pulsed-laser deposition and laser micromachining," in *Proc. SPIE 4941, Laser Micromachining for Optoelectronic Device Fabrication*, 2003, pp. 148-156.

[14] J. Cugat, A. R. d. l. Cruz, R. Sole, A. Ferrer, J. J. Carvajal, X. Mateos*, et al.*, "Femtosecond-Laser Microstructuring of Ribs on Active (Yb,Nb):RTP/RTP Planar Waveguides," *Journal of Lightwave Technology,* vol. 31, pp. 385-390, 2013.

[15] L. Froehly, M. Jacquot, P. A. Lacourt, J. M. Dudley, and F. Courvoisier, "Spatiotemporal structure of femtosecond Bessel beams from spatial light modulators," *Journal of the Optical Society of America A,* vol. 31, pp. 790-793, 2014.

[16] F. Courvoisier, A. Mathis, L. Froehly, R. Giust, L. Furfaro, P. A. Lacourt*, et al.*, "Sending femtosecond pulses in circles: highly nonparaxial accelerating beams," *Optics Letters,* vol. 37, pp. 1736-1738, 2012.

[17] T. R. Thomas, "Characterization of surface roughness," *Precision Engineering,* vol. 3, pp. 97-104, 1981.

[18] D. J. Whitehouse and J. F. Archard, "The Properties of Random Surfaces of Significance in their Contact," *Proceedings of the Royal Society of London A: Mathematical, Physical and Engineering Sciences,* vol. 316, pp. 97-121, 1970.

[19] J. Stampfl, S. Scherer, M. Gruber, and O. Kolednik, "Reconstruction of surface topographies by scanning electron microscopy for application in fracture research," *Applied Physics A,* vol. 63, pp. 341-346, 1996.

[20] D. Samak, A. Fischer, and D. Rittel, "3D Reconstruction and Visualization of Microstructure Surfaces from 2D Images," *CIRP Annals - Manufacturing Technology,* vol. 56, pp. 149-152, 2007.

[21] W. Slówko, "Directional detection of secondary electrons for electron beam profilography," *Vacuum,* vol. 52, pp. 441-449, 1999.

[22] J. R. Wilson, W. Kobsiriphat, R. Mendoza, H.-Y. Chen, J. M. Hiller, D. J. Miller*, et al.*, "Three-dimensional reconstruction of a solid-oxide fuel-cell anode," *Nature Materials,* vol. 5, pp. 541-544, 2006.

[23] S. Dhillon and R. Kant, "Quantitative roughness characterization and 3D reconstruction of electrode surface using cyclic voltammetry and SEM image," *Applied Surface Science,* vol. 282, pp. 105-114, 2013.

[24] M. Domenech Vargas, "Láseres integrados en guías de onda basados en iones Nd3+," Departamento de Física de Materiales, Universidad Autónoma de Madrid, 2004. PhD Thesis.

[25] J. Martínez de Mendívil, "Láseres integrados en dobles tungstatos y niobato de litio basados en guías de onda ridge," Departamento de Física de Materiales, Universidad Autónoma de Madrid, 2015. PhD Thesis.

[26] G. Palmer, S. Gross, A. Fuerbach, D. G. Lancaster, and M. J. Withford, "High slope efficiency and high refractive index change in direct-written Yb-doped waveguide lasers with depressed claddings," *Optics Express,* vol. 21, pp. 17413-17420, 2013.

Chapter 5
Modelling of nonlinear propagation of laser beams

This chapter is dedicated to the modelling of nonlinear propagation and absorption of ultrashort laser pulses inside dielectrics in the low repetition rate regime. The chapter is divided in two main sections. The first one describes the propagation software developed during this thesis. The second one is devoted to analyze the results generated by the program and the comparison with experimental results. The code and some of their applications are also described in [1, 2].

5.1. Numerical simulation code

5.1.1. Nonlinear propagation model

Many approaches have been proposed for modeling the propagation of ultrashort laser pulses inside dielectric materials. **Section 2.1.1** showed a basic linear propagation model derived from Maxwell equations (**Equation 2.13**), where some additional terms were later on introduced to include nonlinear effects like nonlinear refraction (**Equation 2.27**) and multiphoton absorption (**Equation 2.36**). A comprehensive review describing most of the proposed models for propagation of ultrashort laser pulses in dielectrics can be found in [3].

One of these models is based on integrating the nonlinear Schrödinger equation (NSE), [1, 4] which describes the beam evolution along the propagation direction Z as follows:

$$\partial_z A = \frac{i}{2k}\left(\partial_{xx} + \partial_{yy}\right)A + \frac{ikn_2|A|^2}{2\eta_0}A - ik''\partial_{tt}A - \frac{W_{PI}(|A|)E_g}{2|A|^2}A - \frac{\sigma_{IB}(1+i\omega\tau_c)\rho_e}{2}A \qquad \textbf{5.1}$$

A being the electric field (scalar), n_2 the nonlinear refractive index, η_0 the vacuum impedance, $k'' = (\partial_{\omega\omega}k)_{\omega_0}$, W_{PI} the photo-ionization rate, E_g the bandgap energy of the material, σ_{IB} the inverse Bremsstrahlung cross section, τ_c the average free carrier time and ρ_e the electron density. Several assumptions and approximations are made in this expression: the beam remains linearly polarized, the slow-varying envelope approximation (SVEA, $\Delta\omega \ll \omega_0$) and the paraxial approximation ($|\partial_{zz}A| \ll 2k_0|\partial_z A|$).

In **Equation 5.1** the first term accounts for diffraction, the second for nonlinear refraction, the third for group-velocity dispersion (GVD), the fourth for photo-ionization (PI) and the last for plasma absorption and defocusing effects. Other effects like space-time focusing/defocusing, higher order phenomena, modulation instabilities, beam reshaping, or Raman scattering can take place during propagation. A detailed description of these additional effects can be found in [3, 5, 6].

Even without considering them, **Equation 5.1** is very costly in terms of computational power. Nevertheless, it is not always necessary to have a detailed description of laser intensity or the generated free carrier density in terms of temporal evolution. This is the case when trying to make an *a priori* first guess of the best sub-surface laser irradiation conditions in materials laser processing [7, 8], or when simulating spatial soliton formation [9]. In this case, it is possible to neglect GVD and plasma effects, and approximate the photoionization term with a multiphoton absorption expression.

With these simplifications, the NSE is reduced to [1]:

$$\partial_z A = \frac{i}{2k_0}\left(\partial_{xx} + \partial_{yy}\right)A + \frac{ik_0 n_2 |A|^2}{2\eta_0}A - \frac{\beta_K}{2}\left(\frac{n_D}{2\eta_0}\right)^{K-1}|A|^{2K-2}A \qquad \textbf{5.2}$$

This is the same as **Equation 2.36**. Since no temporal phenomena are explicitely considered, it is much more computationally efficient not to consider the temporal dependency of the electric field. Instead, the beam is represented when it shows highest intensity, where nonlinear effects are more intense. This is equivalent to consider the beam propagation as calculated in a pseudo-stationary regime where a square pulse with constant width (τ_{sq}) and limited energy propagates changing only its amplitude.

5.1.2. Description of the program

The code "*Propagador*" has been written in MATLAB for version R2012b (or higher). It includes a Graphical User Interphase (GUI) with several windows that allows the user to introduce the relevant parameters in the simulation. They are shown in **Appendix A**.

During the calculation of the propagation, the beam is represented by the electric field. The model is scalar, so polarization-dependent effects cannot be explicitly considered. The model is based on propagation, i.e., calculations are performed in steps where $A(x, y, z + \Delta z)$ is calculated from $A(x, y, z)$. The program neglects temporal-dependencies to work in a pseudo-stationary regime, with a square pulse with constant width τ_{sq}.

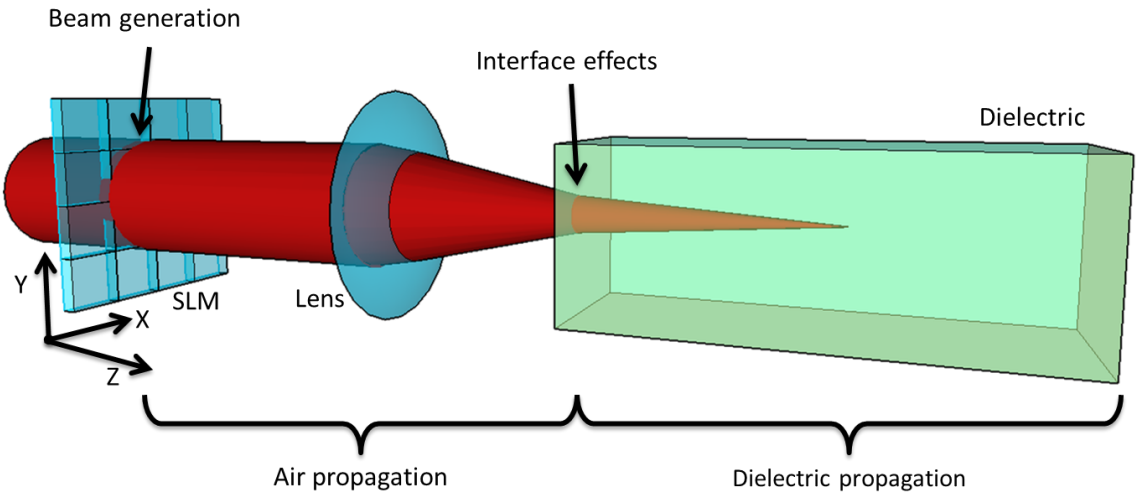

Figure 5.1: *Schematic diagram of the experiment simulated by the program, indicating the four main stages: beam generation, linear propagation in air, interface effects and nonlinear propagation inside the dielectric material. Figure adapted from [2].*

Propagador is aimed at providing a rapid optimization tool for laser processing. The code is divided in four stages: beam generation, linear propagation from the laser source to the dielectric material, introduction of interface effects (including spherical aberration), and propagation inside the dielectric material. **Figure 3.1** shows the scheme of the different stages.

5.1.2.1. Beam generation

The initial beam is represented in terms of amplitude and phase by a matrix with a determined number of points N_x and N_y in each dimension (so the total number of matrix elements is $N_x N_y$):

$$A_{ini}(x,y) = |A(x,y)|e^{i\varphi(x,y)} \qquad \textbf{5.3}$$

This is analogous to start with a spatially shaped beam produced by a SLM. Cartesian coordinates were chosen for similitude with SLMs and for simplicity in the fast-Fourier transforms calculation. The electric field spatial amplitude $|A(x,y)|$ is set by the user. During the simulations shown in this thesis only elliptical Gaussian profiles were used (although different beam types could be used):

$$|A(x,y)| = A_0 \exp\left(-\frac{x^2}{R_x^2} - \frac{y^2}{R_y^2}\right) \qquad \textbf{5.4}$$

where R_x and R_y are the beam radii at $1/e^2$ in intensity. A_0 is an amplitude parameter that is calculated in a way that a pulse with temporal Gaussian profile with pulse duration τ (intensity half-width at $1/e^2$) and pulse energy E_{pulse} has the same peak amplitude:

$$A_0 = \left(\frac{\sqrt{2} E_{pulse}}{\sqrt{\pi}\tau \iint |A(x,y)|^2 dx\, dy} \right)^{1/2} \quad \textbf{5.5}$$

The wavefront of the field can be generated in two different ways. The first one is introducing it from an external file. The second is representing it as a sum of different Zernike polynomials, each one with different amplitude:

$$\varphi(x,y) = \sum_{i=0}^{n} Z_i P_i(r,\theta) \quad \textbf{5.6}$$

where $r = \sqrt{x^2 + y^2}/R_{ref}$ and θ are normalized radial coordinates, and R_{ref} is the reference radius. This parameter represents the size of the Zernike polynomial distribution, since all Zernike polynomial fulfill the condition $P_i(1,\theta) = 1$. In this thesis, R_{ref} is taken as the maximum of the beam radii (R_x, R_y) except otherwise indicated. Regarding the number of polynomials, *Propagador* calculates up to n = 37.

5.1.2.2. Propagation in air

The air propagation stage of *Propagador* has to calculate one of the two configurations shown in **Figure 5.2**. The first configuration (**Figure 5.2a)** corresponds to the propagation of the initial field directly to the dielectric interface. In the second configuration (**Figure 5.2b**), the beam is focused. The focusing element is modeled as a thin lens.

The propagation of the beam electric field is calculated using the operators method described in [10]. It consists on separating the Fresnel diffraction equation in several simpler operations. The Fresnel diffraction equation is:

$$A(x,y,z) = \frac{e^{ikz}}{i\lambda z} \iint_{-\infty}^{\infty} A(x',y',0) e^{\frac{ik}{2z}\left[(x-x')^2 + (y-y')^2\right]} dx' dy' \quad \textbf{5.7}$$

which can be used to calculate free-space propagation when $z \gg \lambda$. However, this equation is costly to integrate in terms of computation time. Nevertheless, it can be interpreted as an operator:

$$A(x,y,z) = \mathcal{R}[z]\{A(x',y',0)\} = \frac{1}{i\lambda z} \iint_{-\infty}^{\infty} A(x',y',0) e^{\frac{ik}{2z}\left[(x-x')^2 + (y-y')^2\right]} dx' dy' \quad \textbf{5.8}$$

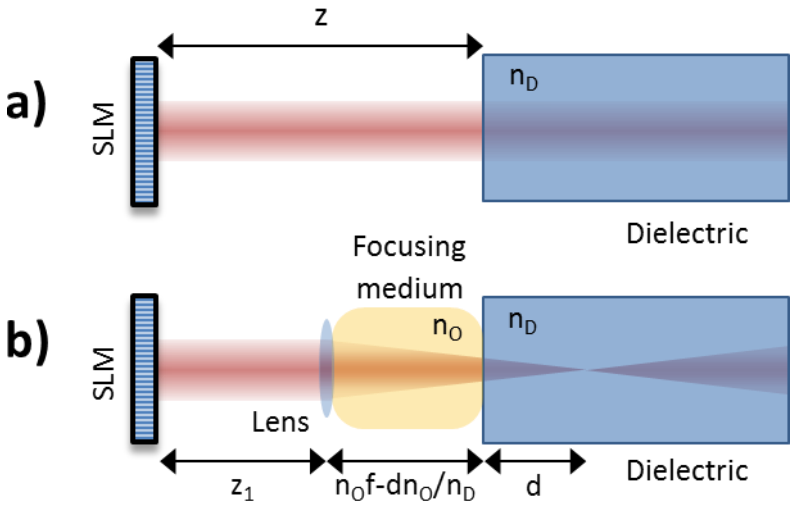

Figure 5.2: *Scheme of the two possible configurations of the propagation towards the dielectric interface. (a) The field is directly propagated to the interface. (b) The beam is focused by a thin lens through a medium (typically air) into the sample at a depth d.*

i.e., the operator $\mathcal{R}[z]$ acting over the field $A(x, y, 0)$. Operator $\mathcal{R}$ coincides with the Fresnel equation except the constant phase e^{ikz}, which can be neglected in this case. The main advantage to move to the operator formalism is that $\mathcal{R}$ can be divided in much less costly operators:

$$\mathcal{R}[z] = Q\left[\frac{1}{z}\right] \upsilon\left[\frac{1}{\lambda z}\right] \mathcal{F}\, Q\left[\frac{1}{z}\right] \qquad \textbf{5.9}$$

where

$$Q[b]\{A(x,y)\} = e^{\frac{ikb}{2}(x^2+y^2)} A(x,y) \qquad \textbf{5.10}$$

is a multiplication by a quadratic-phase exponential,

$$\upsilon[c]\{A(x,y)\} = c\, A(cx, cy) \qquad \textbf{5.11}$$

is a scaling by a constant, and

$$\mathcal{F}\{A(x',y')\} = \iint_{-\infty}^{\infty} A(x',y') e^{-i2\pi(x'x+y'y)} dx'dy' \qquad \textbf{5.12}$$

is a Fourier transform. It is straightforward to see that Q and υ can easily be computed, and $\mathcal{F}$, thanks to discrete fast-Fourier algorithms, is not very costly to compute.

The operator for the configuration shown in **Figure 5.2a** corresponds to $S_1 = \mathcal{R}[z]$. In the second case, as the field is also focused by a lens, the operator for this configuration is slightly more complicated:

$$S_2 = \mathcal{R}[f' - d']\, Q\left[-\frac{1}{f'}\right] \mathcal{R}[z_1] \qquad \textbf{5.13}$$

f' being $n_O f$ and $d' = n_O d/n_D$. The use of S_2 requires to perform two Fourier transforms. However, using the properties of the operators described in **Appendix B**, **Equation 5.13** can be simplified to

$$S_2 = Q\left[\frac{f'^2}{\alpha d'^2} - \frac{1}{d}\right] v\left[\frac{f'}{\lambda \alpha d'}\right] \mathcal{F}\, Q\left[\frac{1}{\delta}\right] \qquad \textbf{5.14}$$

with

$$\delta = z_1 + f'\left(\frac{f'}{d'} - 1\right) \qquad \textbf{5.15}$$

With this simplification, only one Fourier transform is required, which reduces the computation time and also aliasing related problems.

It is worth noting that even this sub-section is called “Propagation in air”, the medium between the lens and the dielectric can be filled by a medium different than air ($n_O > 1$), as in the case of oil-immersion microscope objectives. In that case, the electric field has to be divided by a factor of $\sqrt{n_O}$.

5.1.2.3. Medium change effects

Several effects appear when the beam transverses the air-dielectric interface. First, part of the beam is reflected if the refractive index of both media is different. The transmission coefficients are given by the Fresnel law:

$$t_s(\phi_i) = \frac{2n_O \cos(\phi_i)}{n_O \cos(\phi_i) + n_D \cos(\phi_t)} \qquad \textbf{5.16}$$

$$t_p(\phi_i) = \frac{2n_O \cos(\phi_i)}{n_O \cos(\phi_t) + n_D \cos(\phi_i)} \qquad \textbf{5.17}$$

ϕ_i being the incidence angle and ϕ_t the transmitted angle, given by the Snell law. Knowing the polarization of the beam, the effect of the reflection can be calculated as:

$$A_t(\phi_i) = \sqrt{[|p_s|t_s(\phi_i)]^2 + \left[|p_p|t_p(\phi_i)\right]^2}\, A_i(\phi_i) \qquad \textbf{5.18}$$

A_i and A_p being the incident and transmitted electric fields, $\vec{p}$ the Jones polarization vector of the beam. **Equation 5.18** can be simplified for an incidence angle of 0°:

$$A_t = \frac{2n_O}{n_O + n_D} A_i \qquad \textbf{5.19}$$

Along with reflection, a change of refractive index produces a variation in the electric field amplitude:

$$A_t = \sqrt{\frac{n_O}{n_D}} A_D \qquad \textbf{5.20}$$

The other major effect due to the change of medium is spherical aberration (SA). It is caused by rays incident with different angles that are refracted differently, according to the Snell law. They are thus focused at different depths, as described in **Section 2.1.1.6**. *Propagador* introduces the effects of SA as an additional phase before starting the propagation inside the dielectric material. This phase is given by **Equation 2.21**.

5.1.2.4. Nonlinear propagation inside the dielectric

Nonlinear propagation is calculated using a generalized adaptive fast-Fourier evolver (GAFFE) [11, 12]. It is a split-step method, i.e. the algorithm divides the propagation of the pulse in several steps (Δz) and calculates the field matrix in $A(x, y; z + \Delta z)$ from the field matrix in $A(x, y; z)$. **Figure 5.3** shows the flow diagram of *Propagador*.

Before starting the propagation procedure, the program tests the represented field searching for aliasing, which may appear in computational calculations when continuous variables are discretized. If aliasing appears, the results from the calculations are not reliable.

According to Nyquist theorem [13], a signal is discretized without aliasing if the representation frequency is at least twice the highest frequency of the original signal (Nyquist frequency). If sampling frequency is smaller than the Nyquist frequency, the missing higher frequencies will be improperly reflected inside the representation window, adding to the represented frequencies and distorting the represented signal. **Figure 5.4** shows an example of the field of a beam with severe aliasing (**Figure 5.4a**) and without aliasing (**Figure 5.4b**).

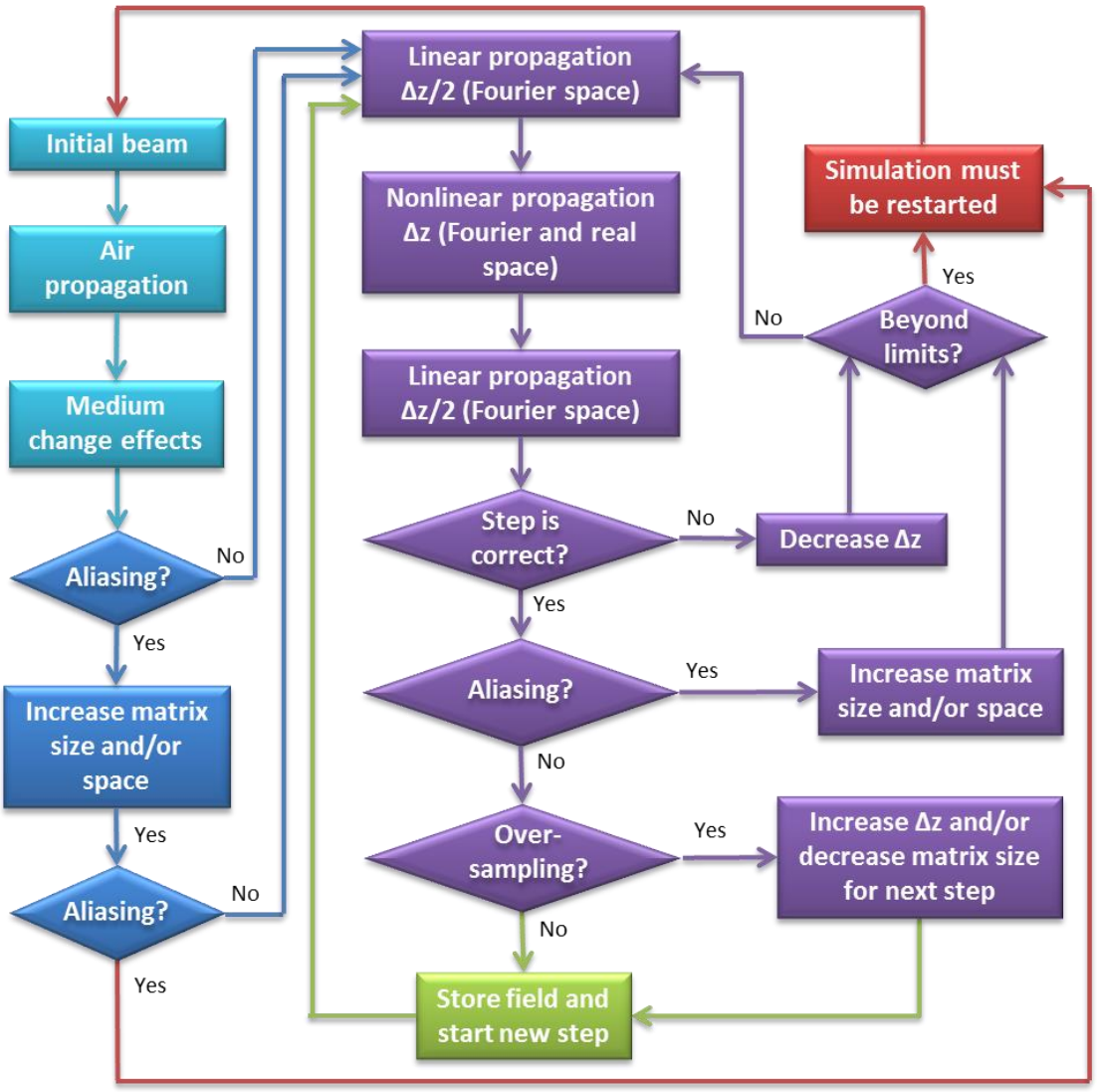

Figure 5.3: *Flow diagram of Propagador. Light blue is used to mark the steps described in previous sub-sections. Dark blue marks the subsequent steps where the program tests the field for aliasing, and if found, tries to eliminate it. All the calculations and tests the program performs in each step during nonlinear propagation in the dielectric are shown in violet. If the program fails to solve any of the steps, the simulation ends and the user has to modify the initial parameters. If the field passes all tests, the step result is stored and the next step is calculated, until reaching the specified propagation depth. Figure adapted from [1].*

Nyquist theorem cannot be strictly applied in the case *Propagador*, as Gaussian distributions have an infinite Nyquist frequency. However, for sufficiently large frequencies, their amplitude can be approximated by zero, and Nyquist theorem applied. The aliasing test is done by calculating the amount of energy present in the outer region of the field matrix (this region will be called guard band) both in real and Fourier spaces, as shown in **Figure 5.4c**. If the ratio between that energy and the total pulse energy is smaller than a certain tolerance (typically 10^{-6}) the field is assumed to be free of aliasing and nonlinear propagation starts.

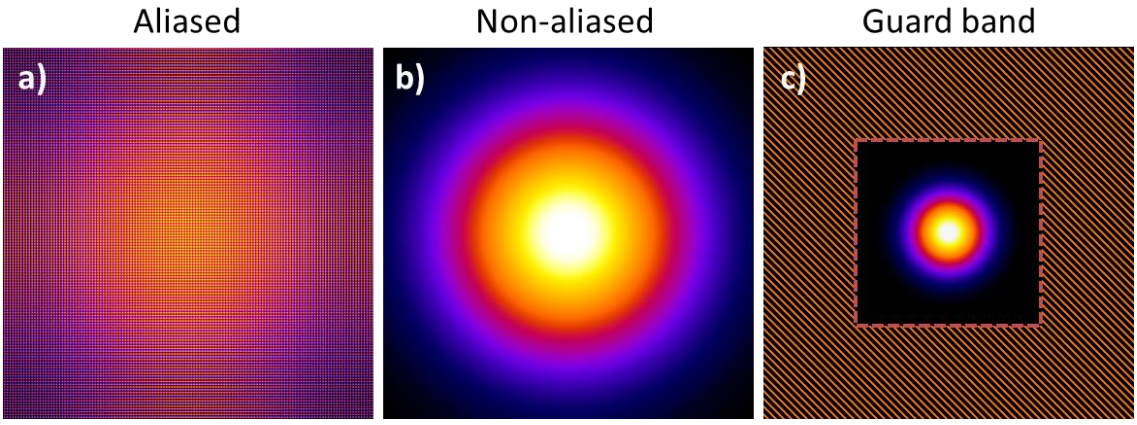

Figure 5.4: *(a) Aliased intensity distribution. (b) Same intensity distribution than (a) free of aliasing. (c) Intensity distribution with the guard band marked in orange texture.*

If the program detects that the beam is slightly aliased in one of the spaces it tries to solve it automatically. If the beam is aliased in the real space, the program takes the beam in the Fourier space and increases the resolution of the beam by interpolation (increasing N_x and/or N_y). Then, by an inverse-Fourier transform it is taken again to the real space. That effectively increases the representation range in the real space. If the beam is aliased in the Fourier space, the program increases the resolution of the beam in the real space in a similar way. The program increases the resolution of the beam in small steps, trying to minimize aliasing but not using too many sample points that would increase the memory usage and processing time. However, there is a limit for what this method is able to accomplish. If the aliasing is severe, or the field is aliased in both spaces, the program is unable to solve it. The user has to change the mesh of the initial beam: resolution and representation range.

When the field is considered as free of aliasing, the propagation inside the dielectric begins. In the first step, the program predicts which should be the initial Δz value from the predicted phase change expected from diffraction and nonlinear refraction. The step size will be re-evaluated after each propagation step, as explained below.

The discretized solution of **Equation 5.2** is

$$A(x,y;z+\Delta z) = e^{(\hat{L}+\hat{N}\hat{L})\Delta z} A(x,y;z) \qquad \textbf{5.21}$$

where

$$\hat{L} = \frac{i}{2k}\left(\partial_{xx} + \partial_{yy}\right) \qquad \textbf{5.22}$$

is the linear operator, and

$$\widehat{NL} = \frac{ikn_2|A|^2}{2\eta_0}A + \frac{\beta_K}{2}\left(\frac{n_D}{2\eta_0}\right)^{K-1}|A|^{2K-2} \quad \textbf{5.23}$$

the nonlinear operator. However, is more time consuming to compute $\hat{L}$ in the real space due to the derivatives. This is much simpler when the calculation is performed in the Fourier space where the derivatives are transformed in multiplications. We can apply $\hat{L}$ in the Fourier space and $\widehat{NL}$ in the real space if **Equation 5.21** is approximated by

$$A(x,y;z+\Delta z) = e^{i(\hat{L}+\widehat{NL})\Delta z}A(x,y;z) \approx e^{\hat{L}\Delta z/2}e^{\widehat{NL}\Delta z}e^{\hat{L}\Delta z/2}A(x,y;z) \quad \textbf{5.24}$$

Equation 5.24 is an approximated expression of **Equation 5.21** because the operators $\hat{L}$ and $\widehat{NL}$ do not commute. However, this approximation has an error of the order of $(\Delta z)^3$ which can be neglected for a sufficiently small Δz values. **Equation 5.24** can be understood as if each propagation step is divided in three sub-steps. First the field is Fourier transformed and linearly propagated half the step. Then, the field is inverse-Fourier transformed and nonlinearly propagated the full step. Finally, the beam is Fourier transformed again and linearly propagated the remaining half-step and inverse-Fourier transformed to the real space. Both field representations (real and Fourier spaces) are stored to avoid performing unnecessary Fourier transforms.

After the calculation of the step is finished, the program performs some tests to check the accuracy of the propagation step. First, it tests if the step size is correct. It does it calculating a second $A'(x,y,z+\Delta z)$ from the value in the previous step $A(x,y,z-\Delta z)$ and performing the propagation with a step size of double length $2\Delta z$:

$$A'(x,y;z+\Delta z) = e^{i(\hat{L}+\widehat{NL})2\Delta z}A(x,y;z-\Delta z) \quad \textbf{5.25}$$

Then, the program compares A and A':

$$h = \frac{\sum_{x,y}|A'(x,y)-A(x,y)|}{\sum_{i,j}|A(x,y)|} \quad \textbf{5.26}$$

If h is higher than a certain tolerance (typically 10^{-6}), the step is considered too large. Then, the program reduces Δz and recalculates the step again. On the other hand, if h is lower than a different tolerance ($\sim 10^{-8}$), Δz is considered to be too small and increased for the next step to reduce calculation time and memory usage.

Depending on the calculation parameters, it may happen that Δz has to be severely reduced. This can increase memory usage beyond the computer RAM memory, or requires a

calculation time similar to more complex models. If the program needs to use a Δz value smaller than a user-defined value ($\sim 10^{-10}$) the code stops the propagation of the field.

After testing Δz, the programs tests the representation field for aliasing in the same way performed before nonlinear propagation started. If the field is aliased in one of the representation spaces, the program solves it by increasing the resolution in real or Fourier space, as required. After the nonlinear propagation stage starts, the program shouldn't find aliasing in either space. If this happens, the program reduces Δz and recalculates the step. On the other hand, if the program finds the field far from being aliased, it reduces the mesh in order to reduce memory usage and calculation time for the next steps.

Propagation steps are performed as many times as needed until the field is propagated to the required depth inside the dielectric. Then, the program moves to the data post-processing and representation stages.

It is worth noting that the program allows the user the option of performing fast-Fourier transforms using Graphical Processing Unit calculations instead of CPU calculations to decrease computation time if the computer hardware and software allows it.

5.1.2.5. Extraction of relevant parameters

Relevant information regarding the beam propagation and parameters is extracted from the propagation data at certain steps. This is not performed in each one as this would increase the calculation time up to two orders of magnitude, depending on the simulation. Afterwards, intermediate values are obtained by interpolation.

Intensity. Most of the parameters are calculated from the spatial intensity distribution, which is calculated from the field as:

$$I(x,y;z) = \frac{n_0}{2\eta_0}|A(x,y;z)|^2 \qquad \textbf{5.27}$$

The program generates $X-Y$, $Z-X$ and Z–Y sections of the intensity distribution. As Δz, X and Y resolution may vary between propagation steps, the program necessarily needs to interpolate to generate the figures.

Radius. The program determines the radius of the beam at a given depth in two different ways. First, it interpolates the intensity matrix to increase the resolution and calculates the FWHM. Second, it calculates the first and second order momenta of the intensity:

$$C_x = \frac{\sum_{x,y} x\, I(x,y;z)dx\, dy}{\sum_{x,y} I(x,y;z)dx\, dy} \quad \textbf{5.28}$$

$$R_x(z) = \frac{\sum_{x,y}(x - C_x)^2 I(x,y;z)dx\, dy}{\sum_{x,y} I(x,y;z)dx\, dy} \quad \textbf{5.29}$$

(Similar expressions hold for C_y and R_y). For Gaussian beams, these first and second order momenta coincide with the beam center position and radii at $1/e^2$ in intensity.

Circularity. Circularity C of a Z-X or Z-Y distribution is defined as:

$$C = \frac{4\pi S}{\wp^2} \quad \textbf{5.30}$$

where S is the area of the region of a distribution equal or above a certain value (typically 1/2 or $1/e^2$ of the maximum value), and $\wp$ is its perimeter. The area is calculated using MATLAB function *bwarea* [14] and perimeter using the function *regionprops(perimeter)* [15].

Energy. The program calculates the loss of energy due to multiphoton absorption as:

$$\Delta E(z) = \sqrt{\frac{\pi}{2K}}\tau \left(\sum_{x,y} I(x,y;z-\Delta z)dx\, dy - \sum_{x,y} I(x,y;z)dx\, dy \right) \quad \textbf{5.31}$$

and

$$E(z) = E(z-\Delta z) - \Delta E(z) \quad \textbf{5.32}$$

The factor $\sqrt{\pi/2K}\,\tau$ is obtained from the integration of the field in the temporal dimension assuming a Gaussian profile, and taking into account that multiphoton absorption is proportional to I^K. Then, $\tau_{sq} = \sqrt{2\pi/K}\tau$. This is equivalent to define the duration of the square pulse τ_{sq} so the absorbed energy is the same as for a Gaussian pulse of pulse duration τ.

Free electron density. The electron density profile is calculated from the absorption of energy and is proportional to I^K:

$$\rho_e(x,y;z) = \frac{\Delta E(z)}{\Delta z K E_{ph}} \frac{I^K(x,y;z)}{\sum_{x,y} I^K(x,y;z)dx\, dy} \quad \textbf{5.33}$$

where E_{ph} is the energy of beam photons.

5.1.3. Alternative algorithms

The propagation algorithms described in the previous sections are very versatile, but under certain conditions it may be desirable to have alternative propagation algorithms. ABCD matrices algorithm can be used for calculating the propagation of strictly Gaussian beams under linear conditions. When no wavefront is introduced in the initial field, this algorithm is much faster than the air propagation algorithm based in operators described in **Section 5.1.2.2**. A second advantage is that it does not involve a discrete Fourier transforms, so it produces less aliasing problems. Also, it is useful to have an alternative algorithm for calculating the linear beam propagation inside the dielectric under non-paraxial conditions. It will be used in **Section 5.1.4.3** to test the behavior of the nonlinear propagation algorithm for moderate NA conditions.

5.1.3.1. ABCD matrices algorithm

Propagation of Gaussian beams can be calculated by using the ABCD matrices formalism [16]. However, the simulated beams are restricted to elliptical Gaussian beams whose wavefront is described by a curvature radius. For propagation in air, the ABCD propagation matrix is:

$$M_A = \begin{pmatrix} 1 & f' - d' \\ 0 & 1 \end{pmatrix} \begin{pmatrix} 1 & 0 \\ -1/f' & 1 \end{pmatrix} \begin{pmatrix} 1 & z_1 \\ 0 & 1 \end{pmatrix} \quad \textbf{5.34}$$

Using this algorithm for air propagation is very useful for simulations with initial beams with flat or focusing wavefronts for the reasons described above. After propagation in air using ABCD matrices, the user may choose to introduce the interface effects and calculating the propagation inside the dielectric using the nonlinear algorithm, or continuing with ABCD linear propagation algorithm:

$$M_D = \begin{pmatrix} 1 & z \\ 0 & 1 \end{pmatrix} \begin{pmatrix} 1 & 0 \\ 0 & n_O/n_D \end{pmatrix} \quad \textbf{5.35}$$

Using the ABCD algorithm for calculating the propagation inside the dielectric facilitates a rapid first guess of the intensity distribution in linear regime, as the calculations using this algorithm last ~5 seconds in an ordinary laptop.

5.1.3.2. High NA algorithm

Both the nonlinear and ABCD algorithms use the paraxial approximation. This “high NA” algorithm uses the equations described in [17] without the paraxial approximations

description. It calculates directly the propagation of the field from the initial beam in spherical coordinates through the lens and the dielectric. According to [17]:

$$A(x,y;z) = \frac{-i\,f k_t^2}{2\pi k_i}\iint \sqrt{\cos(\varphi_i)}\,\sin(\varphi_i)\,T(\varphi_i,\theta)A_{ini}(\varphi_i,\theta) \times e^{-1d[k_i\cos(\varphi_i)-k_t\cos(\varphi_t)]}e^{ik_t\cos(\varphi_t)z} \times e^{ik_O[x\cos(\theta)+y\sin(\theta)]\sin(\varphi_i)z}d\varphi_i d\theta \quad \textbf{5.36}$$

where k_t and k_i are the wavenumbers in the transmitted and incidence media, θ and φ are spherical coordinates and

$$T = \left\{\left[t_p\cos(\varphi_t)\cos^2(\theta) + t_s\sin^2(\theta)\right]^2 + \left[t_p\cos(\varphi_t)\cos(\theta)\sin(\theta) - t_s\cos(\theta)\sin(\theta)\right]^2 + \left[-t_p\sin(\varphi_t)\cos(\theta)\right]^2\right\}^{1/2} \quad \textbf{5.37}$$

is the transmission factor which accounts for Fresnel reflection.

5.1.4. Limits of the nonlinear propagation model

As described in **Section 5.1.1**, the nonlinear model makes use of several approximations which need to be carefully validated.

5.1.4.1. Slow varying envelope approximation and pulse broadening

SVEA assumes that the spectral content of the field is much narrower than the central frequency. This condition may be violated for very short laser pulses. During the development of this thesis, the shortest pulse duration used has been 100 *fs* at 800 *nm*, which corresponds to $\omega_0 = 2.4\times10^{15}\ rad/s$ and $\Delta\omega = 2.8\times10^{13}\ rad/s$, which can be considered to satisfy the condition.

Propagador also assumes that the pulse duration and spectrum are constant during propagation, but this depends on the irradiation and material parameters. Space-time focusing [18], self-phase modulation [19] or self-steepening [20] effects may occur, affecting the pulse duration and spectrum. The spectrum broadening due to self-phase modulation by propagating a distance L inside a dielectric is:

$$\Delta\omega = \int_0^L n_2 |\partial_t I|_{max} \frac{\omega_0}{c} dz \qquad \textbf{5.38}$$

For a Gaussian beam focused at $L/2$ depth inside a dielectric and ignoring further distortions due to other nonlinear effects, the spectral broadening is:

$$\Delta\omega = \frac{2 n_2 \omega_0 I_{max}}{\sqrt{e} c \tau} z_R \operatorname{atan}\left(\frac{L}{2 z_R}\right) \qquad \textbf{5.39}$$

where $z_R = n_0 \lambda / \pi NA^2$ is the Rayleigh length of the focused beam. For a pulse of 100 fs at 800 nm, maximum intensity of 4×10^{17} W/m^2 focused with a lens of 0.40 NA inside a material with n_0 = 1.55 and n_2 = 2×10^{-20} m^2/W, the resulting spectrum broadening for $L \gg 2z_R$ is $\Delta\omega \approx 2 \times 10^{12}$ rad/s. This broadening is not enough to violate the SVEA (it is only ~10% of the initial pulse spectrum width), so the calculated results should be sufficiently accurate. Space-time focusing of transform-limited pulses requires that self-phase modulation increases the pulse spectrum width before space-time focusing can shorten the pulse duration. With the negligible self-phase modulation values above considered, space-time focusing effects can be neglected.

Self-steepening [20] is an effect that may occur to laser pulses propagating in Kerr media. The temporal profile of the pulse is steepened by the effect of nonlinear refraction (similarly to the self-focusing effect produced in the spatial dimensions, **Section 2.1.2.2**), producing optical shocks. The characteristic distance of shock formation for a Gaussian beams is:

$$z_{SS} = 0.19 \frac{\tau c}{n_2 I} \qquad \textbf{5.40}$$

For the same parameters before indicated, the characteristic shock distance results in $z_{SS} \approx 700\ \mu m$. As the focal region (where the intensity is highest) is usually of a few microns, the conditions are far from SVEA violation.

5.1.4.2. Group velocity dispersion

GVD is an important effect for very short pulses, highly dispersive materials or long propagation distances [21]. If we take fused silica as an example, it has a GVD coefficient k'' = 36 fs^2/mm for 800 nm. The dispersive length (length for increasing pulse duration in ~40%) can be calculated as [5]:

$$L_{GVD} = \frac{\tau^2}{2k''} \qquad \textbf{5.41}$$

The shortest pulse duration used in this thesis is 100 fs, corresponding to a dispersive length of 13.9 cm. The considered depths have been shorter than 2 cm, much lower than L_{GVD}.

5.1.4.3. Paraxial approximation

Paraxial approximation allows transforming a second-order wave equation in Z dimension to a first-order equation (the NLSE), which greatly simplifies the calculations. However, it restricts the problem to relatively low NAs (low angles). It is possible to determine the range of NAs where this simplification can be made by comparing a set of simulations performed using *Propagador* (with nonlinear parameters set to zero to work in linear regime) with another set calculated using the high NA linear propagation algorithm described in **Section 5.1.3.2**.

Figure 5.5 shows the axial intensity profiles of the same beam for three different algorithms: the nonlinear algorithm (in linear regime: $n_2 = \beta_K = 0$), the high NA algorithm and the ABCD matrices algorithm that calculates the propagation not taking into account SA effects for a beam focused 0.5 mm below the surface. For NA = 0.05, the three algorithms show a similar result. The difference between them is below the resolution of the simulations. For NA = 0.10, nonlinear and high NA algorithms show a small broadening and a tiny shift of the focal region. Also, a small reduction in peak intensity due to the higher beam waist can be appreciated. For NA = 0.15 and NA = 0.20 this effect is more severe, and the shift is slightly higher for the high NA algorithm.

For NA = 0.25, the difference between nonlinear and high NA algorithms is more noticeable. For the high NA algorithm the main peak shift due to SA is higher ($\sim$2 μm) than for the nonlinear algorithm. Also, the modulations and asymmetries typical of intensity profiles with severe SA (see **Section 2.1.1.6**) start to be visible. For NA $\geq$ 0.30, the shift decreases for the nonlinear algorithm, becoming a shift towards the surface for NA = 0.40. This is not a real physical effect but an artifact, as shown by the high NA algorithm. The difference in the shift sign is produced by the combination of two effects: the tolerance in Δz had to be increased, and the paraxial approximation starts to be inaccurate. Anyway, the profiles generated by the nonlinear and the high NA algorithms are very similar, although shifted respect to each other.

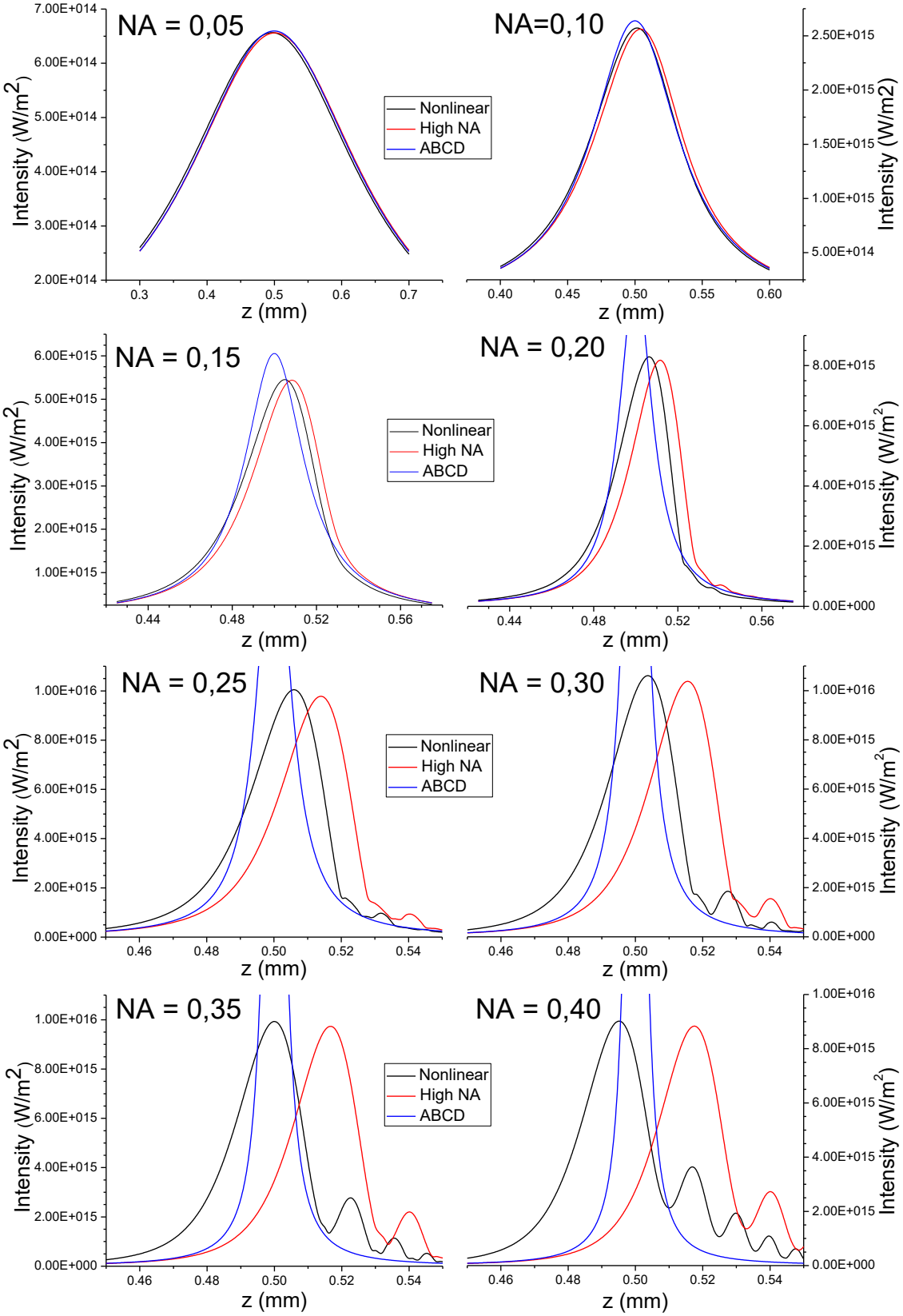

Figure 5.5: *Axial intensity profiles for a beam focused with different NAs calculated with three different propagation algorithms: the nonlinear algorithm (Propagador), and the two alternative algorithms (high NA and ABCD matrices). The parameters of the initial beam and setup are the following: Rx = Ry = 3.5 mm, E = 3 nJ, τ_{FWHM} = 100 fs, λ = 800 nm, n_O = 1, d = 0.5 mm and n_D = 1.55. Nonlinearities have been eliminated for the nonlinear algorithm by setting n_2 = 0 and β_3 = 0. Tolerances in the nonlinear algorithm had to be increased to 10^{-5} (NA = 0.30 and 0.35) and to 10^{-4} (NA = 0.40).*

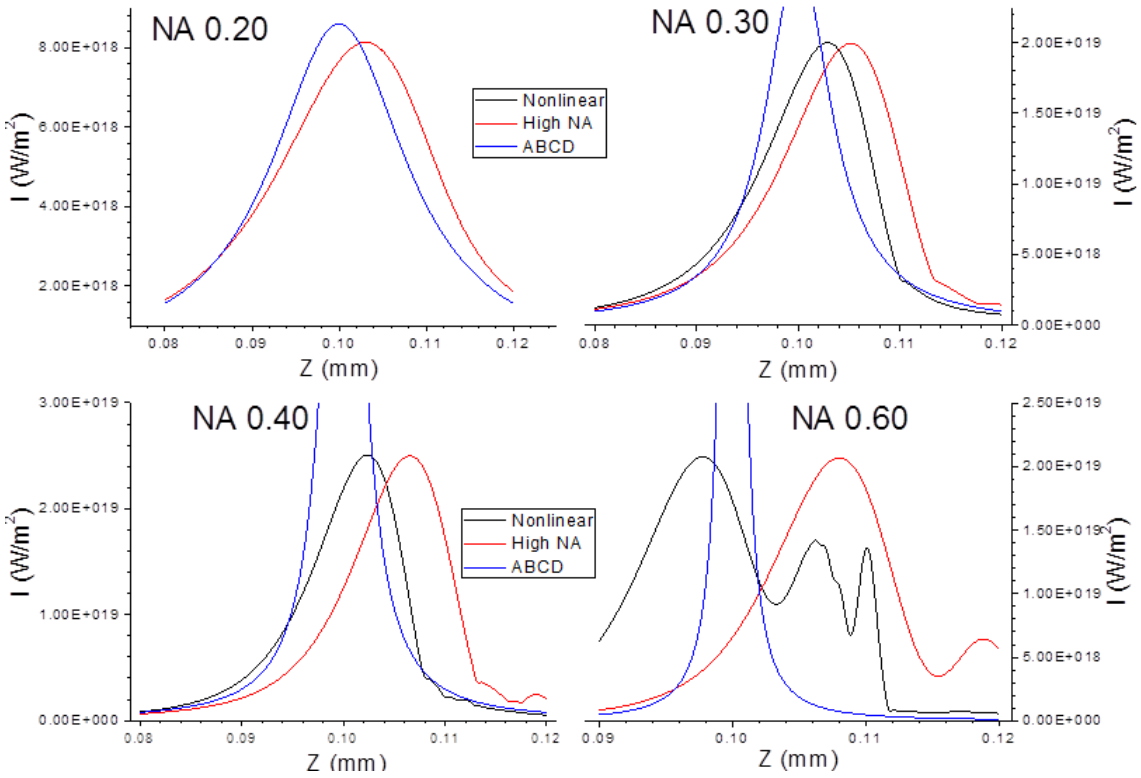

Figure 5.6: *Axial intensity profiles for a beam focused with different NAs calculated with three different propagation algorithms: the nonlinear algorithm (Propagador), and the two alternative algorithms (high NA and ABCD matrices). The parameters of the initial beam and setup are the same as in* ***Figure 5.5****, except that d = 0.1 mm.*

Figure 5.6 shows a set of simulations with parameters similar than those on **Figure 5.5** for a focusing depth of 100 μm. Due to the lower propagation distance, paraxial approximation holds almost perfectly for NA = 0.20. For 0.30 and 0.40 NAs the intensity profile using the nonlinear algorithm presents the same shape than the one calculated with the high NA model but with the maximum of the distribution shifted towards the surface. Finally, NA = 60 (a condition far from paraxial approximation) the intensity profile start to get severely distorted, and again wrongly shifted towards the surface. Due to the lower focusing depth, the effect of SA at 100 microns depth is in general less severe than for 500 microns.

In conclusion, paraxial approximation can be considered accurate for NAs lower than ~0.20 (the exact value depending on the propagation distance). Beyond 0.20, the intensity distributions calculated using the nonlinear algorithm can be considered reasonable, except for the shift in the peak intensity position, which may be inaccurate for higher NAs. For very high NAs (~0.60 or higher) the intensity profiles may be not only shifted, but also distorted. A secondary result that can be derived from these calculations is that SA limits the peak intensity that can be achieved upon beam focusing inside the material.

5.1.4.4. Multiphoton ionization

Nonlinear propagation algorithm approximates photoionization as a pure K-photon absorption process. Both processes were described in detail in **Section 2.2.2**. This section will analyze the limits of this approximation.

In the Keldysh formulation of photoionization, this approximation is valid when $\gamma \ll 1$, i.e., for fields with intensities below $\sim 10^{17}$ W/m^2 (the exact value depends on the material) [22, 23]. It is possible to extend the range of intensities where this approximation is valid by using a multiphoton absorption coefficient that depends on the local intensity. In practice, *Propagador* uses a constant multiphoton absorption coefficient. However, the user can introduce different coefficients for different pulse and/or focusing conditions to achieve better results. This will change the coefficient during the whole propagation. But as the absorption occurs mainly in the region where the intensity of the beam is higher (the focal region), the effect in the rest of regions will be small.

Figure 5.7 shows the result of fitting with *Propagador* the axial intensity profiles calculated using the full **Equation 5.1** in [24] for the propagation of laser pulses of different energies in fused silica. Here, different β_6 coefficient values have been used in order to obtain the best possible fit. It is important noting that this value is constant during the whole simulation and not intensity dependent. For pulse energies ≤ 0.50 μJ ($I_{max} < 5\times10^{17}$ W/m^2), the estimated absorption coefficient remains constant at a value of 5×10^{-83} m^9/W^6. For higher pulse energies, the absorption coefficient decays rapidly until reaching a nearly saturation value of 1×10^{-83} m^9/W^6. In conclusion, multiphoton ionization model remains valid for intensities lower than 5×10^{17} W/m^2. For higher intensities, the results calculated using

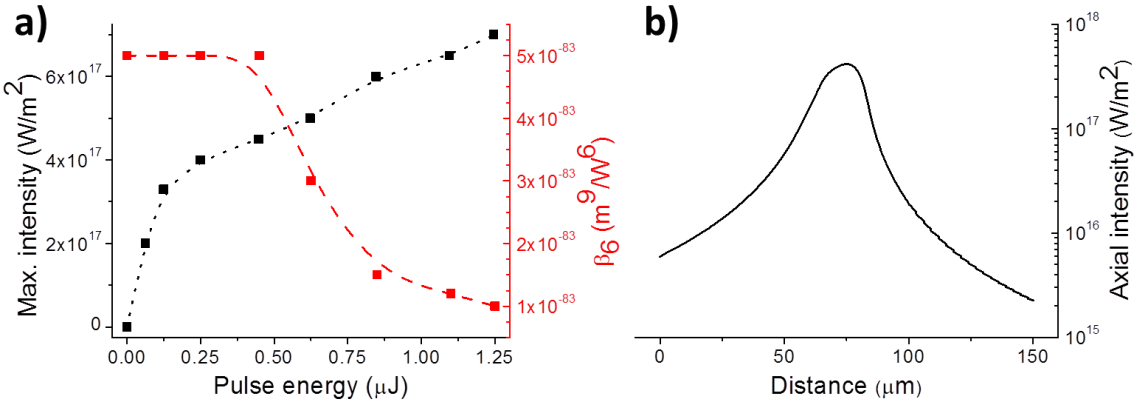

Figure 5.7: *Figure showing a set of simulations with a multiphoton absorption coefficient dependent of the intensity: (a) maximum intensity and absorption coefficient for different pulse energies, (b) axial intensity for a pulse of 0.25 μJ. The rest of the parameters are:* τ_{FWHM} *= 160 fs,* λ *= 800 nm, NA = 0.5, d = 75 μm,* n_D *= 1.45 and* $n_2 = 2.25\times10^{-20}$ m^2/W *(fused silica parameters). Dashed lines correspond to B-spline interpolation. Figure adapted from [1].*

Propagador start to be inaccurate.

Additionally, NLSE (**Equation 5.2)** neglects the avalanche ionization mechanism described in **Section 2.2.3**. Rethfeld and coworkers, using a multiple rate equations model, demonstrated that the transition between the multiphoton absorption dominated regime and avalanche dominated regime lies in the region where $I \times \tau_{FWHM}$ is ~10 J/cm^2 [25], the exact value being material dependant. For comparison, for the highest energy in **Figure 5.7** this parameter is exactly 11 J/cm^2, the region where approximating the rigorous Keldysh model with multiphoton ionization starts to be inaccurate.

5.1.4.5. Plasma defocusing

It is difficult to establish when plasma defocusing effects can be neglected. Using the Drude model, carrier excitation contributes to the refractive index as [26]:

$$\Delta n_e(\rho_e) = -\frac{2\pi q_e^2 \rho_e}{n_0 m_e^* \omega_0^2} \qquad \textbf{5.42}$$

q_e and m_e^* being the charge and effective mass of electrons, and ρ_e the excited electron density. ρ_e can be easily calculated for Gaussian pulses in a pure multiphoton absorption regime. Neglecting avalanche ionization and electron recombination:

$$\rho_e = \int_{-\infty}^{\infty} W_{MP} dt = \sqrt{\frac{\pi}{2K}} \frac{\tau}{K E_{ph}} \beta_K I_0^K \qquad \textbf{5.43}$$

I_0 being the maximum pulse intensity. As the ionization rate has been integrated for the whole pulse, electron recombination processes have been neglected, and Keldish ionization rate is equal or lower than the multiphoton ionization rate, the value of ρ_e calculated in **Equation 5.43** is an upper limit for the electron density. By substituting **Equation 5.43** in **Equation 5.42** and comparing it with the Kerr contribution to refractive index ($\Delta n_{NL} = n_2 I$), the intensity where both contributions cancel each other can be calculated:

$$I = \left(\sqrt{\frac{K^3}{\pi^3}} \frac{n_0 n_2 m_e \omega_0^2 E_{ph}}{\beta_K q_e^2 \tau} \right)^{1/(K-1)} \qquad \textbf{5.44}$$

For the experimental conditions in **Figure 5.7** using the highest value of β_6, the corresponding intensity is ~10^{19} W/m^2. This value is well above the intensity where the multiphoton ionization approximation remains valid (~5×10^{17} W/m^2). Therefore, neglecting

plasma defocusing effects can be considered valid below that limit. However, this "safe" value may be reduced when avalanche ionization severely dominates.

On the other hand, according to Brodeur and coworkers [19], the compensation of nonlinear refractive index ($n_2 I$) by electron plasma requires a carrier generation rate above $\gtrsim 10^{18}$ $cm^{-3}fs^{-1}$, with the exact value depending on the material bandgap, nonlinear refractive index and pulse wavelength. This rate is reached for intensities $\gtrsim 10^{17}$ W/m^2. These intensity values are only reached in the center of the focal region, so plasma defocusing may only slightly affect the energy deposition profile in our working conditions.

5.1.4.6. Conclusion

The limits of *Propagador* model have been thoroughly established. The SVEA is maintained in the conditions considered in this thesis (pulse duration higher than 100 fs, intensities lower than $\sim 5\times 10^{17}$ W/m^2). Paraxial approximation remains valid for NAs lower than $\sim$0.20 (the exact value depending on the propagation distance). For NAs between 0.20 and 0.60 the magnitude of the shift in the focal region calculated by *Propagador* due to SA is not accurate, but the shape of the intensity profile is similar to the ones calculated using more accurate models. In the case of NAs higher than 0.60, the intensity profile may be distorted as well. The multiphoton ionization approximation used by *Propagador* is valid for local intensities lower than $\sim 5\times 10^{17}$ W/m^2. Finally, plasma defocusing can be neglected for intensities lower than $\sim 10^{17}$ W/m^2. These high intensities are only reached in the focal volume, so it is still possible to use *Propagador* for most applications.

5.2. Influence of the nonlinear parameters

In this section the influence of the nonlinear parameters in the intensity and energy deposition profiles is briefly analyzed. In order to visualize better the role of n_2 and β_K, elliptical Gaussian beams will be used. The reason is that elliptical Gaussian beams (similar to slit-shaped beams) produce disk-shaped intensity distributions in the focal region (very useful for waveguide fabrication) where nonlinear effects can be more clearly seen. As a comment on the performance of *Propagador*, each simulation in this sub-section took an average of $\sim$100 seconds in an ordinary laptop.

5.2.1. Nonlinear refraction

Nonlinear refraction is governed by the nonlinear refractive index n_2. This parameter depends on the material and the wavelength. **Figure 5.8** shows several images of the intensity

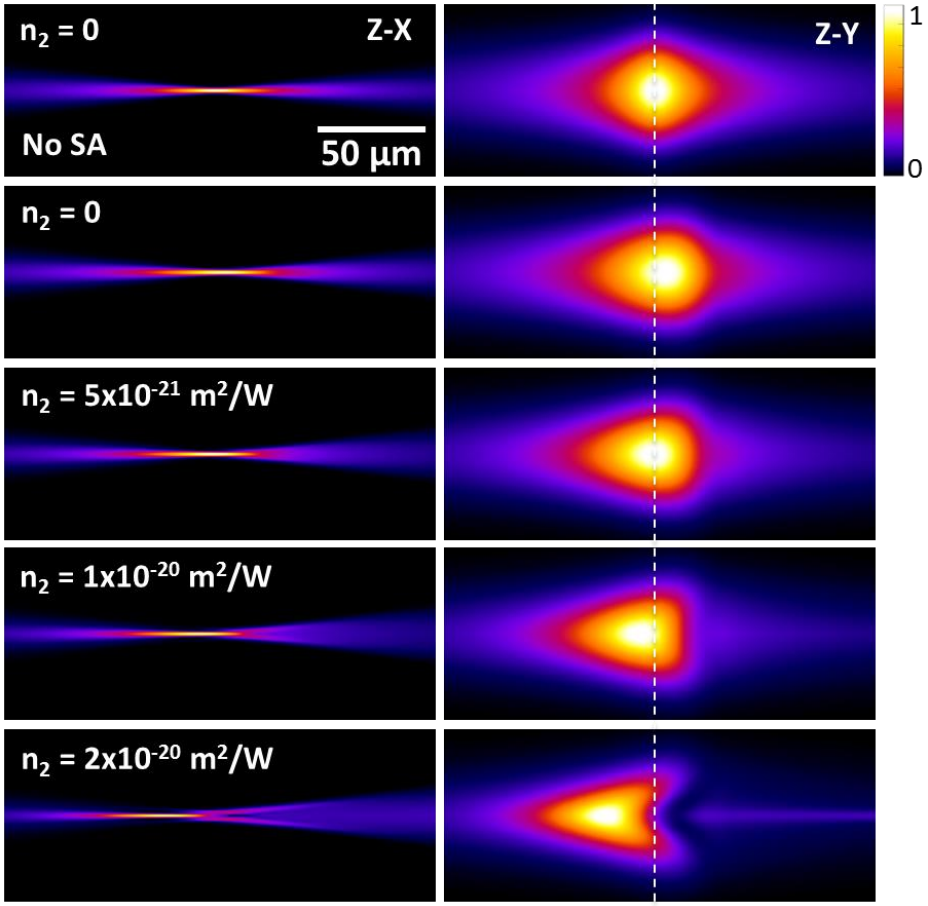

Figure 5.8: *Influence of n_2 in a disk-shaped intensity distribution at the focal region. The parameters of the initial beam and setup are the following: Rx = 3.5 mm, Ry = Rx/20, E = 3 μJ, τ_{FWHM} = 100 fs, λ = 800 nm, f = 20 mm (NA = 0.17), d = 0.5 mm and n_D = 1.55. The dotted white line represents the paraxial focal plane. All images are normalized to the global maximum.*

distribution in the focal region for different n_2 values. The differences between the simulation results are more distinguishable in the Z-Y plane. The first two rows show the intensity distribution upon linear propagation ($n_2 = 0$) with and without the SA effects. Without SA the distribution is a nearly circular disk. Introducing SA effects, the distribution slightly shifts inside the dielectric.

When nonlinear refraction is introduced, the shape of the distribution acquires a triangular shape, narrower in the vertical (Y) direction as n_2 is increased. Also, it is shifted towards the surface. Self-focusing (see **Section 2.1.2.2)** effects are clear for $n_2 = 2 \times 10^{-20}$ m^2/W. After the focal region, it can be appreciated the appearance of a filament where nonlinear refraction compensates diffraction and the beam propagates without diffraction.

5.2.2. Multiphoton absorption

Multiphoton absorption is described by two parameters: the number of photons involved in the process (K) and the absorption coefficient (β_K). **Figure 5.9** shows the influence of the multiphoton absorption coefficient in the absorbed energy distribution for K = 3 and K = 6. In both cases, multiphoton absorption causes pre-focal depletion: the energy of the pulse starts to be absorbed before reaching the focal region.

The first image has been calculated with a negligible β_K value of 10^{-99}. It serves as a reference. The rest of the images show the influence of β_K. The shorter tails towards the surface shows that the effect of pre-focal depletion is lower for K = 6 than for K = 3, i.e., the absorption of the pulse is more localized in the focal region. For K = 3, pre-focal depletion is so severe that the energy absorbed in the focal region starts to be reduced for the highest β_3, while for K = 6 it remains relatively constant for the different coefficient values ranging over two orders of magnitude. Also, pre-focal depletion is more localized in the center of the beam for K = 6 than for K = 3 (indicated by the narrower distributions and tails). These differences

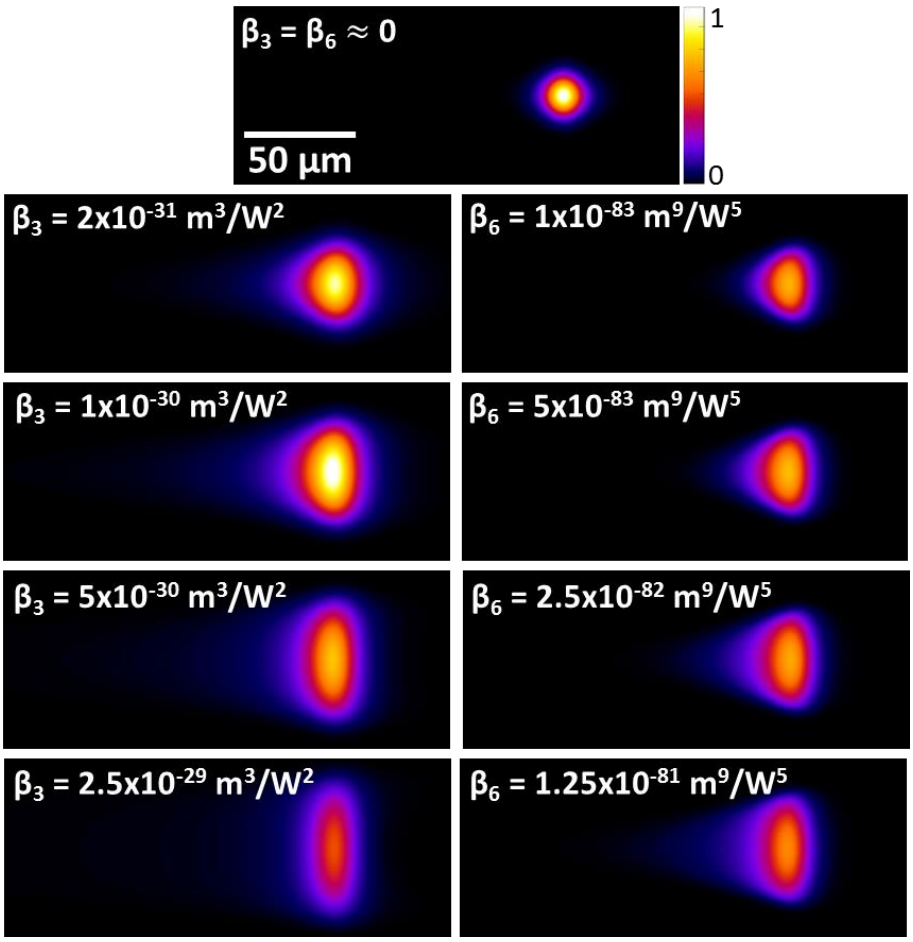

Figure 5.9: *Influence of β_K in a disk-shaped Z-Y energy absorption distribution in the focal volume. The parameters of the initial beam and setup are the same as in* ***Figure 5.8*** *(n_2 = 0). All images are normalized to the global maximum value, except the top one.*

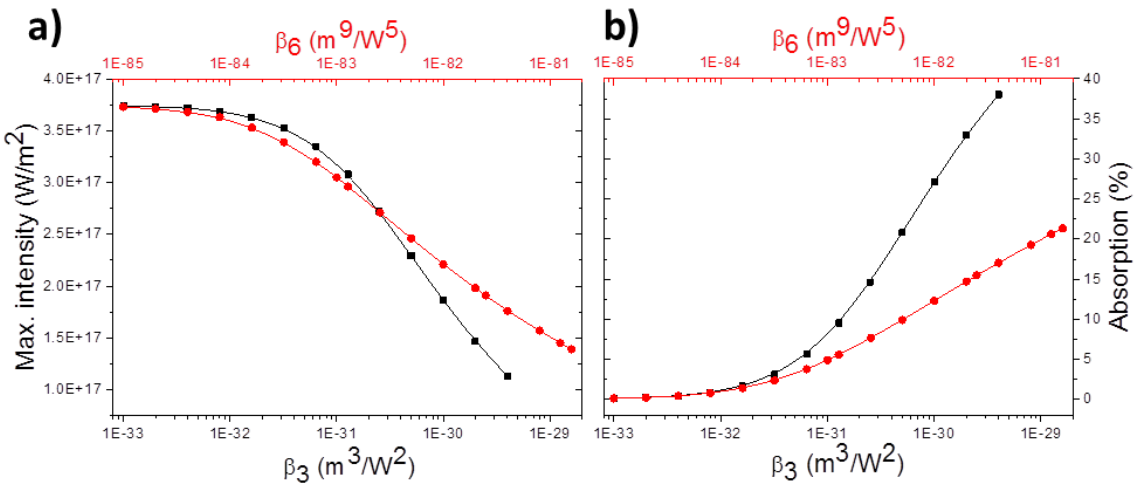

Figure 5.10: *Peak intensity (a) and fraction of absorbed energy (b) for β_3 (black) and β_6 (red). The rest of the parameters are the same as for* ***Figure 5.9****. Lines correspond to B-spline interpolation*

are caused by the dependence of the absorption with the power of the intensity (I^K). For K = 6, the absorption in the low intensity regions is many orders of magnitude smaller than for K = 3, so the absorption of energy is restricted to the regions with higher intensity: the focal region and the center of the beam.

Figure 5.10a shows the peak intensity achieved in the focal region as a function of β_3 and β_6. Horizontal scale is set so both curves cover four orders of magnitude. Initially, the peak intensity for K = 3 is higher than for K = 6 (the absorption in the focal region is higher for K = 6), but after a certain point the higher pre-focal depletion for K = 3 turns around the situation.

The fraction of energy absorbed by the material is shown in **Figure 5.10b**. For low absorption coefficients, the absorption is similar for both K values. However, as β_K value increases, the absorbed energy is much higher for K = 3 due to the higher fraction of energy absorbed before the focal region.

5.2.3. Combined effect of nonlinear refraction and absorption

In a real situation, both nonlinear refraction and multiphoton absorption play a significant role. **Figure 5.11** shows the intensity distributions for several combinations of nonlinear parameter values. The central image of each set has a combination of parameters where neither nonlinear refraction nor multiphoton absorption dominates in the energy deposition profile. The rest of the images show the intensity distribution when one of the coefficients is increased or decreased by one order of magnitude, so one effect dominates.

For a three-photon process, when both nonlinear effects play a significant role, the intensity distribution acquires a triangular shape (caused by nonlinear refraction as shown in

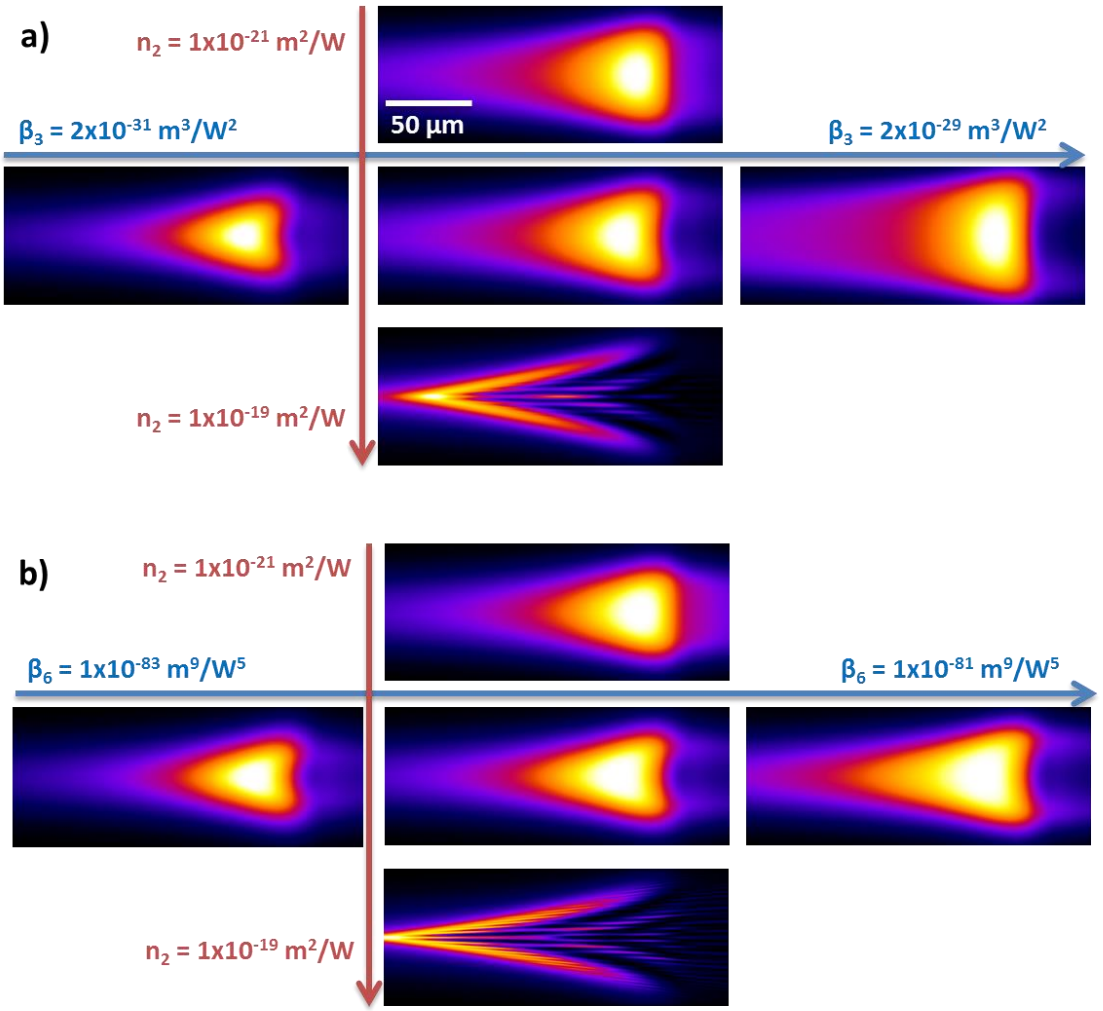

Figure 5.11: *Z-Y intensity distributions in the focal region for several combinations of n_2 and β_3 (a) or β_6 (b) values over two orders of magnitude. The rest of the parameters are the same than for* ***Figure 5.8****. All images are rescaled to their maximums. Figure partly adapted from [1].*

Figure 5.8) showing also pre-focal depletion effects. When n_2 is decreased by one order of magnitude, the intensity distribution is stretched towards the surface and slightly loses the triangular shape. When it is increased by one order of magnitude the distribution is heavily distorted looking like an arrow-head, it is shifted towards the surface by self-focusing, and shows multiple filaments. When β_3 is decreased by one order of magnitude, nonlinear refraction dominates and the intensity distribution is very similar to the ones in **Figure 5.8** where only nonlinear refraction was present, although showing a small amount of pre-focal depletion. On the other hand, when it is increased an order of magnitude the distribution shows severe pre-focal depletion and is stretched in the vertical direction.

The behavior for a six-photon process is similar. The most significant differences are the lower pre-focal depletion caused by the higher-order of the absorption process, and that the distribution starts to show the arrow-head shape that acquires for higher n_2. Increasing or

decreasing β_6 by one order of magnitude increases or decreases the effect of pre-focal depletion. However, the variation is smaller than for the three-photon process. In the case of n_2 the result is quite similar: a decrease of one order of magnitude smoothens the triangular shape and a similar increase produces again the arrow-head shape.

5.3. Determination of nonlinear coefficients

This section describes the use of *Propagador* to determine the nonlinear coefficients n_2 and β_K of dielectric materials by comparing simulated results with experimental ones. The computation time required for performing the simulations ranged between thirty seconds and five minutes.

5.3.1. Low intensity regime

Low intensity regime is referred to as the situation where the laser beam does not modify the structural or optical properties of the material but still nonlinear propagation effects are important. These are the ideal conditions for the use of Propagador, as nonlinear refraction and multiphoton absorption play a significant role, while the other neglected nonlinear effects do not.

In this sub-section, simulations performed by *Propagador* will be compared with experimental results and simulations calculated using more complex models [9, 27]. The simulated experiment is the formation of spatial solitons with circular [9] and elliptical [27] Gaussian beams. The spatial soliton is formed by the counteracting effect of nonlinear refraction and three-photon absorption.

Figure 5.12 shows the configuration of the experiment performed by Pasquazi and coworkers. They focused a Gaussian beam of 25 ps pulses at 820 nm on the surface of a 25 Nb_2O_5 – 25 PbO – 50 GeO_2 mol.% (NPG) nonlinear glass. Then, the beam travels the whole

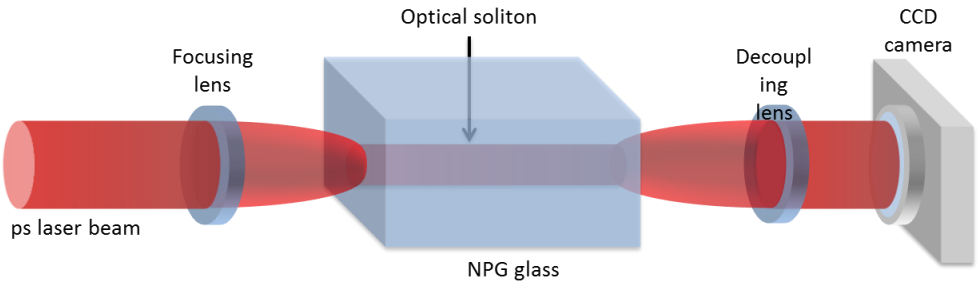

Figure 5.12: *Schematic representation of the experiment performed by Pasquazi and coworkers [8,26] for soliton shaping in a nonlinear glass. The laser beam is loosely focused at the surface of the glass and propagates through it. Then, the beam at the output facet of the sample is imaged by a CCD camera.*

length of the sample (5.7 mm) and an image of the intensity distribution of the beam at the exit facet of the sample is recorded with a microscope objective and a CCD camera.

5.3.1.1. Circular beam

The experiment with the circular beam was performed using different pulse energies. The beam was focused at the input glass facet with a beam waist (FWHM) of 22 μm. It was experimentally observed that for 2.8 μJ pulses, the output beam diameter was the same than that of the input beam. This means that an optical soliton was formed.

A set of preliminary simulations was first performed. The initial n_2 values were chosen in the range 10^{-18} – 10^{-19} m^2/W, as previously determined by four-wave mixing experiments [28]. The initial value of β_3 was estimated between 10^{-28} – 10^{-30} m^3/W^2 based on values measured in other nonlinear glasses of similar composition.

It was found that the result for 0.4 μJ was much more sensitive to n_2 than to β_3, which determined the strategy for fitting the experimental values. First, n_2 was calculated using only the lowest energy with an initial value of $\beta_3 = 10^{-29}$ m^3/W^2. Then, β_3 value was adjusted using the whole curve and maintaining a constant n_2 value. The mean square difference between calculated and experimental values was used as optimization parameter. Subsequently, n_2 was fitted using a constant value for β_3. The last two steps were repeated several times, resulting in $n_2 = (5.50 \pm 0.25) \times 10^{-19}$ m^2/W and $\beta_3 = (5.5 \pm 0.5) \times 10^{-28}$ m^3/W^2.

Figure 5.13a shows both experimental and calculated intensity distributions for different pulse energies, while **Figure 5.13b** shows the FWHM of the output beams. The formation of the soliton was observed at pulse energy of 2.8 μJ, the same as in the experiment. For 3.8 μJ, the beam was not anymore a Gaussian beam, presenting a ring surrounding the central lobe. This is reminiscent to the transformation of Gaussian beams to Gauss-Bessel beams by multiphoton absorption reported in [29]. This behavior is also reproduced by the simulations.

In [9] the authors obtained fit values of $n_2 = 5.5 \times 10^{-19}$ m^2/W and $\beta_3 = 3.0 \times 10^{-28}$ m^3/W^2 using a more complex model which includes the temporal dimension in the calculation. The value obtained using the simpler and faster model of *Propagador* is the same for n_2, and almost the double for β_3. It is common to find in the literature values for nonlinear parameters that differ by one or more orders of magnitude (as shown in [24] in the case of fused silica), so the difference between β_3 values can be considered as quite reasonable. Simulations using *Propagador* required 20 times less computation time than the more complex model. Even if small differences in the nonlinear parameters values are produced, the method is compatible

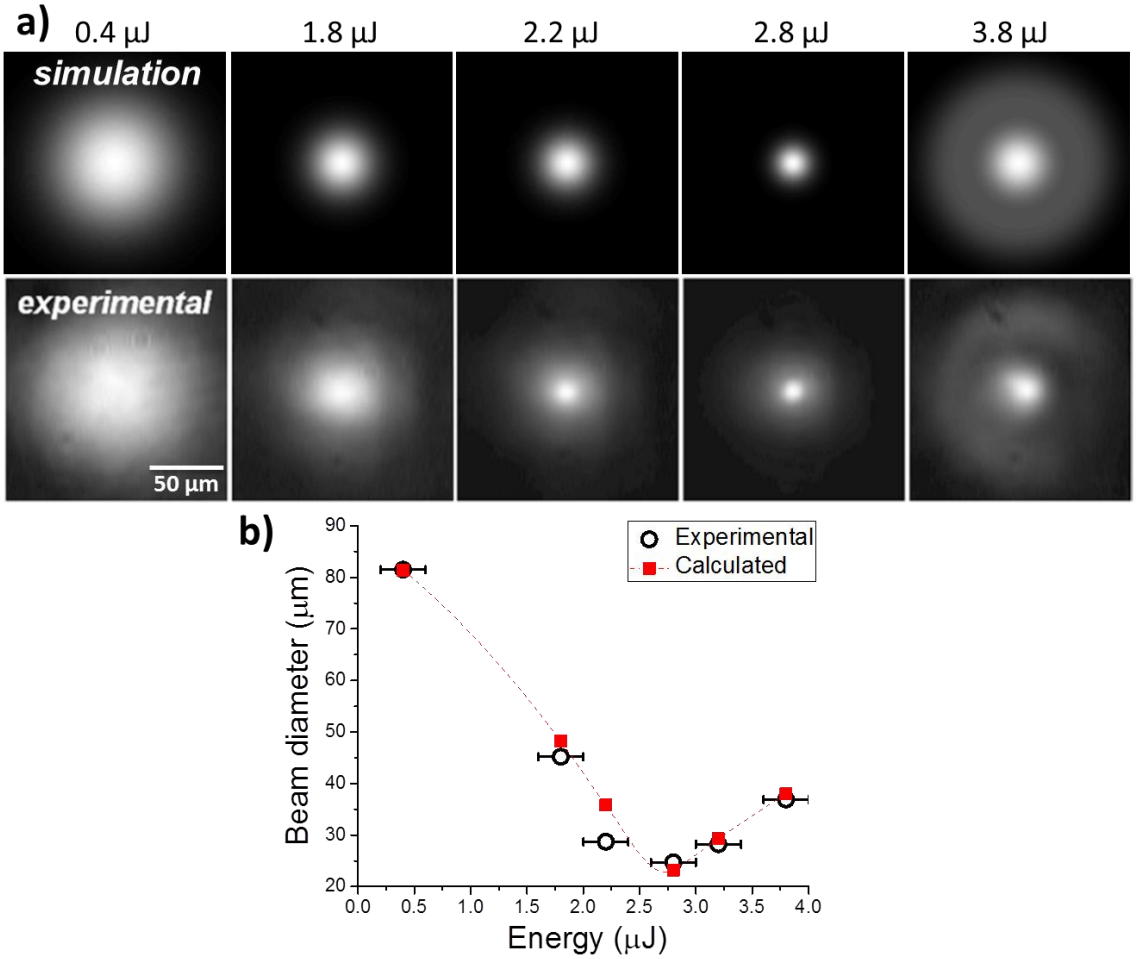

Figure 5.13: *(a) Comparison between experimental and calculated intensity profiles of the beam at the exit facet of the glass for different energies. (b) FWHM of the output beam as a function of pulse energy. The nonlinear parameters used are* $n_2 = 5.5\times10^{-19}$ m^2/W *and* $\beta_3 = 5.5\times10^{-28}$ m^3/W^2*. The dashed line is the Akima-spline interpolation of simulated data. Experimental data was taken from [8]. Figure adapted from [1].*

with the real time evaluation of the material parameters by the direct monitoring of beam reshaping at the output facet of the material.

5.3.1.2. Elliptical beam

In [27], Pasquazi and coworkers repeated the same experiment using an elliptical Gaussian beam of 130 × 13.5 μm waist (FWHM) at the entrance facet of the glass. They showed that for high pulse energies, the initially elliptical beam is split into several filaments. This is due to the appearance of modulation instabilities which act as precursor of multiple soliton formation [30].

Replicating this experimental effect is not possible using a perfect Gaussian intensity profile. This can be done in the simulations by introducing a pseudo-random noise source proportional to the intensity at the surface of the glass:

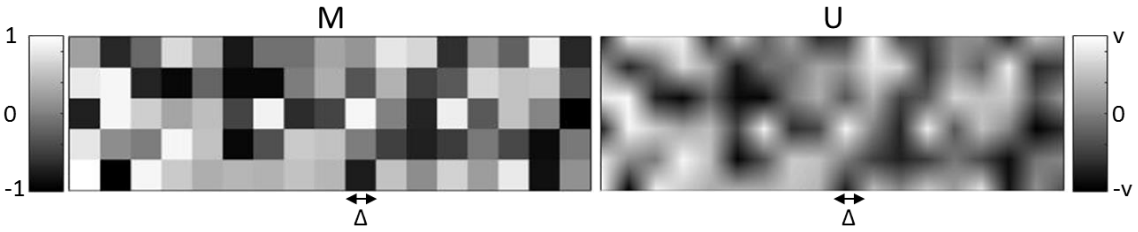

Figure 5.14: *Example of M and U matrices. Δ represents the space dimensions of M matrix elements, and u the amplitude of the U matrix.*

$$A_{noise}(x,y) = [1 + U(x,y)]A(x,y) \qquad \textbf{5.45}$$

$U(x,y)$ was generated in the following way. First, a pseudo-random matrix M of size S with values between -1 and 1 was created using MATLAB *rand(S)* function [31]. S was selected so each value in the matrix represented a spatial surface of size Δ^2 (higher than the surface represented by each element of the electric field matrix). Then, M was interpolated to have the same size as $A(x,y)$. Finally, M was multiplied by an amplitude constant v. This produced a pseudo-random U matrix with a value between $-v$ and v and an intrinsic dimension Δ. One example is shown in **Figure 5.14**.

It was found that U must have a v value higher than 0.05 and a Δ value higher than 5λ in order to replicate the experimental results. **Figure 5.15** shows the experimental and calculated intensity cross-section. The calculated intensity profile does not exactly correspond to the experimental profile, as thus depends on the exact values of the pseudo-random U matrix. However, the number of filaments, its shape and the mean separation between them is the same.

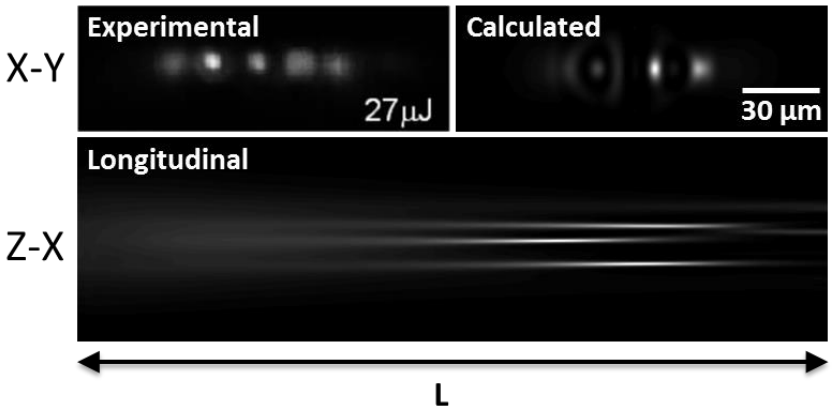

Figure 5.15: *Experimental and calculated transversal (X-Y) and calculated longitudinal (Z-X) intensity distribution profiles for the propagation of an elliptical beam in the NPG glass. Transversal images are represented with the same scale, longitudinal image size is 5700 × 145 μm. Proportions are not maintained to allow visibility. Experimental data were taken from [26]*

5.3.2. High intensity regime

In the high intensity regime, the laser produces the modification of the structural and/or optical properties of the material. In the previous section, the nonlinear parameters of a glass were determined by comparing simulations with nonlinear propagation experiments. In this sub-section, the simulations will be compared to microscopy images of the modifications produced in waveguide writing experiments using the slit shaping technique. In this case, the modification is not produced by a single pulse, but by the action of hundreds or thousands of pulses.

5.3.2.1. Post-irradiation modification in fused silica

The experimental irradiations were performed in fused silica (Schott, Lithosil). The waveguides fabrication is described in detail in [32]. They were produced using the sub-surface waveguide writing setup described in **Section 3.1.2.2** using the low repetition rate laser source (LS1). In this case, the inscribing beam was linearly polarized. The focusing MO had 20 mm focal length, and the sample was moved at a speed of 100 $\mu m/s$ for producing the waveguides.

The trans-illumination microscopy images of the produced waveguides are shown in the central columns of **Figure 5.16**, while the right columns show their guided modes at 633 nm. They show that for the same energy, increasing the writing depth stretches the energy distribution profile in the Z direction due to the higher influence of SA and self-focusing, producing an arrow-head shape. Reducing the slit width increases the height and reduces the length of the structure, despite the increase in pulse energy.

Left columns of **Figure 5.16** show the calculated energy deposition profiles for each waveguide. The energy absorption profiles for negligible nonlinearities and no SA are also shown for reference. Since the maximum intensity was lower than 3×10^{17} W/m^2, β_6 value was taken from **Section 5.1.4.4** (5.0×10^{-83} m^9/W^5). n_2 was used as an adjustable parameter in order to reproduce the characteristic shape of the transformed region. The best fitting value found was $n_2 = (7.5 \pm 2.5) \times10^{-21}$ m^2/W.

It is noticeable that the value determined for the nonlinear refractive index is lower than the reported values for the un-irradiated material, typically $2.0–2.5\times10^{-20}$ m^2/W [24, 33]. However, the fit value is perfectly consistent with the observations reported by Blömer and coworkers [34] in optical waveguides. Their measurements, based on self-modulation measurements during the propagation of fs-laser pulses in fs-laser written waveguides,

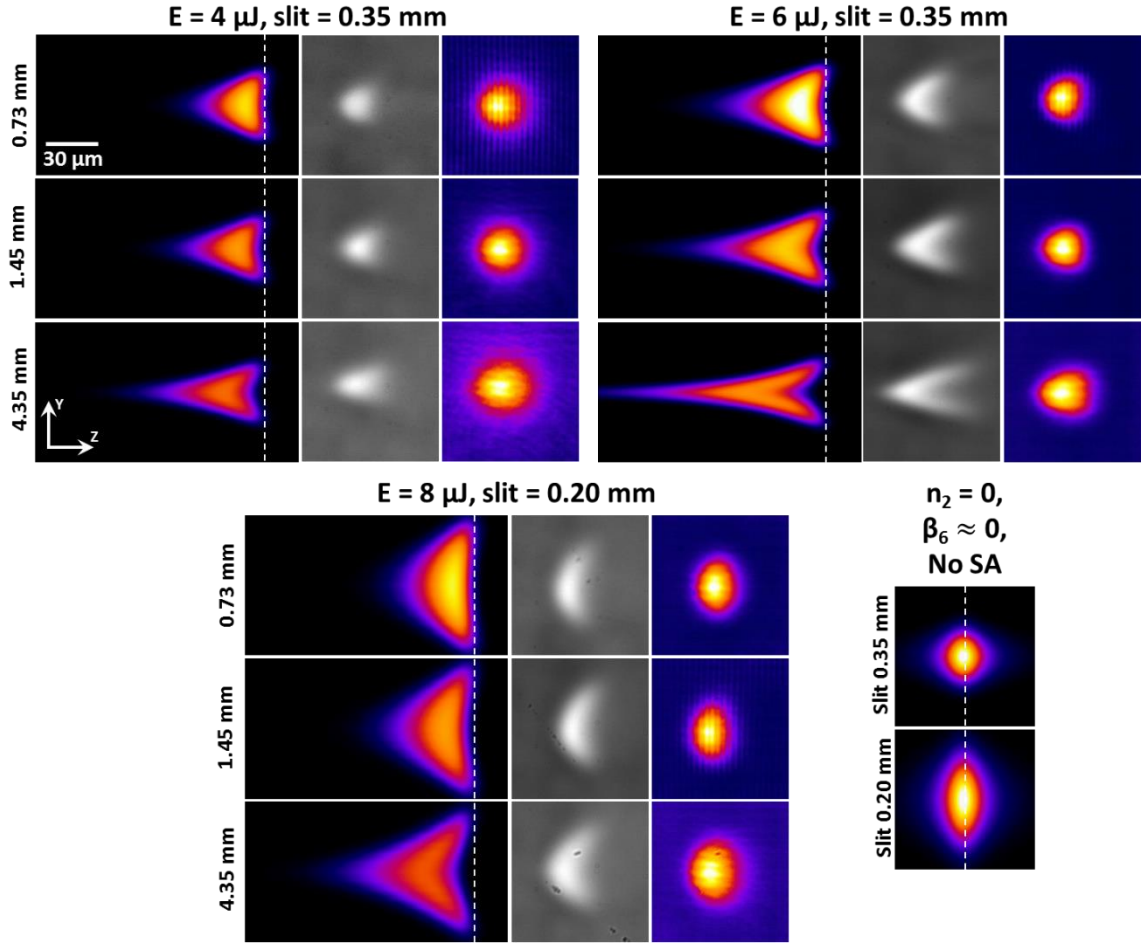

Figure 5.16: *(Central columns) Trans-illumination microscopy images of waveguides generated in fused silica upon irradiation with different pulse energies, depths and slit widths. Small asymmetries in experimental images may be due to a small tilt in the irradiating beam. (Right columns) Waveguides guided modes at 633 nm. (Left columns) Simulated energy deposition profiles. The dashed line represents the position of the paraxial focal plane. Fitting parameters are* $n_2 = 7.5\times10^{-21}$ m^2/W *and* $\beta_6 = 5.0\times10^{-83}$ m^9/W^5*. Tolerance in step size was increased to* 10^{-5} *for simulations of 4.35 mm depth. The laser is incident from the left. All simulation images are normalized to the maximum value, except the ones for* $\beta_6 \approx 0$*. Figure partly adapted from [1].*

showed a substantial decrease of n_2 in the laser irradiated material, up to a factor ~4 for the maximum dose analyzed. The fit value (reduced by a factor of ~3) is consistent with their work. It is worth noting that all the irradiations were performed at 100 µm/s (a velocity typical of waveguide writing at low repetition rate regime), resulting in ~30 pulses per focal volume. In case that different irradiations are used, the factor between both values of n_2 will probably change. Additionally, the simulations show that this reduction in n_2 is not an after-effect, it occurred during the interaction as it conditioned the energy deposition profile during the writing process.

It is important noting that these simulations are above certain discussed limits for neglecting plasma defocusing effects. In the simulations, the highest free-electron density is

$\sim 10^{21}$ cm^{-3}, with a generation rate of $\sim 10^{19}$ $cm^{-3}fs^{-1}$. These values are consistent with experimental measurements from plasma densities generated in waveguide writing conditions [35]. However, even if the electron ionization rate exceeds the plasma defocusing limit determined by Brodeur and coworkers (10^{18} $cm^{-3}fs^{-1}$, see **Section 5.1.4.5**), simulations and experimental results show an excellent agreement. There may be several reasons for this agreement. On one hand, the highest electron densities are reached in the focal region, where the beam is strongly depleted by nonlinear absorption, reducing the effects of plasma defocusing. Also, plasma build-up time could soften plasma defocusing effects to some extent, while dynamical nonlinear refractive index changes, as observed in these simulations, dynamically affect the carrier generation rate. Anyway, the results derived from these simulations show that for elliptical beams, *Propagador* model may suffice for determining nonlinear parameters of materials and predicting energy deposition profiles under waveguide writing conditions at low repetition rate.

5.3.2.2. Post-irradiation modification in phosphate glass

The same procedure was repeated for waveguides produced in phosphate glass (Kigre, MM2). They were inscribed similarly as in the previous section but with a constant slit width of 0.35 mm as described in [36]. **Figure 5.17a** shows the trans-illumination images of several waveguides. Two modification regimes can be appreciated. The bright white regions correspond to the region of higher absorbed energy, and have a positive Δn. On the other hand, the dark regions surrounding the bright ones are formed where less energy is absorbed, and have negative Δn. These regions show irregular profiles, and are probably formed by the generation of defects.

Waveguides produced with linearly polarized 110 fs pulses and three different pulse energies are shown in **Figure 5.17a1-3**. The size of the modification slightly increases with the energy, and a second small lobe appears before the main lobe. Increasing the pulse duration to 260 fs (**Figure 5.17a4-6**) reduces pre-focal depletion effects. This can be appreciated by the severe reduction of the black regions which appear before the focal region and the increase of width of the structures (and energy deposition profiles). This decrease of pre-focal depletion has a second effect: the absorbed energy in the focal region is strongly increased. This can be clearly appreciated in the simulations. Also, the higher amount of absorbed energy weakens the glass structure, which chips upon polishing, as shown in **Figure 5.17a5-6.**

Increasing the depth of the structure (**Figure 5.17a7**) stretches the modified region in the beam propagation direction. This is due to the higher influence of nonlinear refraction and

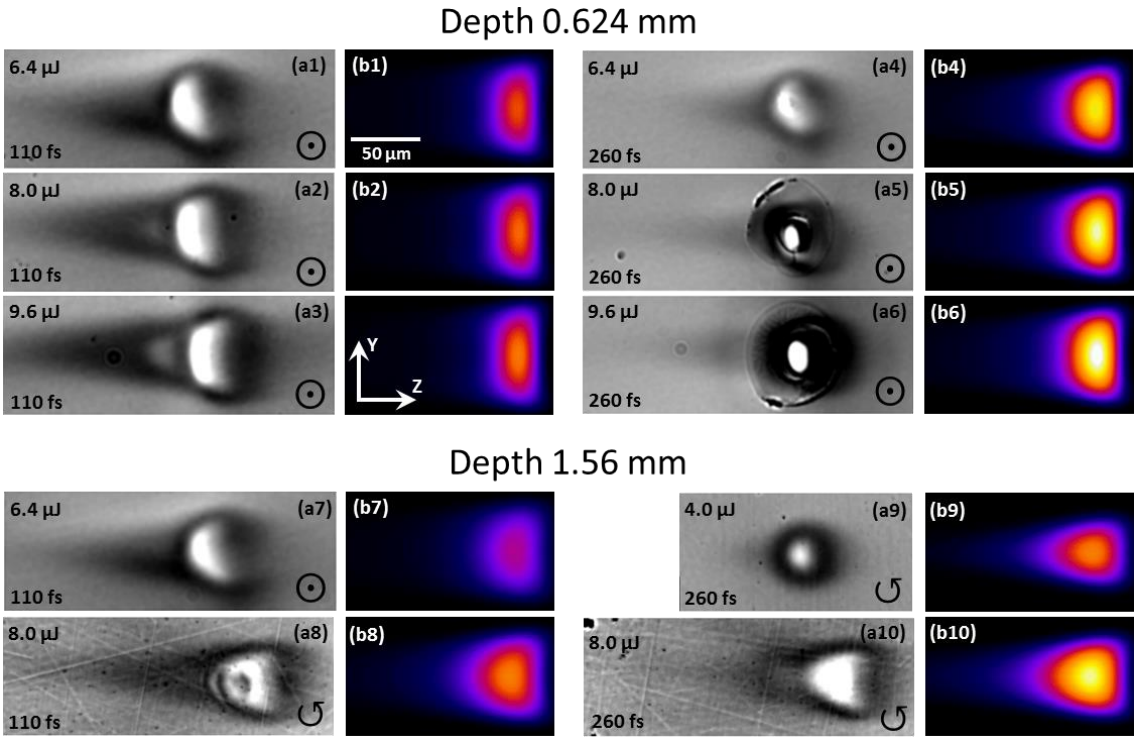

Figure 5.17: *Trans-illumination microscopy images (a) and calculated energy deposition profiles (b) for several waveguides produced in phosphate glass. Pulse energy, pulse duration and beam polarization (⊙ = linear, ↺ = circular) are shown in each waveguide image. Asymmetries in experimental images may be due to a small tilt in the irradiating beam. Nonlinear fit parameters are of* n_{2L} *= 1.1×10*$^{-20}$ *m*^{2}*/W and* β_{3L} *= 4.0×10*$^{-29}$ *m*^{3}*/W*^{2} *for linear polarization and* n_{2C} *= 7.3×10*$^{-21}$ *m*^{2}*/W and* β_{3C} *= 1.0×10*$^{-29}$ *m*^{3}*/W*^{2} *for circular polarization. The laser is incident from the left. All simulation images are scaled to the global maximum value. Figure partly adapted from [1].*

SA, as in fused silica. Changing linear polarization to circular (**Figure 5.17a8-10**) produces less pronounced modifications, as the contrast of the images must be highly increased in order to visualize the waveguides.

The initial simulations were performed only for waveguides inscribed with linearly polarized beams. The initial value for n_{2L} was 5.85×10^{-20} m^2/W, reported in [35] for un-irradiated phosphate glass. The initial value for β_{3L} was 10^{-30} m^3/W^2. The fitting process produced values of $n_{2L} = (1.1 \pm 0.3) \times 10^{-20}$ m^2/W and $\beta_{3L} = (4.0 \pm 1.0) \times 10^{-29}$ m^3/W^2. The obtained value of n_{2L} for waveguides is again lower than for un-irradiated material, by a factor ~5 in this case (again, it is probable that different scanning velocities and/or laser repetition rates would result in different factors). This indicates that the reduction in n_2 upon multiple laser pulses exposure also occurs in phosphate glass.

In isotropic media, nonlinear refractive index is lower for circularly polarized beams by a factor of 1.5 [37]. This relation was preserved in the simulations for circularly polarized beams, using $n_{2C} = 7.3 \times 10^{-21}$ m^2/W as a fixed parameter and β_{3C} as an adjustable parameter. The obtained result is $\beta_{3C} = (1.0 \pm 0.3) \times 10^{-29}$ m^3/W^2, showing a decrease by a factor of ~4

with respect to the linear polarization case. This reduction in the multiphoton absorption coefficient for circular polarization has been reported by Temnov and coworkers upon fs-laser irradiation of crystalline and amorphous dielectrics when $K \leq 4$ [38].

5.4. Wavefront design

In the previous section it has been shown that it is possible to determine the nonlinear refractive index and multiphoton absorption coefficient of a given material by comparing simulations performed by *Propagador* with experimental results of irradiation experiments. This information can be used to design wavefronts that modify the energy deposition profile producing advantageous situations, for example, in waveguide writing. In this section, two examples of wavefront design are shown.

5.4.1. Pre-compensation of nonlinear distortions

As shown in **Sections 5.2.3** and **5.3.2.1**, SA, nonlinear refraction and absorption distort the circular disk intensity distribution that can be produced by slit shaping in the linear regime. However, it may be possible to pre-compensate the nonlinear distortions by shaping the beam wavefront.

One method for calculating a pre-compensating wavefront is using *Propagador* simulations and an optimization algorithm which varies the wavefront in a base of Zernike polynomials. Using a whole set of Zernike polynomials for describing the wavefront is highly computationally costly, even with the low calculation time achieved by *Propagador*. In order to reduce calculation time and show the capabilities of the method, only one polynomial was used: first-order spherical aberration ($P_8(r) = Z_8(6r^4 - 6r^2 + 1)$). It was shown in **Section 5.2.1** that SA modifies the intensity distribution profile in a way similar to nonlinear propagation for low energies, so wavefronts with negative values of Z_8 may approximately pre-compensate nonlinear distortion. The reference radius of the polynomial was set as the beam radius.

The optimization parameter used was circularity (c) at half-maximum level for the Z-Y energy deposition profile, as defined in **Equation 5.30**. Mathematically, c value is 1 for a perfect circular profile, and lower otherwise. In the case of discretized profiles, c can reach values above 1, as perimeter and surface cannot be perfectly determined.

The first and third columns of **Figure 5.18** show the absorbed energy distributions for irradiations calculated using the same setup and material parameters calculated in **Section**

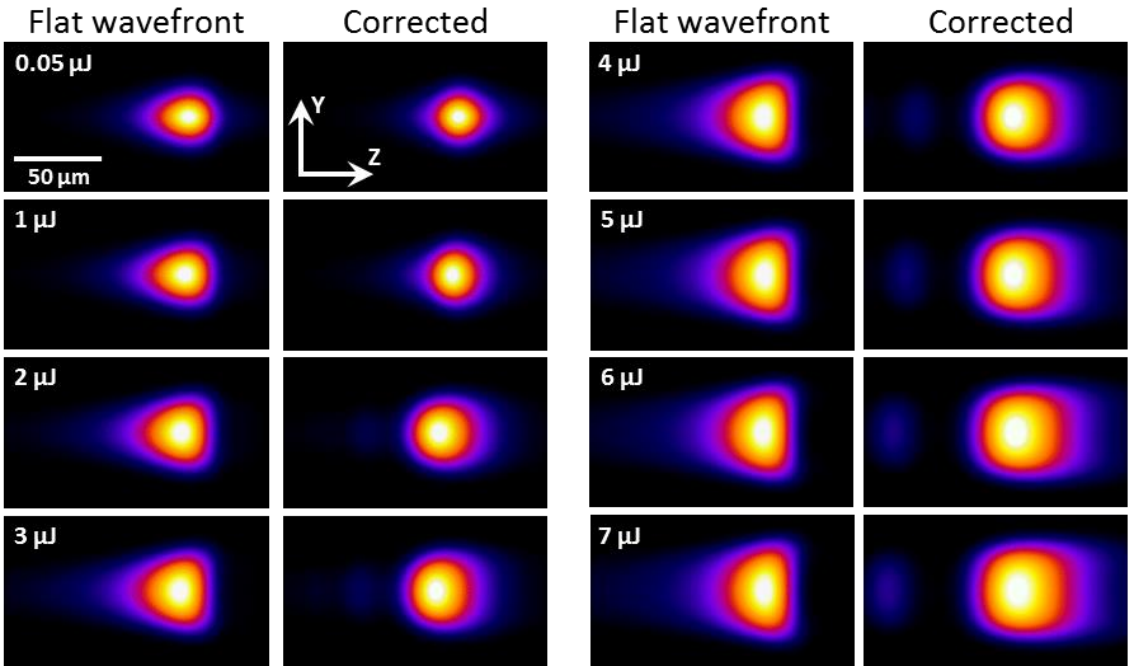

Figure 5.18: *Uncorrected (first and third columns) and corrected (second and fourth columns) energy deposition profiles for several pulse energies of slit-shaped beams beams of 260 fs and circular polarization in phosphate glass. The correction is performed introducing first-order SA. The coefficients are plotted in* ***Figure 5.19****. The laser is incident from the left. All simulation images are scaled to their maximum.*

5.3.2.2, with pulses of 260 fs and circular polarization focused 0.5 mm inside the material. For the smallest energy, the nonlinear effects are negligible, and the small asymmetry in the Z direction is due only to SA. As pulse energy increases, the distribution is stretched in the Y direction and acquires a triangular shape.

Second and fourth columns show the result of the correcting beam wavefront to generate circular distribution. The correcting amplitude Z_8 parameters are shown in **Figure 5.19a**. Their uncertainty is calculated as the range of Z_8 parameters for with $c \geq 1$ if it reaches values higher than 1, or where it decreases 0.005 from the maximum c value otherwise. For 0.05 μJ, the correction corresponds to the pre-compensation of SA. In the case of 1 and 2 μJ, the corrected distribution shows a nearly perfect circular profile. For higher energies, the distribution starts to acquire a squared shape, more clearly visible for the highest energies. The correction values can be fitted to the line $Z_8 = mE + b$. The result is m = -8.44 $\pm$ 0.68 $nm/\mu J$ and b = -2.9 $\pm$ 2.1 nm (R-square of the fit is 0.957). It is worth noting that even if the amplitude of the coefficients is small, the fourth power of the polynomial increases significantly its influence.

Figure 5.19b shows the circularity of the uncorrected and corrected distributions. The uncorrected c values remain below 1 even for the smallest pulse energies, but this simply shows that the used slit is not optimal for producing a circular shape at half maximum value of

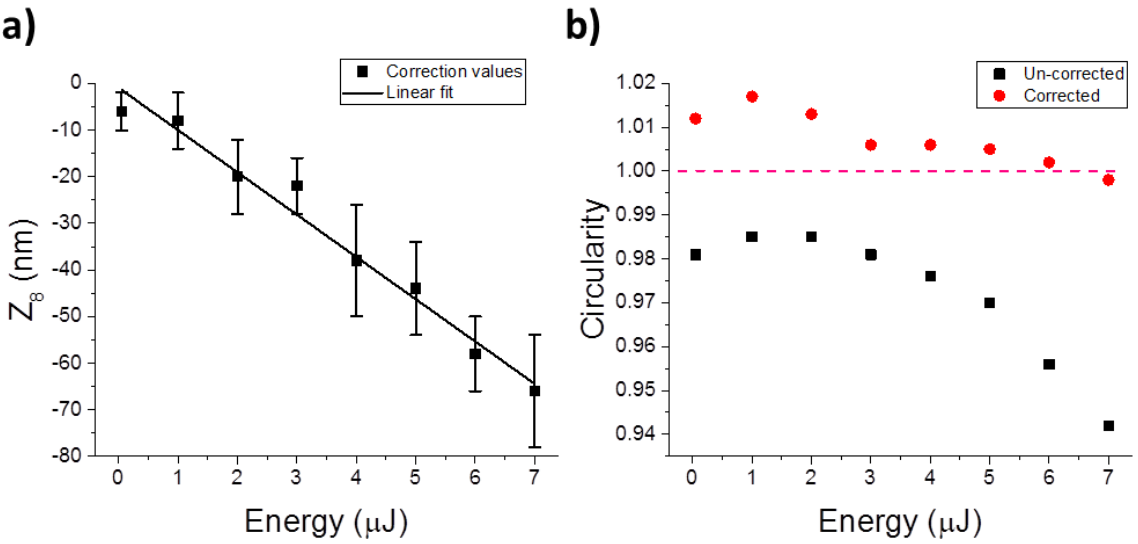

Figure 5.19: *Correction parameters (a) and un-corrected and corrected distributions circularity (b). Dashed red line marks the theoretical maximum circularity of 1 for a circle.*

ΔE. The circularity increases for 1 and 2 μJ, as gentle nonlinear effects improve the circularity of the distribution. For higher energies, the circularity decreases in an almost parabolic trend.

For the corrected distributions, the highest circularity values are achieved for the lowest energies. In the case of pulse energies below 3 μJ, the corrected result shows an excellent visual appearance. For higher energies, the corrected distribution starts to show a squared-shape, decreasing the maximum obtained circularity. However, in all cases the circularity is greatly improved.

The great improvement in c using only one Zernike coefficient shows the capabilities of the method. Nearly perfect circularity is achieved for energies lower than 3 μJ, while for higher energies the result may be good enough to be used in waveguide writing. If higher circularity is required, more Zernike polynomials could be used, or alternatively the reference radius could be introduced as an adjustable variable. Also, a more precise parameter than circularity at half maximum may help to obtain better results.

5.4.2. "Exotic" energy deposition profiles

Despite the usefulness of using *Propagador* for determining the nonlinear parameters of dielectrics or pre-compensating the distortion produced by nonlinear effects in intensity distributions, the capabilities of the program go well beyond it. *Propagador* can also be used to simulate irradiation situations with ad-hoc wavefronts and design energy deposition profiles for numerous applications.

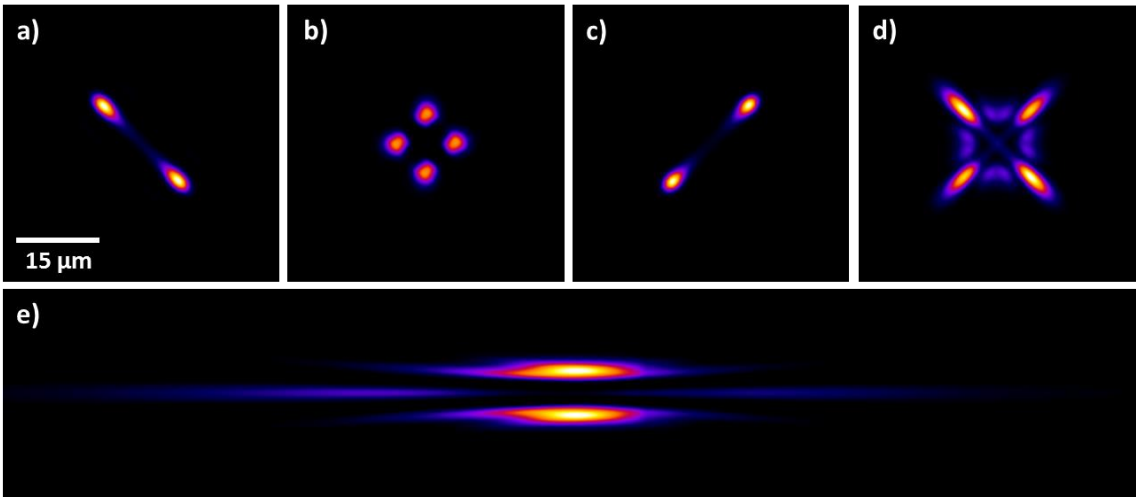

Figure 5.20: *Figure showing $X-Y$ energy deposition profiles at 0.4 (a), 0.5 (b) and 0.6 (c) mm depth. Image d shows the integration of ΔE in the Z direction. Image e shows the $Z-X$ ΔE distribution from 0.3 to 0.7 mm depth. Images in (a-c) are scaled to their maximum value during the propagation, (d-e) to their maximum values. The size of the image in (e) is 400×50 µm. Figure partly adapted from [2].*

Figure 5.20 shows an example of an exotic energy deposition profile. **Figure 5.20a-c** show the $X-Y$ cross sections of the energy deposition profile at 0.4, 0.5 and 0.6 mm depth. This profile was achieved using a spatial wavefront distribution $\varphi(r,\theta) = Z_{14}(10r^4 - 12r^2 + 3)r\ sin\theta$ with Z_{14}= 1 μm and R_{ref} = 12.5 mm. The setup and material conditions are same as for the previous section, except that no slit is used.

Figure 5.20a shows the ΔE cross-section at 0.4 mm of depth. It shows two spots of high absorption. **Figure 5.20c** (0.6 mm depth) is almost similar, rotated 90° and slightly decreased in value. **Figure 5.20b** (0.5 mm depth) shows four points of lower absorbed energy in a diamond configuration. **Figure 5.20d** shows the integration of the whole ΔE distribution along the Z dimension. It has four high absorption points in a square configuration, corresponding to the absorption of energy at 0.4 and 0.6 mm.

This may be a useful energy deposition profile for waveguide writing at low repetition rate. It could be used in materials where the refractive index is decreased upon laser irradiation. Moving the sample in the Z direction, the modified profile may be similar to **Figure 5.20d**, creating four tracks of decreased refractive index, leading to light guiding in the central region. Similar structures are shown in **Section 2.6.2**, with the difference that this waveguide would be produced with a single irradiation scan instead of several ones.

5.5. Summary and conclusion

Propagador is a simulation tool capable of calculating the propagation of Gaussian ultrafast laser pulses with arbitrary wavefront inside dielectric materials, including spherical aberration (SA), nonlinear propagation and multiphoton absorption effects. The main advantage of this model is a severe reduction in the calculation time required to perform the calculations, to the order of few minutes in an ordinary computer. The conditions where this formalism can be used have been thoughtfully analyzed. In order to confirm the validity of the model, calculations were successfully compared to experimental results in NPG, fused silica and phosphate glasses.

Propagador was used for determining the nonlinear parameters of different materials by comparing simulations with experiments. The first experiment consisted on the propagation of ps-laser pulses at 820 nm in NPG glass. The output beam diameter at different pulse energies was compared with the simulations, obtaining $n_2 = 5.5\times10^{-19}\ m^2/W$ and $\beta_3 = 5.5\times10^{-28}\ m^3/W^2$. The obtained values coincide more than reasonably with the results obtained by other groups using more complex models. In the second case, the calculated energy deposition profiles were compared with waveguides produced by fs-laser irradiation at low repetition rate. This allowed determining $n_2 = 7.5\times10^{-21}\ m^2/W$ and $\beta_6 = 5.0\times10^{-83}\ m^9/W^5$ for fused silica and $n_2 = 1.1\times10^{-20}\ m^2/W$ and $\beta_3 = 4\times10^{-29}\ m^3/W^2$ for phosphate glass. These values were lower than the typically reported ones by a factor of ~3-5. This effect has been previously observed in repetitively irradiated materials. As this effect is reproduced by the simulation, it indicates that the reduction in the nonlinear parameters occurred during the irradiation. Also, a reduction in both nonlinear parameters for waveguides performed with circularly polarized beams is deduced from the simulations, n_2 in a 2/3 factor (predicted for isotropic mediums), and β_3 in a factor of ~4 when compared to the linearly polarized case. This demonstrates the feasibility of calculating energy deposition profiles in waveguide writing conditions (at low repetition rate). **Section 6.1** shows an example of the application of *Propagador* to help finding the right irradiation conditions in sub-surface waveguide writing experiments.

Finally, *Propagador* was used for designing wavefronts capable of modifying the energy deposition profile in desired ways. In waveguide writing at low repetition rate, it is desirable to produce circularly shaped energy deposition profiles. These energy deposition profiles can be easily tailored in linear regime (for example by using slit-shaped beams), but nonlinearities and SA distorts them. The code was used for increasing the circularity of the energy deposition profiles by pre-compensating the nonlinear distortion by modifying the

beam wavefront. In this case, negative first-order SA was used. Finally, an exotic energy deposition profile based in a higher order Zernike polynomial was analyzed. This energy deposition profile could potentially be used to produce a Type II modification based waveguide with a single scan.

5.6. References

[1] J. d. Hoyo, A. R. de la Cruz, E. Grace, A. Ferrer, J. Siegel, A. Pasquazi*, et al.*, "Rapid assessment of nonlinear optical propagation effects in dielectrics," *Scientific Reports,* vol. 5, p. 7650, 2015.

[2] J. Hoyo, M. Galván-Sosa, A. Ruiz de la Cruz, E. J. Grace, A. Ferrer, J. Siegel*, et al.*, "Modeling of single pulse 3-D energy deposition profiles inside dielectrics upon fs laser irradiation with complex beam wavefronts," 2014, pp. 91310G-91310G-8.

[3] A. Couairon, E. Brambilla, T. Corti, D. Majus, O. de J. Ramírez-Góngora, and M. Kolesik, "Practitioner's guide to laser pulse propagation models and simulation," *The European Physical Journal Special Topics,* vol. 199, pp. 5-76, 2011.

[4] L. Sudrie, A. Couairon, M. Franco, B. Lamouroux, B. Prade, S. Tzortzakis*, et al.*, "Femtosecond Laser-Induced Damage and Filamentary Propagation in Fused Silica," *Physical Review Letters,* vol. 89, 2002.

[5] A. Couairon and A. Mysyrowicz, "Femtosecond filamentation in transparent media," *Physics Reports,* vol. 441, pp. 47-189, 2007.

[6] G. I. Stegeman and M. Segev, *Nonlinear optics: Phenomena, Materials and Devices*: Wiley, 2012.

[7] R. Osellame, G. Cerullo, and R. Ramponi, *Femtosecond Laser Micromachining: Photonic and microfluidic devices in transparent materials*: New York Springer, 2012.

[8] A. Marcinkevičius, V. Mizeikis, S. Juodkazis, S. Matsuo, and H. Misawa, "Effect of refractive index-mismatch on laser microfabrication in silica glass," *Applied Physics A,* vol. 76, pp. 257-260, 2003.

[9] A. Pasquazi, S. Stivala, G. Assanto, C. N. Afonso, J. Gonzalo de los Reyes, and J. Solís Céspedes, "Near-infrared spatial solitons in heavy metal oxide A glasses," *Optics Letters,* vol. 32, pp. 2103-2105, 2007.

[10] J. Goodman, "Introduction to Fourier Optics," in *Electrical and Computer Engineering*, 2nd ed: McGraw-Hill, 1996.

[11] E. Grace, "Asymmetric waveguide writing model with GAFFE," in *OSA Technical Digest, Proceedings of "Frontiers in Optics"*, 2009.

[12] E. J. Grace. (2009). *A toolbox for solving evolutionary nonlinear PDEs* Available: www.mathworks.co.uk/matlabcentral/fileexchange/24016

[13] H. Nyquist, "Certain Topics in Telegraph Transmission Theory," *Trans. AIEE,* vol. 47, pp. 617-644, 1928.

[14] MathWorks. (15/06/2015). *Matlab documentation: bwarea*. Available: http://es.mathworks.com/help/images/ref/bwarea.html

[15] MathWorks. (15/06/2015). *Mathlab documentation: regionprops*. Available: http://es.mathworks.com/help/images/ref/regionprops.html

[16] S. Wang and D. Zhao, *Matrix Optics*. Berlin: Springer-Verlag, 2000.

[17] P. Török, P. Varga, Z. Laczik, and G. R. Booker, "Electromagnetic diffraction of light focused through a planar interface between materials of mismatched refractive indices: an integral representation," *Optical Society of America A,* vol. 12, pp. 325-332, 1995.

[18] J. E. Rothenberg, "Space–time focusing: breakdown of the slowly varying envelope approximation in the self-focusing of femtosecond pulses," *Opt. Lett. ,* vol. 17, p. 3, 1992.

[19] A. Brodeur and S. L. Chin, "Ultrafast white-light continuum generation and self-focusing in transparent condensed media," *Journal of the Optical Society of America B,* vol. 16, pp. 637-650, 1999.

[20] F. DeMartini, C. H. Townes, T. K. Gustafson, and P. L. Kelley, "Self-Steepening of Light Pulses," *Phys. Rev.,* vol. 164, pp. 312-323, 1967.

[21] M. Kolesik, G. Katona, J. V. Moloney, and E. M. Wright, "Physical Factors Limiting the Spectral Extent and Band Gap Dependence of Supercontinuum Generation," *Phys. Rev. Lett.,* vol. 91, p. 043905, 2003.

[22] A. Locatelli, F. M. Pigozzo, D. Modotto, A. D. Capobianco, and C. De Angelis, "Bidirectional beam propagation method for multilayered dielectrics with quadratic nonlinearity," *Selected Topics in Quantum Electronics, IEEE Journal of,* vol. 8, pp. 440-447, 2002.

[23] C. B. Schaffer, A. Brodeur, and E. Mazur, "Laser-induced breakdown and damage in bulk transparent materials induced by tightly focused femtosecond laser pulses," *Measurement Science and Technology,* vol. 12, p. 1784, 2001.

[24] A. Couairon, L. Sudrie, M. Franco, B. Prade, and A. Mysyrowicz, "Filamentation and damage in fused silica induced by tightly focused femtosecond laser pulses," *Physical Review B,* vol. 71, p. 125435, 2005.

[25] B. Rethfeld, "Free-electron generation in laser-irradiated dielectrics," *Physical Review B,* vol. 73, p. 035101, 2006.

[26] Y. P. Raĭzer, "Breakdown and heating of gases under the influence of a laser beam," *Soviet Physics Uspekhi,* vol. 8, p. 650, 1966.

[27] A. Pasquazi, S. Stivala, G. Assanto, J. Gonzalo, and J. Solis, "Transverse nonlinear optics in heavy-metal-oxide glass," *Physical Review A,* vol. 77, p. 043808, 2008.

[28] D. Munoz-Martin, A. R. de La Cruz, J. M. Fernandez-Navarro, C. Domingo, J. Solis, and J. Gonzalo, "Structural origin of the nonlinear optical properties of lead niobium germanate film glasses," *Journal of Applied Physics,* vol. 110, p. 023522, 2011.

[29] A. Dubietis, E. Gaižauskas, G. Tamošauskas, and P. Di Trapani, "Light Filaments without Self-Channeling," *Physical Review Letters,* vol. 92, p. 253903, 2004.

[30] A. Dubietis, G. Tamošauskas, G. Fibich, and B. Ilan, "Multiple filamentation induced by input-beam ellipticity," *Optics Letters,* vol. 29, pp. 1126-1128, 2004.

[31] MathWorks. *Matlab documentation: Rand*. Available: http://es.mathworks.com/help/matlab/ref/rand.html

[32] A. Ferrer, V. Diez-Blanco, A. Ruiz, J. Siegel, and J. Solis, "Deep subsurface optical waveguides produced by direct writing with femtosecond laser pulses in fused silica and phosphate glass," *Applied Surface Science,* vol. 254, pp. 1121-1125, 2007.

[33] I. M. Burakov, N. M. Bulgakova, R. Stoian, A. Mermillod-Blondin, E. Audouard, A. Rosenfeld*, et al.*, "Spatial distribution of refractive index variations induced in bulk fused silica by single ultrashort and short laser pulses," *Journal of Applied Physics,* vol. 101, p. 043506, 2007.

[34] D. Blömer, A. Szameit, F. Dreisow, T. Schreiber, S. Nolte, and A. Tünnermann, "Nonlinear refractive index of fs-laser-written waveguides in fused silica," *Optics Express,* vol. 14, pp. 2151-2157, 2006.

[35] W. Gawelda, D. Puerto, J. Siegel, A. Ferrer, A. Ruiz de la Cruz, H. Fernández*, et al.*, "Ultrafast imaging of transient electronic plasmas produced in conditions of femtosecond waveguide writing in dielectrics," *Applied Physics Letters,* vol. 93, p. 121109, 2008.

[36] A. Ferrer, "Conformación de haces láser de pulsos ultracortos para la optimización de la escritura de guías de onda en dieléctricos," Departamento de Física de Materiales, Universidad Autónoma de Madrid, 2011. PhD Thesis.

[37] R. L. Sutherland, D. G. McLean, and S. Kirkpatrick, *Handbook of nonlinear optics*, 2nd ed.: Marcel Dekker, 2003.

[38] V. V. Temnov, K. Sokolowski-Tinten, P. Zhou, A. El-Khamhawy, and D. von der Linde, "Multiphoton Ionization in Dielectrics: Comparison of Circular and Linear Polarization," *Physical Review Letters,* vol. 97, p. 237403, 2006.

Chapter 6
Sub-surfaces waveguide writing

This chapter describes the production of active and passive sub-surface waveguides in phosphate glasses. The first section analyzes the influence of the laser-writing and material parameters, and follows discussing the waveguide formation mechanism. The last section describes the fabrication and performance of several waveguide-based amplifiers and lasers emitting at 1534 nm.

The waveguides were produced using the sub-surface irradiation setup at the GPL-CSIC group described in **Section 3.1.2.2**, using the high repetition rate (HRR) laser source (LS3). All waveguides were characterized in the setups described in Chapter 3 at GPL-CSIC labs, except the gain and lasing characterization of the waveguides produced in GPL-glass samples, which was performed at APD-Unizar.

6.1. Influence of writing and material parameters

The modification produced in the material upon sub-surface laser structuring is mostly determined by the energy deposition profile of the laser beam. *Propagador* (**Chapter 5**) allows calculating it when heat accumulation effects for consecutive laser pulses can be neglected (low repetition rate regime). However, the waveguides described in this chapter were fabricated using a HRR laser source in order to improve their performance (waveguides written in HRR regime usually show lower losses [1]). A model considering heat accumulation effects would be thus required for determining the energy deposition profile, as described in **Section 2.3.4**. Nevertheless, even if the simulations performed for the LRR regime do not provide a totally realistic energy deposition profile, the information extracted from the influence of the irradiation parameters may prove useful in some cases. In principle, this should allow designing an optimization strategy for the writing parameters.

Along with the laser processing parameters, the thermo-optical properties of the material will determine the result of the laser writing process. The material bandgap will determine the number of photons involved in the multiphoton ionization process, which along with the refractive index and nonlinear coefficients will determine the absorbed energy (ΔE) profile in the LRR regime, as shown in **Chapter 5**. Heat capacity and thermal conductivity (and their transient evolution), along with the laser repetition rate, will determine the temperature

profile, and thus the produced modifications. Also, later on this chapter it will be shown how choosing the right material composition allows generating a large refractive index contrast.

Finally, the production of active devices such as amplifiers and lasers requires that the material is doped with ions capable of producing light emission at the wavelength of interest. In this case, the desired emission was around 1.5 μm (in the C-telecomunication band), so the Er^{3+}–Yb^{3+} system (see **Section 2.5.2**) was selected. The phosphate glass host matrix was chosen due to the high solubility of rare-earths (which allows the production of heavily doped samples and thus short length devices), and the high absorption and emission cross sections [2] of rare earths. For low OH^- levels, the phosphate glass matrix may enable long lifetimes for the $^4I_{11/2}$ level of Er^{3+} [3].

6.1.1. Pulse energy and pulse duration

The first parameter to be considered is the pulse energy. **Figure 5.17a** shows the total absorbed energy (ΔE_{total}) and **Figure 5.17b** the maximum intensity achieved during propagation calculated by *Propagador* for different pulse energies and pulse durations (FWHM). The irradiation conditions (in the LRR regime) are: no slit, beam focused by AL1 (f = 6.24 mm, NA = 0.32) 100 μm below the surface and nonlinear coefficients for phosphate glass calculated in **Section 5.3.2.2** (n_2 = 7.3×10^{-21} m^2/W and β_3 = 1.0×10^{-29} m^3/W^2). The rest of the beam parameters are the corresponding to LS3 (λ = 1030 nm, R_x = R_y = 4.2 mm). The results in **Figure 5.17a** shows that ΔE_{total} scales linearly with pulse energy, with pulse duration slightly affecting the intercept but not the slope of the curves.

It is important noting that *Propagador* does not compute avalanche ionization effects.

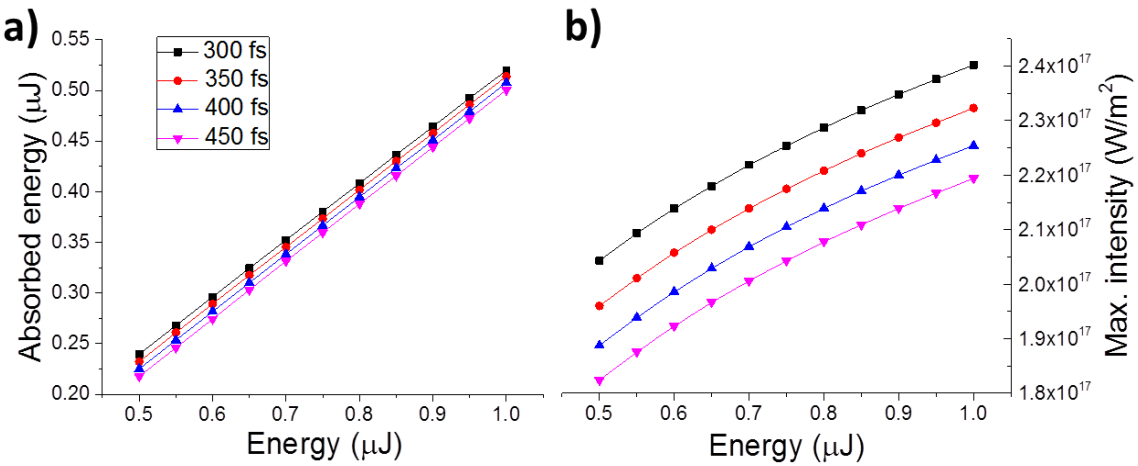

Figure 6.1: *(a) Total absorbed energy for different pulse energies and pulse durations (FWHM) in the LRR regime. (b) Maximum intensity value obtained during propagation. Simulations performed using* Propagador*, described in* ***Chapter 5****. The lines correspond to B-spline interpolation.*

For the highest pulse energy and pulse duration shown, the product of pulse duration and peak intensity is 9.9 J/cm^2, very near to the limit of 10 J/cm^2 calculated in [4] for the preeminence of the avalanche regime. As avalanche is a less controllable absorption mechanism than multiphoton ionization, it is desirable to remain below that limit.

6.1.2.Slit shaping

The width of the slit used strongly influences the energy deposition profile. Reducing the beam diameter in one dimension increases the size of the intensity distribution profile in that dimension, as shown in **Section 2.1.1.3**. **Figure 6.2a** shows the Z-Y and Z-X intensity and ΔE distribution profiles for pulses of 0.75 μJ and 400 fs for different slit widths. Both profiles are stretched along the Y dimension as the slit gets narrower, going from a "stick" shape to a more triangular shape. However, in the X dimension the profile remains nearly unchanged, even for the smallest calculated slit. In all cases, the profile shows a very similar size along the Z axis.

In the images for no slit, the effect of SA is visible on the two small side lobes present after the focus in the intensity profile. However, the NA in the Y dimension (NAy) is reduced when the beam is slit-shaped, and the effect of SA becomes nearly negligible in the ΔE

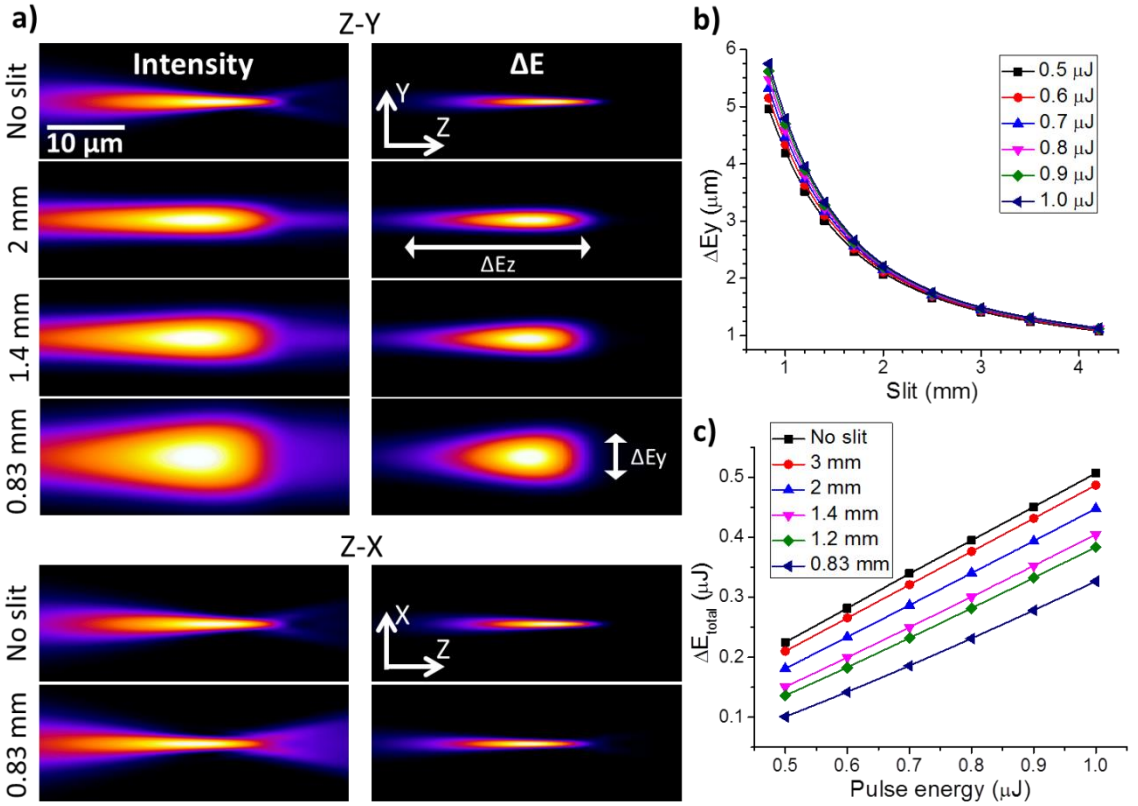

Figure 6.2: *(a) Normalized Z-Y and Z-X intensity and energy deposition profiles for different slit widths. (b) ΔEy versus slit width for different pulse energies. (c) Total absorbed energy versus pulse energy for different slit widths.*

profiles. The image for the Z-X plane with a slit width of 0.83 mm still show signs of SA effects, as NAx is not altered by slit shaping. However, the difference in NAy between the slit-less and slit-shaped beam simulations still produces a small difference between both Z-X absorption profiles.

Figure 6.2b show the values of the waist diameter ($1/e^2$) of the ΔE profile along the Y dimension (ΔEy) versus slit width for different pulse energies. The reduction in slit width increases ΔEy from 1.1 μm for a slit-less beam to 5.75 μm for the narrowest slit. More importantly, this parameter shows a negligible variation for different pulse energies. Finally, **Figure 6.2c** shows ΔE_{total} versus the pulse energy for different slit width values. It can be seen that the dependence is almost linear. For all slit width values the slope is similar, only varying the intercept.

6.1.3. Numerical aperture

The focal length of the lens also strongly conditions the ΔE spatial profile. For higher NAs (shorter focal lengths) the beam is focused more tightly, reducing the focal volume and increasing the amount of absorbed energy.

The reduction of the focal volume for increasing NAs can be seen in **Figure 6.3** for a slit width of 1.4 mm, 400 fs and 0.75 μJ. Also, higher NAs increase the influence of SA. For the lowest NAs, there is a small filament located after the paraxial focus. As NA increases, the beginning of the filament is transformed into a lobe, typical of high NA profiles. For the highest NA, the reminiscent filament is transformed in a second lobe. This effect is visible in the intensity profile, but the absorbed energy in these lobes is so small that it can't be appreciated

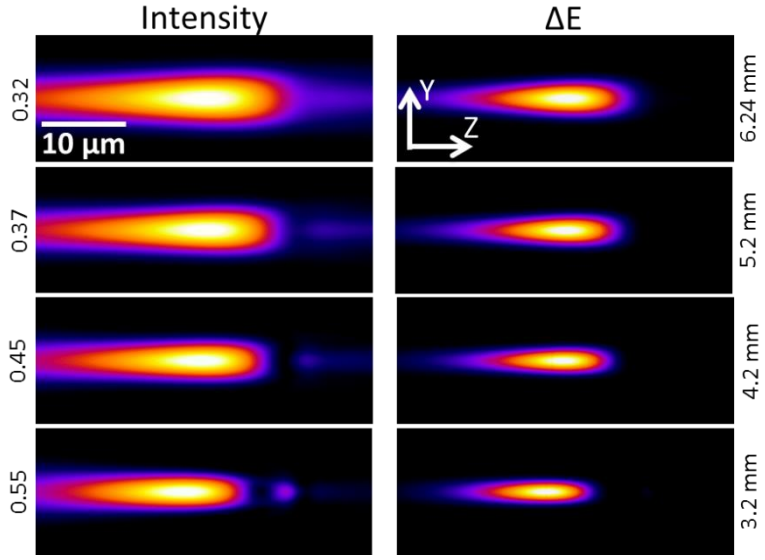

Figure 6.3: *Normalized intensity and energy deposition profiles for different NAs. The NA is indicated at the left of the images. The equivalent focal length is indicated at the right.*

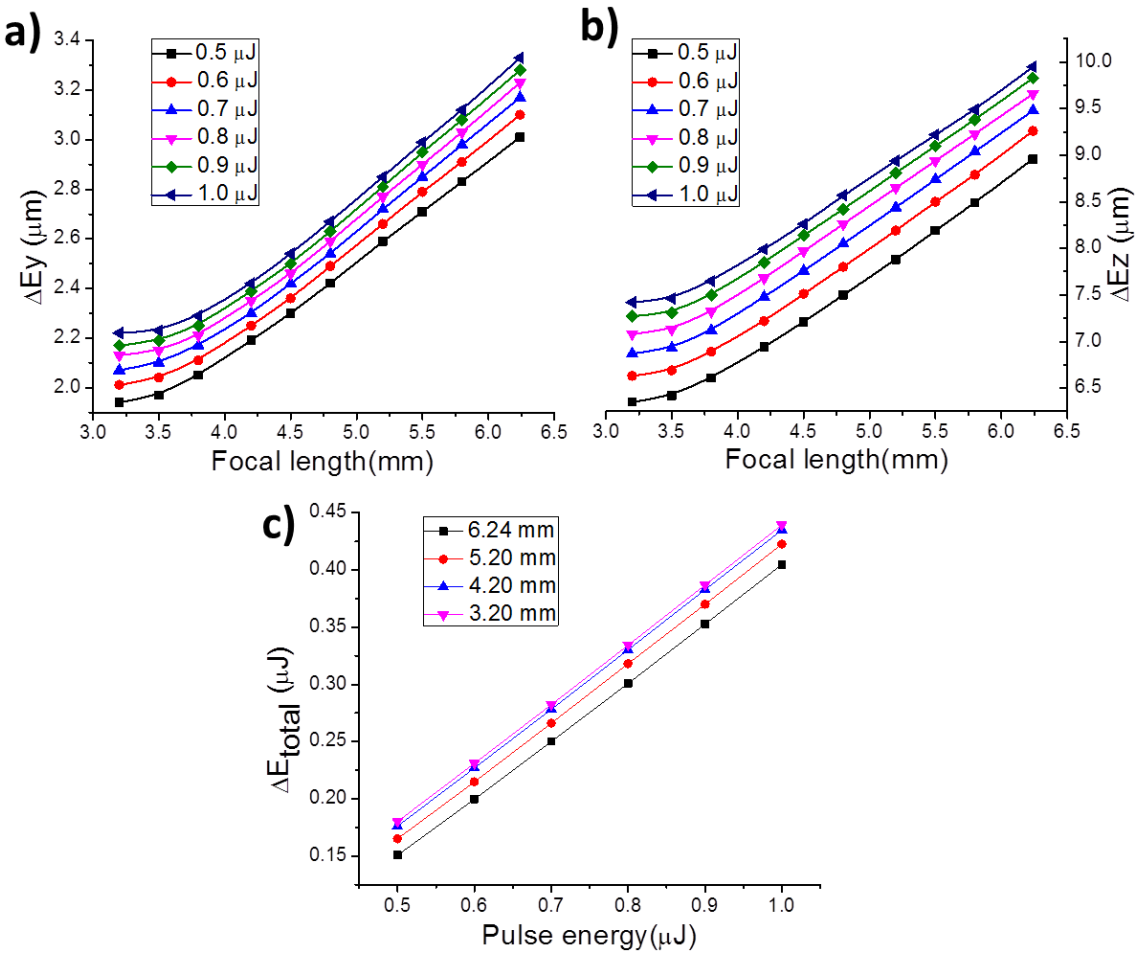

Figure 6.4: *ΔEy (a) and ΔEz (b) versus focal length for different pulse energies. (c) ΔE_{total} versus pulse energy for different focal lengths.*

in the ΔE profiles.

ΔEy and ΔEz values for different pulse energies are plot as a function of the focal length in **Figure 6.4a-b**. It can be seen that the reduction in both magnitudes is almost linear respect to the focal length, until saturating for $f < 4\ mm$ due to SA. The evolution of ΔE_{total} versus pulse energy for different focal lengths is shown in **Figure 6.4**c. Again, this magnitude scales linearly as a function of pulse energy, varying the intercept but not the slope.

6.1.4. Other parameters

Nonlinear coefficients (in this case n_2 and β_3) are smaller for circularly polarized beams than for linearly polarized ones, as shown in **Section 5.3.2**. This reduction has two positive implications for waveguide writing. On the one hand, it reduces the nonlinear distortion of the intensity profile upon propagation. On the other hand, a reduced nonlinear absorption coefficient increases the controllability of the fabrication process. Also, it prevents the

formation of nanogratings perpendicular to the laser polarization [5], which drastically increase the waveguide losses.

Scanning speed and laser repetition rate determine the total number of pulses that irradiate a certain volume of material. This influences the maximum temperature reached and the time lapse that the material remains heated, which determines the final modification of the material.

Finally, the feasibility of irradiating at different depths is one of the main advantages of sub-surface writing with fs-laser pulses, enabling the production of 3D structures. The focusing depth affects the ΔE profile for two reasons. First, SA distortion is higher for higher focusing depths. Second, higher depths increase the influence of nonlinear propagation in the ΔE profile.

6.1.5. Waveguide writing parameters determination

It is possible to apply the information discussed in the previous sections for the LRR regime to minimize the optimization time of writing parameters in the HRR case. First, avalanche ionization effects have to be minimized, therefore the shortest available pulse duration was used (350 – 400 fs). Circular polarization was utilized for reducing nonlinear coefficients and prevent the formation of nanogratings [5].

Then, the size of ΔE profile has to be selected. ΔEz is mainly set by focusing lens NA (**Section 6.1.3**), while ΔEy is mainly determined by the combination of NA and slit width (**Sections 6.1.2** and **6.1.3**). The overall size of the produced modification is determined by the combination these two parameters. As the exact size of the modification in HRR regime can't be calculated by *Propagador*, different combinations had to be tested. Fine tuning of the size of ΔE profile was performed using the pulse energy.

6.2. Waveguide morphology

The waveguide morphology, along with the refractive index change, determines the passive properties of the waveguide: guided modes number and size, and propagation losses. This section describes the morphology of the waveguides produced in phosphate glass.

6.2.1. Longitudinal morphology

A major source of propagation losses is the scattering produced at the envelope of the waveguide [6]. The longitudinal morphology of the waveguide is thus an essential parameter to achieve low propagation losses.

Figure 6.5 shows microscopy images of three illustrative examples of waveguides with different degrees of roughness. They were produced in Com1 glass at 60 $\mu m/s$ with pulses of 350 fs and 520, 550 and 580 nJ respectively, using AL2 to focus the beam and no slit. **Figure 6.5**a shows a good waveguide, whose longitudinal structure shows a very smooth envelope. The guiding region corresponds to the white stripe in the image (see **Section 6.2.2**). Waveguides in this glass showing this smooth structure have propagation losses $\lesssim 1\ dB/cm$.

The waveguide in **Figure 6.5b** presents a modulated longitudinal envelope much rougher. These stressed waveguides are able to guide light but with very high losses, up to 10 dB/cm. This modulation is produced by the periodic effect of strong nonlinear self-focusing and plasma defocusing. The waveguide in **Figure 6.5c** shows a series of periodic micro-explosions during the writing process and does not support guiding.

The relation between the waveguide roughness and the irradiation parameters is not always clear. Nonlinear propagation effects, beam filamentation temperature distribution, maximum temperature and cooling time, etc., may influence the longitudinal morphology. A thorough thermal distribution model, including all the above mentioned physical mechanisms could be performed. However, the combination of multiple effects highly increases the complexity of such a model. Instead, the optimum writing conditions were determined experimentally.

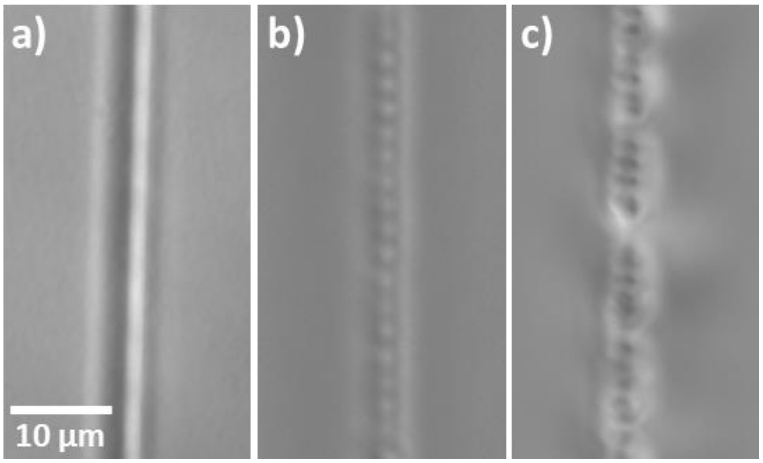

Figure 6.5: *Microscopy longitudinal trans-illumination images illustrative of a good (a), a stressed (b) and a damaged waveguide (c).*

6.2.2. Cross-section morphology

The cross-section morphology of the structures has first been studied by transmission optical microscopy. **Figure 6.6a-c** show the images of the cross section of three waveguides produced in the GPL2 glass sample. They were inscribed at 300 $\mu m/s$ using a slit width of 0.83 mm. The beam was focused by AL2 (0.68 NA) 100 μm below the surface. They were produced using 350 fs laser pulses at 500 kHz, with pulse energies of 390, 420 and 450 nJ respectively. Even for these small differences in energy, the morphologies are very different, and the guiding region can be clearly distinguished only in the waveguide produced with highest energy (**Figure 6.6c**).

In contrast, **Figure 6.6d** shows a waveguide produced in the commercial glass sample (Com1) at 60 $\mu m/s$ scanning speed and 790 nJ of pulse energy. The strong reduction of the scanning speed and increase of pulse energy has a strong effect in the cross section morphology. Three different regions can be clearly appreciated: bright, dark and halo regions. The bright area corresponds to the region of increased refractive index change ($\Delta n > 0$), the guiding region, as it collects and guides the illumination light of the microscope. The dark region corresponds, for the same reason, to a decreased Δn region. The halo region shows almost the same gray level as the bulk material, and its small refractive index modification must likely be caused by gentle heat diffusion effects. This morphology is similar in all the guiding waveguides produced in Com1 glass. Due to this similarity, it was possible to study the

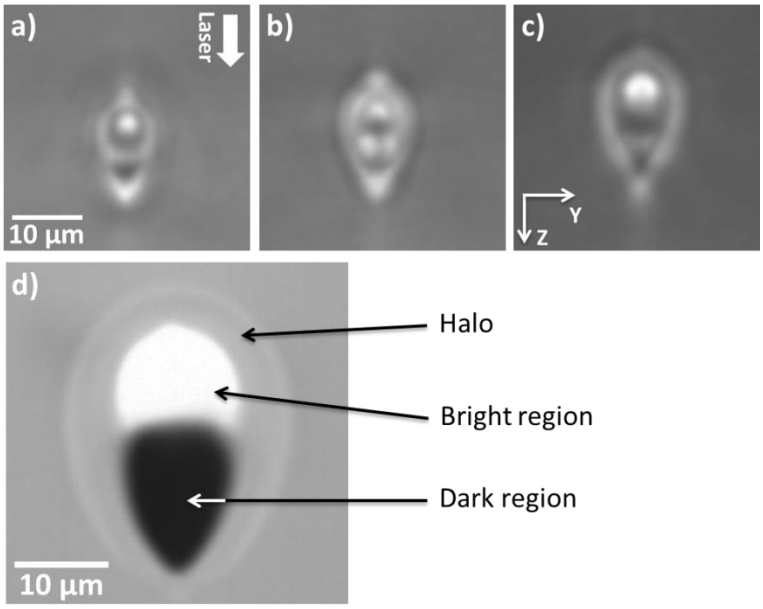

Figure 6.6: *(a-c) Optical microscopy images of waveguides produced in GPL2 glass at 390 µJ (a), 420 µJ (b) and 450 µJ (c) at 300 µm/s and a slit of 0.83 mm. (d) DIC microscopy image of a waveguide produced in Com1 glass at 790 nJ with a slit of 1.2 mm at 60 µm/s. All waveguides were produced with 0.68 NA and a repetition rate of 500 kHz.*

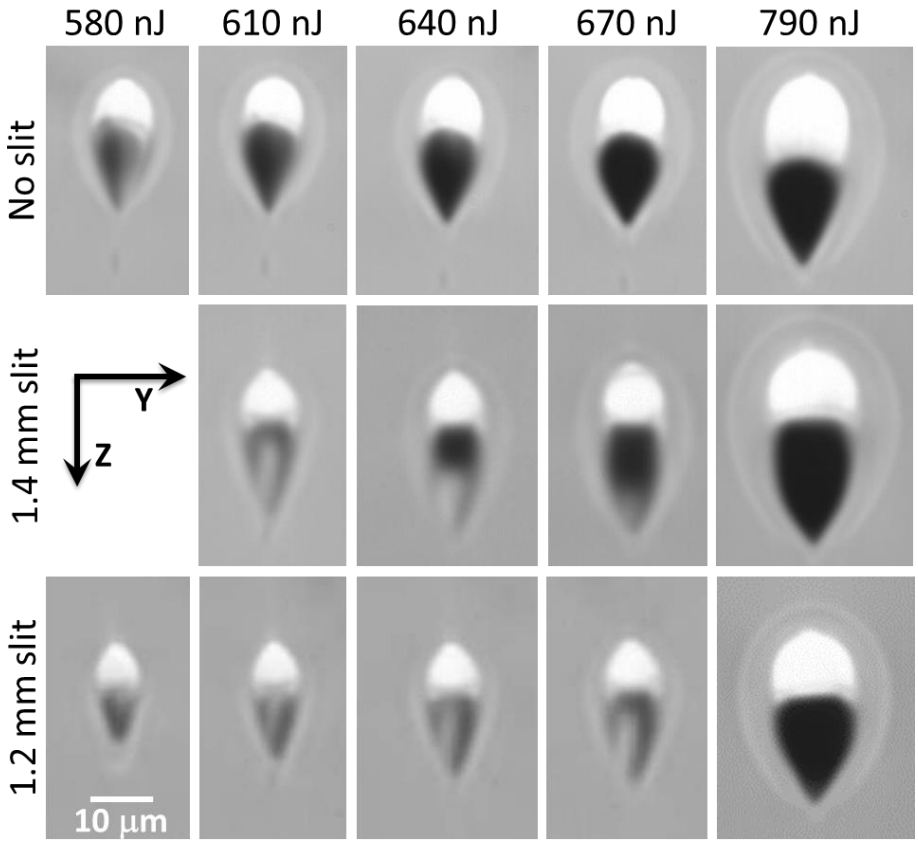

Figure 6.7: *DIC microscopy images showing the cross-section of the produced structures for different pulse energies and slit widths at 60 μm/s in Com1 glass. Figure adapted from [7].*

influence of writing parameters in the guiding region morphology.

The size of the guiding region can be controlled with the slit width and the pulse energy [7]. **Figure 6.7** shows Differential Interference Contrast (DIC) microscopy images of several waveguides produced at different pulse energies and slit widths in Com1 glass. Unlike what was expected from the simulations in **Section 6.1.2**, waveguides produced without slit are larger in both dimensions than the ones produced with a slit. The reason for this behavior is analyzed in **Section 6.3.3**.

Figure 6.8 shows the transverse dimensions of the guiding region along the Y and Z axis (Gy and Gz respectively). It can be seen that counterintuitively, smaller slit width values produce smaller guiding regions. Also, faster inscribing speeds produce slightly smaller guiding regions. Along the Y axis, the guiding region formation threshold is 550 nJ for slit-shaped beams (lower energies produce modified structures, but without light guiding). Above threshold Gy shows a fast growth until 580 nJ, where it shows a quasi-plateau behavior with values between 6 and 8 μm. Around 750 nJ, Gy shows a second sudden increase, reaching values similar to the ones obtained without slit. Higher energies produce highly-stressed

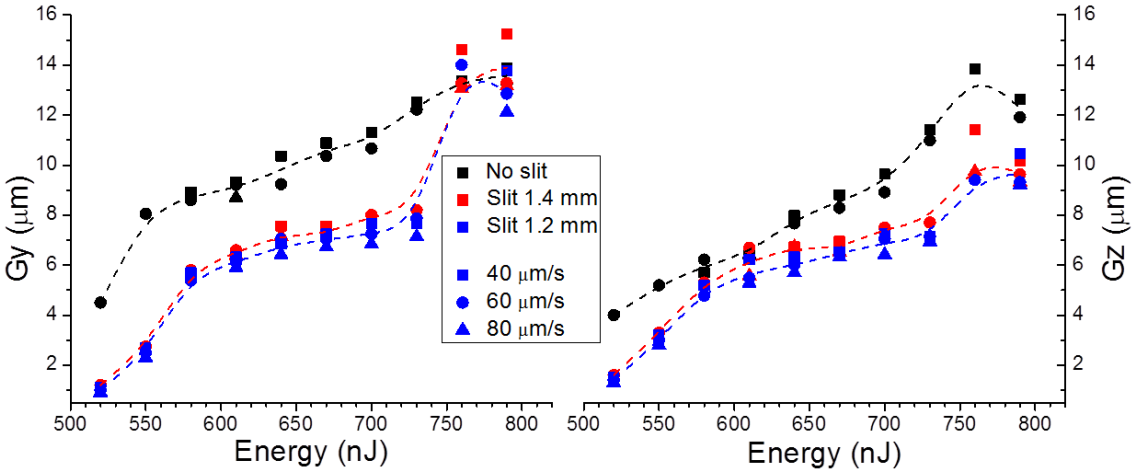

Figure 6.8: *Transverse dimensions of the guiding regions along the Y (Gy) and Z (Gz) axes as a function of pulse energy for different slit widths and scanning speeds. The dashed lines are the B-spline interpolations of the mean values for the different scanning speeds. Figure partially adapted from [7].*

waveguides. For slit-less waveguides, the formation threshold is lower (due to the higher absorbed energy caused by the higher effective NA), while the growth versus pulse energy after the formation threshold is more pronounced. The behavior of Gz for the slit-shaped waveguides is very similar to the one of Gy, although the sudden increase for the higher energies ($\sim$750 nJ) is less pronounced. The slit-less waveguides also show a second slope change in Gz for higher energies.

In summary, a combination of slit, pulse energy and scanning speed allows the production of waveguides with a guiding region of the desired size, in the 6 - 14 μm range (similar to the guided mode size of standard single mode fibers, as the ones shown in **Table 3.6**). This range was obtained using AL2 (0.68 NA), but by using different focusing lenses, a broader range of possible guiding region sizes could be achieved.

6.3. Waveguide formation

6.3.1. Waveguide formation mechanism

The most common mechanisms for producing refractive index change (Δn) upon sub-surface fs-laser writing in glasses were described in **Section 2.4.4**. The formation mechanism of waveguides produced by fs-laser irradiation in HRR regime in phosphate glass was studied in detail by the GPL group [8, 9]. It was determined that the main formation mechanism in La_2O_3 - K_2O - P_2O_5 glasses is the migration of different glass components along the laser propagation direction in the region heated by laser. This mechanism changes the local composition of the glass, which in turn modifies the local refractive index, where the produced Δn was found to

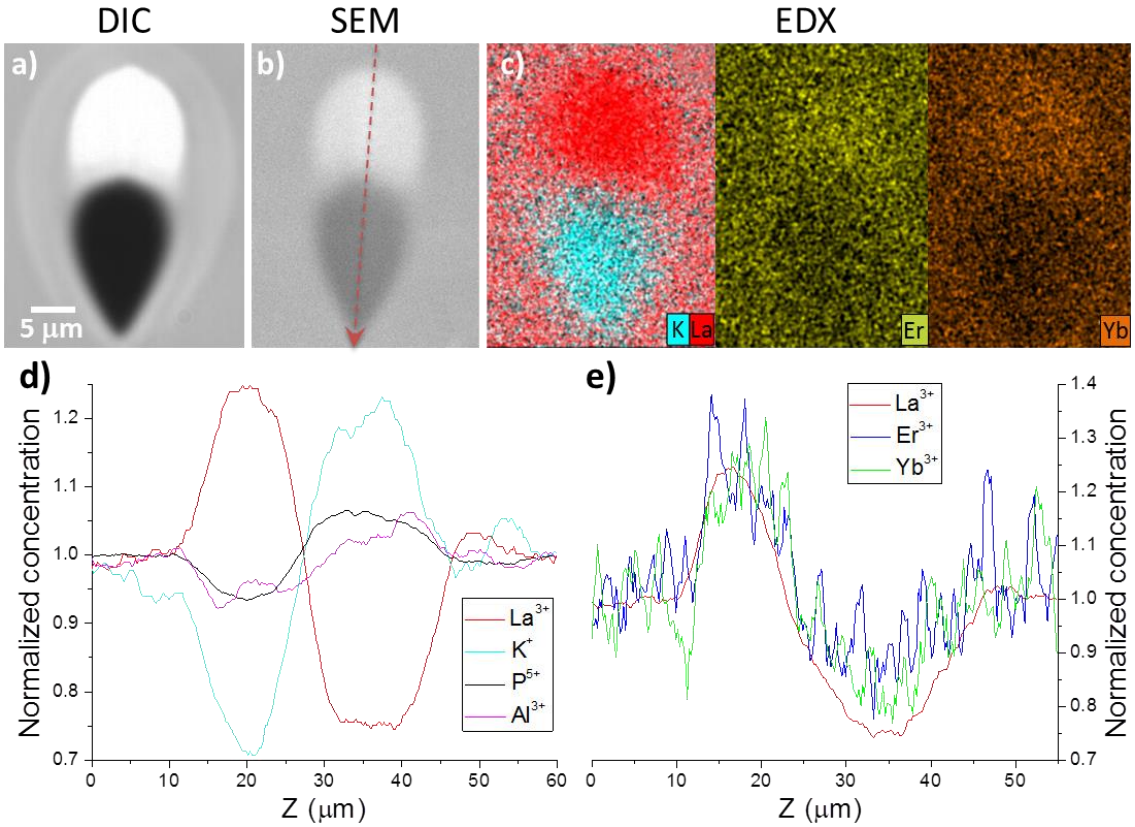

Figure 6.9: *Transmission DIC microscopy image (a), SEM image (b) and EDX La-K, Er and Yb compositional maps (c) for a waveguide written without slit at 730 nJ and 60 µm/s. (d) Longitudinal EDX compositional measurement of the same waveguide for the main glass components. (e) Longitudinal EDX compositional measurement for lanthanides in a waveguide written with 1.4 mm slit, 790 nJ and 60 µm/s. Er^{3+} and Yb^{3+} values are averaged with their 4 closest neighbors a second time in order to reduce noise. The longitudinal measurements are performed in the longest dimension of the waveguides, indicated by the red arrow in (b).Figure adapted from [8] and [9].*

be proportional to the increase of the local concentration of La^{3+} (as described in **Section 6.3.2**) [7-9].

The local composition of the guiding structures was measured by energy-dispersive X-ray spectroscopy (EDX). **Figure 6.9a-c** show the DIC, SEM and EDX compositional maps of a waveguide produced with no slit and 730 nJ of pulse energy at 60 $\mu m/s$. SEM image shows an increase of the average Z number in the guiding region, while the negative Δn region shows a decrease. EDX measurements allow correlating this increase with an increase in La^{3+}, Er^{3+} and Yb^{3+} concentration, as well as depletion of the rest of elements. The opposite occurs in the negative Δn region. La^{3+}, Er^{3+}, Yb^{3+} and K^{+} are the elements that show higher degree of compositional change, suggesting an ion cross-migration mechanism during the formation of the waveguide. This is further supported by the fact that they have very similar ionic radii, while the rest of the constituents (P^{5+}, Al^{3+} and Si^{2+}) of the glass present smaller values, as shown in **Figure 6.11** [10].

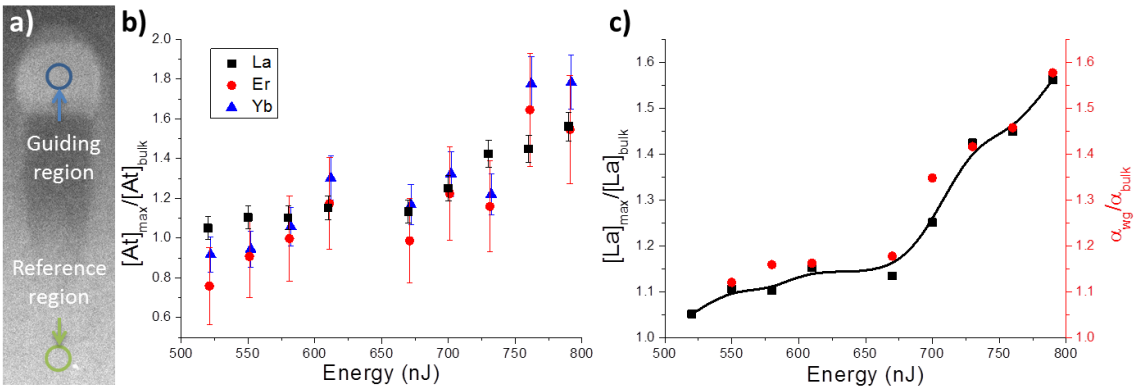

Figure 6.10: *(a) SEM image of a waveguide showing the different measurement regions in point EDX experiments. (b) Relative concentration of La^{3+}, Er^{3+} and Yb^{3+} versus pulse energy for 1.4 mm slit width waveguides. (b) Relative La^{3+} concentration and average relative absorption at 1534 nm versus pulse energy. The line is the B-spline interpolation of La^{3+} relative concentration values.*

Figure 6.9d shows a quantitative EDX compositional measurement along the line indicated by the red arrow in **Figure 6.9b**. It shows the relative concentration of the main components of the glass (except oxygen). Due to their lower concentration in the glass and smaller X-ray emission cross section, Er^{3+} and Yb^{3+} determination is subject to a larger error than the concentration of the rest of the glass constituents. **Figure 6.9e** shows a longitudinal compositional measurement performed in a different waveguide, where the behavior of La^{3+}, Er^{3+} and Yb^{3+} is shown. Even after a second averaging procedure, noise is still important. However, it can be clearly seen that both Er^{3+} and Yb^{3+} behave similarly to La^{3+}.

The inherent difficulties associated to the determination of Er^{3+} and Yb^{3+} can be solved by using their optical properties. In particular, the maximum Er^{3+} concentration ($[Er^{3+}]_{max}$) in the guiding region can be determined by measuring the absorption of the waveguide and the bulk material at 1534 nm, as it is proportional to Er^{3+} concentration. Also, the plot in **Figure 6.9e** suggests that the determination of $[Er^{3+}]_{max}$ via absorption measurement could be potentially used to determine $[Yb^{3+}]_{max}$ and $[La^{3+}]_{max}$, and thus the refractive index change associated to this element.

In order to verify the validity of this approach, new waveguides were produced in a longer sample of Com1 glass (to increase the resolution in absorption and loss measurements)

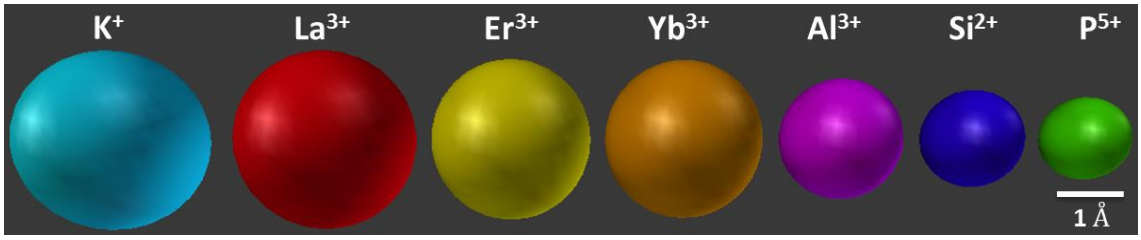

Figure 6.11: *Ionic size of different components of Com1. Data taken from [10].*

with slit-shaped beams. They were produced using the same writing parameters, except for a slightly longer pulse duration (400 *fs*). The measurement region in the EDX characterization was reduced to a small area (~5 μm^2) in the guiding region (point EDX measurements). Another region far from the waveguides was measured for reference, as shown in **Figure 6.10a**.

Figure 6.10b shows the relative concentration in La^{3+}, Er^{3+} and Yb^{3+} versus pulse energy for 1.4 *mm* slit width waveguides writen at 60 $\mu m/s$. This measurement yields a clear behaviour for the local concentration of La^{3+} in the guiding region: it slowly increases for energies lower than 670 *nJ*, and rapidly increases for higher pulse energies. Due to their different concentrations in the bulk glass, the error in the relative concentration is low for La^{3+} (~0.05), moderate for Yb^{3+} (~0.10) and high for Er^{3+} (~0.25).

Figure 6.10c shows the measured relative increment in La^{3+} concentration and absorption at 1534 *nm* in the guiding region as a function of pulse energy. It can be seen that the evolution of both parameters coincide almost perfectly. This implies that absorption at 1534 *nm* can be used to estimate very precisely the concentration of Er^{3+} and La^{3+}. This provides a faster and easier method than EDX measurements for determining the concentration of lanthanides in the guiding region.

6.3.2. Refractive index change

In order to determine the spatial distribution of the refractive index change in the waveguides, refractive index profilometry at 670 *nm* was performed in several waveguides written with different slit widths and pulse energies [7]. **Figure 6.12** shows a comparison between DIC, SEM and Δn profilometry images. They are essentially similar to the La^{3+}

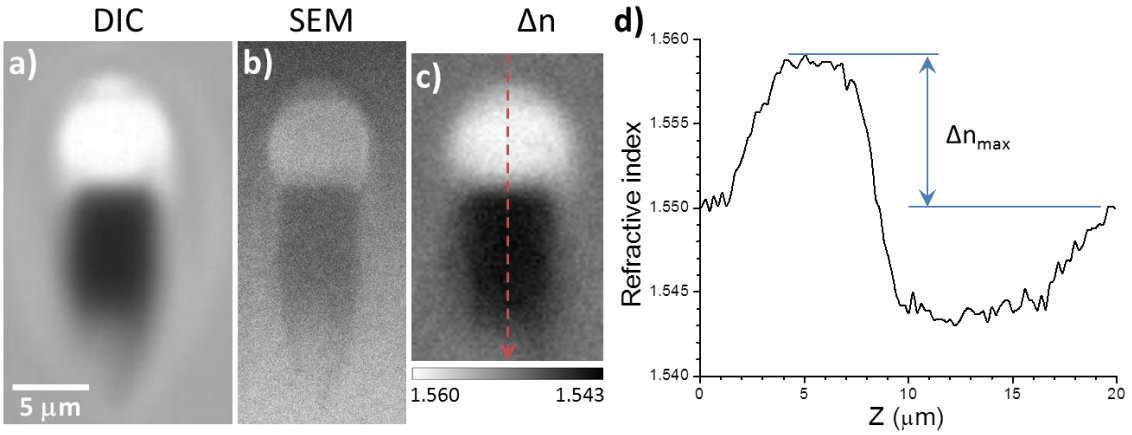

Figure 6.12: *DIC microscopy (a), SEM (b), Δn profilometry (c) images, and line Δn profile for a waveguide written with 1.4 mm slit, 670 nJ at 60 µm/s. The line measurement was performed in the position and direction indicated by the red arrow in (c), which corresponds to the longest dimension of the waveguide. Figure adapted from [7]*

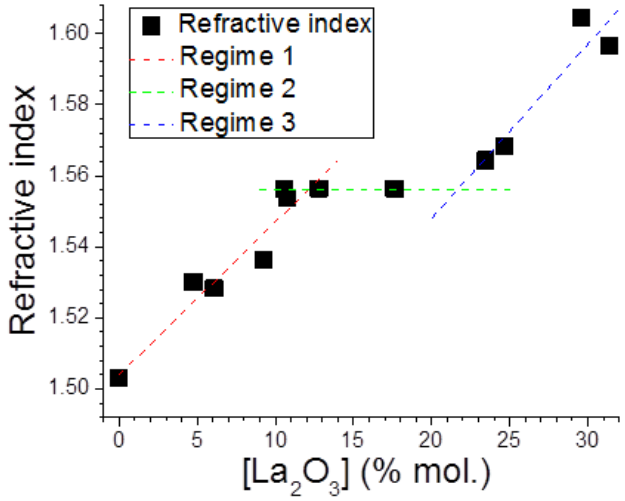

Figure 6.14: *Refractive index of binary phosphate-lanthanum oxide glasses versus La_2O_3 molar concentration. Dashed lines are linear fits for glasses in the three different regimes. Figure adapted from [11].*

concentration profiles measured by EDX: the region enriched in La^{3+} can be clearly identified with the positive Δn region, and the region depleted in La^{3+} with the negative Δn region.

All these measurements support that the positive Δn is produced by an increase of the local La^{3+} concentration. This is in agreement with the work of Brow and coworkers in *La-P* [11] and *Al-La-P* [12] oxide glasses. **Figure 6.14** shows the refractive index at ~590 *nm* of binary La_2O_3- P_2O_5 glasses for different La_2O_3 molar concentrations. Three different regimes can be appreciated [11]. The first one is for La_2O_3 concentrations lower than 12 %mol., where La^{3+} acts is incorporated in the glass matrix in the form of isolated ions. The second regime is for La_2O_3 concentrations between ~12 %mol. and ~22 %mol., where the refractive index remains constant due to La^{3+} polymerization in the glass network. Finally, the third regime is

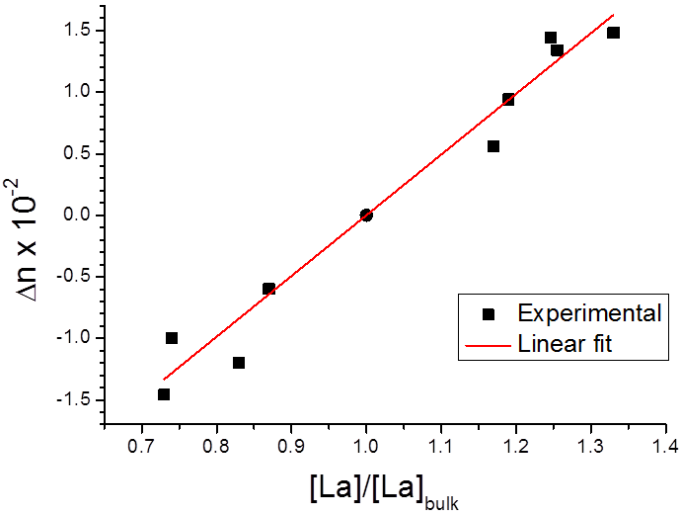

Figure 6.13: *Maximum refractive index change versus La^{3+} concentration in the guiding and negative Δn regions normalized to the glass refractive index. Figure adapted from [7].*

for La_2O_3 concentrations higher than ~22 %mol. where the refractive index increases again with La^{3+} concentration. In this later regime, the phosphate network starts to be modified. Therefore, for La_2O_3 concentrations in regimes 1 or 3, it is possible to increase the local refractive index of the glass by varying the local content of La^{3+} by laser induced ion migration.

Figure 6.13 shows the relation between the refractive index change and the La_2O_3 concentration for several of the waveguides produced in Com1 glass. These values can be fit to a line, producing a slope of $(4.9 \pm 0.3) \times 10^{-2}$. The maximum measured Δn in **Figure 6.13** is 1.5×10^{-2}, corresponding to a relative $[La^{3+}]$ variation around 1.3. With this Δn, it would be possible to produce low-loss waveguides with curvature radius as low as 8 mm [13].

In conclusion, Δn in the guiding region is mainly determined by the local concentration of La^{3+}. However, as shown in **Section 6.3.1**, $[La^{3+}]$ is in turn determined by the pulse energy for a given slit width value. This means that Δn can be directly controlled by the pulse energy. This, along with the feasibility of controlling the guiding region size by the combination of slit width and pulse energy, renders the possibility of controlling the most relevant waveguide properties using only two writing parameters: pulse energy and slit width.

6.3.3. Ion migration mechanism

It was described in **Section 6.3.1** that the waveguide formation is caused by the cross migration of La^{3+} and K^{+} in the phosphate glass sample. During the irradiation, K^{+} (and P^{5+} and Al^{3+} to a smaller extent) migrates towards the negative Δn region (along the propagation direction of the beam), while La^{3+}, Er^{3+} and Yb^{3+} migrate in the opposite direction. However, the origin of this ion migration mechanism remains unclear.

A model describing the ion migration process would require a complete beam propagation and energy deposition description (with detailed temperature-dependent parameters), along with a temperature evolution and ion diffusion model. Several models with different degrees of complexity have been proposed to determine the local temperature distribution in the HRR regime [14-17]. Instead, an experimental approach was used in order to gain a better insight of the laser induced migration process. Plasma emission images acquired during irradiation were used in order to get a snapshot of the steady state energy deposition profile and temperature distribution [18]. The experimental details are described in **Section 3.1.2.2**.

Figure 6.15 shows the acquired plasma emission images upon irradiation with different pulse energies without and with a slit of 1.4 mm width for a sample speed of 60 $\mu m/s$. Several

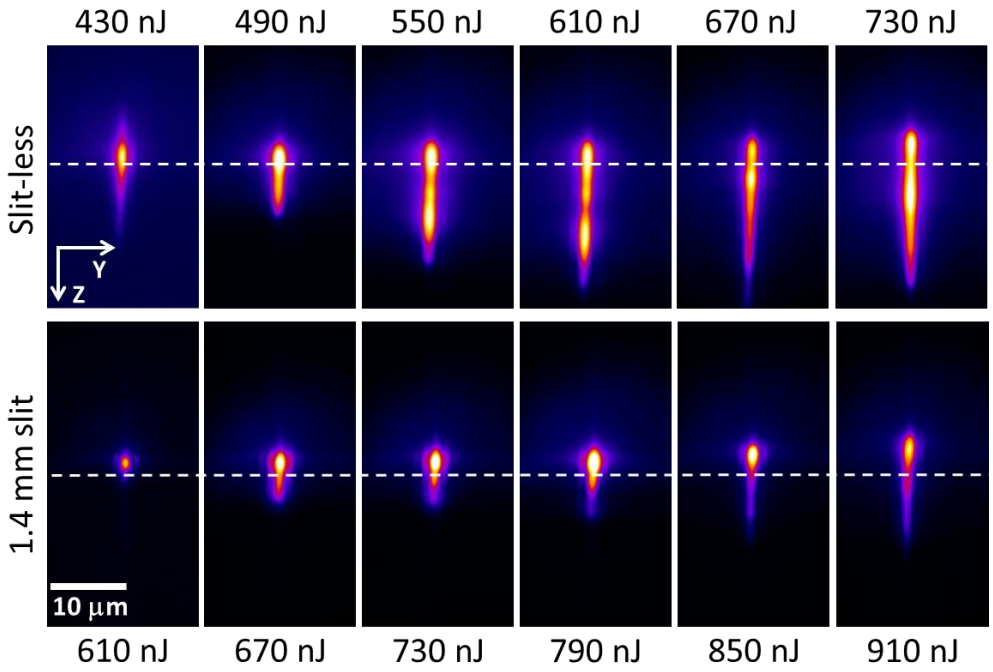

Figure 6.15: *Plasma emission images acquired upon irradiation with different pulse energies and slit widths for a scanning speed of 60 μm/s. The dashed white lines correspond to the paraxial focal plane position. All images are rescaled to their maximum. The laser incides from the topFigure adapted from [18].*

differences can be appreciated between slit-less and slit-shaped irradiation images. The most noticeable is that for slit-less irradiation plasma emission is very sensitive to pulse energy, while the irradiations performed with the slit-shaped beam show a highly regular behavior in the range 610 – 730 nJ of pulse energy. Higher energies produce longer plasma emission distributions, more similar to the ones produced without slit. The behavior of plasma emission is the same as the behavior of waveguide guiding region size shown in **Section 6.2.2**. There, it was shown that the guiding region size is very similar for waveguides inscribed with slit-shaped beams for pulse energies between 610 and 730 nJ, unlike waveguides inscribed without slit.

Luo and coworkers showed how ion migration structures produced upon HRR laser irradiation can be inverted by the introduction of positive or negative SA in the beam [19]. This experiment was conducted for waveguide writing conditions in order to verify if the same effect can be produced in waveguides generated by ion migration. SA was varied by substituting AL2 (0.68 NA) by MO6 (0.85 NA), a dry microscope objective which is SA-corrected for focusing depths of 100 μm in this glass (experimentally determined). When the beam was focused at lower depths, the intensity profile presented negative SA, while for higher depths it presents positive SA. The waveguides were produced without slit and at 60 $\mu m/s$.

Figure 6.16a shows the plasma emission images acquired for negative, negligible and positive SA conditions. The case of positive SA is very similar to the previously shown images.

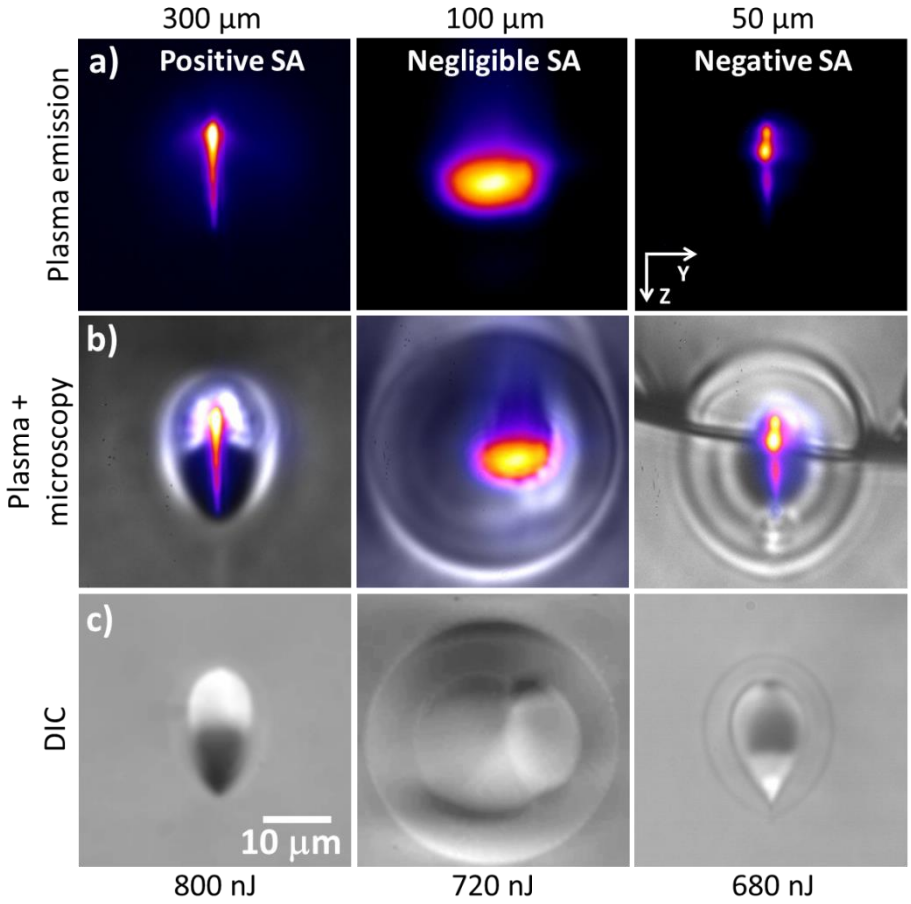

Figure 6.16: *(a) Plasma emission images for different focusing depths and pulse energies. (b) Superposition between plasma emission (false color scale) and in situ white light transmission microscopy (gray scale) images. (c) DIC microscopy images of the polished waveguides. Figure adapted from [18].*

In the case of negligible SA, the plasma emission profile becomes greatly stretched in the Y dimension and compressed in the Z dimension. Finally, for negative SA the plasma emission recovers its longer axis along the Z dimension, but with a profile different than for positive SA.

The superposition between plasma emission and in situ white light microscopy images is shown in **Figure 6.16b**, while **Figure 6.16c** shows DIC images of the produced waveguide structures after polishing. It can be seen that ion migration occurs along the longer axis of the plasma emission distribution. In the case of negligible SA, the structure is rotated 90°, and 180° for negative SA. This indicates that the ion migration occurs along the longer axis of the plamsa, and that the migration direction can be controlled by SA.

In conclusion, the manipulation of the asymmetries in the energy deposition profile by modifying the writing conditions allows controlling the waveguide structure distribution. Slit shaped beams present plasma distributions less sensitive to pulse energy, explaining the better control of the guiding region size. Also, by modifying the energy deposition profile via spherical aberration effects it is possible to control the ion migration direction in the glass. This

effect, as the observed migration direction along the plasma emission long axis, is most likely related to the effect of energy deposition in the thermal gradients responsible for the migration mechanism.

6.4. Waveguide-based amplifiers and lasers

This section is dedicated to the results achieved in the production of low loss waveguides, and waveguide-based active devices (amplifiers and lasers) fabricated using fs-laser induced ion migration.

6.4.1. Search for processing windows

Initially, the search for optimal processing parameters was performed in GPL1 and GPL2 glasses, using AL1 (NA 0.40) and a 0.83 mm slit width. Three processing windows (PW1, PW2 and PW3) were found, as shown in **Table 6.1**. They lead to good waveguiding properties (propagation losses ~0.5 dB/cm), but high overlapping losses due to the big size of the guided modes (> 17 μm). Then, the focusing lens was changed to AL2 (NA 0.68) in order to produce smaller guiding regions, and thus smaller guided modes. Irradiations in GPL3 glass produced waveguides with low mode sizes (between 10 and 14 μm for PW5, slightly higher for PW4), again with low propagation losses (0.4 dB/cm for PW4 and 0.5 dB/cm for PW5). Finally, PW4 parameters were tested in Com1 glass. Pulse energy and slit width had to be increased, probably due to the lower La content of Com1, and thus higher thermal conductivity. Anyway, it yielded excellent results, with very low propagation losses (0.2 dB/cm) and a controllable guiding region size (see **Section 6.2.2**).

Table 6.1: *Writing parameters of the processing windows (PW). Glass composition can be found in* ***Table 3.9****.*

Name	Lens (NA)	Repetition rate (kHz)	Pulse energy (µJ)	Scanning speed (µm/s)	Glass
PW1	AL1 (0.40)	80	1.0 – 2.0	15 – 20	GPL1, GPL2
PW2	AL1 (0.40)	125	0.8 – 1.2	15 – 30	GPL2
PW3	AL1 (0.40)	250	0.7 – 1.0	40 – 60	GPL2
PW4	AL2 (0.68)	500	0.3 – 0.5	40 – 60	GPL3
PW5	AL2 (0.68)	500	0.3 – 0.5	250 – 350	GPL3
PW6	AL2 (0.68)	500	0.5 – 0.8	40 – 60	Com1

6.4.2. Active waveguides in GPL-produced glass

The goal of the waveguides in this sub-section was producing a compact (short length) device capable of producing high optical gain and lasing emission at 1534 nm. For that

purpose, several waveguides were produced in two different samples, GPL3 and GPL4, which were produced at the GPL-CSIC. They were chosen for their high Er^{3+} and Yb^{3+} doping levels, which in principle would lead to a reduction of the length of the active waveguide. The waveguides were characterized in the mode characterization setup at GPL-CSIC, and amplifier and laser characterization setups at APD-Unizar.

6.4.2.1. Waveguides in GPL3 glass

First, the waveguides were produced in a 24 mm length sample of GPL3 glass (Er^{3+} and Yb^{3+} concentration of 3.0 %mol. and 4.8 %mol. respectively). The most efficient waveguide in terms of amplification (Wg1) was produced with the parameters included in PW5 (430 nJ, 0.83 mm slit width, 500 kHz and 60 $\mu m/s$ scanning speed). It showed -5.5 dB net gain upon bidirectional pumping (735 mW) at 976 nm. This low value clearly indicated that the waveguide length was not optimal. Therefore, its active performance was modeled as described in **Section 3.3.1.2** in order to calculate the optimal length for maximizing its net gain. The result is shown in **Figure 6.17**, showing a maximum net gain of ~2 dB for a waveguide length around 13 mm.

Figure 6.18a shows the net gain and enhancement of the waveguide after being cut at 14 mm as a function of the total pump power. The waveguide showed a maximum net gain of 2.3 dB, slightly higher than the maximum predicted value. The evolution of net gain in **Figure 6.18a** shows only slight signs of saturation, indicating that the potentially achievable net gain could be increased for higher pump powers.

This waveguide showed a total loss of 2.1 dB at 1640 nm, so the obtained internal gain was 4.4 dB. Pump transparency was reached around 550 mW (a high value compared with the ones described in the following sections) due to the strong doping levels of Er^{3+} and Yb^{3+}. Measured absorption in the waveguide at 1534 nm was 13.6 dB, which compared with the

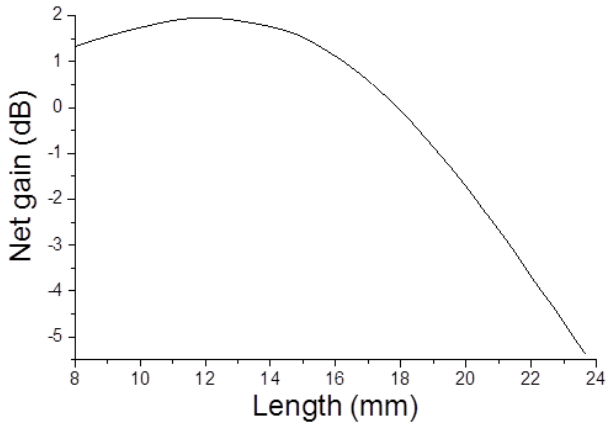

Figure 6.17: *Modeled net gain versus waveguide length for Wg1.*

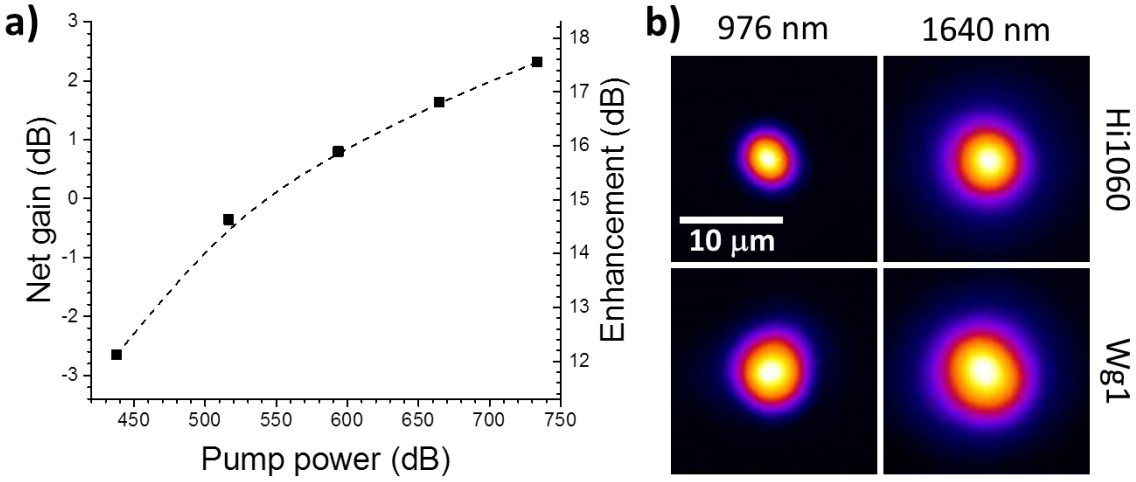

Figure 6.18: *(a) Net gain and enhancement of Wg1 at 1534 nm. The dashed line is a B-spline interpolation. (b) 976 and 1640 nm modes for Hi1060 fiber and Wg1.*

bulk material (11.6 dB) results in an estimation of $[La^{3+}]$ enrichment of 1.17 in the guiding region. This value allows estimating Δn using the data in **Figure 6.14** and the measured $[La^{3+}]$ of the bulk glass (21.8 %mol.), resulting in Δn is 1.8×10^{-2}. It is important noting that in this case, the increased refractive index corresponds to the third regime of Δn versus $[La^{3+}]$ (see **Figure 6.14**).

Figure 6.18b shows the guided modes for Hi1060 fiber and Wg1. It can be seen that Wg1 is single mode at both 976 and 1640 nm, with mode field diameters of 8.5 and 10.9 μm respectively. These values are compatible with $\Delta n \sim 10^{-2}$. Overlapping losses at 1640 nm are 0.37 $dB/facet$, and Fresnel losses are 0.21 $dB/facet$. This results in propagation losses of 0.4 dB/cm, which are very good for a home-made glass. The overlapping losses for 976 nm are higher, 1.15 $dB/facet$.

Although lasing experiments were performed, no lasing emission was observed for pump powers as high as 735 mW. This was attributed initially to the low lifetime (2.9 ms due to the high OH^- content) of the $^4I_{13/2}$ Er level in this glass, but as is described in **Section 6.4.3.2**, the high pump transparency must also contribute.

6.4.2.2. Waveguide in GPL4 glass

New waveguides were produced in home-made glasses with different doping levels. The best result was achieved in GPL4 glass (Er^{3+} and Yb^{3+} concentration of 1.5 %mol. and 2.9 %mol. respectively). This glass was designed for the best compromise between high doping level and Er^{3+} $^4I_{13/2}$ level lifetime (4.1 ms).

The waveguide with the best performance in GPL4 glass (Wg2) was inscribed at 500 kHz, 380 nJ, 1.2 mm slit width at 60 $\mu m/s$ (PW4) in a sample of 22 mm length. The

characterization of the waveguide was used for estimating the optimum length (~16 *mm*). The sample was then cut to 16.5 *mm* and characterized again. **Figure 6.19**a shows the net gain and enhancement as a function of pump power. The point where the second diode is switched on can be identified by the sudden increase in gain. The maximum obtained net gain is 5.0 *dB*, which corresponds to an enhancement of 22.5 *dB*. In this case, the profile shows saturation for high pump powers. Pump transparency occurs at ~ 350 *mW*, just after switching on the second diode. Total losses of this waveguide are 3.6 *dB*, resulting in an internal gain of 8.6 *dB*. This is equivalent to 5.2 *dB/cm* of internal gain per unit of length. This was the highest ever reported value for amplification per unit of length at 1534 *nm* for a fs-laser written amplifier in glass when this result was reported [20], showing the potential of these waveguides.

Figure 6.19b shows the modes of the coupling fiber and Wg2, with mode field diameters of 11.6 and 18.4 *μm* at 976 and 1640 *nm* respectively. Again, the mode of the waveguide is larger than the mode of the fiber, producing coupling losses of 1.0 *dB/facet*. The coupling losses at 976 *nm* are lower in this case, 0.5 *dB/facet*. Propagation losses are moderate, 1.0 *dB/cm*, which are quite acceptable for a home-made glass. However, even if the losses of the waveguide are not low, the result is better than in the previous case. Calculations indicate that this may be likely due to the higher lifetime and lower Er^{3+} doping level of GPL4 (2.9 *ms* and 3.0 %mol.) compared to GPL3 (4.1 *ms* and 1.5 %mol.).

Measured absorption of the waveguide at 1534 *nm* was 13.9 *dB*, which compared to the 11.3 *dB* expected for the unmodified material, yields an estimation for $[La^{3+}]/[La^{3+}]_{bulk}$ of 1.23. This result cannot be extrapolated to calculate a Δn, as the lanthanides concentration falls into the second regime of **Figure 6.14** (refractive index little or no sensitive to La^{3+}

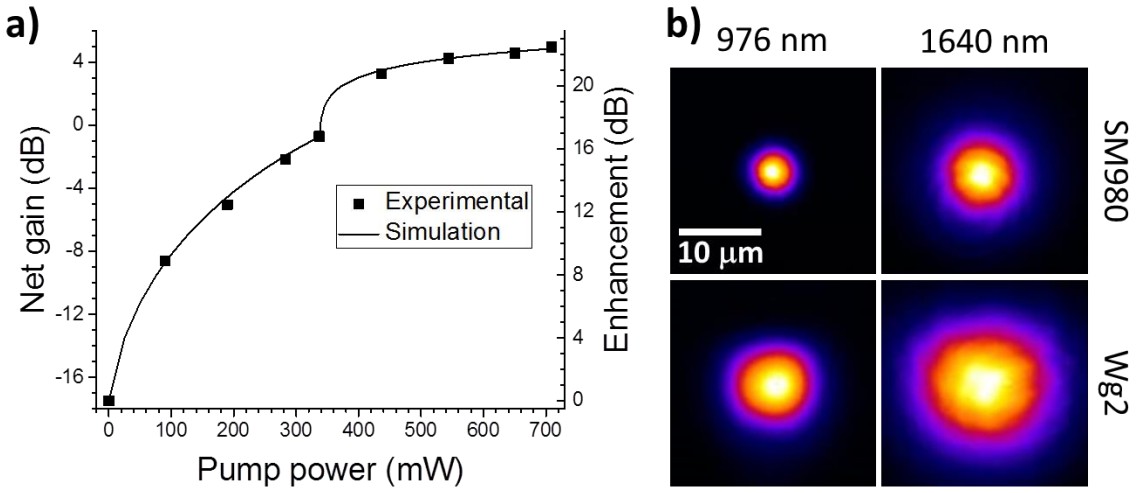

Figure 6.19: *(a) Net gain and enhancement of Wg2 at 1534 nm. The dashed line is a B-spline interpolation. (b) 976 and 1640 nm modes for SM980 fiber and Wg1. Figure adapted from [20].*

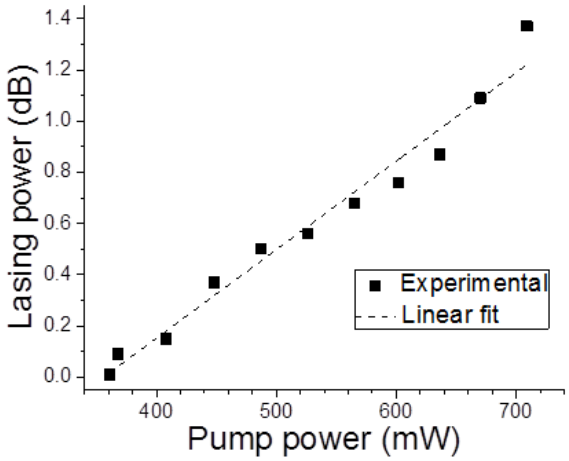

Figure 6.20: *Laser emission power versus incident pump power.*

concentration). This means that the produced Δn must be lower than if the initial glass La^{3+} concentration would have been in regime 1 or 3. The smaller expected Δn in the guiding region in this case when compared to Wg1 and the waveguides in **Section 6.4.3.1** can be appreciated by the larger mode field diameter and higher propagation losses.

Lasing experiments were also performed in Wg2. The linear cavity was constructed using P1 and T1 fiber Bragg gratings (Bragg grating parameters are listed in **Table 3.7**). The result is shown in **Figure 6.20**. A slope efficiency of 0.3% and a lasing threshold around 350 mW were obtained. Although these results are well below the state of the art of fs-laser written lasers in phosphate glass [21], they show the feasibility of producing lasers, even in a home-made low lifetime glass. The spectrum of the laser (and the overall efficiency) was restricted by the grating parameters, so it was centered in 1532.55 nm with a bandwidth of 0.25 nm.

In conclusion, the results achieved in home-made glasses were very promising. Wg1 showed great potential in amplification for pump powers in the order of watts, while Wg2 achieved an internal gain per unit of length as high as 5.2 dB/cm for a total pump power of 710 mW, along lasing emission. However, the relatively high losses of the waveguides and the low lifetime of Er^{3+} in the home-made samples limited the efficiency of the produced devices. For this reason, new waveguides were produced in commercial glass.

6.4.3.Commercial glass

Com1 glass sample, due to its larger scale fabrication process, shows higher homogeneity and higher lifetime (8.5 ms due to the low OH^- content). This makes this glass more suitable for lasing applications, although less efficient for producing short length

amplifiers due to its lower active ion concentration. The characterization setups used were those at GPL-CSIC.

6.4.3.1. Optical amplifiers

Many of the waveguides produced in this glass were found to be highly efficient. Wg3 and Wg4 are two illustrative examples of waveguides with different La^{3+} enrichments in the guiding region. It is worth noting that both of them were produced in the same glass sample. Their writing parameters are listed in **Table 4.1**.

Table 6.2: *Writing parameters of Wg3 and Wg4.*

Wg.	Pulse energy (nJ)	Slit width (mm)	Scanning speed (µm/s)	Pulse duration (fs)	Focusing lens (NA)
Wg3	580	1.4	60	400	AL2 (0.68)
Wg4	760	1.2	80	400	AL2 (0.68)

First, the passive behavior of the waveguides was characterized for a waveguide length of 23 mm. **Figure 6.22** shows the guided modes of SMF28 fiber and the two waveguides at 976 and 1640 nm. Wg3 is strictly monomode at both wavelengths, with mode field diameters of 9.1 and 16.7 μm at 976 and 1640 nm respectively. Wg4 fundamental mode has diameters of 9.3 and 16.6 μm at 976 and 1640 nm respectively, but higher order modes can be excited if the fiber is not correctly aligned with the waveguide. This indicates Wg4 has a high $[La^{3+}]$, and thus a high Δn in the guiding region. The losses of the waveguides are shown in **Table 6.3**. Wg3 shows lower losses in every parameter, although both waveguides show an excellent performance.

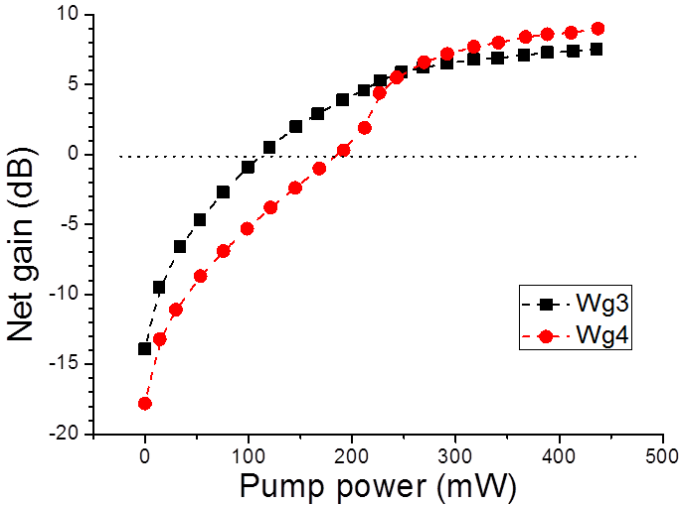

Figure 6.21: *Net gain of Wg3 and Wg4 at 23 mm. Dashed lines are B-spline interpolations. Dotted line indicates a net gain of 0 dB in order to better visualize pump transparency.*

Table 6.3: *Characterization results of Wg3 and Wg4 at 23 mm.*

Passive characterization					
Wg.	Total losses at 1640 nm (dB)	Overlapping losses at 1640 nm (dB)	Displacement losses (dB)	Propagation losses at 1640 nm (dB/cm)	Overlapping losses at 976 nm (dB)
Wg3	1.3	0.31	0.2	0.20	0.82
Wg4	1.8	0.36	0.4	0.28	1.47
Active characterization					
Wg.	Max. net gain (dB)	Max. internal gain (dB)	Absorption at 1534 nm (dB/cm)	Pump transparency (mW)	Enrichment in Er^{3+}
Wg3	7.5	8.8	5.48	110	1.19
Wg4	9.0	10.8	6.96	180	1.50

Figure 6.21 shows the net gain of Wg3 and Wg4 pumped up to a maximum of 475 mW. The most important parameters of the characterization are also listed in **Table 6.3**. In the net gain plot some differences between Wg3 and Wg4 can be appreciated. Wg3 has a maximum net gain of 7.5 dB, while Wg4 reaches 9.0 dB. Also, there is a great difference in the absorption and pump transparency between both waveguides. This is caused by the different $[Er^{3+}]$ enrichments in the guiding region: 1.19 for Wg3 and 1.50 for Wg4. This means that the effective Er^{3+} and Yb^{3+} doping level of Wg4 is higher than for Wg3.

The dependence of the main amplifier parameters with respect to the waveguide length was also studied. The experiment was performed by reducing the length of the sample in steps of ~ 2 mm and measuring all the magnitudes each time. However, some problems arised during the process. Initially, the sample had a small crack near Wg3 which made impossible to measure the waveguide at 21 mm length. Also, specially for the shorter lengths, the pump absorption increased the temperature of the waveguide, which heated the index

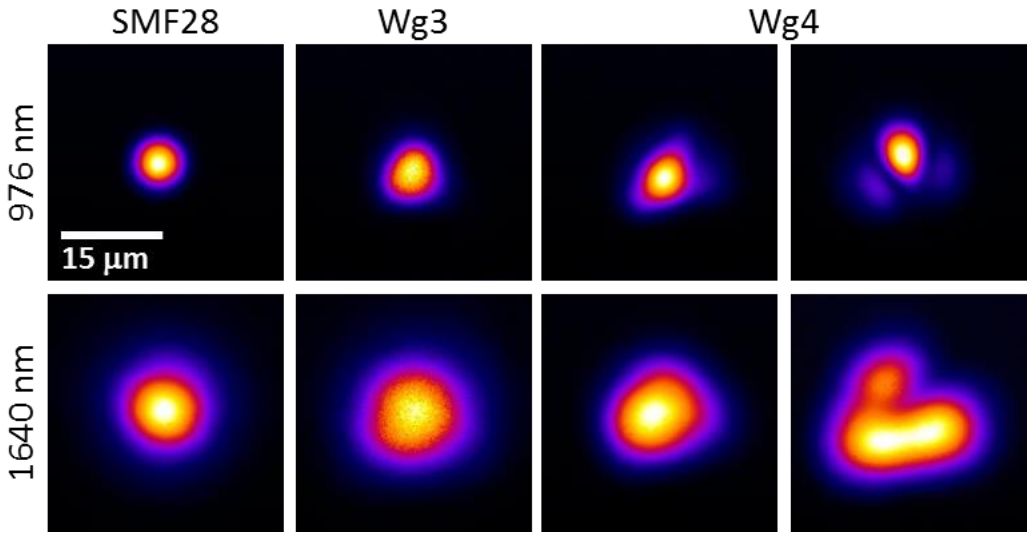

Figure 6.22: *Guided modes of SMF28 fiber, Wg3 and Wg4 at 976 and 1640 nm. For Wg4, fundamental and higher order modes are shown.*

matching gel. Sometimes this lead to the the carbonization of the index matching gel, forcing to repolish the affected facet of the sample. It is worth noting that the maximum achieved internal gain per unit of length was 5.4 dB/cm for Wg4 at 11 mm, slightly higher than in Wg2 due to the shorter length. Also, it is worth noting the lowest achieved losses: 0.7 dB for Wg3 at 11.2 mm, much lower than the results for home-made glass.

Figure 6.23a shows the maximum net gain as a function of the waveguide length for different pump powers around 500 mW. The dashed line plots the simulated maximum net gain at a constant pump power of 500 mW. Although small discrepancies appear between experiment and simulation, the linear tendency is maintained. Also, the difference between experimental and simulated values is smaller for shorter waveguides, as saturation effects increase for shorter lengths.

Net gain increases with the waveguide length, indicating that the optimum length is longer than 23 mm. The calculated net gain at 500 mW pump power for longer waveguides is shown in **Figure 6.23b**. Wg4 has its maximum expected net gain (11.4 dB) at 34 mm, while

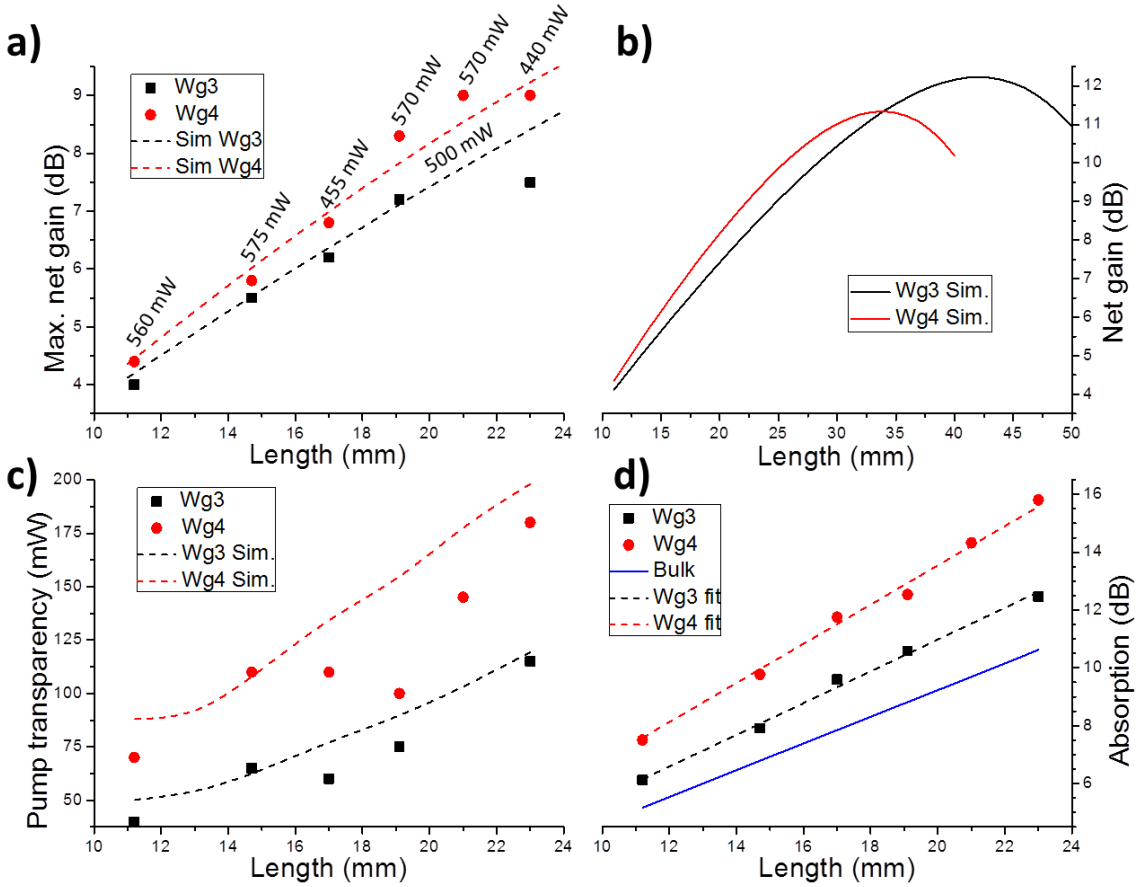

Figure 6.23: *(a) Experimental and calculated maximum net gain, (b) calculated net gain saturation for 500 mW of pump, (c) pump transparency level and (d) absorption versus waveguide length for Wg3 and Wg4. Labels in (a) correspond to maximum pump power. Linear fits in (d) were calculated with the intercept fixed to zero.*

Wg3 has it at 42 mm (12.2 dB). Wg4 shows an optimum length shorter than Wg4 due to its higher Er^{3+} and Yb^{3+} concentration, but the maximum net gain is higher for Wg3 due to its reduced losses.

Figure 6.23c shows the dependence of pump transparency value respect to the waveguide length. This is a parameter difficult to measure acurately: it is very sensitive to small misaligments (between the fiber and waveguide or in the perpendicularity of the polished end-facets) and requires interpolating the measured net gain. In general, calculated values are higher than experimental ones. The simulation shows that this parameter saturates for waveguide lengths below 13 mm for both waveguides.

The evolution of absorption as a function of waveguide length is shown in **Figure 6.23d**. It is possible to calculate an absorption coefficient from the linear fits (with intercept fixed to zero) included in the plot. This is more accurate than a single absorption measurement to estimate the Er^{3+} enrichment in the giding region. From the Er^{3+}enrichment, estimation of enrichment in $[La^{3+}]$ values of 1.20 and 1.47 in Wg3 and Wg4 respectively. From them, estimated Δn values are 1.0×10^{-2} and 2.5×10^{-2} respectively. Saturation regime in La^{3+} concentration may be reached for Wg4 (see **Figure 6.14**), so the real value of Δn may be somewhat lower. However, the multimodal behavior of the waveguide indicates that Δn value must be quite high.

The dependence of net gain as a function of the signal wavelength was measured for a waveguide length of 14.7 mm. The result is shown in **Figure 6.24**. Both waveguides produce over 1 dB of net gain in the range between 1525 and 1570 nm for 575 mW of total pump. Finally, as the waveguides are greatly heated by pump absorption (especially for shorter lengths), the thermal stability of the waveguides was tested. At 11.2 mm, the sample was annealed at 450 ^{o}C for one hour, with no change in the amplification properties of the

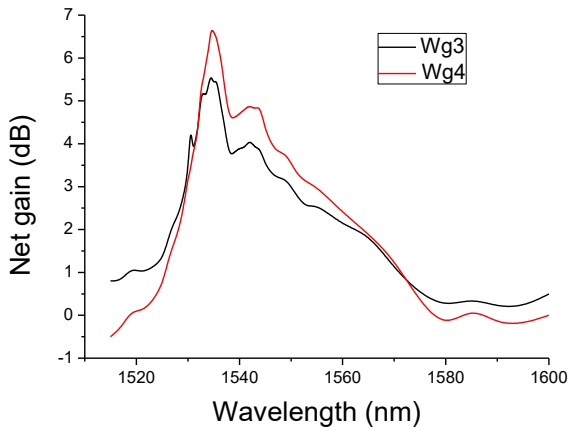

Figure 6.24: *Maximum net gain as a function of the signal wavelength of Wg3 and Wg4 for a waveguide length of 14.7 mm.*

waveguides.

6.4.3.2. Waveguide lasers

Lasing experiments were performed for Wg3 and Wg4 at different lengths. The used Bragg gratings were T2 and P2 (99.9% and 69% reflectivity with 1 nm bandwidth). Absorbed pump power calculation is described in **Chapter 3**. **Figure 6.25a** shows the best result in terms of maximum emitted power for each waveguide. In both cases, laser emission curves start to show saturation for the higher pump values. Maximum achieved laser emission is 112 mW for Wg3 and 68 mW for Wg4, with an absorbed power lasing threshold of 26.7 and 33.6 mW for Wg3 and Wg4 respectively. **Figure 6.25b** shows their corresponding laser emission spectra. Both are centered around 1534.3 nm, the central wavelength of the Bragg gratings, and their bandwidth is around 0.5 nm. The spectra rapidly vary over time, although maintaining the total emission power.

The laser slope efficiency and the absorbed pump lasing threshold as a function of waveguide length are shown in **Figure 6.26**. Slope efficiencies have been calculated fitting the points in the linear regime, excluding the ones near lasing threshold or in saturation regime. Wg3 produce more efficient lasers than Wg4 despite Wg4 shows higher net gain, which may result unexpected. However, Wg3 showed much lower pump transparency level. Laser emission is produced for pump powers that produce net gain, so reduced pump transparency must produce lower lasing thresholds. Anyway, it produces higher efficiencies as well. This means that this magnitude has to be considered in the design of efficient lasers.

Wg3 at 11.2 mm shows an experimental slope efficiency of 38.3% and a lasing threshold of 24.9 mW (shorter waveguides may yield higher efficiency, but saturation will

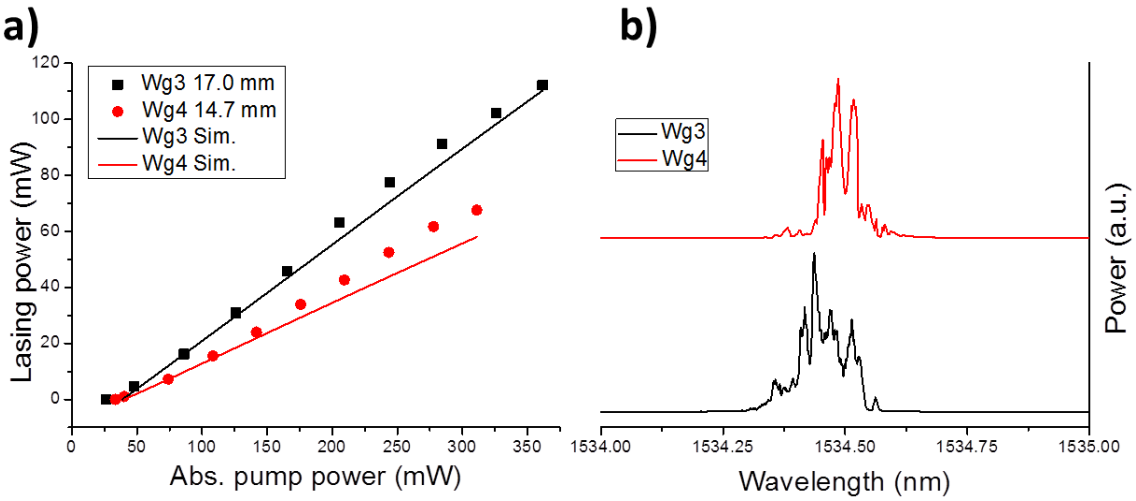

Figure 6.25: *(a) Laser emission as a function of pump power. (b) Lasing spectra of lasers in (a).*

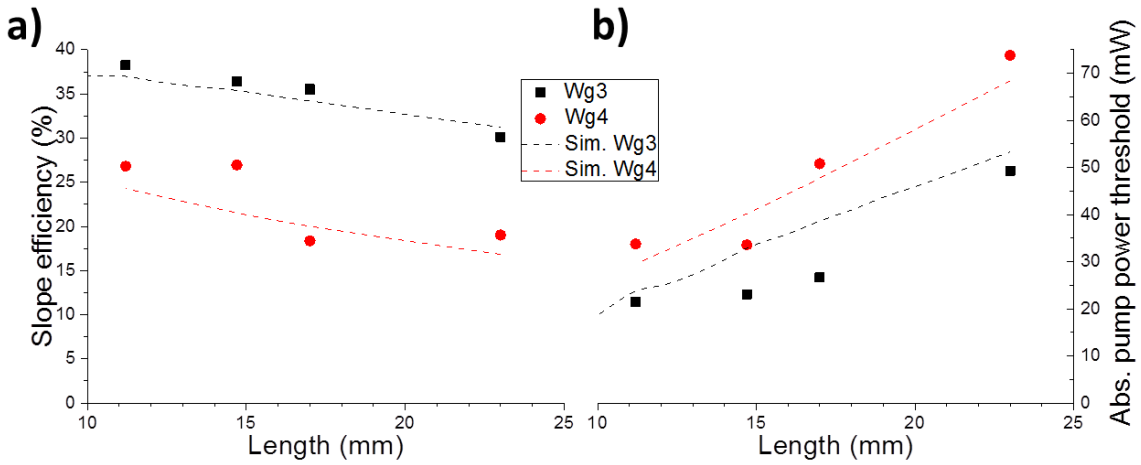

Figure 6.26: *Experimental and simulated slope efficiency (a) and absorbed pump lasing threshold (b) of Wg3 and Wg4 in a linear cavity configuration as a function of waveguide length.*

reduce the output power). This is the highest value achieved, to our knowledge, in a fs-laser written phosphate glass doped with Er^{3+} and Yb^{3+}, improving the result in [21]. It also outperforms some results obtained by other techniques, like the use of short active fibers instead of waveguides [22]; and shows a performance similar to that achieved by other standard techniques like reactive ion exchange [23] (46% slope efficiency with ~140 mW of lasing threshold for a 45 mm waveguide).

This result can be furtherly improved by changing the reflectivity of the output Bragg grating. **Figure 6.27a** shows the calculated slope efficiency versus grating reflectivity at different lengths for Wg3. For most waveguide lengths, a reduced grating reflectivity produces a higher slope efficiency, up to 42.3% for 20% reflectivity at 23 mm waveguide length. The corresponding lasing thresholds are shown in **Figure 6.27b**. As expected, lower reflectivities will produce higher thresholds. The best compromise between efficiency and lasing threshold

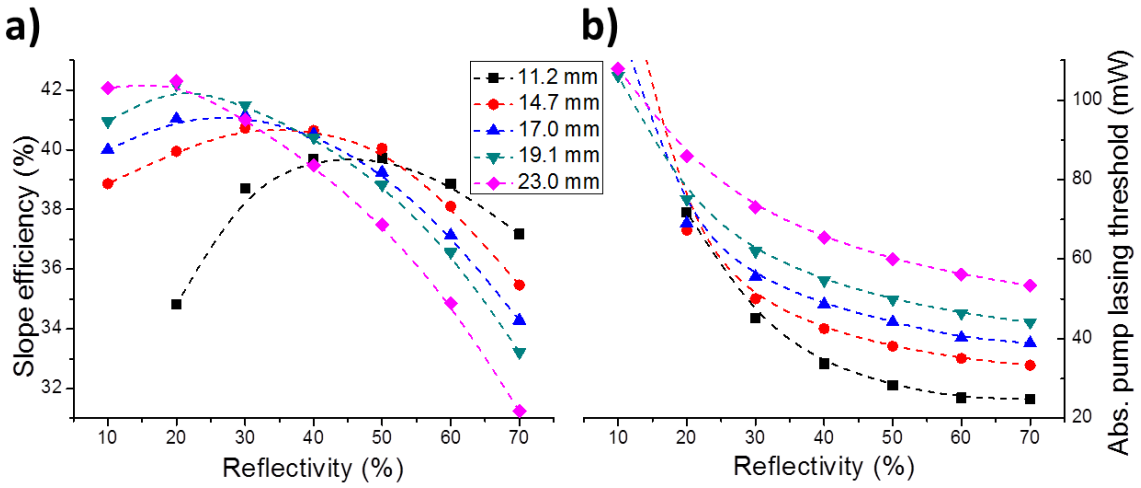

Figure 6.27: *Calculated slope efficiency (a) and absorbed pump lasing threshold (b) versus output Bragg grating reflectivity at different waveguide lengths for Wg3.*

is 40% reflectivity at 14.7 mm length, showing 40.7% slope and 42.5 mW threshold.

Finally, the effect of the Bragg grating bandwidth was studied experimentally for a 23 mm waveguide length using P2 and P3 (69% and 68% reflectivity and 1.0 and 0.2 nm bandwidth respectively), along with T2. The results are listed in **Table 6.4**. The result for P3 was worse in terms of efficiency and threshold, which cannot be attributed to the small difference in reflectivity. The reason is that not all the spectral gain can be used. Laser emission spectra with P2 showed a typical bandwidth around 0.5 nm, so increasing the bandwidth of the gratings should not improve laser efficiency or threshold.

Table 6.4: *Lasing efficiency and threshold of Wg3 and Wg4 using different fiber Bragg grating bandwidths.*

	P2 (Ref = 69%, Δλ = 1.0 nm)		P3 (Ref = 67%, Δλ = 0.2 nm)	
Wg.	Slope efficiency (%)	Abs. pump lasing threshold (mm)	Slope efficiency (%)	Abs. pump lasing threshold (mm)
Wg3	30.1	49.3	10.0	67.9
Wg4	19.0	73.8	13.1	88.0

6.5. Summary and conclusions

In this chapter, the fabrication of sub-surface waveguides in phosphate glasses by ultrashort laser pulses at high repetition rate, along with its application for implementing waveguide-based amplifiers and lasers fabricated by fs-laser irradiation ion migration has been studied.

First the influence of the irradiation parameters in the energy deposition profile at LRR has been analyzed in order to design a strategy for producing high performance waveguides. Then, the waveguide morphology has been studied. It has been found that the guiding region size can be controlled by the combination of numerical aperture, slit width and pulse energy.

It has been confirmed that the waveguides in this case are formed by local modifications of the glass composition caused by an ion migration mechanism. The refractive index change is found to be due to an increase of the La^{3+} local concentration. This mechanism leads to refractive index changes up to 1.5×10^{-2}, although higher values can be achieved using different glass compositions or irradiation conditions. Also, it has been determined that the La^{3+} local concentration of waveguides can be determined in glasses doped with Er^{3+} by measuring the total absorption of the waveguide, and comparing it with the absorption of the unmodified material. The ion migration mechanism has been studied by acquiring microscopy images of the plasma emission during the irradiation. It has been found

that the ion migration occurs along the longest plasma axis, which must be related to the induced thermal gradients. Also, the use of a slit reduces the size of the plasma distribution and its sensitivity to changes in pulse energy, which explains the better control in the structure size for slit-shaped beams. The plasma distribution, and thus the waveguide morphology can be rotated or inverted by adjusting the inscribing beam wavefront introducing spherical aberration.

Several waveguide-based optical amplifiers have been implemented, both in home-made and commercial phosphate glasses doped with Er^{3+} and Yb^{3+}. Short waveguides in home-made heavily doped glass show moderate losses but high internal gain. Wg1 (14 mm) shows intermediate losses (2.1 dB) and internal gain (4.4 dB) upon pumping at 735 mW. However, it is far from saturation regime, so gain can be furtherly increased for higher pump powers. Wg2 (16.5 mm) shows higher internal gain (5.2 dB/cm) and lasing emission, although higher losses (3.6 dB).

The ion migration mechanism enables producing waveguides with different properties in the same glass sample. Wg3 is an example of a moderate increase in La^{3+} concentration (20%) in the guiding region. It shows very low losses (down to 0.7 dB at 11.2 mm) and very efficient lasing emission (38.3% slope efficiency and 25 mW of absorbed pump lasing threshold), although moderate net gain as optical amplifier (7.5 dB at 23 mm pumped with 470 mW). Wg4, which has a larger increase of La^{3+} concentration (47%), shows higher losses (1.3 dB at 11.2 mm) and lower laser efficiency (26.8% slope efficiency and 34 mW threshold), but higher net gain (9.0 dB at 23 mm). Both amplifiers and lasers performance can be furtherly increased by adjusting the waveguide length, or the fiber Bragg grating reflectivity in the case of lasers.

6.6. References

[1] S. M. Eaton and P. R. Herman, "Passive photonic devices in glass," in *Femtosecond Laser Micromachining: Photonic and microfluidic devices in transparent materials*, R. Osellame, G. Cerullo, and R. Ramponi, Eds., ed: New York Springer, 2012.

[2] M. J. Weber, "Science and technology of laser glass," *Journal of Non-Crystalline Solids,* vol. 123, pp. 208-222, 1990.

[3] J. D. B. Bradley and M. Pollnau, "Erbium-doped integrated waveguide amplifiers and lasers," *Laser & Photonics Reviews,* vol. 5, pp. 368-403, 2011.

[4] B. Rethfeld, "Free-electron generation in laser-irradiated dielectrics," *Physical Review B,* vol. 73, p. 035101, 2006.

[5] Y. Shimotsuma, P. G. Kazansky, J. Qiu, and K. Hirao, "Self-Organized Nanogratings in Glass Irradiated by Ultrashort Light Pulses," *Physical Review Letters,* vol. 91, p. 247405, 2003.

[6] J. A. Valles, J. Solis, J. A. Sanchez-Martin, A. R. d. l. Cruz, M. A. Rebolledo, and A. Ferrer, "Assessment of Rayleigh and non-Rayleigh Contributions to the Transmission Losses in fs-Laser Written Er/Yb- Codoped Phosphate Glass Waveguides," *Journal of Laser Micro/Nanoengineering,* vol. 5, pp. 39-42, 2010.

[7] J. del Hoyo, R. M. Vazquez, B. Sotillo, T. T. Fernandez, J. Siegel, P. Fernández*, et al.*, "Control of waveguide properties by tuning femtosecond laser induced compositional changes," *Applied Physics Letters,* vol. 105, p. 131101, 2014.

[8] T. Toney Fernandez, P. Haro-González, B. Sotillo, M. Hernandez, D. Jaque, P. Fernandez*, et al.*, "Ion migration assisted inscription of high refractive index contrast waveguides by femtosecond laser pulses in phosphate glass," *Optics Letters,* vol. 38, pp. 5248-5251, 2013.

[9] T. T. Fernandez, B. Sotillo, J. d. Hoyo, J. A. Vall, x00E, V. R. M*, et al.*, "Dual Regimes of Ion Migration in High Repetition Rate Femtosecond Laser Inscribed Waveguides," *IEEE Photonics Technology Letters,* vol. 27, pp. 1068-1071, 2015.

[10] R. Shannon, "Revised effective ionic radii and systematic studies of interatomic distances in halides and chalcogenides," *Acta Crystallographica Section A,* vol. 32, pp. 751-767, 1976.

[11] R. K. Brow, E. Metwall, and D. L. Sidebottom, "Properties and structure of lanthanum phosphate glasses," *Proc. SPIE Inorganic Optical Materials II,* vol. 4102, p. 7, 2000.

[12] M. Karabulut, E. Metwalli, and R. K. Brow, "Structure and properties of lanthanum–aluminum–phosphate glasses," *Journal of Non-Crystalline Solids,* vol. 283, pp. 211-219, 2001.

[13] A. Arriola, S. Gross, N. Jovanovic, N. Charles, P. G. Tuthill, S. M. Olaizola*, et al.*, "Low bend loss waveguides enable compact, efficient 3D photonic chips," *Optics Express,* vol. 21, pp. 2978-2986, 2013.

[14] S. M. Eaton, H. Zhang, M. L. Ng, J. Li, W.-J. Chen, S. Ho*, et al.*, "Transition from thermal diffusion to heat accumulation in high repetition rate femtosecond laser writing of buried optical waveguides," *Optics Express,* vol. 16, pp. 9443-9458, 2008.

[15] Y. Dai, G.-J. Yu, G.-R. Wu, H.-L. Ma, X.-N. Yan, and G.-H. Ma, "The effect of spherical aberration on temperature distribution inside glass by irradiation of a high repetition rate femtosecond pulse laser," *Chinese Physics B,* vol. 21, p. 025201, 2012.

[16] I. Miyamoto, K. Cvecek, and M. Schmidt, "Evaluation of nonlinear absorptivity in internal modification of bulk glass by ultrashort laser pulses," *Optics Express,* vol. 19, pp. 10714-10727, 2011.

[17] M. Sun, U. Eppelt, W. Schulz, and J. Zhu, "Role of thermal ionization in internal modification of bulk borosilicate glass with picosecond laser pulses at high repetition rates," *Optical Materials Express,* vol. 3, pp. 1716-1726, 2013.

[18] T. T. Fernandez, J. Siegel, J. Hoyo, B. Sotillo, P. Fernandez, and J. Solis, "Controlling plasma distributions as driving forces for ion migration during fs laser writing," *Journal of Physics D: Applied Physics,* vol. 48, p. 155101, 2015.

[19] F. Luo, J. Song, X. Hu, H. Sun, G. Lin, H. Pan*, et al.*, "Femtosecond laser-induced inverted microstructures inside glasses by tuning refractive index of objective's immersion liquid," *Optics Letters,* vol. 36, pp. 2125-2127, 2011.

[20] J. Hoyo, V. Berdejo, T. T. Fernandez, A. Ferrer, A. Ruiz, J. A. Valles*, et al.*, "Femtosecond laser written 16.5 mm long glass-waveguide amplifier and laser with 5.2 dB cm −1 internal gain at 1534 nm," *Laser Physics Letters,* vol. 10, p. 105802, 2013.

[21] G. Della Valle, S. Taccheo, R. Osellame, A. Festa, G. Cerullo, and P. Laporta, "1.5 µm single longitudinal mode waveguide laser fabricated by femtosecond laser writing," *Optics Express,* vol. 15, pp. 3190-3194, 2007.

[22] S. H. Xu, Z. M. Yang, T. Liu, W. N. Zhang, Z. M. Feng, Q. Y. Zhang*, et al.*, "An efficient compact 300 mW narrow-linewidth single frequency fiber laser at 1.5 µm," *Optics Express,* vol. 18, pp. 1249-1254, 2010.

[23] G. D. Valle, A. Festa, G. Sorbello, K. Ennser, C. Cassagnetes, D. Barbier*, et al.*, "Single-mode and high power waveguide lasers fabricated by ion-exchange," *Optics Express,* vol. 16, pp. 12334-12341, 2008.

Chapter 7
Conclusions

In this thesis, different aspects of the fabrication of photonic devices by fs-laser structuring of dielectrics have been studied. The thesis had three main objectives: producing efficient photonic devices on the surface of crystalline materials, developing a low computational cost simulation tool capable of simulating the nonlinear propagation of ultrashort laser pulses inside dielectric materials, and generating high efficiency optical amplifiers and lasers by fs-laser induced ion migration effects.

The production of waveguides in the surface of crystalline samples using different types of laser beams has been analyzed. Optimized ablation channels inscribed using multiplexed Gaussian beams show a wall roughness with a feature size of ~250 nm. This enables the production of waveguides with propagation loses of the order of 1 dB/cm. In the case of $KY(WO_4)_2$ doped with Yb^{3+}, propagation losses lower than 1.5 dB/cm have been obtained using this approach. A mirror-less laser cavity was implemented in this waveguide (8.2 mm), achieving a 78% of slope efficiency at 1001 nm. The losses of the waveguides could be reduced even further (below 0.5 dB/cm) for waveguides in load configuration. This reduction potentially enables producing even more efficient lasers.

A simulation code (*Propagador*) capable of simulating the nonlinear propagation inside dielectric materials in realistic laser processing conditions at low repletion rate (LRR), with calculation time of the order of few minutes in an ordinary computer has been developed. The conditions where the approximations made in the *Propagador* model remain valid have been thoroughly discussed. Simulations performed using *Propagador* matched the results obtained in soliton shaping experiments, enabling the determination of the nonlinear coefficients of the glass where these experiments were performed. The calculated values were nearly identical to the ones obtained using more complex models. Also, the comparison between *Propagador* simulations and sub-surface laser-written waveguides (at LRR) again allowed determining of the material nonlinear coefficients upon multiple pulse exposure. Finally, some other applications of *Propagador* were shown, like the use of SLMs for pre-compensating the distortion generated in the energy deposition profiles by spherical aberration and nonlinear propagation and absorption.

The feasibility of producing highly efficient active photonic devices inside glasses using ion migration induced by fs-laser irradiation at high repetition rate (HRR) has been demonstrated. Waveguides are produced by a cross-migration mechanism between K^+ and La^{3+} ions, Δn being determined by the local enrichment in La^{3+}. A maximum Δn value of 1.5×10^{-2} was achieved, which can potentially be increased for different glass compositions or irradiation conditions. The feasibility of controlling the size of the guiding region, and the refractive index change via laser-writing parameters has been similarly demonstrated. It has been shown that the enrichment in La^{3+} ions, and thus Δn, can be determined by measuring the optical properties of waveguides co-doped with Er^{3+}. The control of the waveguide features via laser writing parameters enables fabricating highly efficient waveguides with different active properties in the same glass. Two active waveguides were fabricated in the same sample doped with Er^{3+} and Yb^{3+}, one with a net gain of 9 dB, and another with lasing slope efficiency of 38% and lasing threshold of 22 mW at 1534 nm. This is the highest slope efficiency at 1534 nm ever achieved in a fs-laser written waveguide in phosphate glass.

Appendix A
Computer codes

This appendix is dedicated to show the different programs written during the development of this thesis. All of them were written in MATLAB R2012b, and they will run in newer and older versions (except *Propagador* which will run only in newer versions due to its use of Graphical User Interfaces, GUIs). The programs can be found here:

https://www.cubbyusercontent.com/pl/Programs/_512e817f9fe1449cbc95c30f00c72c6b.

A.1. Propagador

Propagador is the program used for simulating the nonlinear propagation of laser pulses inside dielectric materials. The model and the results derived from it were described in **Chapter 5**. The GUI allows users to change parameters without varying the code, and includes utilities like storing all the simulation parameters, saving the images in many formats or printing the main simulation parameters and results as .txt files.

Figure A.1 shows the GUI where the main simulation parameters are set, from the initial pulse properties as wavelength and energy, to the focal length utilized for focusing the beam or the material nonlinear parameters. It includes a prediction of the focal volume size

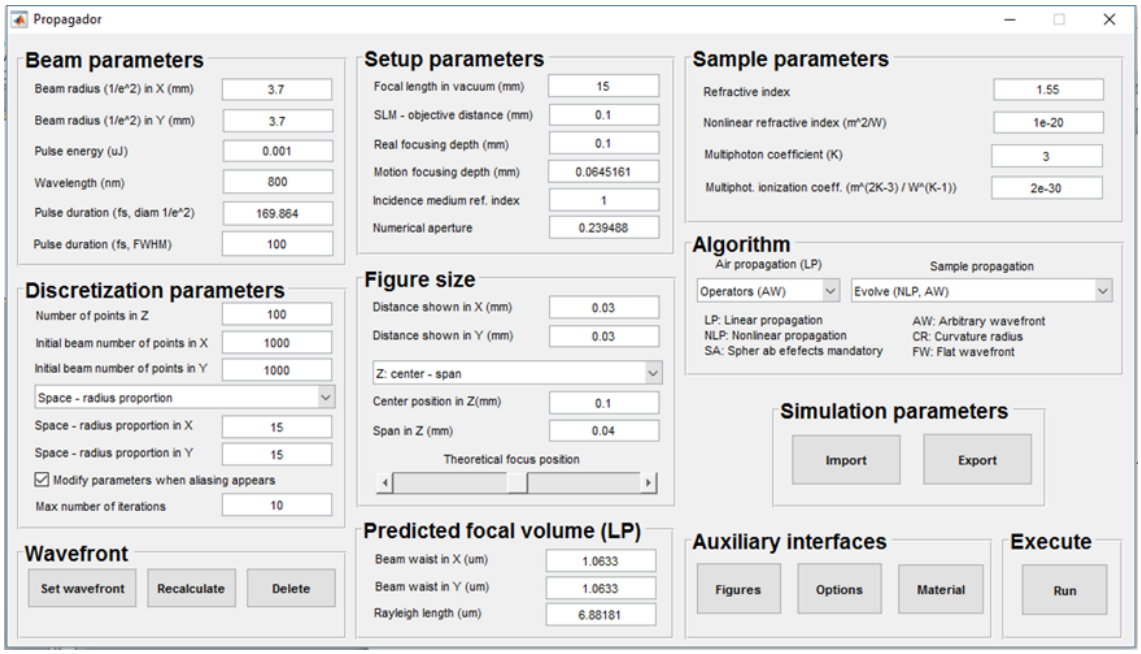

Figure A.1: *Propagador main simulation parameters GUI.*

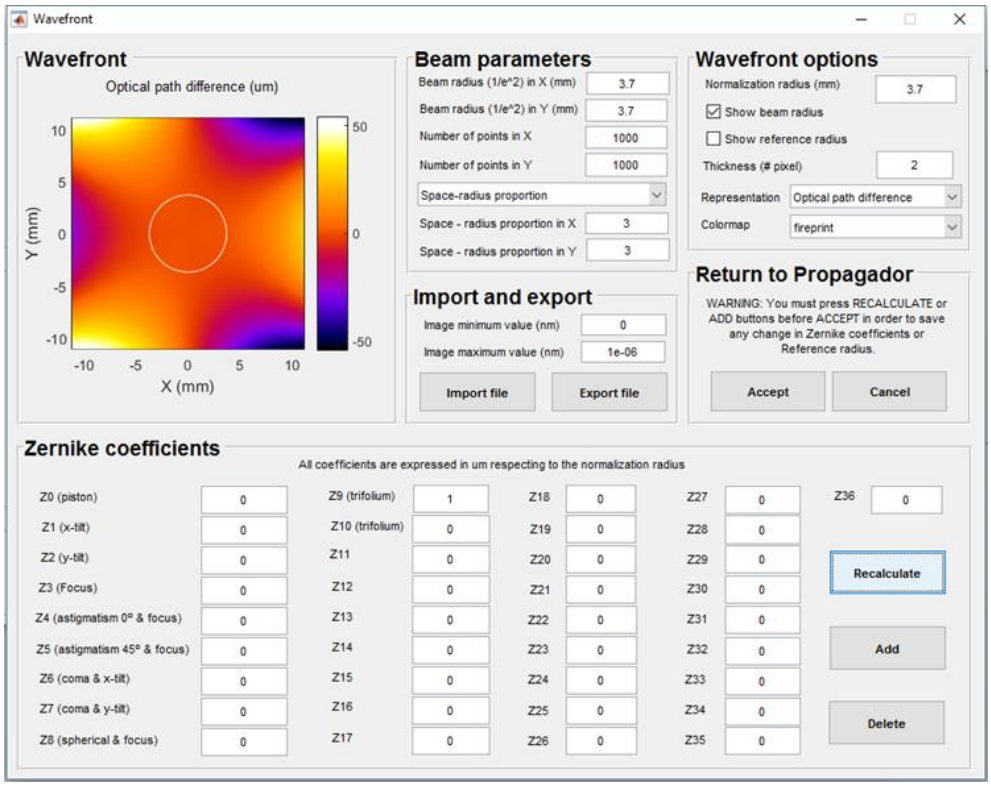

Figure A.2: *Propagador initial beam wavefront GUI.*

upon linear propagation, and setting the algorithms for air and material propagation. It may open new windows for selecting many other parameters of the simulation.

Figure A.2 shows the GUI for setting the wavefront of the beam at the beginning of propagation. It may calculate it in a base of the 36 first Zernike polynomials, or can be inserted from an external file. Also, the beam wavefront may be plotted in optical path difference or phase representation.

Figure A.3 shows the GUI for setting which 1D and 2D figures of the magnitudes of the

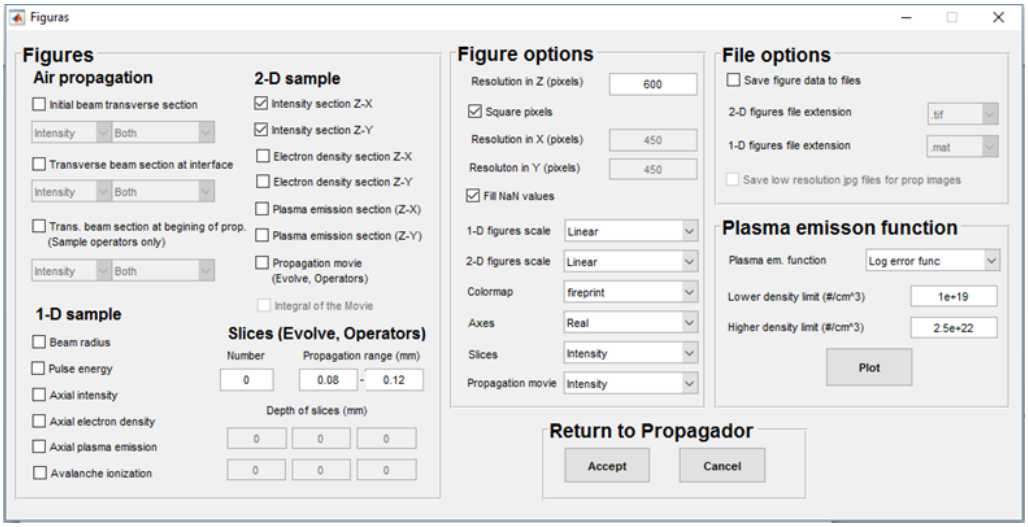

Figure A.3: *Propagador figures GUI.*

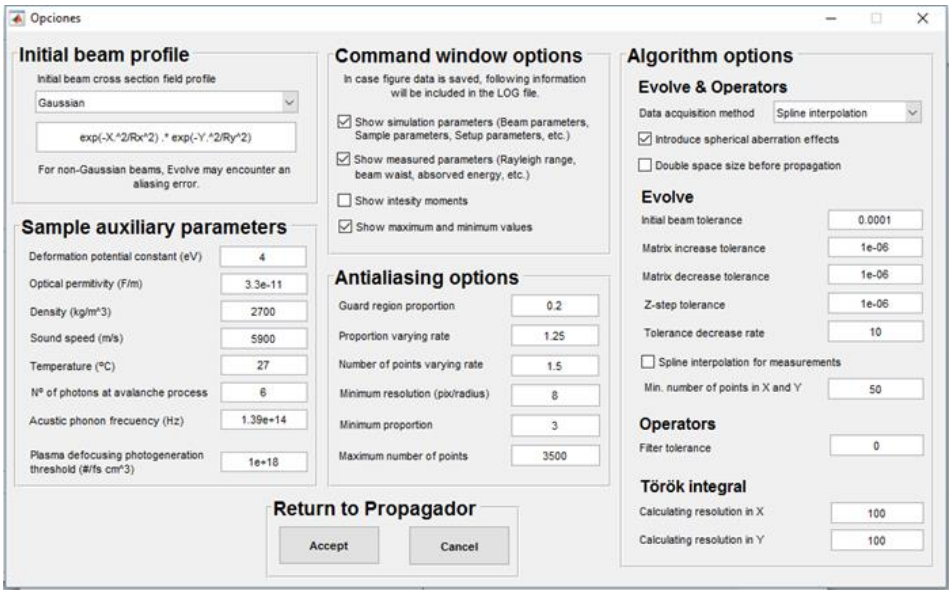

Figure A.4: *Propagador options GUI.*

beam are going to be plot. One interesting feature is plotting the cross section of the beam while it is propagating inside the dielectric sample, like a movie. It also includes some of the figure options, like resolution, false color scale (colormap), or whether plots are going to be saved and in which format.

Figure A.4 shows the options GUI, which includes some of the algorithm options that are not often changed between simulations. There is a fifth window (Material) intended for storing the refractive index and nonlinear parameters for several materials, but it has not been implemented.

Propagador is a long and complex program (weights ~2.5 MB without any saved file), and would not make sense to print here its full extension here.

A.2. Gerchbert-Saxton algorithm

The calculation of the phase map required for multiplexing the beam is performed by using a weighed Gerchbert-Saxton algorithm. The algorithm was described in **Chapter 3**. The code of the program is the following:

```
function WGS
clc;
%% Variables
% Files
filename = '7dots_7pixSep_768x768';
formatIn = 'bmp';
fileIntensity = []; % 'FFT_20x20mm_Stinray 5-2-1'; %  BMP only
% SLM
sizeX = 20e-3;          sizeY = 20e-3;
pixelsX = 768;          pixelsY = 768;
maxLevel = 220;         minLevel = 0;
% Save
```

```
formatOut = 'bmp';      turns = 0;
FIflipH = false;        FIflipV = false;
FIturn = false;
% Illumination (Beam radius)
Rx = 3.5e-3;            Ry = Rx;
% Algorithm
max_error=0.3E-2;       max_iter=100;
typePhase = 'random';   linearAng = 1e10;
% Plot figures
figuras = [1 1];

%% Focal plane desired intensity distribution
I_deseada = double(imread(filename,formatIn));% Load file
if ndims(I_deseada) > 2
    I_deseada = I_deseada(:,:,1);
end
I_deseada = double(I_deseada > 0);

%% Initial field
% Space
x_o=linspace(-sizeX/2,sizeX/2,pixelsX);
y_o=linspace(-sizeY/2,sizeY/2,pixelsY);
[X_O,Y_O] = meshgrid(x_o,y_o);
% Initial
if ~isempty(fileIntensity)
    % From file
    I = double(imread(fileIntensity,'bmp'));
    s = size(I);
    xaux = linspace(-sizeX/2,sizeX/2,s(2));
    yaux = linspace(-sizeY/2,sizeY/2,s(1));
    [Xaux,Yaux] = meshgrid(xaux,yaux);
    Uo = sqrt(interp2(Xaux,Yaux,I,X_O,Y_O));
    Aj = abs(Uo);
    Aj = Aj - min(Aj(:));
    Aj = Aj/max(Aj(:));
    if FIflipH
        Aj = flipdim(Aj,2);
    end
    if FIflipV
        Aj = flipdim(Aj,1);
    end
    if FIturn
        Aj = Aj';
    end
else
    % Gaussian beam
    Uo = exp(-X_O.^2/Rx^2 - Y_O.^2/Ry^2);
    Aj=abs(Uo);     % Only amplitude
end

%% Plot initial field and desired distribution
if figuras(1)
    figure(1);              clf(1,'reset')
    subplot(1,2,1);         pcolor(Aj.^2)
    shading flat;           axis image;
    title('Amplitud inicial en el SLM');
    xlabel('Position (m)'); ylabel('Position (m)');
    subplot(1,2,2);         pcolor(I_deseada)
    shading flat;           axis image;
    title('Amplitud deseada en el plano focal')
    xlabel('Position (m)'); ylabel('Position (m)');
    figure(2)
    clf(2,'reset');         title('Error')
end

%% Algorithm main loop
% Calculate initial phase in Fouries space
switch typePhase
```

```
    case 'random'
        theta_m = rand(pixelsY,pixelsX);
    case 'linear'
        theta_m = wrapTo2Pi(linearAng*(X_O.*Y_O).^2);
end
Am = ifftshift(I_deseada);          Ws = Am;
% Iterations
for k=1:max_iter
    % Create the field in Fourier space with last phase and weighs
    Um = Ws.*exp(1i.*theta_m);
    % Back-propagation to real space
    Uj = ifft2(Um);
    % Extract phase
    theta_j = angle(Uj);
    % New field with the calculated phase and the real amplitude
    Uj_new = Aj.*exp(1i.*theta_j);
    % Propagation to Fourier space
    Um = fft2(Uj_new);
    % Normalize amplitude
    Um_norm = abs(Um)./(max(max(abs(Um))));
    % Calculate error
    error_rmse = rmse(Um_norm, Am);
    % Plot error
    plot(k,error_rmse,'*','MarkerSize',6);
    refreshdata(2)
    drawnow;                hold on
    % Results of iteration
    theta_m = angle(Um);    % Extract phase
    Ws = Pesos(abs(Um), Am, Ws);    % Calculate new weighs
end
hold off
Um_mask=Um.*Am;
u=1-(max(abs(Um(find(Um_mask))))-
min(abs(Um(find(Um_mask))))/(max(abs(Um(find(Um_mask))))+min(abs(Um(find(Um_m
ask)))))

%% Save files
switch formatOut
    case 'mat'
        fn = filename;
        var = minLevel + mat2gray(wrapTo2Pi(theta_j)).*(maxLevel-minLevel);
        var = uint8(var);
        save(fn,'var');
        if turns
            % Flip horizontal
            var = flipdim(var,2);   fn = [filename,'_flipH'];
            save(fn,'var');
            % Flip horizontal & vertical
            var = flipdim(var,1);   fn = [filename,'_flipHV'];
            save(fn,'var');
            % Flip vertical
            var = flipdim(var,2);   fn = [filename,'_flipV'];
            save(fn,'var');
        end
end

%% Plot final intensity distribution and the phase map that generates it
if figuras(2)
    figure(3);          clf(3,'reset')
    subplot(1,2,1);     pcolor(abs(fftshift(Um)))
    colormap(jet);      shading flat;
    axis image;         colorbar
    title('Final intensity')
    subplot(1,2,2);     pcolor(wrapTo2Pi(theta_j))
    shading flat;       axis image;
    title('Phase map')
end
shading flat
```

```
function r=rmse(data,estimate)
% Function to calculate root mean square error from a data vector or matrix
% and the corresponding estimates.
% Note: data and estimates have to be of same size

% delete records with NaNs in both datasets first
I = ~isnan(data) & ~isnan(estimate);
data = data(I); estimate = estimate(I);
r=sqrt(sum((data(:)-estimate(:)).^2)/numel(data));

function Mat_pesos = Pesos(U_calculada, U_deseada, Weights)

% Function for calculating the weights corresponding to each point of the
% intensity distribution. Extracted from Leonardo et al. Computer generation
% of optimal holograms for optical trap arrays. Opt. Express (2007) vol.
% 15 pp. 1913.
U_mask = U_calculada .* U_deseada;
U_mask_prom = mean(abs(U_mask(logical(U_deseada))));
Mat_pesos = Weights .* (U_mask_prom ./ abs(U_mask));
U_mask = logical(U_deseada);
Mat_pesos(~U_mask) = 0;
```

A.3. Mean texture size determination

This program helps the user to calculate the mean grain size from SEM images of the channel. The user has to manually “draw” rectangles containing the features and the program calculates the mean and the standard deviation for the value and its error.

```
function getSEMroughness3
% Beggining of function
tic;                                clc;
% Variables
global X Y Z indM indC medida Dmedida tipoError puntos dx nPerror ...
    nMedidas calBar calibraciones datos
nChStart = 45;                  nChanels = 45;
nMedidas = 16;                   tipoError = 1;
rugosity = zeros(1,nChanels);    Drugosity = zeros(1,nChanels);
nameSalvar = 'test.mat';         nChMedidos = 0;
namePuntos = [];                 nPerror = 5;
IncluirIncertidumbreIndividual = 0;
limitToBreak = 2e-5;             calBar = 5e-6;
% List of names
names = cell(1,nChanels);
for ind = 1:nChanels
    names{ind} = ['Ch_' num2str(ind) '.tif'];
end
% List of points
calibraciones = zeros(nChanels,1);
if isempty(namePuntos)
    puntos = zeros(2,2,nMedidas,nChanels);
    automatic = false;
else
    try
        load(namePuntos,'puntos');
        if isempty(namePuntos)
            puntos = zeros(2,2,nMedidas,nChanels);
            automatic = false;
        else
            automatic = true;
            fprintf('Automatic\n')
        end
    catch ME
        fprintf('Unable to load image\n');
```

```
        ME.message;
        for ind = 1:length(ME.stack)
            ME.stack(ind)
        end
    end
end
% Start figure
hfig = figure(1);                clf;
hax = axes;

%% Main loop
for ind = nChStart:nChanels
    indC = ind;
    try
        % Load image
        info = imfinfo(names{ind});      Z = imread(names{ind},'tiff');
        Z = double(Z(:,:,1));            Z = flipdim(Z,1);
        fprintf(['\n\n\nImage: ',names{ind},'.\n\n'])
        % Create image space
        dx = 1e-6/info.XResolution;      s = size(Z);
        x = dx * (1:s(2));               y = dx * (1:s(1));
        [X,Y] = meshgrid(x,y);
        % Plot image
        hline = pcolor(X,Y,Z);           shading flat;
        colormap('gray');                axis image;
        % Set the plot to accept clicks
        cosa = allchild(hax);
        for ind2= 1:length(cosa)
            if strcmp(get(cosa(ind2),'Type'), 'surface')
                set(cosa(ind2),'HitTest','Off');
            end
        end
        % Measure
        medida = zeros(1,nMedidas);      Dmedida = zeros(1,nMedidas);
        for ind1 = 1:nMedidas
            indM = ind1;
            if automatic
                HacerCalculos(puntos(2,:,indM,indC),puntos(1,:,indM,indC));
            else
                str = ['Medida ',num2str(indM),' de ',num2str(nMedidas)];
                title(str);              set(hax,'Visible','On');
                set(hax,'ButtonDownFcn',@OnClickAxes);
                waitfor(hax,'Visible','Off');
            end
            if medida(indM) > limitToBreak && indM > 1
                break;
            end
        end
        % Store measurements
        if IncluirIncertidumbreIndividual
            [rugosity(ind),Drugosity(ind)] = ...
                MedidaError(medida,Dmedida,Dmedida(1));
        else
            [rugosity(ind),Drugosity(ind)] = ...
                MedidaError(medida,Dmedida,0);
        end
        fprintf('\nMedida final. Rugosidad: %g. Error: %g\n',...
            rugosity(ind),Drugosity(ind));
        nChMedidos = nChMedidos + 1;
    catch ME
        fprintf('Unable to load image\n');       ME.message
        for ind = 1:length(ME.stack)
            ME.stack(ind)
        end
    end%End try
end %End for
%% Save data
% Take out nonimportant data
```

```
datos = cell(nChMedidos,3);
indS = 1;
for ind = 1:nChanels
    datos{ind,1} = names{ind};          datos{ind,2} = rugosity(ind);
    datos{ind,3} = Drugosity(ind);
end
% Store
save(nameSalvar,'datos','puntos','nMedidas','calibraciones');       toc
end% End function

function OnClickAxes( hax, evt )
%% Extract relevant data
% Select the data
point1 = get(hax,'CurrentPoint'); % corner where rectangle starts
rbbox
point2 = get(hax,'CurrentPoint'); % corner where rectangle stops
HacerCalculos(point1,point2);
% End
set(hax,'Visible','Off');
end

function HacerCalculos(point1,point2)
% Variables
global indC indM medida Dmedida dx nPerror puntos nMedidas listaDX ...
    calBar calibraciones
% Measure distance
x = abs(point1(1,1) - point2(1,1));         y = dx * nPerror;
if indM == 1 && nMedidas > 1
    % Use the first one as calibration
    calibraciones(indC) = x;
    fprintf('Calibracion: %g +- %g\n',x,y);
elseif nMedidas == 1
    % When taking only one measurement per image, store it
    medida(1) = x;                          Dmedida(1) = y;
    fprintf('Rugosidad: %g +- %g\n',medida(1),Dmedida(1));
else
    % Use the rest of the readings to measure rugosity
    medida(indM-1) = x;                     Dmedida(indM-1) = y;
    fprintf('Rugosidad: %g +- %g\n',medida(indM-1),Dmedida(indM-1));
end
% Store data
puntos(2,:,indM,indC) = point1(1:2);
puntos(1,:,indM,indC) = point2(1:2);
end

function [medida,error] = MedidaError(setM,setE,varargin)
    % Variables
    global tipoError
    if nargin > 2
        Eind = varargin{1};
    else
        Eind = 0;
    end
    % Direct measures
    if tipoError == 1
        S = length(setM);               Sx = sum(setM);
        Sxx = sum(setM.^2);
    else
        S = sum(1./setE.^2);            Sx = sum(setM./setE.^2);
        Sxx = sum(setM.^2./setE.^2);
    end
    % Results
    medida = Sx/S;              error = 2 * sqrt((S*Sxx-Sx^2)/(S^2*(S-1)));
    error = sqrt(error^2 + Eind^2);
end
```

A.4. Waveguide modes analysis

This program calculates the mode diameter and overlapping losses by calculating the highest overlapping integral between the waveguide and fiber modes. The images are previously cut to eliminate the majority of the area at levels near to zero to reduce the influence of noise in the calculation. The code is:

```
function CaracterizacionPasiva
clc;
% Create name of files
Filenames = {'SM980_980 cut.tif'
    'Wg4c_980 20x20.tif'};
% Resolution of the images (pixels/um)
res = 7.256;
% Declare variables
l = length(Filenames) - 1;          Losses = inf * ones(1,l);
SizeX = zeros(1,l);                 SizeY = zeros(1,l);
% Main loop
[SizeXf,SizeYf] = CalcularTamano(Filenames{1},res);
for ind = 1:l
    [SizeX(ind),SizeY(ind)] = CalcularTamano(Filenames{ind+1},res);
    Losses(ind) = CalcularPerdidas(Filenames{1},Filenames{ind+1});
end
% Organize results
datos = cell(l+2,4);
datos{1,1} = 'Waveguide';               datos{1,2} = 'Losses (dB)';
datos{1,3} = 'X diameter (um)';         datos{1,4} = 'Y diameter';
datos{2,1} = Filenames{1};              datos{2,2} = 0;
datos{2,3} = SizeXf;                    datos{2,4} = SizeYf;
for ind = 1:l
    datos{ind+2,1} = Filenames{ind+1};      datos{ind+2,2} = Losses(ind);
    datos{ind+2,3} = SizeX(ind);            datos{ind+2,4} = SizeY(ind);
end
c = [150,80,80,80];                     p = [20,20,20+sum(c),40*(l+1)];
% Plot results
figure(1);                      clf
h = uitable();                  set(h,'Data',datos)
set(h,'Position',p);            set(h,'ColumnWidth',c)

function [Dx,Dy] = CalcularTamano(File,varargin)
% Function to calculate diameters of modes of a waveguide
try
    % Load image
     I = double(imread(File,'tif'));
    % If resolution is known, use it
    if nargin > 1
        res = varargin{1};
    else
        res = 1;
    end
    % Create space
    s = size(I);                x = 1:s(2);
    y = 1:s(1);                 [X,Y] = meshgrid(x,y);
    % Calculate center of mass
    s = sum(I(:));                  cx = round(sum(I(:).*X(:))/s);
    cy = round(sum(I(:).*Y(:))/s);
    % Fit
    Ix = I(cx,:);                       fitObjectX = fit(x',Ix','gauss1');
    Iy = I(:,cy);                       fitObjectY = fit(y',Iy,'gauss1');
    Dx = sqrt(2) * fitObjectX.c1;       Dy = sqrt(2) * fitObjectY.c1;
catch
    warning('Unable to load file')
    Dx = NaN;                           Dy = NaN;
end
```

```
function Loss = CalcularPerdidas(Filename1,Filename2)
% Function that calculates the overlaping integral of two mode images.

% Load images
try
    e1 = double(imread(Filename1,'tif'));
    e2 = double(imread(Filename2,'tif'));
    % Generate space variables
    s1 = size(e1);                          s2 = size(e2);
    d = s2-s1;                              N = prod(d);
    x1 = 1:s1(2);                           x2 = 1:s2(2);
    y1 = 1:s1(1);                           y2 = 1:s2(1);
    [X1,Y1] = meshgrid(x1,y1);              [X2,Y2] = meshgrid(x2,y2);
    % Adjust resolution so both images has the same
    Prop = 1;
    if Prop ~= 1
        % Recalculate space
        s2b = round(s2 * Prop);                 x2 = linspace(1,s2(2),s2b(2));
        y2 = linspace(1,s2(1),s2b(1));          [X2b Y2b] = meshgrid(x2,y2);
        % Interpolate image
        e2 = interp2(X2,Y2,e2,X2b,Y2b);         X2 = X2b;
        Y2 = Y2b;                               s2 = s2b;
    end
    % Calculate electric field
    e1 = sqrt(e1);                          e2 = sqrt(e2);
    % Substract background level
    e1 = e1 - min(e1(:));                   e2 = e2 - min(e2(:));
    % Main loop: overlping integrals
    K = zeros(d);                           Se1 = sum(e1(:).^2);
    Se2 = sum(e2(:).^2);                    n=0;
    fprintf('000%%')
    for ind1=1:d(1)
        for ind2=1:d(2)
            n = n+1;                                p = int8(ceil(n*100/N));
            fprintf('\b\b\b\b%0.3d%%',p);           e1aux = zeros(s2);
            e1aux(ind1:ind1+s1(1)-1,ind2:ind2+s1(2)-1) = e1;
            K(ind1,ind2) = sum(e1aux(:).*e2(:))^2/(Se1*Se2);
        end
    end
    fprintf('\n\n\n')
    % Max K
    Kmax = max(K(:));                   Loss = -10*log10(Kmax);
catch
    % If the files can't be loaded
    Loss = NaN;
end
```

Appendix B
Calculation of Equations 3.10 and 5.13

This appendix is dedicated to show the calculation of **Equations 3.10** and **5.13**.

B.1. Equation 3.10

The equation for calculating the phase map for accelerating beams is calculated from **Equations 2.22** and **2.23** [1], and the desired caustic trajectory (**Equation 3.9**):

$$\partial_{y_F}\varphi(y_F) = k\frac{c(z) - z\,c'(z)}{f} \tag{B.1}$$

$$y_F = f\frac{c'(z)}{\sqrt{1+[c'(z)]^2}} \tag{B.2}$$

$$c(z) = -\sqrt{\Re^2 - z^2} + d \tag{B.3}$$

The first step is calculating $z(y_F)$. In order to do that, $c'(z)$ has to be calculated:

$$c'(z) = \frac{z}{\sqrt{\Re^2 - z^2}} \tag{B.4}$$

Then, substituting **Equation B.4** in **Equation B.2**, $z(y_F)$ can be calculated:

$$z = \frac{\Re}{f}y_F \tag{B.5}$$

Then, the caustic trajectory and its derivative can be expressed as functions of y_F:

$$c(y_F) = -\frac{\Re}{f}\sqrt{f^2 - y_F^2} + d \tag{B.6}$$

$$c'(y_F) = \frac{y_F}{\sqrt{f^2 - y_F^2}} \tag{B.7}$$

This allows substituting **Equations B.5**-**B.7** in **Equation B.1**:

$$\partial_{y_F}\varphi(y_F) = \frac{kd}{f} - \frac{k\Re}{\sqrt{f^2 - y_F^2}} \tag{B.8}$$

Equation **B.8** can be integrated, obtaining the result:

$$\varphi(y_F) = \frac{k d y_F}{f} - k\Re \operatorname{atan}\left(\frac{y_F\sqrt{f^2 - y_F^2}}{f^2 - y_F^2}\right) \quad \textbf{B.9}$$

B.2. Equation 5.13

The operator in **Equation 5.13** is:

$$S_2 = \mathcal{R}[f' - d']\, Q\left[-\frac{1}{f'}\right] \mathcal{R}[z_1] \quad \textbf{B.10}$$

$\mathcal{R}$ and Q operators have the property [2]:

$$\mathcal{R}[z]Q[b] = Q[(b^{-1} + z)^{-1}]\, v[(1 + bz)^{-1}]\, \mathcal{R}[(z^{-1} + b)^{-1}] \quad \textbf{B.11}$$

Using it, **Equation B.10** can be written as:

$$S_2 = Q\left[-\frac{1}{d'}\right] v\left[\frac{f'}{d'}\right] \mathcal{R}\left[\left(\frac{1}{f' - d'} - \frac{1}{f'}\right)^{-1}\right] \mathcal{R}[z_1] \quad \textbf{B.12}$$

Now, using the property of $\mathcal{R}$ operator [2]:

$$\mathcal{R}[z_1]\mathcal{R}[z_2] = \mathcal{R}[z_1 + z_2] \quad \textbf{B.13}$$

Equation B.13 can be simplified to:

$$S_2 = Q\left[-\frac{1}{d'}\right] v\left[\frac{f'}{d'}\right] \mathcal{R}\left[\left(\frac{1}{f' - d'} - \frac{1}{f'}\right)^{-1} + z_1\right] \quad \textbf{B.14}$$

If we define the parameter δ as:

$$\delta = \left(\frac{1}{f' - d'} - \frac{1}{f'}\right)^{-1} + z_1 = z_1 + f'\left(\frac{f'}{d'} - 1\right) \quad \textbf{B.15}$$

Equation B.15 can be written as:

$$S_2 = Q\left[-\frac{1}{d'}\right] v\left[\frac{f'}{d'}\right] \mathcal{R}[\delta] \quad \textbf{B.16}$$

Operator $\mathcal{R}$ can be expanded as **Equation 5.9**:

$$\mathcal{R}[z] = Q\left[\frac{1}{z}\right] \upsilon\left[\frac{1}{\lambda z}\right] \mathcal{F}\, Q\left[\frac{1}{z}\right] \quad \textbf{B.17}$$

Then, substituting it in **Equation B.16** results in:

$$S_2 = Q\left[-\frac{1}{d'}\right] \upsilon\left[\frac{f'}{d'}\right] Q\left[\frac{1}{\delta}\right] \upsilon\left[\frac{1}{\lambda\delta}\right] \mathcal{F}\, Q\left[\frac{1}{\delta}\right] \quad \textbf{B.18}$$

Operators Q and υ can be commuted using the relation [2]:

$$\upsilon[c]Q[b] = Q[c^2 b]\upsilon[c] \quad \textbf{B.19}$$

So:

$$S_2 = Q\left[-\frac{1}{d'}\right] Q\left[\frac{f'^2}{d'^2\delta}\right] \upsilon\left[\frac{f'}{d'}\right] \upsilon\left[\frac{1}{\lambda\delta}\right] \mathcal{F}\, Q\left[\frac{1}{\delta}\right] \quad \textbf{B.20}$$

Finally, using the properties [2]:

$$\upsilon[c_1]\upsilon[c_2] = \upsilon[c_1 c_2] \quad \textbf{B.21}$$

$$Q[b_1]Q[b_2] = Q[b_1 + b_2] \quad \textbf{B.22}$$

Equation B.20, and thus **Equation 5.13 ,** is simplified to:

$$S_2 = Q\left[\frac{f'^2}{\alpha d'^2} - \frac{1}{d}\right] \upsilon\left[\frac{f'}{\lambda\alpha d'}\right] \mathcal{F}\, Q\left[\frac{1}{\delta}\right] \quad \textbf{B.23}$$

B.3. References

[1] A. Mathis, F. Courvoisier, R. Giust, L. Furfaro, M. Jacquot, L. Froehly, *et al.*, "Arbitrary nonparaxial accelerating periodic beams and spherical shaping of light," *Optics Letters,* vol. 38, pp. 2218-2220, 2013.

[2] J. Goodman, "Introduction to Fourier Optics," in *Electrical and Computer Engineering*, 2nd ed: McGraw-Hill, 1996.

Appendix C
Publications, communications and awards

C.1. Publications

Journal articles directly related to the thesis

1. **Name:** "Femtosecond-laser-induced compositional changes for high-performance photonics"
   Authors: J. Solís, T. T. Fernandez, J. Hoyo, P. Moreno-Zarate.
   Reference: SPIE Newsroom DOI: 10.1117/2.1201511.006127 (2015).

2. **Name:** "Mirrorless Yb3+ doped monoclinic double tungstate waveguide laser combining liquid phase epitaxy and multiplexed beam fs laser writing"
   Authors: J. Martínez de Mendívil, J. Hoyo, J. Solís, G. Lifante.
   Reference: J. Light. Tech. 33 4726–4730 (2015).

3. **Name:** "Channel waveguide fabrication in KY (WO4)2 combining liquid-phase-epitaxy and beam-multiplexed femtosecond laser writing"
   Authors: J. Martínez de Mendívil, J. Hoyo, J. Solís, M. C. Pujol, M. Aguiló, F. Díaz, G. Lifante.
   Reference: Opt. Mat. 47 304–309 (2015).

4. **Name:** "Controlling plasma distributions as driving forces for ion migration during fs laser writing"
   Authors: T. T. Fernandez, J. Siegel, J. Hoyo, B. Sotillo, P. Fernandez, J. Solis.
   Reference: J. Phys. D: Appl. Phys. 48, 155101 (2015).

5. **Name:** "Rapid assessment of nonlinear optical propagation effects in dielectrics"
   Authors: J. Hoyo, A. Ruiz de La Cruz, E. Grace, A. Ferrer, J. Siegel, A. Pasquazi, G. Assanto, J. Solis.
   Reference: Scientific Reports 5, 7650 (2015).

6. **Name:** "Dual regimes of ion migration in high repetition rate femtosecond laser inscribed waveguides"
   Authors: T. T. Fernandez, B. Sotillo, J. Hoyo, J. Valles, R. Martinez-Vazquez, P. Fernandez, J. Solis.
   Reference: IEEE Phot. Tech. Lett. 27 , 10 (2015).

7. **Name:** "Control of waveguide properties by tuning femtosecond laser induced compositional changes"
   Authors: J. Hoyo, R. Martinez Vazquez, B. Sotillo, T. T. Fernandez, J. Siegel, P. Fernández, R. Osellame, J. Solis.
   Reference: Appl. Phys. Lett. 105, 131101 (2014).

8. **Name:** "Femtosecond laser written 16.5 mm long glass-waveguide amplifier and laser with 5.2 dB cm^{-1} internal gain at 1534 nm"
   Authors: J. del Hoyo, V. Berdejo, T. T. Fernandez, A. Ferrer, A. Ruiz, J. A. Vallés, M. Á. Rebolledo, I. Ortega-Feliu, J. Solis.
   Reference: Laser Phys. Lett. 10 (2013) 105802 (7pp).

9. **Name:** "Ridge waveguide laser in Nd:$LiNbO_3$ by Zn-diffusion and femtosecond-laser structuring"
   Authors: J. Martínez de Mendívil, J. Hoyo, J. Solís, G. Lifante.
   Submitted to: Optical Materials

10. **Name:** "High efficiency waveguide-based optical amplifiers and lasers fabricated by ion migration assisted fs-laser structuring"
    Authors: J. del Hoyo, P. Moreno-Zárate, J.Vallés, M. A. Rebolledo, A. Villafranca, J. Solis.
    In preparation.

Articles in proceedings

11. **Name:** "Modeling of single pulse 3-D energy deposition profiles inside dielectrics upon fs laser irradiation with complex beam wavefronts"
    Authors: J. Hoyo, M. Galván-Sosa, A. Ruiz de la Cruz, E. J. Grace, A. Ferrer, J. Siegel, J. Solis.
    Reference: Proc. of SPIE Vol. 9131, 91310G 1-8, (2014).

12. **Name:** "Strong ion migration in high refractive index contrast waveguides formed by femtosecond laser pulses in phosphate glass"
    Authors: J. Hoyo, B. Sotillo, M. Hernandez, T. Toney Fernandez, P. Haro-González, D. Jaque, P. Fernandez, C. Domingo, J. Siegel, J. Solis.
    Reference: Proc. of SPIE Vol. 9131, 91315G 1-7, (2014).

13. **Name:** "Femtosecond-laser inscription via local modification of the glass composition in phosphate glasses"
    Authors: J. Hoyo, B. Sotillo, J. Siegel, T. T. Fernandez, P. Fernandez, P. Haro, D. Jaque, M. Hernandez, C. Domingo, J. Solis.
    Reference: Conference Paper, CLEO: Science and Innovations, San Jose, California United States, June 8-13, 2014, ISBN: 978-1-55752-999-2, Laser-Driven Dynamics in Materials (STh4B).

Other journal articles

14. **Name:** "Modeling of astigmatic-elliptical beam shaping during fs-laser waveguide writing including beam truncation and diffraction effects"
    Authors: A. Ruiz de la Cruz, A. Ferrer, J. del Hoyo, J. Siegel, J. Solis.
    Reference: Applied Physics A (2011) 104: 687-693.

C.2. Communications

1. **Name:** "Waveguide optical amplifiers and lasers produced by fs-laser induced ion migration in phosphate glass"
   Authors: P. Moreno-Zarate, J. Hoyo, J. Vallés, M. A. Rebolledo and J. Solis.
   Conference: SPIE Photonics West 2016 (Poster presentation, February 2016, San Francisco, USA).

2. **Name:** "Influence of composition on ion migration processes in femtosecond laser written optical waveguides in K2O-La2O3-P2O5 glasses"
   Authors: P. Moreno Zarate, L. Labrador-Paez, J. Hoyo, F. Muñoz, J. Siegel and J. Solís.
   Conference: ICG 2016 (Poster presentation, April 2016, Shangai, China).

3. **Name:** "Local composition control by ion migration induced by femtosecond-laser inscription for the fabrication of high performance active and passive waveguides"

Authors: J. Hoyo, P. Moreno Zárate, J. Vallés, M. A. Rebolledo, L. Labrador-Páez, J. Siegel, and J. Solís.
Conference: USTS 2015 (Poster presentation, November 2015, Madrid, Spain).

4. **Name:** "Tuning the local composition of glasses by fs-laser irradiation for producing high performance active and passive waveguides"
Authors: J. Hoyo, P. Moreno, T. T. Fernandez, J. Siegel, J. Solis.
Conference: Optoel 2015 (Poster presentation, July 2015, Salamanca, Spain).

5. **Name:** "Ridge waveguide laser in Nd:LiNbO3 by Zn-diffusion and fs-laser structuring"
Authors: J. Martinez de Mendivil, J. Hoyo, J. Solis, G. Lifante.
Conference: Optoel 2015 (Poster presentation, July 2015, Salamanca, Spain).

6. **Name:** Mirrorless KYW:Yb waveguide laser combining liquid phase epitaxy and multiplexed beam fs laser writing"
Authors: J. Martinez de Mendivil, J. Hoyo, J. Solis, G. Lifante.
Conference: Optoel 2015 (Poster presentation, July 2015, Salamanca, Spain).

7. **Name:** "Active properties of femtosecond laser written waveguides produced by ion migration in Er/Yb codoped phosphate glasses"
Authors: J. Hoyo, P. Moreno, J. Siegel, J. Solis.
Conference: E-MRS 2015 spring meeting (Poster presentation, May 2015, Lille, France)

8. **Name:** "Femtosecond-laser inscription via local modification of the glass composition in phosphate glasses"
Authors: J. Hoyo, B. Sotillo, J. Siegel, T. T. Fernandez, P. Fernandez, P. Haro-González, D. Jaque, M. Hernandez, C. Domingo, J. Solis.
Conference: CLEO 2014 US (Oral presentation, June 2014, San Jose, US)

9. **Name:** "Strong ion migration in high refractive index contrast waveguides formed by femtosecond laser pulses in phosphate glass"
Authors: T. T. Fernandez, J. Hoyo, P. Haro-González, B. Sotillo, M. Hernandez, D. Jaque, P. Fernandez, C. Domingo, J. Siegel, J. Solis.
Conference: SPIE Photonics Europe 2014 2014 (Oral presentation, April 2014, Brussels, Belgium)

10. **Name:** "Shaping the effective focal volume inside dielectrics upon fs laser processing with complex beam wavefronts"
Authors: J. Hoyo, M. Galván-Sosa, A. Ruiz de la Cruz, E. J. Grace, A. Ferrer, J. Siegel, J. Solis.
Conference: SPIE Photonics Europe 2014 (Oral presentation, April 2014, Brussels, Belgium)

11. **Name:** "Waveguide mode conditioning via slit shaped femtosecond laser pulses"
Authors: T. T. Fernandez, J. Hoyo, V. Berdejo, A. Ferrer, A. Ruiz, J. Vallés, M. A. Rebolledo, I. Ortega, J. Solis.
Conference: Euromat 2013 (Poster presentation, September 2013, Seville, Spain)

12. **Name:** "Guía escrita con láser de femtosegundos en un vidrio fosfatado codopado con Er/Yb con ganancia interna de 5.2 dB/cm"
Authors: J. Hoyo, V. Berdejo, T. T. Fernandez, A. Ferrer, A. Ruiz, J. A. Vallés, M. Á. Rebolledo, I. Ortega, J. Solis.
Conference: Optoel 2013 (Poster presentation, July 2013, Alcalá de Henares, Spain)

13. **Name:** "High Gain Short Length Optical Amplifier in Heavily Doped Phosphate Glass for Miniature Optics"
Authors: T. T. Fernandez , J Hoyo, V. Berdejo, A. Ruiz, A. Ferrer, I. Ortega-Felui, J. Vallés, M. A. RebolledoJ. Solis.
Conference: CLEO Europe 2013 (Poster presentation, June 2013, Munich, Germany)

14. **Name:** "Modeling of single pulse 3-D energy deposition profiles inside dielectrics upon fs laser irradiation with complex beam wavefronts"
Authors: J. Hoyo, A. Ruiz de la Cruz, A. Ferrer, J. Siegel, J. Solis.
Conference: E-MRS Spring meeting 2013 (Oral presentation, May 2013, Strasbourg, France)

15. **Name:** "High gain active waveguides produced by high repetition rate fs laser writing in Er-Yb codoped phosphate glasses"
Authors: J. Hoyo, V. Berdejo, A. Ferrer, J. A. Vallés, A. Ruiz de la Cruz, M. Á. Rebolledo, J. M. Fernandez-Navarro, J. Solis.
Conference: E-MRS Spring meeting 2012 (Oral presentation, May 2012, Strasbourg, France)

Invited papers

16. **Name:** "Expanding the parameter space in optimising femtosecond laser written waveguides for photonics devices"
Authors: T. T. Fernández, J. Hoyo, J. Siegel, J. Solís.
Conference: ICOOPMA 2014 (Oral presentation, Agoust 2014, Leeds, United Kingdom)

17. **Name:** "Ion migration assisted femtosecond laser inscription of high performance active and passive waveguides for photonic devices"
Authors: J. Solis, T. T. Fernandez, J. Hoyo, J. Siegel.
Conference: Advanced Laser technologies 2014 (Oral presentation, October 2014, Casis, France)

18. **Name:** "Active waveguides for mid-IR (3–4 μm) wavelengths fabricated by femtosecond laser inscription in Dy^{3+} doped tellurite glass"
Authors: T. T. Fernandez, B. Richards, G. Jose, A. Jha, J. Hoyo, A. Ruiz De la Cruz, J. Solis.
Conference: ICTON 2013 (Oral presentation, June 2013, Cartagena, Spain)

C.3. Awards

- **I Premio Carlos Gómez-Reino.** Prize to the best poster paper presented in Optoel 2015 conference by a PhD student (July 2015). **Awarded to J.Hoyo for the work:** "Tuning the local composition of glasses by fs-laser irradiation for producing high performance active and passive waveguides". J. Hoyo, P. Moreno-Zárate, J. Siegel, J. Solis.